ULB UNIVERSITÉ LIBRE DE BRUXELLES, UNIVERSITÉ D'EUROPE

Université Libre de Bruxelles

Faculty of Applied Sciences
Chemicals and Materials Departement

« A contribution to the study of cold gas dynamic spraying of copper: Influence of the powder characteristics on the mechanical properties of the coating»

Thesis

Submitted for the degree of

Doctor of Applied Sciences

By

Kairet Thomas

Thesis supervisor:

Prof. Marc Degrez

November 2007

Abstract

The cold gas dynamic spray process developed in the middle of the 80's reached the industrial stage in development. Even so, many scientific investigations still go on. The nature of the bond between the coating and the substrate is the subject of some controversy. The development of the process will be improved by understanding how the properties of the powder and the mechanical properties of the substrate influence the bonding process. This study analyses the basic dynamics of the process when copper is sprayed.

- The one dimensional isentropic model of the gas behaviour in a Laval type nozzle allows evaluating the effect of the gas stagnation pressure P_0 and temperature T_0 on the impact velocity and temperature of the powder particle.

- The analysis of single splats on two substrates (aluminium and steel) shows the influence of the substrate on the deformation of single particles and the influence of the impact speed on the impact shape.

- Coatings are made of with powders with a specific size distribution. Two copper powders with a different size distribution are compared based on the deposition efficiency (D.E.) and the mechanical properties of the coating. The mechanical properties tested are the microhardness, the bond strength and the nanohardness.

- X-ray diffraction will show that the two powders have an initial very different microstructure. The consequence of this is a different deformation mechanism during the coating build up.

- An Auger analysis of the interface has shown the presence of diffusion zone when copper was sprayed on the Al and TA6V substrate.

It appears that the size distribution will determine the final impact conditions of the powder. The microstructure of the powder and the oxide content of the powder yield different deformation processes and may explain the differences in D.E. and mechanical properties. The Auger analysis of the interface has yielded diffusion zone that were not expected but some mechanisms under impact loading can explain there presence.

Résumé

Le procédé de projection thermique à froid a été développé dans le milieu des années 80 et il arrive au stade industriel. Néanmoins, plusieurs développements scientifiques sont encore en cours. La nature de du lien entre la poudre et le substrat est toujours l'objet de certaines controverses. Le développement futur du procédé nécessite une bonne compréhension de l'influence des de la poudre et des propriétés du substrat sur le mécanisme d'adhérence. Cette étude va mettre en évidence les principaux facteurs influençant la projection de cuivre.

- Le modèle unidimensionnel isentropique du gaz parfait dans une buse convergente/ divergente permet de déterminer l'influence de la pression de stagnation et de la température de stagnation sur la vitesse et la température d'impact des particules de poudre.

- L'analyse d'impact unique sur les substrats d'acier et d'alliage d'Al (AA2014) montre l'influence du substrat sur la déformation des particules de poudre. La vitesse d'impact a une conséquence importante sur la forme d'une particule projetée sur une surface.

- Les revêtements sont fabriqués à partir de poudre avec une granulométrie donnée. Deux poudres avec une distribution de taille différente sont comparées par leur rendement de dépôt et les propriétés mécaniques des revêtements obtenus. Les propriétés mécaniques testées sont la microdureté, l'adhérence et la nanodureté.

- La diffraction par rayons-X montre que les deux poudres ont initialement une microstructure très différente. Lors de l'impact, les deux poudres vont se déformer de manière différente et ceci se traduit dans la microstructure.

- La spectroscopie Auger montre qu'une zone de diffusion s'est formée à l'interface entre le cuivre et les deux substrats d'Al et de TA6V.

La distribution de taille des poudres a une influence considérable sur la vitesse et la température d'impact des particules de poudres mais il apparaît que d'autres facteurs ont aussi énormément d'influence. Le taux d'oxyde dans la poudre a une influence très importante sur le rendement et l'adhérence du dépôt. Les deux poudres projetées ont une microstructure initiale très différente et ceci se traduit par une déformation différente des particules de poudre dans le revêtement.

Remerciements

Ce travail est réalisé dans l'équipe CREA-SURF du service Matières & Matériaux de l'Université Libre de Bruxelles dans le cadre d'un projet FIRST EUROPE objectif 3 financé par la Région wallonne et par le FSE (Fonds Social Européen).

Je tiens à exprimer mes plus vifs remerciements au Professeur Marc Degrez pour les conseils avisés qu'il a su me donner tout au long de mon travail et lors de la rédaction de ce texte.

Je tiens à remercier le Prof. D.G. Mc Cartney de Nottingham University pour ses critiques constructives et ses suggestions judicieuses qui m'ont guidé dans la partie de ce travail réalisée en Angleterre (School of Material, Mechanical and Manufacturing Engineering).

Je remercie vivement Monsieur Campana, ingénieur de recherche de la société Advanced Coating, pour son aide et ses conseils dans la réalisation des essais de projection thermique à froid.

Je remercie également M. G. Foucart, J-M Barbier, J. Vialle, T. Grine, K. Imed, C. Secouard, étudiant venu faire leur stage chez Advanced Coating pour leur collaboration fructueuse.

Par ailleurs, un très grand merci à Monsieur Gaëtan Di Stefano, ingénieur civil chimiste, pour m'avoir guidé et aidé pendant la première partie de mon travail.

Les mesures Auger ont été réalisées en collaboration avec la VUB et le département « META » dirigé par le Prof. J. Vereecken. Les mesures ont été réalisées par Mr O. Steenhaut et je le remercie de son aide.

Je remercie Mr D. Bultreys de FEI Europe pour les découpes de lame mince utilisée dans le TEM.

Ce travail n'aurait certainement pu être mené à bien sans les compétences techniques et la dextérité des ouvriers d'Advanced Coating. Leur précieuse coopération m'a permis d'avancer rapidement et de mieux maîtriser la technologie.

Merci aussi à tous mes collègues de Nivelles et de Bruxelles, qui ont su m'accorder une partie de leur temps précieux lors de la réalisation de ce travail.

Merci à tous mes proches pour leur soutien lors des différentes étapes de ce travail. Leur soutien moral et pratique m'a permis de m'épanouir au cours de mon travail et de le mener à son terme.

« Le jour viendra que, par une étude suivie de plusieurs siècles, les choses actuellement cachées paraîtront avec évidence, et la postérité s'étonnera que des vérités si claires nous aient échappé »
Sénèque cité par Laplace à propos du mouvement des comètes

List of Figures

List of Tables

Chapter 1 Introduction - The Cold Gas Dynamic Spray Process and the Thermal Spray Family

1.1 Thermal Spray Processes

The thermal spray technologies regroup a set of various surface treatment processes based on common principles. The thermal spray processes transform a metallic powder (with a given size distribution and composition) into a coating deposited on a substrate surface. The steps between the original powder and the final coating are determined by the process characteristics.

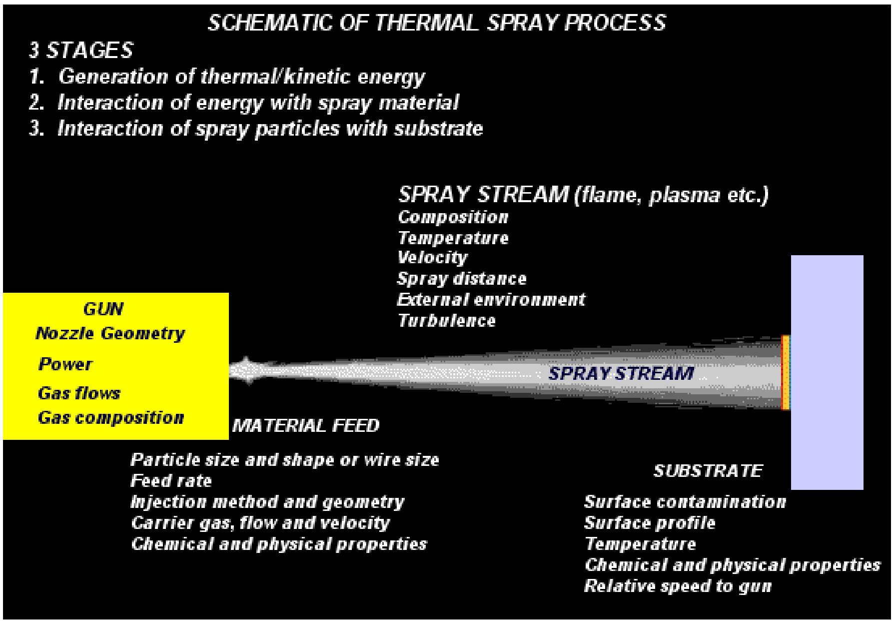

Figure 1-1: Thermal spray process schematic. [1]

Three different stages can be isolated in the process:

- The powder in the thermal spray process receives kinetic and thermal energy through an exchange with a heated carrier gas and/or a flame. This stage is done inside a nozzle.
- The powder is carried by the gas stream to the substrate's surface where the coating builds up. Before reaching the surface, the powder interacts with the gas stream and the surrounding atmosphere.
- Once the powder reaches the surface, the final state of the powder with its thermal and kinetic energy will interact with the surface and determine the quality of the coating and the bonding.

Figure 1-1 summarizes all the different influences on thermal spray processes.

When the powder particle impacts the surface, it flattens; so, complex energy and metallurgical processes insure a good bonding. The flattened powder particle is called a "splat". The study of single splats gives precious information on the quality of the surface to particle interaction. The build up of a coating starts with the understanding of single splats.

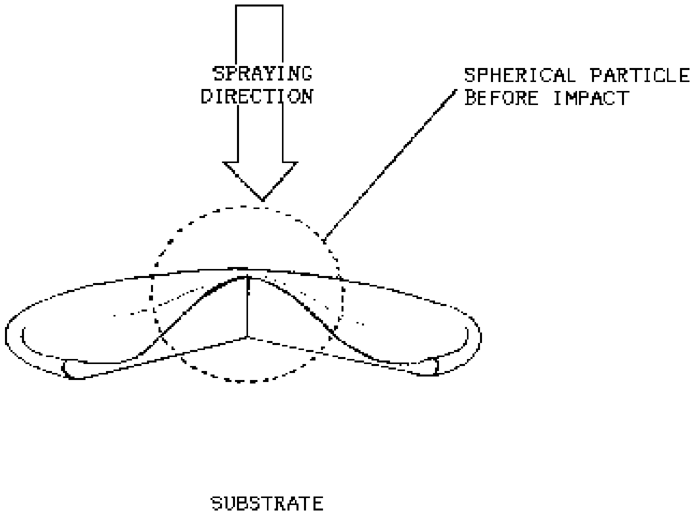

Figure 1-2: Schematic of a single splat. [1]

Figure 1-2 shows a schematic of a single splat. A spherical particle flattens on the contact of a hard surface. The importance of this flattening is called the "flattening ratio". Its value is a complex function of materials properties and thermal and kinetic states of the particle before impact. It's common to see studies of the flattening ratio of powder particles for a thermal spray process.

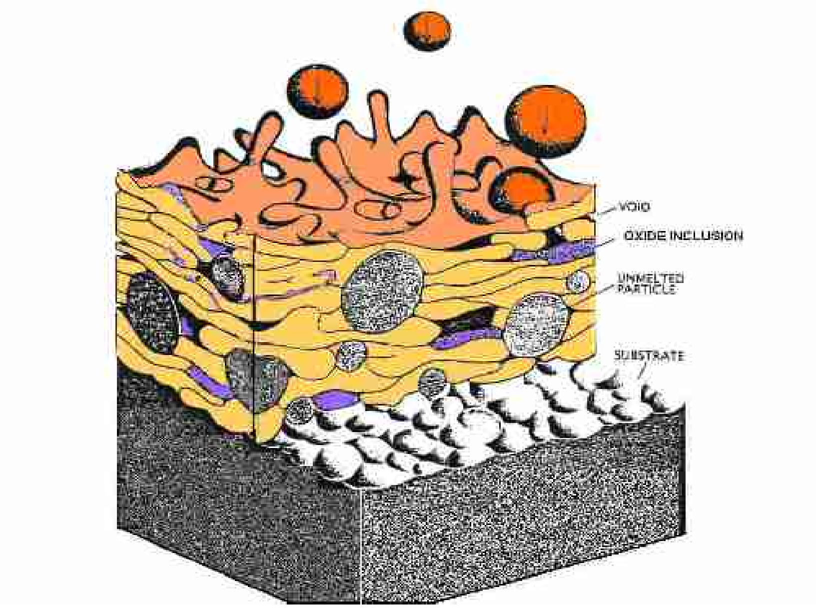

Figure 1-3: Schematic of a thermal spray coating. [1]

Finally, the coating is an assembly of many single splats pilled up like pancakes. Unfortunately before reaching the substrates surfaces, the powder particles degrade in the gas stream. They get oxidized by interacting with oxygen in the atmosphere. Depending on the thermal spray process particularities, powder particles melt totally or partially. Voids are also present in the coating. During cooling, the materials in the coating contract and voids form.

They are highly present in high temperature processes like plasma spraying. High velocity processes like HVOF reduce porosity and voids by high speed impacts that compress the coating. Unmelted particles are also present in the coating. Figure 1-3 shows a schematic of the coating build up.

1.2 Limitations of Thermal Spray Processes

Thermal spray processes involve heating the powder to high temperatures (close to the melting temperature or higher). The heating sources have different natures:

- In the High Velocity Oxy-Fuel Process (HVOF), the heating is done by a flame. A combustion fuel (propane, kerosene…) is injected in the nozzle with oxygen in order to generate a flame.
- In the plasma process, a gas is ionized and transformed into plasma. The powder injected in the plasma flow is directed towards the substrate surface.
- In the wire arc spray process, a wire made with the spray material is melted by an electric arc and a gas jet atomizes the molten material towards the substrate.

Degradation of the powder is unavoidable when process temperature is high.

- Materials like copper, titanium, aluminium, … will oxidize immediately.
- Other degradations like decarburisation occur when carbides are sprayed at high temperature.
- Internal stresses are not favourable for good bonding.

The trend in the industry is to reduce the exchange of thermal energy with the powder by increasing the powder's speed in the nozzle. The trend is to replace the thermal energy by the kinetic energy. This has justified the development of the "cold gas dynamic spray process" (CGDS) called "cold spray".

1.3 The Cold Gas Dynamic Spray Process

The process was developed in the Middle of the 80's at the Institute of Theoretical and Applied Mechanics of the Russian Academy of Science in Novosibirsk by A. Papyrin and his colleagues. The process is based on the acceleration of powder particles by a cold gas stream to very high velocities (300 to 1200 m/s). The gas is accelerated in a Laval Nozzle to supersonic speeds and the drag applied to each powder particles accelerates them to high velocities. The gas is heated in order to increase the expansion of the gas in the nozzle and therefore the gas velocity. This heating remains well below the melting temperature of most materials.

Figure 1-4 shows a schematic of the cold gas dynamic spray process. The gas is injected at high pressure in the nozzle. It is separated into two flows:

- The first flow goes to the powder feeder and injects the powder in the nozzle.
- The second flow is the main flow. It goes to the gas heater where it heats up and is injected in the nozzle.

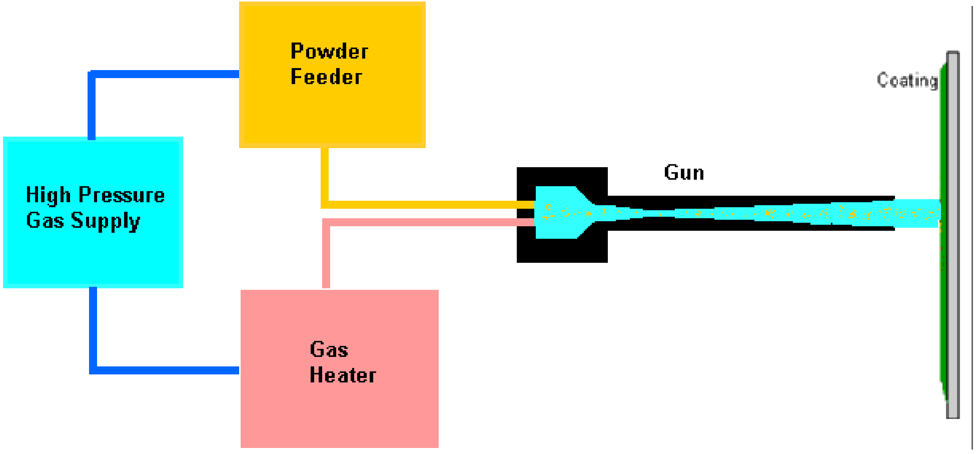

Figure 1-4 : Schematic of the cold gas dynamic spray process. [1]

The main advantage of this process is that it opens the possibility to make coatings with unoxidized materials. The composition of the coating will be determined by the original composition of the powder. This is the main advantage of this technology.

The formation of the coating is due to impact of single splats on the surface. Upon impact, the kinetic energy is converted into thermal energy. The nature of the bond between the surface and the particle is still subjected to a large number of scientific investigations.

Table 1-1 : Comparison between the Cold Spray Process and other thermal spray processes (HVOF and plasma). [2]

	T° gas stream (K)	Gas speed (m.s^{-1})	T° of the powder (K)	Powder's speed (m.s^{-1})	Density of the coating (%)	Oxidation level
Cold spray	300-900	1000-2500	<800	300-1200	>95	none
HVOF	2700	500-1200	2000	200-1000	>95	moderate
plasma	15000	300-1000	>3800	200-300	90-95	Moderate to elevated

Table 1-1 shows a comparison between the CGDS process and other thermal spray processes. It appears clearly that the process temperature is well below the temperature involved in other spray processes.

1.4 Context and Development of this Work

This project is the result of collaboration between the “Chemicals & Materials Service” in the department of Applied Sciences of The University of Brussels and the private company “Advanced Coating S.A.”. The project started in October 2003 for a period of 4 years. The financing from the Walloon Government allowed the researcher to do 6 month training abroad within the University of Nottingham. Work has been done in the “School of M3”with Professor D.G. McCartney.

The cold gas dynamic spray equipment is property of Advanced Coating S.A. hence developments were done on their industrial installation used for production. All developments have been done with an industrial perspective. The demand for pure coatings is real. Copper is a material that has a high thermal conductivity and a high electrical conductivity. The CGDS process allows depositing copper very easily. The possibility to exploit the purity of this material in a number of applications is open. For an industry a number of steps need to be done:

- The determination of the optimal set of process conditions.
- The determination of the best powder characteristics. It is a necessity to understand which powder is best suitable for the process based on grain size distribution and mechanical properties.
- The evaluation of bonding is an important part of the evaluation of the coating. The role of the substrate on bonding must be assessed through bond strength.

From a scientific point of view, the CGDS process submits materials to extreme deformation conditions. High values of strain rate $\left(\dot{\varepsilon} \approx 10^9\right)$, a high value of temperature gradient $\left(\dot{T} \approx 10^9\, K \cdot s^{-1}\right)$ and high pressure (5-15 GPa) during 40 ns pushes standard understanding of materials to extreme limits. The bonding mechanism under conditions has not been fully understood yet. This thesis attempts to understand the basics of the bonding mechanisms and how material properties determine the quality of the bonding.

1.5 The Scope of This Thesis

The outline of this thesis will follow the description of thermal spray processes like in Figure 1-1:

- The generation of the kinetic energy inside the nozzle. The influence of the powder’s size distribution, shape, density and mechanical properties will determine the value of kinetic and thermal energy of the particle before it reaches the substrate’s surface and bond. This section is related to the aerodynamical characteristics and behaviour of the powder in the nozzle. The influence of the geometry of the nozzle will be linked to the generation of kinetic and thermal energy. The interaction of the powder with the environment (exterior of the nozzle) before reaching impact on the substrate can be treated by understanding the aerodynamics of gas at the exit of a Laval nozzle.

- The last stage is the bonding of the powder on the surface. In the case of cold spray, the onset of bonding is associated with the formation of adiabatic shear bands at the interface between particle and substrate. Many questions remain unsolved on the nature of the bonding. The bond can be mechanical or chemical. The influence of surface properties on the bonding is not evident. This work will attempt to explain the nature of the bonding based on analysis of the interface.

This thesis will start by a state of the art of copper cold spraying. The generation of the kinetic energy and the influence of the powder characteristics on the final impact will be modelled in Chapter 3. The last stages of the coating build up will be analyzed in the following chapters. Chapter 4 will describe the impact of single splats since they are the fundamental unit in the coating build up. The next stage is the optimisation of the process (done in Chapter 5). The next chapters will give an analysis of the mechanical properties of the coatings, an X-ray diffraction analysis of both powders and coatings and, finally, an interfacial analysis.

The outline of the different chapters is the following:

Chapter 2: This chapter describes the state of the art on CGDS technology with a special focus on the cold spraying of copper coatings. The process fundamentals will be described. This material has been extensively studied in the scientific literature. Another part of this chapter will focus on the microstructural evolution of copper submitted to extreme mechanical conditions close to the one’s present in the CGDS process.

Chapter 3: Based on a simple model of the nozzle, the aerodynamics of the powder flow in the nozzle can be linked to particle speed and temperature. This model will then be compared to laser velocimetry measurements done with the DVP2000/ CPS2000 instrument.

Chapter 4: The study of single splats gives a significant insight on the process. They are the building blocks of the coating. This chapter will compare single splats of copper on two substrates: steel and aluminium alloy (2024). The substrates were heat treated in order to get different hardness values.

Chapter 5: This chapter will describe the design of experiment used to optimise the process and the method used to compute the efficiency of the process.

Chapter 6: Mechanical properties have been measured using standard techniques. Microhardness, bond strength, nanoindentation have been used in order to assess the quality of the coating. They give a number of information on the bonding mechanism.

Chapter 7: X-ray diffraction of the powder and the coating allow characterising the microstructure of the powder before the impact on the coating and the coating’s microstructure. The mechanical deformation induced by the plastic deformation will induce changes in the microstructure that will be influenced by the original state of the powder.

Chapter 8: Interfacial analysis of the coatings. Auger and TEM analysis of the coating allow analysing the coating within a few nanometres. It will be an attempt to identify the materials present at the interface.

Conclusion

Chapter 2 The Cold Gas Dynamic Spray Process: State of the Art

2.1 Introduction

Recently, the cold gas dynamic spray process (CGDS), referred to as “cold spray”, integrates the wide family of thermal spray technologies (HVOF, plasma, detonation gun arc spray and others). The process is a high rate coating fabrication technique that involves accelerating fine solid powders (generally 1-50µm) in a supersonic jet of compressed gas (with velocities ranging between 500-1200m/s) on a substrate where, upon impact, the particle undergoes severe plastic deformation and bond to the surface. A wide range of pure metals, metallic alloys, polymers and composites can be deposited on to a variety of substrate materials. The gases used are Helium, nitrogen and air and the inlet pressure in the Laval tube reaches 30 bars. Higher gas velocities can be achieved by preheating the gas up to temperatures of 900K.
The process can be separated in 3 mains stages:

- The first stage is the generation of the transfer of kinetic energy to the powder by the high speed gas in the nozzle. The parameters influencing these stages are the size of the powder particles, its density, the choice of gas, the geometry of the nozzle, … . All these parameters can be linked by hydrodynamical models describing how powder interacts with a gas flow.
- The second stage is the transfer of the powder particle from the exit of the nozzle to the surface of substrate. The powder interacts with the turbulences at the exit of the nozzle and the surrounding atmosphere. The design of the nozzle, the gas used, and the standoff distance will influence the interaction of the powder with the turbulences.
- The last stage is the bonding of individual powder grains on the surface of the substrate. Complex metallurgical mechanisms occur at the interface between the particle and the surface.

The state of the art will separate the last stage from the two first stages. The two first stages are determined by the gas hydrodynamics in the process and have been described extensively in the scientific literature. They will determine the particle impact conditions (its temperature and speed).
The last stage is influenced by the interaction between complex material properties and mechanical solicitations with the particle’s impact conditions. This chapter will describe the scientific literature on this stage separately since it involves more material science. The influence of the powder characteristics (shape, oxidation state,…) and the surface preparation will also be described in this state of the art.

2.2 Description of the Process

The cold gas dynamic spray process (CGDS) is based on the injection of a main carrier gas at a given pressure and temperature in the Laval type nozzle (Figure 2-2). The initial value of the gas pressure before entering the convergent part of the nozzle is called the "stagnation pressure **P_0**" and the initial value of the gas temperature is called the "stagnation temperature **T_0**". The Figure 2-1 shows a schematic of the process.

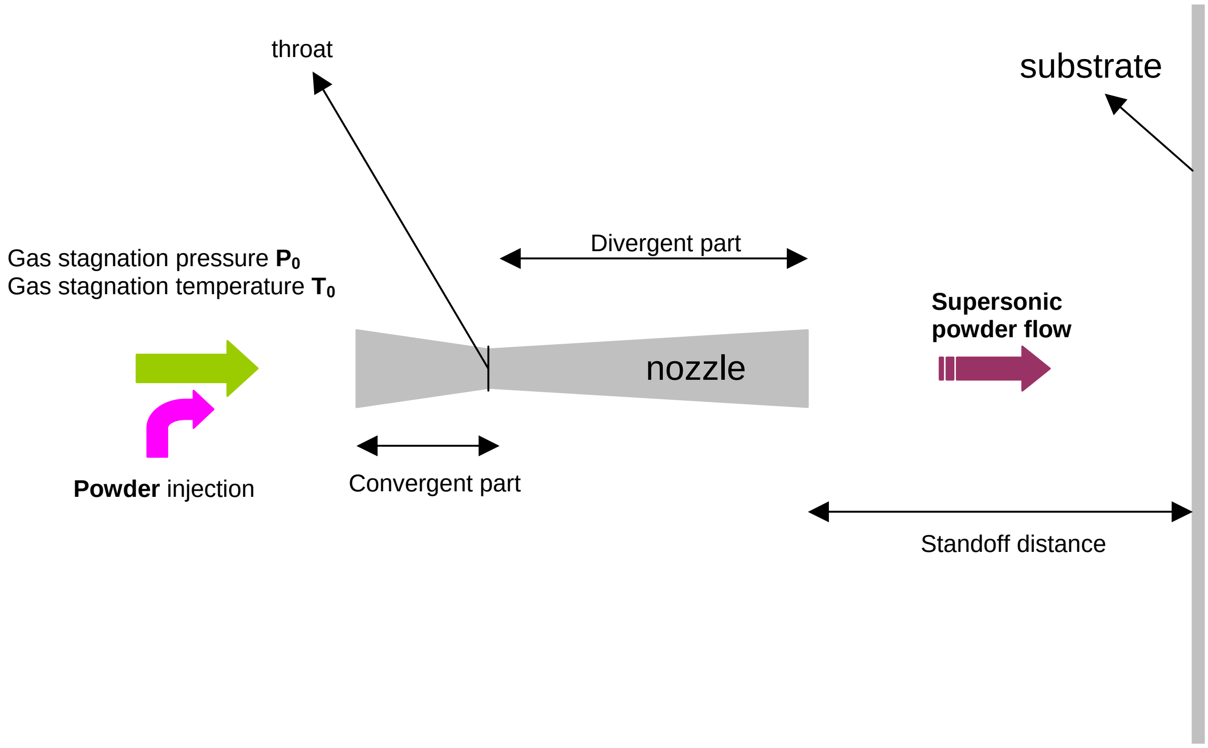

Figure 2-1 : Schematic of the cold gas dynamic spray process.

The gas is heated and injected at high pressure in the convergent part of the nozzle. In this section the gas speed is subsonic (the gas speed is below Mach number =1). At the throat, the gas speed reaches its sonic value (Mach number value equals one). When the gas passes the throat, its speed is increased beyond sonic values. In this part, the gas speed is supersonic. The value of the gas speed and temperature in the nozzle is determined by the geometry of the nozzle and the gas physical properties.

Once the gas leaves the nozzle, several phenomena are possible.

- The gas can be underexpanded. A recompression will occur at the exit of the nozzle. This means that the gas pressure at the exit of the nozzle is below the ambient pressure. The external pressure will compress the gas stream exiting the nozzle.
- The nozzle can be adapted to the external pressure. The gas stream at the exit of the nozzle will neither be compressed or overexpanded.
- The gas stream at the exit of the nozzle can be overexpanded. The gas pressure at the exit of the nozzle is higher that the ambient pressure, the gas needs to continue its expansion to reach the external pressure.

The most favourable situation is the case when the nozzle is adapted to external pressure. In the case of an exit pressure below the ambient pressure, the gas stream is recompressed through as series of oblique shock waves called the “mach disks”. These disks disturb the powder flow in the process.

Another phenomenon is the oscillation of the gas stream jet between the exit of the nozzle and the substrate surface. It is more complex to describe but this effect can be limited by limiting the standoff distance.

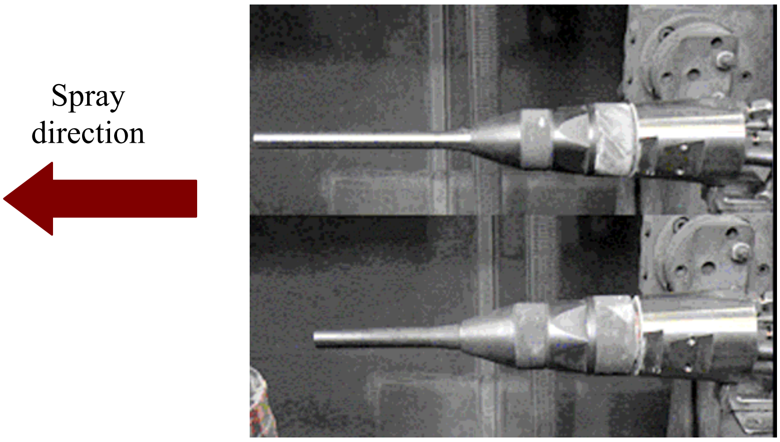

Figure 2-2 : Example of two WC cold spray nozzles with different lengths.

The powder is injected at ambient temperature but at the stagnation pressure $\mathbf{P_0}$ in the convergent part of the nozzle near the throat. The gas in the convergent part is subsonic and heated; the powder’s time of flight on this part has to be limited in order to avoid temperature effects. Most of the acceleration of the powder is done in the divergent part where the gas is supersonic. In this part, the gas speed increases significantly while its temperature drops. The gas expansion is accompanied by a decrease in the temperature. Since the gas expands in the divergent part, its density also drops. The increase in the powder’s velocity will depend on the gas speed, the gas density and the powders characteristics (size distribution, density …). High gas speed will be favourable to high powder velocity, while low gas density has the opposite influence.

Near the substrate, the supersonic gas stream recompresses. A shock wave above the substrate’s surface makes the transition from a supersonic flow to a subsonic flow in contact with the surface. The gas stream’s properties changes from a supersonic expanded flow to a low velocity, high temperature gas in an abrupt way. The powder flow arrives to the surface carried by the supersonic flow and passes through the shock wave. The sudden drop in gas velocity and increase in gas density will decrease significantly the speed of the powder particles with insufficient inertia.

The physics of a gas flow in a convergent-divergent nozzle are well described in several text books. Several publications [3] in the cold spray used a one dimensional model of the process to understand the interaction between the parameters and the powders velocity and temperature. Only 3D fluid dynamics calculations allow taking into account complex phenomena like boundary layer in the nozzle, geometrical effect and shock wave dynamics but this requires heavy computer fluid dynamics calculations. The next section will develop the one dimensional model in order to give a simple link between spray parameter and powder characteristics upon impact.

Once the powder particle reaches the surface with a given speed and temperature, the bonding with the surface has to be analysed. In the cold gas dynamic spray process, a coating is obtained when the powder particle reaches the surface with a minimum value of speed. This minimum value of powder speed to obtain a coating is called the "**critical speed**" (examples of values in Table 2-1). Beyond this value of speed, the powder does not erode the surface or rebound but it bonds to the surface.

The value of this critical speed depends on several factors:

- The mechanical properties of the materials (substrate and powder)
- Thermal properties of the materials (substrate and powder)
- The oxidation state of the powder and the substrate

Several authors have showed that the value of the critical speed corresponds to the formation of adiabatic shear bands at the interface powder/ substrate. These adiabatic shear bands form on the rim of the impact and jets of material appear. The jets of materials correspond to the zone where the shear and the heating are very important. Figure 2-3 shows where the jets form in the case of a perpendicular simulated impact.

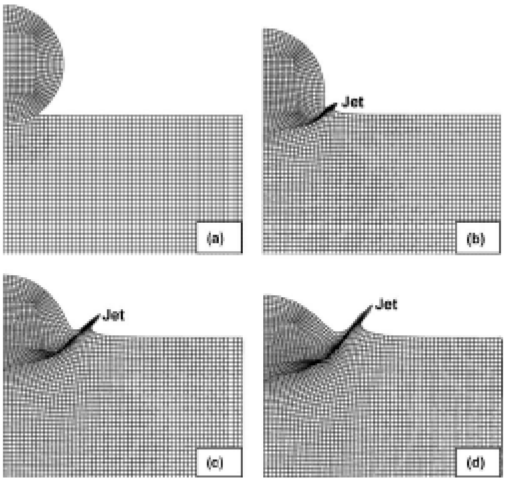

Figure 2-3 : Temporal evolution of a 25 µm Cu particle and the substrate materials during the particle collision with the substrate. The initial particle speed is 550 m.s^{-1}.Particle/substrate contact time: (a) 4.4 ns; (b) 13.2 ns; (c) 22.0 ns and (d) 30.8 ns.[4]

Table 2-1 : Examples of critical speeds computed with FEM analysis.[4] No oxide shell was included in the model.

Particle material	Substrate material	Critical speed (m.s^{-1})
Copper	Copper	575-585
Aluminium	Aluminium	760-770
Nickel	Nickel	620-630
Titanium	Titanium	650-660
Copper	Aluminium	510-530
Aluminium	Copper	600-630
Nickel	Copper	570-580

2.3 One Dimensional Modelling of Cold Spray Process

First, the behaviour of the gas in the convergent-divergent nozzle will be modelled. The equations will link the gas stagnation pressure $\mathbf{P_0}$, its temperature $\mathbf{T_0}$ and the geometry of the nozzle to the gas speed and temperature in the nozzle.
The powder's behaviour in the nozzle will be modelled by assuming:

- The powder's presence will not affect the flow
- Powder particles do not interact together.

The gas shock wave present at the surface of the substrate will influence the powder velocity. This effect will be modelled by taking an empirical model of the shock wave in literature.
This section will set the basic equation between the spray parameters and the powder particle velocity and temperature at the surface of the substrate before bonding to it. Dykhuizen et al [3] has used this model to describe with some success the CGDS principles. This model will overestimate the real value of the particle speed but the values are reasonable to understand the process.

2.3.1 Gas Model in the Nozzle

The one dimensional mode of an isentropic flow is used to describe the flow properties in the convergent/divergent nozzle [3]. It is based on the following hypothesis:

- Stationary flow;
- No heat flow($dQ = 0$);
- No work generated by the flow;
- No boundary layers;
- No obstacle in the nozzle;
- The flow is isentropic($ds = 0$);

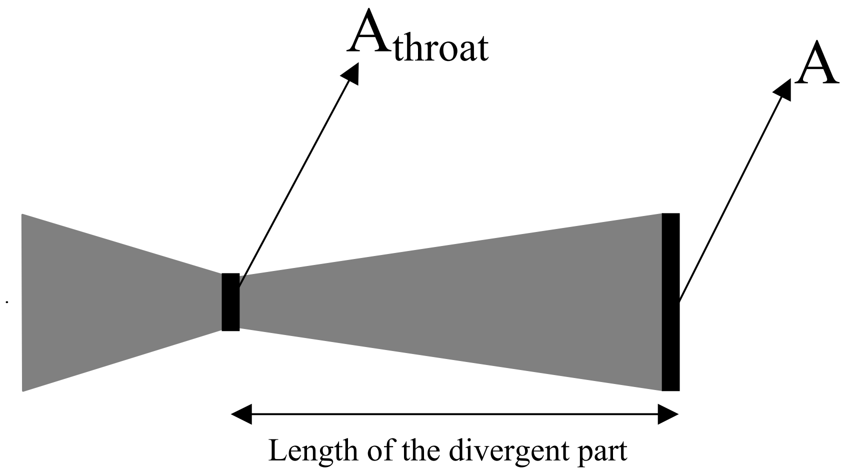

Figure 2-4 : Model of the nozzle.

The following developments are based on a nozzle with cylindrical symmetry. Figure 2-4 shows a schematic of the nozzle model and the different cross sections.

The fundamental equation of the model gives the relation between the Mach number (*M*) of the gas in the Laval nozzle and the nozzle cross section. A demonstration can be found in any text book on fluid mechanics [5].

$$\frac{A}{A_{throat}} = \frac{1}{M}\left[\frac{2}{\gamma+1}\left(1+\frac{\gamma-1}{2}M^2\right)\right]^{\frac{\gamma+1}{2(\gamma-1)}}$$

A : cross section of the nozzle
A_{throat} : throat cross section
M : Mach number
γ : specific heat ratio

It is important to note that the Mach number at any point in the nozzle is linked to the design of the nozzle through de ratio of cross sections. More precisely, the relation shows that the Mach number of the gas (at any point in the nozzle) depends on the type of the gas (through the specific heat ratio) and on the ratio $\frac{A}{A_{throat}}$ where the Mach number is computed.

Once the evolution of the Mach number inside the nozzle is known, it is possible to compute the evolution of the gas speed, pressure, density and temperature along the nozzle by using the perfect gas laws.

$$P = \rho_{gas} \cdot r \cdot T$$
$$h = C_P \cdot T$$

The gas characteristics evolution inside the nozzle can be linked to the stagnation pressure $\mathbf{P_0}$ and temperature $\mathbf{T_0}$ by the following equations.

$$\frac{T_0}{T} = 1+\frac{\gamma-1}{2}M^2$$
$$\frac{P_0}{P} = \left(1+\frac{\gamma-1}{2}M^2\right)^{\frac{\gamma}{\gamma-1}}$$
$$\frac{\rho_0}{\rho_{gas}} = \left(1+\frac{\gamma-1}{2}M^2\right)^{\frac{1}{\gamma-1}}$$

P : gas pressure at any point in the nozzle
P_0 : gas stagnation pressure
T : gas temperature at any point in the nozzle
T_0 : gas stagnation temperature
ρ_{gas} : gas density at any point in the nozzle
ρ_0 : gas density at stagnation conditions
h : gas enthalpy
C_P : constant pressure specific heat

Based on the definition of the Mach number, the value of the gas speed can be obtained:

$$M = \frac{v_{gas}}{v_{sound}}$$

Where,

v_{gas} : gas velocity
v_{sound} : sound velocity in the gas

In the case of a perfect gas: $v_{sound} = \sqrt{\gamma \cdot r \cdot T}$

These developments show that the gas properties inside of the nozzle depend on:

- The stagnation conditions $\mathbf{P_0}$ and $\mathbf{T_0}$
- The nozzle design
- The gas properties through γ and r

2.3.2 Gas Model from the Exit of the Nozzle to the Substrate

The behaviour at the exit of the nozzle is complex. A lot of literature is available on the gas at the exit of a convergent-divergent nozzle but they involve 2D computer models [6],[7],[8],[9],[10],[11]. There is no simple one dimensional model available for cold spray. The basic assumption made in this section is the gas stream properties do not change between the exit of the nozzle and the substrates surface.

When 2D models are used, it is possible to simulate turbulence and the presence of Diamond shocks at the exit of the nozzle on the speed of the powder particles. The model results are usually compared to laser velocimetry measurements. Work by Jodoin et al presents such a comparison [7].

2.3.3 Modelling of the Powder Behaviour in the Gas Flow

Measuring the speed of the powder particles in the nozzle is not possible. So only modelling is possible to understand the influence of the nozzle design and spray condition on the powder's exit velocity. The one dimensional model developed is based on two hypotheses:

- Powder particles in the gas stream do not interact together.
- The presence of the powder in the gas stream does not affect the gas evolution in the nozzle.

The last hypothesis means that the transfer of kinetic energy between the gas stream and the powder in very small. The kinetic energy is mainly transported by the gas. These two hypotheses are not valid if the amount of powder injected in the nozzle is too important.
The modelling of the powder's speed under the conditions is reduced to solving the equation of movement on a single particle of powder.

$$\vec{F} = M_P \vec{a} = \frac{1}{2} C_D \rho_{gas} \frac{\pi d_P^2}{4} \left(\vec{v}_{gas} - \vec{v}_P\right) \left|\vec{v}_{gas} - \vec{v}_P\right| = \rho_P \frac{\pi}{6} d_P^3 \frac{d\vec{v}_P}{dt}$$

ρ_P : density of the powder particle
d_P : diameter of the powder particle
$\vec{v}_P$: speed of the particle
C_D : drag coefficient of the powder particle
ρ_{gas} : gas density
$\vec{v}_{gas}$: gas speed
M_p : powder particle mass
$\vec{F}$: force applied on the powder particle
$\vec{a}$: acceleration of the powder particle

The equation of movement of the powder particle shows that the best approach to increase the particle speed is to increase the gas density and the gas velocity. The particle's velocity is sensitive to the difference in speed between the gas and the particle. Therefore, the acceleration of the particle will be high at initial stages when its speed is low.

The gas temperature in the process can reach 800-900K. The main role of this heat is to favour the expansion of the gas in the divergent part of the nozzle and allow the gas to reach very high velocities. The temperature evolution in the nozzle is complex. In the convergent part of the nozzle, the gas temperature does not change significantly but once the gas enters the divergent part, the expansion of the gas leads to an important drop in its temperature. The powder in the gas stream will absorb a part of the gas temperature, but the final particle temperature will depend on the time of flight of the particle in the nozzle.

$$\frac{dT_P}{dt} = \frac{hA_P}{m_P C_P}\left(T_g - T_P\right)$$

A_P : area of the particle's cross section
m_P : mass of the powder particle
T_g : temperature of the gas
T_P : temperature of the powder particle
h : thermal convecticity coefficient

The temperature exchange with the gas stream starts at the surface of the powder particle and the temperature inside the particle increases progressively. In this model, the gradient of temperature in the particle is neglected.

In the convergent part of the nozzle where the temperature of the gas is high, the particle's temperature will increase. Once the particle enters the divergent part of the nozzle, the gas temperature drops quickly and the heated particle's temperature will drop.

2.3.4 Gas Shock Wave at the Surface of the Substrate

The behaviour of the gas in contact with the substrate's surface changes abruptly. The supersonic stream changes to a subsonic stream by a shock wave (also called 'Bow Shock'). The dimension on the shock wave is on the scale of several hundreds of nanometres. This shock wave takes place a few millimetres above the substrate's surface. After the Bow Shock, an impingement zone with very different gas characteristics than a supersonic stream is present.

After the shock wave, the gas stream:

- sees its velocity drop to subsonic values [6].
- has an increase in the gas density.
- has an increase in temperature since the gas is compressed.

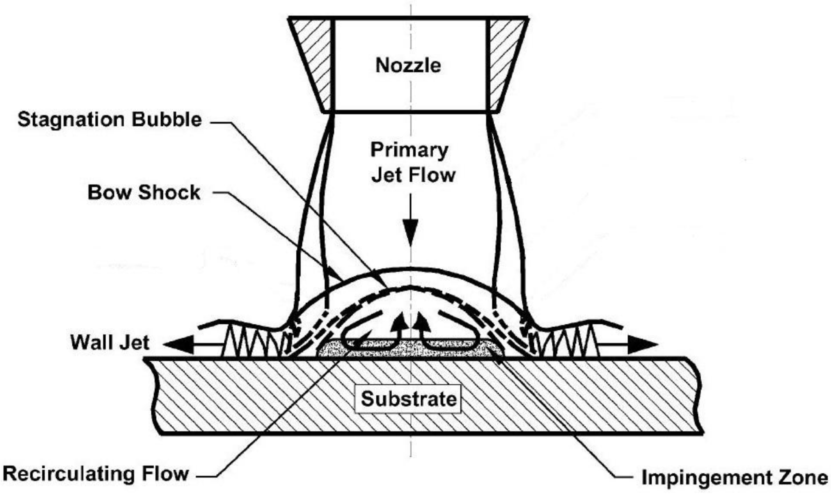

Figure 2-5 : Gas jet impact on the substrate surface. [12]

Figure 2-5 shows the complexity of the behaviour of the gas in contact with the surface, several shocks can occur before the impingement zone is reached. This zone can only be modelled rigorously by using 3D fluid dynamic computations. There is an empirical model used to model the bow shock called the "Billing's approximation" [13] :

$$\Delta l = 0{,}143 \cdot D_e \cdot e^{\frac{3{,}24}{M_e^2}}$$

D_e : diameter of the exit section of the nozzle

M_e : Mach number at the exit of the nozzle

Δl : thickness of the impingement zone

To finish the description of the shock wave, a relation on the evolution of the Mach number passed the shock front is needed (see [13]).

$$M^2 = \frac{\left[M_e^2 + \frac{2}{\gamma - 1} \right]}{\left[\frac{2\gamma}{\gamma - 1} M_e^2 - 1 \right]}$$

The Mach number after the shock front is a function of the Mach number at the exit of the nozzle. It's supposed that the Mach number decreases linearly pass the shock front and reaches zero at the substrate.

This model allows the determination of the gas characteristics passed the shocked front in the stagnation bubble with a one dimensional model. By using the one dimensional model of the powder particle's temperature and speed in the nozzle, it is possible to estimate the value of the powder particle's speed and temperature passed the shock front. These values are called the particle impact conditions "**PIC**".

In order to get bonding with the surface, a minimum value of speed needs to be reached by the powder particle. Using this one dimensional model, it is possible to optimise the powder's size distribution.

2.3.5 Influence of the Operating Gas

In the CGDS process, the choice of operating gas is guided by the critical velocity needed to reach coating formation. For materials with high critical velocities, the operating gas must be able to accelerate particles to such velocities. Typically, two gases are used in the cold spray process: nitrogen and helium (Table 2-2 has the gas characteristics).

The differences between these gases are to be found in the value of their molecular mass and the value of the specific heat ratio γ. The consequence of this is that He with a low molecular mass accelerates easily. Hence the gas speed of helium will be much higher than nitrogen. This high gas speed is favourable for accelerating powder particles. The low value of molecular mass has an inconvenient effect. It hinders the efficiency of momentum transfer between the gas and the powder particles. Nitrogen with a higher molecular mass will transfer momentum from the gas to the powder particle more efficiently but it is still insufficient to equal the performance of helium. When using nitrogen instead of helium, the gas speed drops to 60% of the He performance at constant pressure and temperature [2] .

Helium offers the best performance in gas velocities and powder particles velocities. The main obstacle to its use is its cost. The cost of He is 10 times higher than nitrogen. Many materials have a critical velocity attainable by heated nitrogen.

Table 2-2 : Gas characteristics used in the cold gas dynamic spray process.

	Specific heat ratio γ	Molecular mass
He	1.66	4
N_2	1.4	28

2.3.6 Particle Characteristics in the Process

The evolution of the particle velocity is described in Figure 2-6. In the convergent part, the particle is not highly accelerated since the gas speed is low. Near the nozzle's throat, the gas speed increases rapidly hence the particle velocity increase quickly. In the divergent part, the gas density drops therefore the efficiency of the momentum transfer between the gas and the particle drops also. Hence, the particle is less efficiently accelerated at the end on the divergent part of the nozzle. Before reaching the bow shock the gas conditions are supposed to be constant. The particle velocity increases slightly with the standoff distance. Once the particle hits the bow shock and enters the impingement zone, its velocity drops. If the particle has insufficient inertia, it may slow below the critical velocity for bonding to the substrate. For copper particles, calculations have shown that particles with a diameter smaller than 5 µm will slow below the critical value.

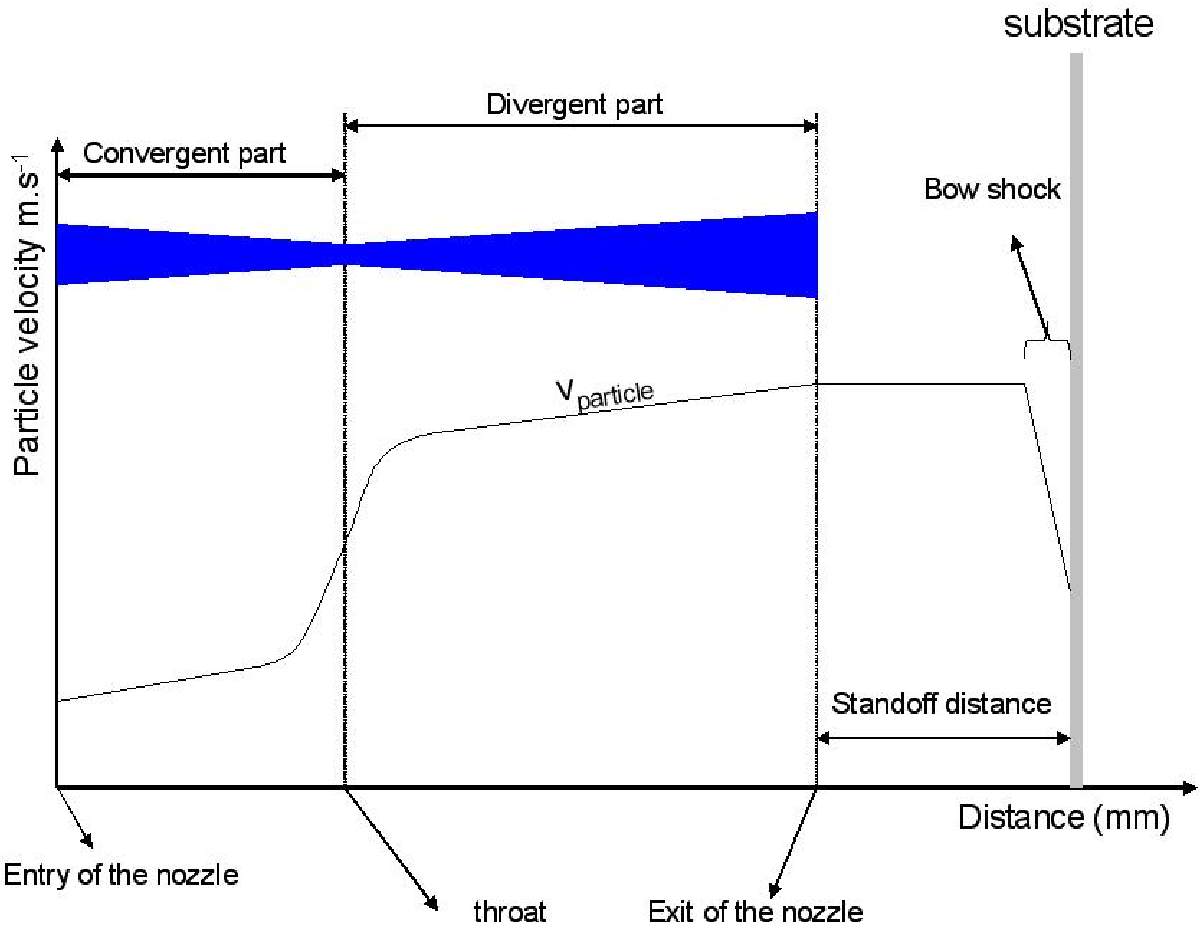

Figure 2-6 : Schematic of the evolution of the particle speed in the nozzle.

When the powder particle enters the convergent part of the nozzle (Figure 2-7), the gas temperature is high and its temperature will increase. The temperature of the particle reached in this part depends on the particle size and thermal conductivity. In the divergent part of the nozzle, the gas expands and its temperature drops. The particle has accumulated some heat and will restore this heat progressively to the exterior gas. The final particle temperature will remain above the gas temperature. After the passage of the bow shock, the particle temperature increases. The final value of temperature reached before contact with the surface, will depend on the thermal inertia of the particle.

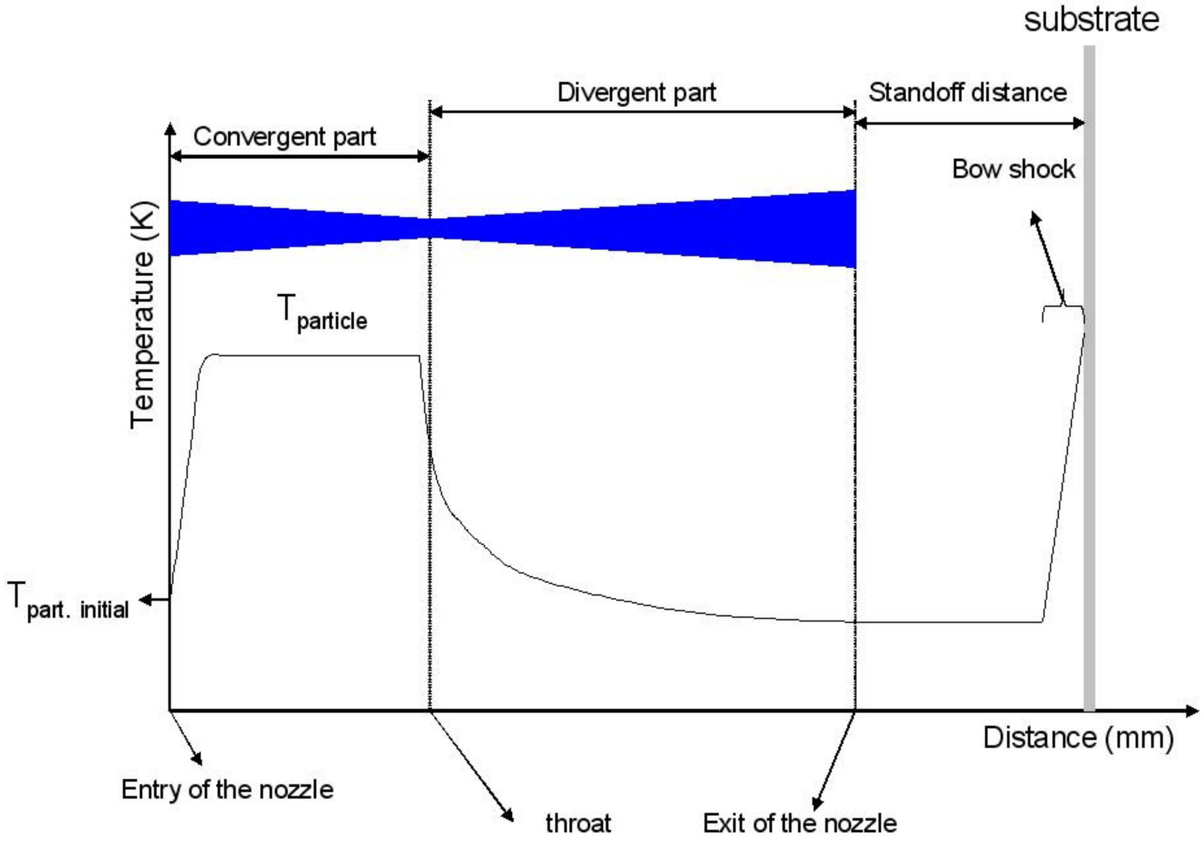

Figure 2-7 : Schematic of the evolution of the particle's temperature.

2.4 Optimisation of the Process

The process optimisation needs a good understanding of the different influences on the value of the critical speed. Work by T. Schmidt et al [14] has aimed to develop an analytical model of the critical speed. The first step is to establish a simple model that will predict impact dynamics such as bonding and erosion. This will give a "**Window of Sprayability**" (WS) and powder particles with impact conditions in this window will bond to the surface.
The powder "**particle's impact conditions**" (PIC) are:

- its temperature.
- its speed.

The critical speed has to be linked to the PIC by the model.

Table 2-3 : Nomenclature used to establish the model of the window of sprayability.

Nomenclature	
$C_p\ (J.kg^{-1}.K^{-1})$	Specific heat at constant pressure
$d_{crit}\ (\mu m)$	Critical diameter of the powder particle
F_1, F_2	Empirical factors
$T_i\ (K)$	Impact temperature
$T_m\ (K)$	Melting temperature
$T_R\ (K)$	Reference temperature (293K)
$t\ (s)$	Time
$v\ (m.s^{-1})$	Velocity
$\rho\ (kg.m^{-3})$	Material density
$\sigma_{TS}\ (MPa)$	Tensile strength
$\lambda\ (J.m^{-1}.K^{-1}.s^{-1})$	Thermal conductivity

2.4.1 Deposition Efficiency

A measurement of the performance of the process is called the "Deposition efficiency" (**DE**). It expresses the ratio between the amount of powder that bonds on to the surface and the amount of powder that exited the nozzle. The optimisation of process is done by using this ratio.

$$DE(\text{deposition efficiency}) = \frac{\text{mass of powder in the coating}}{\text{total of mass of powder that exits the nozzle}}$$

2.4.2 Influence of the Particle Size

The size effect of the particle will influence the attainable temperature at the interface. For very small dimensions, the occurrence of shear instabilities can be hindered by high cooling rate, which arises due to the very high temperature gradients within a small particle. The

strain rate hardening can be more intense in smaller particles since the strain rate is higher. Also the viscous shear strength in the jetting region will be higher for smaller particles.
All these dynamic effects hinder localized deformation and increase critical velocity. During powder production, small particles are exposed to higher quench rates and therefore show an intrinsically higher strength since they have a smaller microstructure.
The high surface to volume ratio of small particles implies that they have higher impurity content. Surface contaminations like oxide shells will significantly influence the bonding mechanism. The following equation [14] gives a critical particle diameter above which thermal diffusion is slow enough to allow localized shear instabilities to occur at the surface of an impacting particle. It has been established by using “Finite Element Modelling” by Schmidt et al .

$$d_{crit} = 36 \cdot \frac{\lambda}{C_P \cdot \rho \cdot v_{particle}}$$

Figure 2-8 shows calculated minimum diameters for several selected materials. This figure shows that materials like copper, silver, tin are more limited by thermal diffusion than titanium or 316L steel.

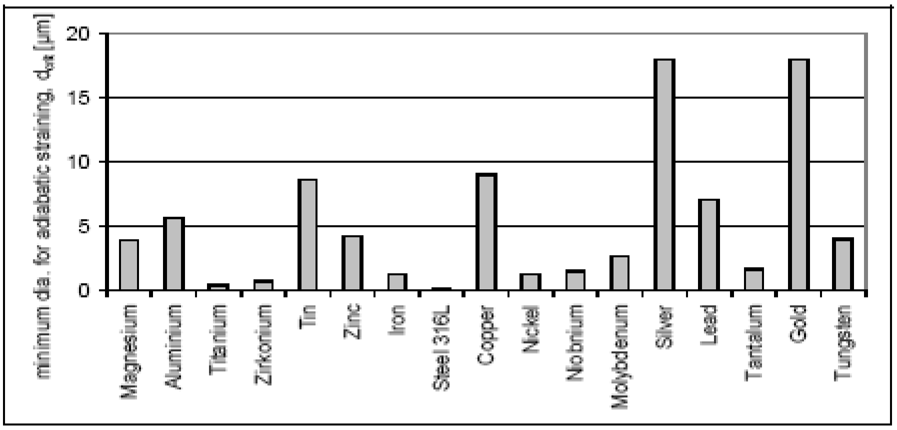

Figure 2-8 : Minimum value of particle size for bonding [14].

2.4.3 Influence of the Particle Properties

It is necessary to link the material physical properties to the value of the critical speed (Table 2-3). The work by Schmidt et al allows establishing a model of the critical speed as a function of material properties by calibrating the results on existing data.

$$v_{crit}^{theorical} = \sqrt{\frac{F_1 \cdot 4 \cdot \sigma_{TS}\left(1 - \frac{T_i - T_R}{T_m - T_R}\right)}{\rho} + F_2 \cdot C_P \cdot \left(T_m - T_i\right)}$$

By calibrating this equation with existing data on cold spray critical velocities, it is possible to give a value for the calibrating factors F_1, F_2. Values for cold spray velocities are : $F_1 = 1.2$ and $F_2 = 0.3$.

If impact velocity is increased far beyond the critical velocity for bonding, a transition to a hydrodynamics penetration regime occurs. This will cause erosion of the surface. The material and temperature dependent velocity, where deposition changes to erosion, is called erosion velocity. The calibration factors F_1, F_2 were determined by correlation with experimental results. Values for erosion velocities are : $F_1 = 4.8$ and $F_2 = 1.2$.

2.4.4 The Window of Sprayability

To establish the window of sprayability, it is needed to plot the particles impact velocity as a function of its temperature. Figure 2-9 shows such a plot. On the same plot, using the previous equation, the value of the critical speed and the erosion speed are plotted as a function of its temperature. In order to bond, the powder particle must have PIC between the two limits. The powder particle must not adopt a brittle behaviour upon impact. The formation of adiabatic shear bands requires a ductile behaviour of the material hence bonding will not be possible at low temperature.

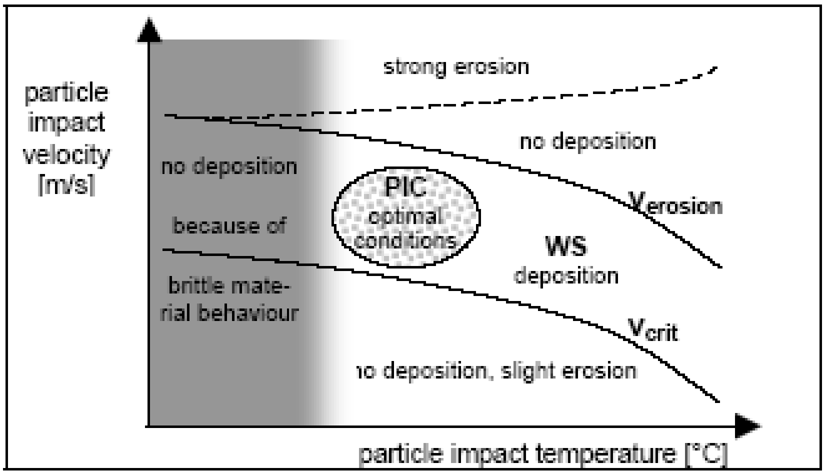

Figure 2-9 : Description of the « Window of Sprayability » (WS). The PIC must be in the range defined by the critical speed and the erosion speed. [14]

Figure 2-9 will give the optimal PIC for a given material. The next step is the optimisation of the powder's size distribution. The critical velocity for bonding is also dependent on the particle's size.

Figure 2-10 shows a plot of the particle's speed and its critical velocity as a function of the particle's diameter in µm. Three distinct regions can be identified. In the left region, no deposition occurs. The powder particles are slowed down below the critical velocity by the gas bow shock. The middle region is the optimum region. The coating will be dense and the efficiency of the deposition will be high. The last region on the right hand side of the Figure 2-10 corresponds to a region where the coating will see its porosity increase and the deposition efficiency drop.

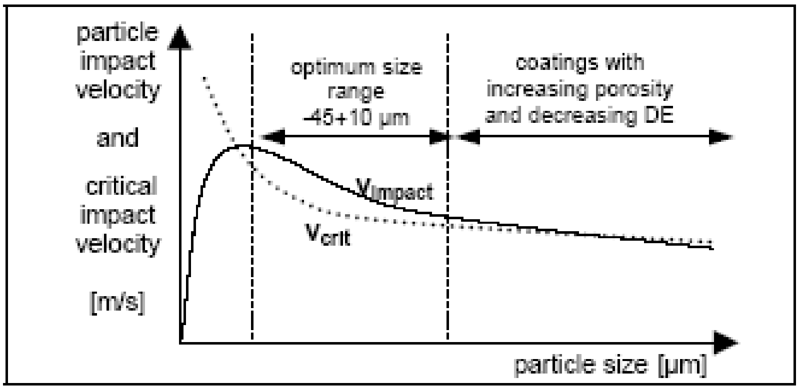

Figure 2-10 : Particle speed $v_{particle}$ and critical speed $v_{critical}$ as a function of particle diameter. [14]

2.5 In Depth Analysis of a Single Impact

The fundamental element of a coating's build up is the good quality of the bond between a powder particle and the surface. It is necessary to associate the value of critical speed with changes in the mechanical properties of the materials. This work has been done by using FEM analysis. Several authors have investigated the impact of a spherical powder on a substrate. The work by Assadi et al [15] has linked the critical speed to the formation of adiabatic shear bands at the interface between the particle and the substrate. The work by Grujicic et al [16] has studied the material behaviour in the case of a spherical copper powder particle impinging an Al surface at high speed.

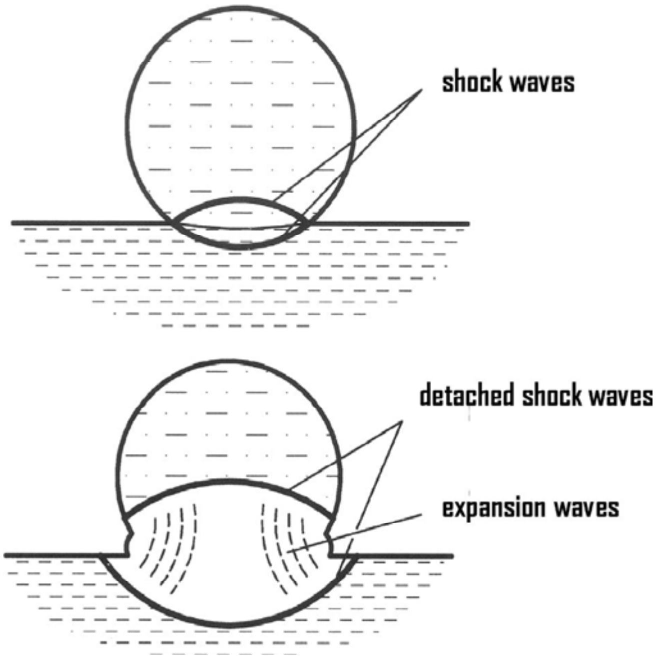

Figure 2-11 : High velocity impacts: formation of shock and expansion waves in both the particle and the impacted body, and inception of a jetting motion.[17]

Figure 2-11 shows the development of the pressure wave in the case of high velocity impacts. These shock pressure waves are in the range of several GPa. The geometry of the impact implies complex strain and stress fields during the impact. Simulations using Finite Element Analysis have been done to evaluate the evolution of flow parameters during impact deformation.

2.5.1 Axisymetric Modelling

On Figure 2-12, the substrate is fixed at the bottom, and horizontal displacement is not allowed at the axis of symmetry and at the outer edge. The profiles of field variables are investigated along meridian and radial paths as shown in the figure. The development of these variables with time is studied at selected nodes at the surface, which are subject to highest amount of deformation.

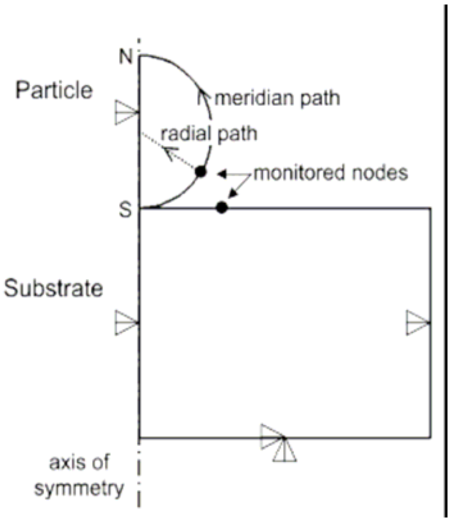

Figure 2-12 : Initial configuration and boundary conditions for an axisymmetric model. [15]

The work done by Assadi et al [15] used FEM analysis to understand the development of plastic strain, temperature and flow stress. The following explanation is given : "Figure 2-13 shows the development of plastic strain, temperature and flow stress in a so-called critical element at the particle surface which undergoes the highest amount of deformation within the particle. As shown in Figure 2-13 (a), the plastic strain increases very rapidly at a rate of up to $\dot{\varepsilon} = 0.5 \times 10^9$ s^{-1}, before reaching its final value of about 4 for three velocities of 450, 500 and 550 m.s^{-1}. For the velocity of 580 m.s^{-1} the trend is nevertheless different, showing a further increase of strain up to a final value of about 10. The increase of strain at this velocity could be the result of a change in mechanism from plastic to viscous flow. The temporal development of temperature in the critical element (Figure 2-13(b)) is similar to that of strain, but with small differences which are due to differences in frictional and viscous dissipations. The heating rates $\dot{T}$ for all impact velocities are around 10^9 K.s^{-1} in the first step. For the impact velocity of 580 m.s^{-1}, the temperature approaches the melting temperature of copper, whereas in other cases it remains well below it. Figure 2-13 (c) shows the temporal development of the equivalent stress. For lower or medium velocities of up to 550 m.s^{-1}, there is a drop in stress after 0.05 µs, which can be attributed to the loading conditions from the substrate. But for the impact velocity of 580 m.s^{-1}, there is a significant change in trend of temporal development of stress at an earlier time of 0.03 µs. Beyond this time, the stress variation is accompanied with large fluctuations, as well as a decrease in the overall value. The change in stress variation coincides with the increase of strain and temperature in the critical element, as shown in Figure 2-13 (a)and (b). The fluctuations in temporal development of stress at a high velocity (580 m.s^{-1}) could be explained with respect to a change in deformation mechanism from plastic to viscous flow. Near the conditions for thermal softening, the resistance of material to shear flow is generally low. This means that by approaching the melting temperature, the material loses its shear strength and undergoes excessive deformation for any amount of imposed shear stress. On the other hand, this excessive deformation would create a viscous-type resistance which would hinder further deformation, particularly under high pressure. In the present analysis, this effect will be due to the increase in the second term of the Johnson-Cook model which accounts for strain-rate hardening.

The change of material's flow properties is associated with the formation of adiabatic shear bands. The phenomenon is supposed adiabatic because the time scale of an impact is smaller than the time needed to evacuate heat. In other words, the heat generation is faster than the heat dissipation."

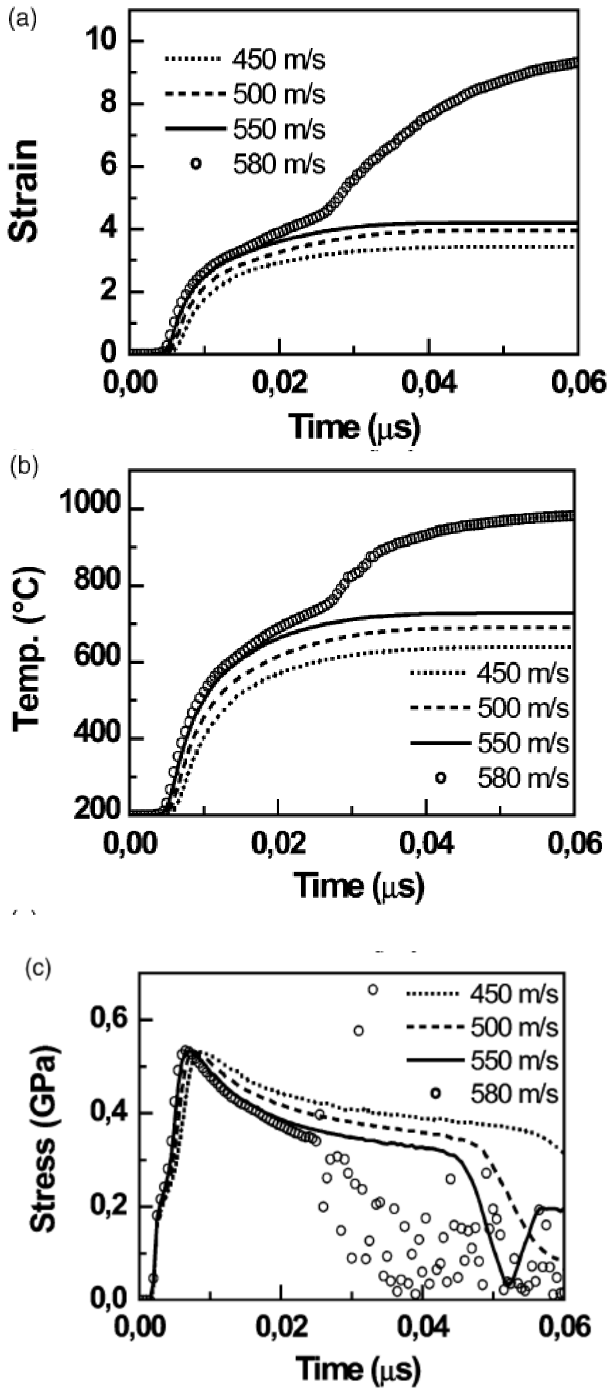

Figure 2-13 : Calculated temporal development of (a) plastic strain (b) temperature and (c) flow stress at the critical node of a sprayed particle (as indicated in Figure 2-12) for various impact velocities. There is a change in trend of variation of these variables with time, as the initial copper particle velocity is increased from 550 to 580 m/s, indicating shear instability. [15]

2.6 Shear Bands

Shear localization occurs when plastic deformation localizes on a thin region of a specimen. It is very important because it is often a precursor to failure. In most cases, shear localization is associated with a local softening of the structure. This softening can be due to thermal or geometrical reasons. In geometrical softening, the structure orients itself to a direction that is easier (i.e., requires less stress) for glide. The rotation of crystallographic slip planes in response to straining in ductile crystalline solids is an example. However, shear localization is not restricted to crystalline solids; metallic glasses and partially crystalline polymers are very prone to shear localization. Granular and fragmented ceramics and rocks undergo shear localization. For these cases, thermal softening is replaced by structural softening, such as particle breakdown. In special cases, shear localization has been predicted to occur even during hardening. In thermal softening, the local increase in temperature can result in a softening that leads to shear localization. In the extreme case when the strain rate is so high that the local heat generated cannot escape from the deformation area, these bands are called adiabatic shear bands. Regardless of the initial softening mechanism, the shear localized deformation leads to an acceleration of strain rate. Eventually, there are heat concentration and thermal effects in most situations.

At the microstructural level, the material is not a homogeneous continuum [18]. The initiation of shear localization is a critical event, which can be triggered either by external, geometrical factors, or internal, microstructural factors. External initiation sites are regions of stress and strain concentration; microstructural sites are regions that undergo localized softening by some mechanism.

- A dislocation pile-up, upon bursting through a grain boundary, can generate the local temperature rise and plastic deformation that would initiate shear band. Calculations performed indicate that the heat generated in a pile-up release is sufficient to initiate a shear band.
- Possible microstructural initiation sites are fractured second phase particles, dislocation pile-ups being released as an avalanche, geometrical softening resulting from the rotation of atomic planes towards orientations with a lower Schmid factor, and preferential slip paths produced by martensite transformation and twinning. The increase in Schmid factor of a grain with plastic deformation leads to localized softening which can initiate a shear band. The localized deformation of one grain can propagate along a band.
- Another mechanism was advanced by Weertman and Hecker (see [18]). They proposed that local dislocation reorganization produced elongated dislocation-free regions that were initial shear bands.
- Meyers et al (see [18]) made observations of a similar nature on shock-loaded nickel subjected to subsequent tension. Localized regions (shaped like an oblate spheroid), virtually dislocation free, were produced from the densely deformed material, leading to shear failure by a softening mechanism.

The microstructural evolution inside the shear band has been actively studied from the mid-twentieth century, and different processes can occur:

- Dynamic recovery
- Dynamic recrystallization
- Phase transformation

- Strain-induced precipitate dissolution
- Crystallization (in metallic glasses)
- Melting and resolidification
- Amorphization (by rapid quenching from the liquid)

These processes can occur concurrently or separately. It is often very difficult to establish whether the structures observed were produced during deformation or during post-deformation cooling.

2.6.1 Shear Bands in Cold Sprayed Copper: microstructural characteristics

The work by Borchers et al [19] has analysed the microstructure of cold sprayed copper coating with a TEM. Several characteristics of the copper microstructure can be linked to the deformation process in the shear bands. TEM observations have found such characteristics and they are summarized on Figure 2-14.

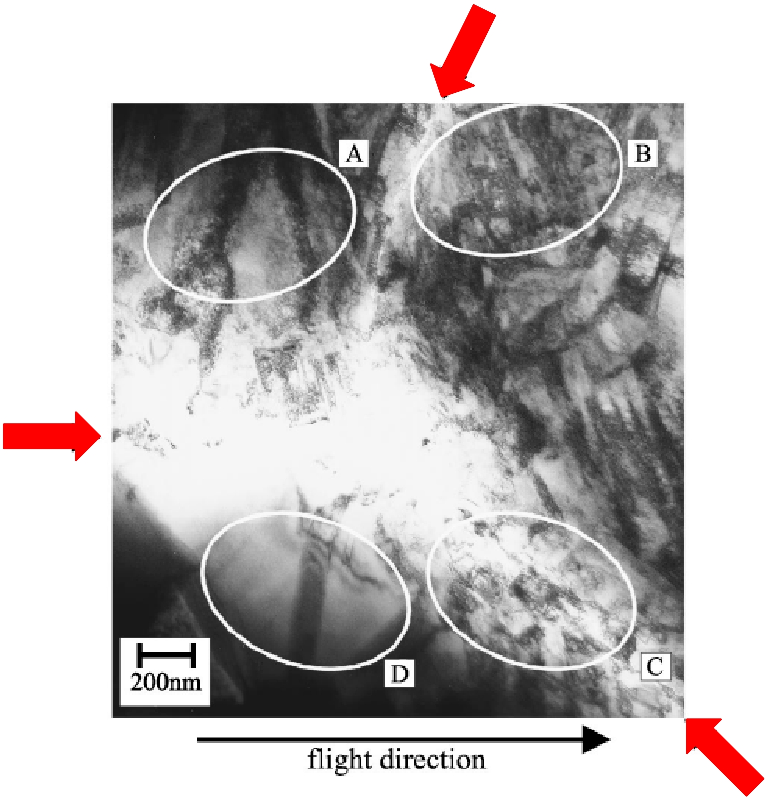

Figure 2-14 : TEM micrograph of an interparticle triple point in a CS copper coating showing typical microstructural features. Particle–particle boundaries are marked with arrows, so is the impact direction. A: high dislocation density with dislocations arranged in walls, grain size above 1 mm. B: aligned elongated grains sized about (50 x 150) nm^2 in projection, featuring nonequilibrium grain boundaries characterized by ultrahigh dislocation densities adjacent to the grain boundaries. C: equiaxed ultrafine grains about 100 nm in diameter. They exhibit heavily deformed zones around the grain boundaries with extremely high dislocation densities, while the inner parts of the grains are rather free of dislocations. D: Dislocation-free region exhibiting twins, grain size above 1 µm. [19]

The region marked A shows a high dislocation density and a grain size above 1 mm. In that area, the dislocations are piled up in walls. The particle–particle boundary near region A is perpendicular to the substrate surface, or 0° to the flight direction. In the region marked B, there are aligned, elongated grains sized about $\approx 50\times 150\,\mathrm{nm}^2$ in projection. These show nonequilibrium grain boundaries characterized by ultrahigh dislocation densities adjacent to the grain boundaries. Here, the particle–particle interface has an angle of about 70° to the flight direction. In the region of the micrograph marked C, there are equiaxed ultrafine grains about 100 nm in diameter. They exhibit heavily deformed zones around the grain boundaries with extremely high dislocation densities, while the inner parts of the grains are rather free of dislocations. The particle–particle interface in this region has an angle of about 45° to the flight direction. The region marked D seems to be recrystallized with a grain size above 1 µm. In this region, no dislocations can be seen, but there are twins. The authors [19] stress that although the features shown in Figure 2-14 are typical for the copper coatings, it is exceptional that they appear in the same micrograph.

Meyers et al (see [20],[18]) classify dynamic recrystallization mechanisms into rotational and migrational types. The first needs concurrent plastic deformation, while the latter can also occur during subsequent annealing in the regime of cooling after adiabatic heating. In region D, there is a course, micron-sized grain exhibiting twins. There are two possibilities for the formation of twins after high strain rate deformation. Twinning can directly occur during or shortly after shock loading or attributed to annealing during migrational recrystallization. Meyer et al [21] gave a minimum twinning pressure for copper as 16-20 GPa for high strain rate deformation. For cold gas spraying of copper particles with a density $\rho = 8900 kg\cdot m^{-3}$ and an average velocity of $v = 570 m\cdot s^{-1}$, the mean impact pressure is $p = \frac{1}{2}\cdot\rho\cdot v^2 = 2.89 GPa$.

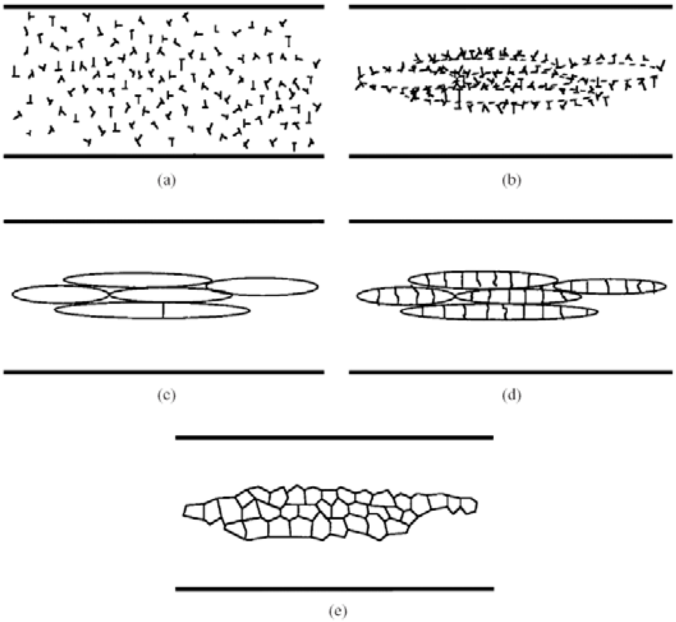

Figure 2-15 : Schematic illustration of microstructural evolution during high strain-rate deformation. (a) Randomly distributed dislocations, (b) Elongated dislocation cell formation (i.e., dynamic recovery), (c) Elongated subgrain formation, (d) Initial break-up of elongated subgrains and (e) Recrystallized microstructure [18].

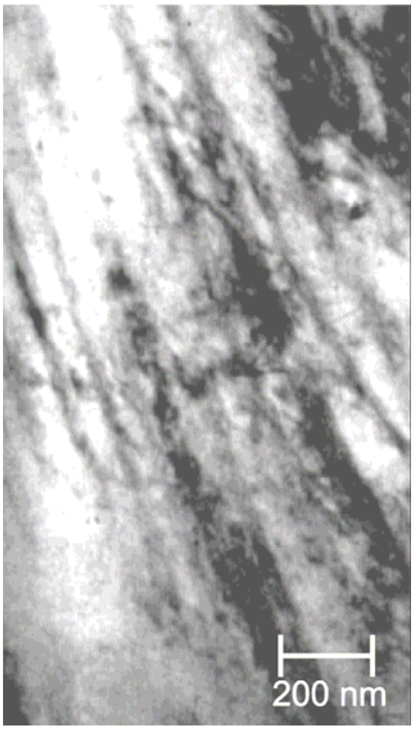

Figure 2-16 : TEM micrograph of a cold spray copper coating showing elongated grains with a width of some tens of nm and a length of several hundreds of nm. [19]

Meyers et al [20] proposed a microstructural evolution during dynamic recrystallization of the rotational type for high strain rate deformation, which is sketched in Figure 2-15. In a first step, randomly distributed dislocations form. Secondly, elongated dislocation cells develop during dynamic recovery; in a third step, these arrange to form elongated subgrains. Finally, fourth step, these cells break up and after they form small equiaxed grains in a recrystallized microstructure. No secondary recrystallization with grain boundary migration accompanied by twinning is observed in this regime. In CGDS copper coatings, randomly distributed dislocations with a high dislocation density can already be found in the feedstock powder, so the first step (Figure 2-15 (a)) will be omitted during the deposition process. In the micrographs Figure 2-14, the features characterizing steps Figure 2-15 (b) – (e) can be seen. Step (b) corresponds to region A in Figure 2-14, step (c) to Figure 2-16, step (d) to region B, and step (e) to region C in Figure 2-14. The higher the temperature rise is in a given region, the more time is available for the microstructure to evolve, before it freezes in. So in region C, the temperature rise must have been the highest, which fits the observation that here, the particle–particle interface has an angle of about 45° to the flight direction. Here, all four steps of dynamic recrystallization up to the formation of small equiaxed grains could be passed. In region B, the initial breakup of elongated subgrains has happened before the temperature has fallen again. Here, the angle between flight direction and particle–particle interface is around 70° (see red arrows on Figure 2-14), so the temperature rise has not reached the maximum as predicted by the modelling. In the region depicted in Figure 2-16, elongated subgrains are observed, while in region A in Figure 2-14, elongated dislocation cells are present, but no subgrains have yet been formed here. The temperature rise will not be as high as in regions B and C.

Since the value of the critical velocity is linked to the formation of the shear bands, it is necessary to understand how they form. The microstructural features of the shear bands are the manifestation of the intense local deformation and heating. This intense local pressure and heating is at the origin of the bond between the impinging material and the surface. As show in section 2.7, several authors have different explanations of the bonding process. Yet the processes that lead to these microstructural features have a link with the nature of the bonding. This link has not been clearly established until now.

2.6.2 Copper Impact on Aluminium

The work of Grujicic et al [16] has tested the evolution of flow properties of a copper particle (stress, pressure, temperature) during an impact on an Al surface (Figure 2-17).

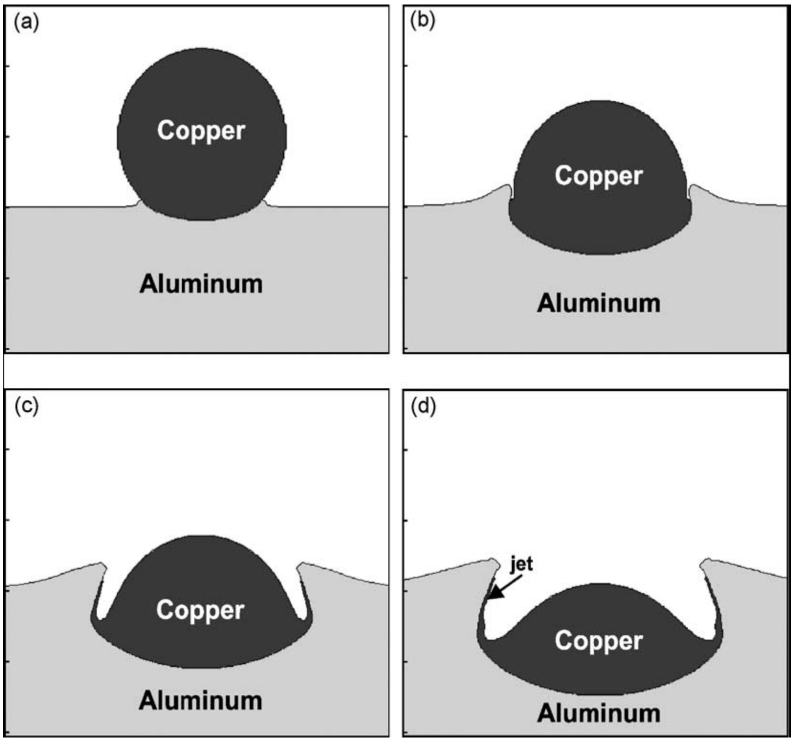

Figure 2-17 : The evolutions of shapes of a 20 µm-diameter copper feed-powder particle and a aluminium substrate-crater for the incident particle velocity of 650 m/s at the times: (a) 5 ns; (b) 20 ns; (c) 35 ns; and (d) 50 ns. [16]

The results depicted in Figure 2-18 show that the maximum temperature at the particle/substrate interface briefly (for ~20 ns with the copper-on-aluminium) exceeds the melting point of aluminium (~940 K) and only at the highest incident particle velocities (1000 m/s) used. The melting point of copper (~1356 K) is never exceeded. It should be noted that the computed maximum temperature values at the particle/substrate interface are overestimated due to the fact that the FEM code used by the authors does not enable modelling of the transfer of heat from the particle/substrate interface region where the heat is generated. A close examination of the temperature distribution over the particle/substrate interface shows that the conditions for melting of the aluminium substrate are met over a very small portion of the interface (approximately 20% of the particle/substrate interfacial). Also, the heat-diffusion distance in the copper particle or the substrate during a typical collision time period of 50 ns is about 3–4 µm suggesting that heat conduction can play a significant role in reducing the maximum interfacial temperature during the particle/substrate collision process. These findings suggest that melting can take place. Its role during the bonding process is unclear with these results.

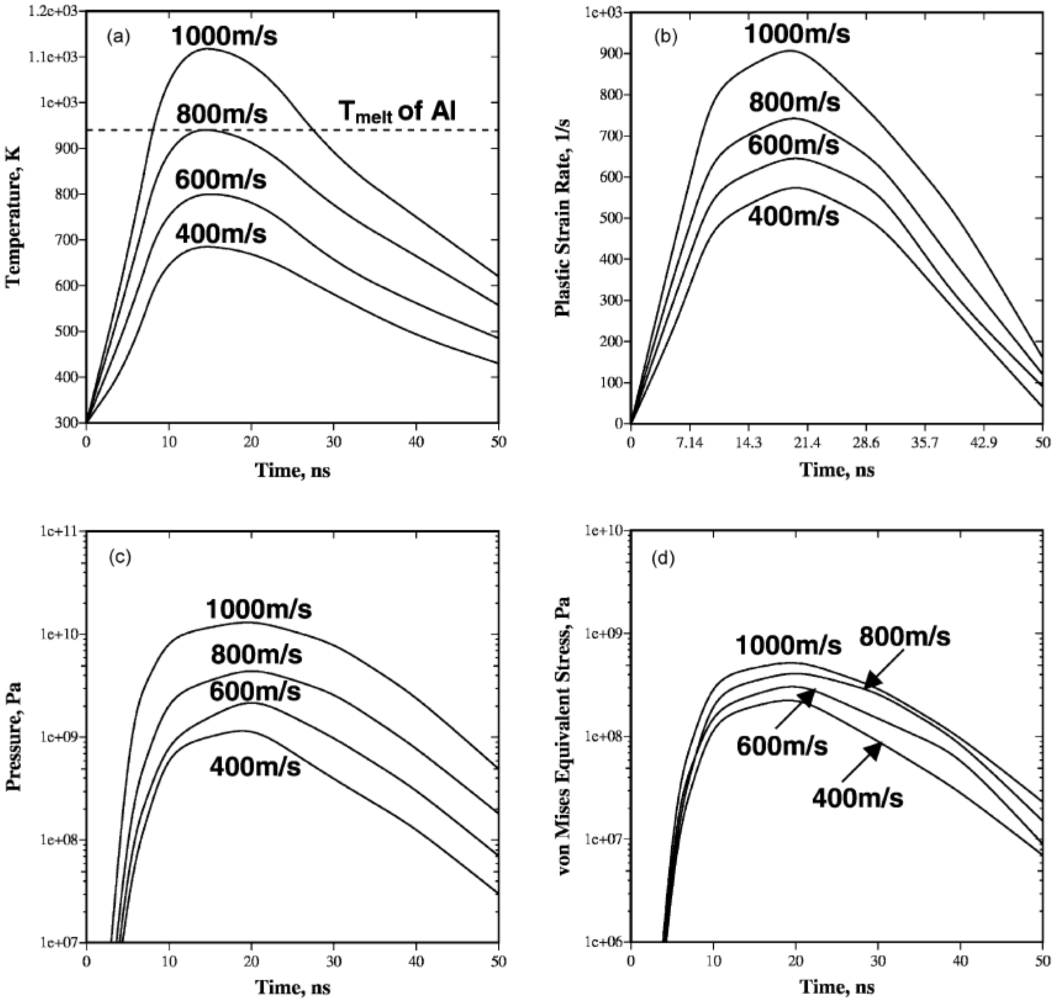

Figure 2-18 : The evolutions of the maximum: (a) temperature; (b) plastic strain rate; (c) pressure; and (d) von Mises equivalent stress at the particle/substrate interface during the deposition of copper-on-aluminium at four particle velocities. [16]

2.6.3 Contact Zone between the Particle and the Substrate

The shear bands are formed in the rim of the impact. This zone is where the pressure is high and the shear rate is very important. Figure 2-19 shows the position where the bonds are created. The extent of this zone depends of the impact speed and the contact time between the particle and the substrate. This zone can reach 15-20% of the crater's surface for an impact speed of 580 m.s^{-1} [15].

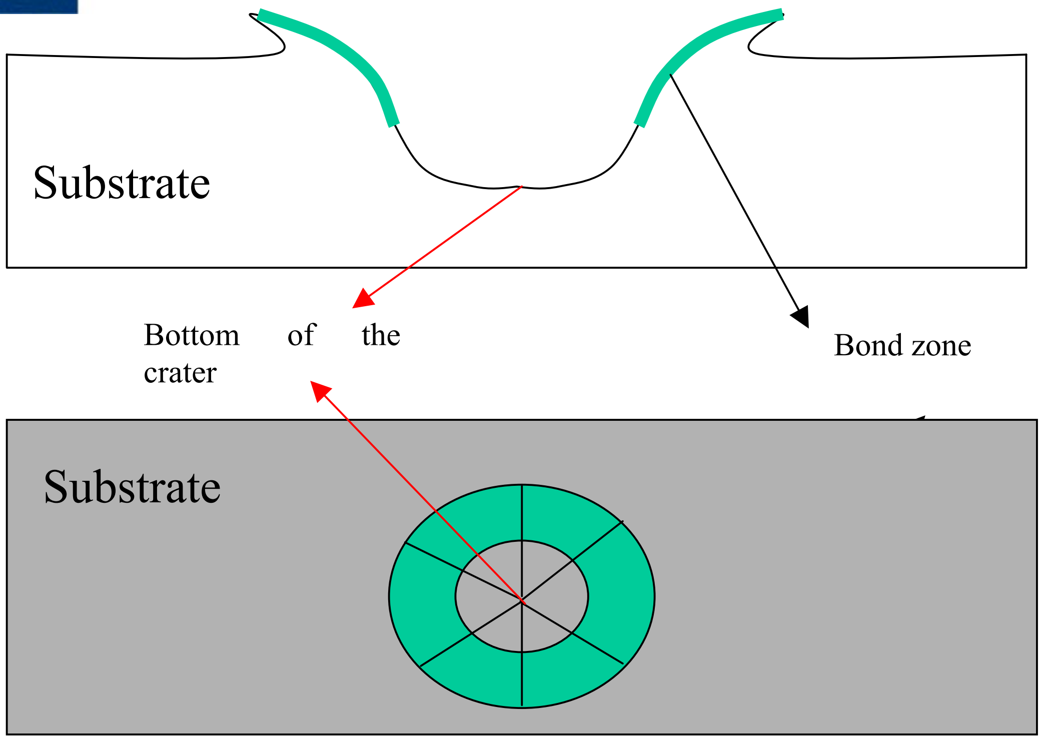

Figure 2-19 : Illustration of the bond zone between the particle and the substrate.

2.7 The Nature of Bonding

Until now, most of the work has shown that the value of critical speed is linked to the formation of adiabatic shear bands at the interface. But very little is known on the true nature of the bonding. The bond can have several natures. Based on the knowledge of existing spraying processes, the bond can be:

- Mechanical
- Related to the mechanism of sticking
- The consequence of "topochemical reactions"
- Caused by diffusion

2.7.1 Mechanical Bonding

The formation of adiabatic shear bands results in a change of behaviour from plastic flow to visquous flow.

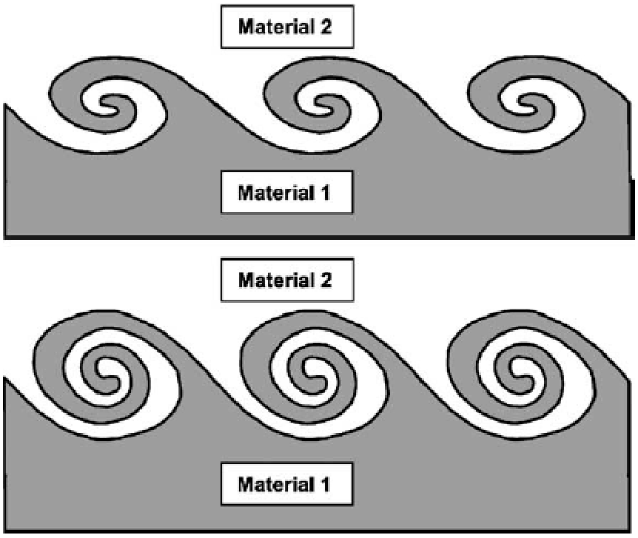

Figure 2-20 : A schematic of the instability-based evolution of the particle/substrate (Material 1/Materia 2) interface and the accompanying formation of interfacial roll-ups and vortices. [16]

Interfacial instability and the resulting formation of interfacial roll-ups and vortices can be, perhaps, best understood within the context of the Kelvin–Helmholtz instability phenomenon. These roll-ups would explain the good bonding between material 1 and 2 as illustrated on Figure 2-20.

2.7.2 Mechanism of Sticking

This mechanism is based on the assumption that particles first stick to the surface due to van der Waals or electrostatic forces. Strong adhesion is formed only later when other particles impact upon sticking particles. Initial sticking of particles can be due to multiple re-impacts. The idea of gradually increasing the strength of adhesion during coating formation was considered in [22], but no detailed estimation was made.

2.7.3 Mechanism of “topochemical reactions”

Here, adhesion is traced to reactions, so-called topochemical reactions, occurring near the interface between the contacting surfaces and resulting in the generation of bonds between the particle and the substrate.[17]

2.7.4 Diffusion

Diffusion is process by witch two metals A & B interact and atoms from one metal penetrate the other’s lattice. This process is essentially sensitive to time and temperature. Several types of mechanisms explain this interpenetration of atoms (Figure 2-22)[23] :

- *Interchange and ring mechanism*. The diffusive motion in this mechanism may take place by a correlated rotation of two or more atoms about a common centre without involving a defect. This mechanism has been found energetically unfavourable in most solids.
- *Interstitial mechanism*. Small interstitial atoms can readily diffuse by meandering in the interstices. Commonly, gas atoms such as O, N, H, and C diffuse easily in the open lattices of BCC metals, for example, Fe, Ta, W, and Mo.
- *Vacancy mechanism*. Atomic diffusion into the missing atomic sites (vacancies) has been found to be the most favourable. Indeed, vacancies are present in pure metals and alloys at all temperatures; their concentration at the melting temperature (T_m) is about 0.01%. This process has been studied extensively in the past century by a variety of techniques, and the results support this mechanism overwhelmingly on a wide basis in metals, alloys, and oxides. The vacancies may also be in the form of dimmers (the divacancies), particularly near the melting temperature (T_m).
- *Sub-boundary mechanism*. The diffusing atom moves along interconnecting dislocation pipes, which result from naturally occurring low-angle boundaries. This mechanism, discussed later, has been found to operate at low temperatures, typically ~0.5 Tm, the absolute melting temperature, in metals such as Au, Ag, and Cu.
- *Relaxion mechanism*. The diffusing atom moves more or less freely within a disordered group of atoms within the lattice. This mechanism has been ruled out in most crystalline solids but has been considered in recent years in the context of radiation damage in amorphous metallic alloys and some polymers.

The work done by Barradas et al [24] has studied the interface between copper particle and Al coatings with several thermal spray processes. It has shown that, in the case of cold sprayed copper on pure aluminium, an intermetallic has formed (Figure 2-21).

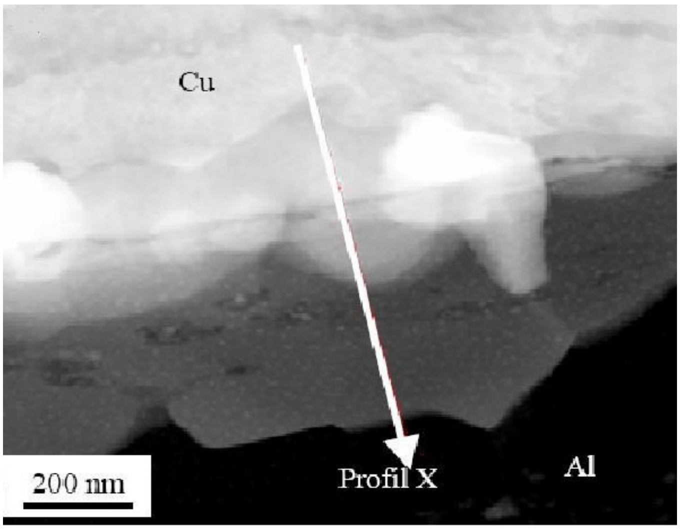

Figure 2-21 : TEM interface between cold sprayed copper coatings sprayed with N_2 at 270°C and 28 bars. [24]

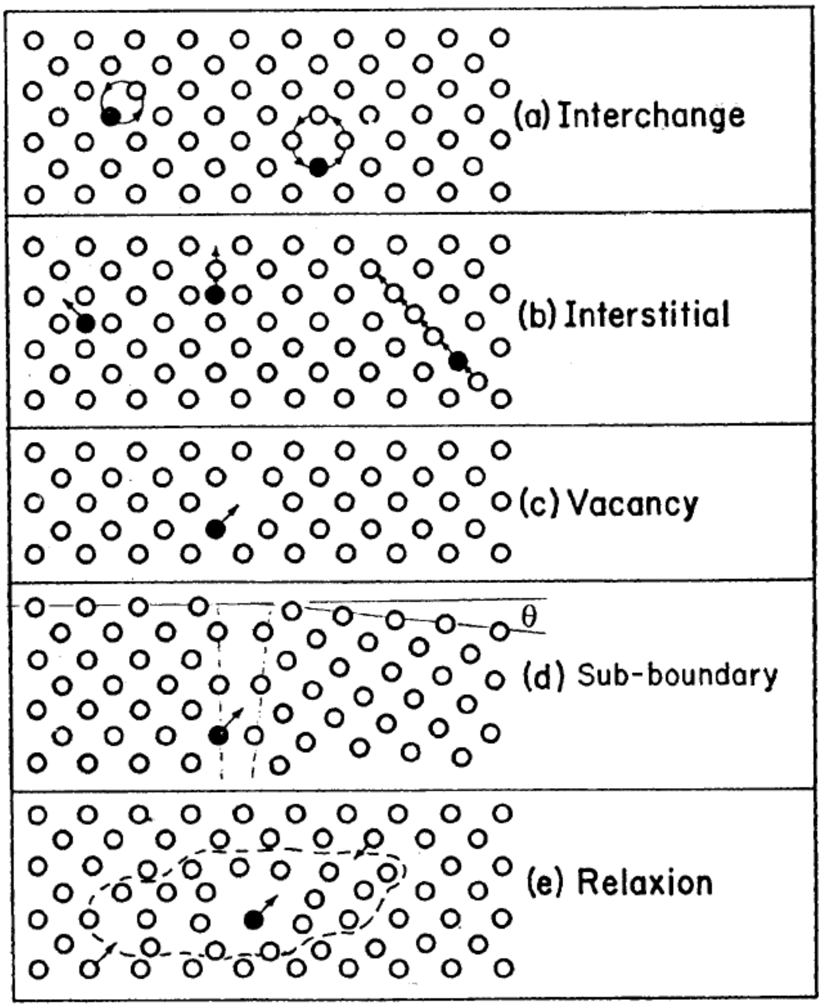

Figure 2-22 : Different type of possible mechanisms for diffusion. [23]

To understand the formation of this intermetallic zone, it is needed to consider the diffusion of copper in Al at a solid state and liquid state. Barradas et al [24] have compared the diffusion distance of copper in solid aluminium and liquid aluminium.

$$L_{\text{diffusion length}} = \sqrt{\mathrm{D} \cdot \mathrm{t}_{\text{diffusion time}}}$$

where,

$L_{\text{diffusion length}}$: diffusion distance
D : diffusion coefficient
$\mathrm{t}_{\text{diffusion time}}$: diffusion time

The interaction time for a cold spray impact is about ~20 ns. The diffusion coefficient for the copper in solid Al is about 10^{-12} $m^2.s^{-1}$ at 900K, whereas the diffusion coefficient of copper in liquid Al is about 10^{-8} $m^2.s^{-1}$. Table 2-4 shows the diffusion length of copper in solid and liquid Al.

Table 2-4 : Diffusion length for copper in Al in solid and liquid state.

	Diffusion coefficient ($m^2.s^{-1}$)	Diffusion length (nm)
Cu in solid Al (at 900K)	10^{-12}	0.15
Cu in liquid Al	10^{-8}	15

This confirms that a diffusion zone can form due to melting of the Al substrate during the cold spray deposition.

The work done by Bolesta et al [25] has also confirmed the possibility for an intermetallic compound to be formed at the interface. A Ni coating has been sprayed on an Al substrate and analysed with synchrotron radiation using the X-ray grazing diffraction. Results have shown the presence of a $NiAl_3$ interface with a thickness of 20-50 nm. Work by Wank et al has also observed an intermetallic zone when Zn was cold sprayed on the aluminium alloy AA7022 and Mg alloys [26].

The presence of a diffusion zone can be favourable to the bond strength between the powder particle and the substrate but observations of such zones in cold spraying are not common. It shows the intimate contact between the materials involved in the process.

2.8 Technological Influences on the Cold Spray Process

Many other factors influence the process. For an industrial case, several powders can be chosen and different surface preparations can be considered. It is necessary to asses these influences.

2.8.1 Oxide Content of the Powder

The oxide content is considered as an important factor influencing the performance of the cold spray process. Several authors have noticed that the critical speed for bonding increases when the oxide content in the powder increases. The work by C.-J. Li et al resumes such concerns [27]. The oxide forms a shell around the powder grain. Upon impact, the oxide shell must be removed in order to get a good quality bonding because a clear and conformal contact is needed. The presence of the oxide shell could explain the increase in value of the critical speed. This effect has been proven when Al is sprayed [28] by using FEM modelling. Indeed, the critical speed for Al is around 660 $m.s^{-1}$ when it is 550 $m.s^{-1}$ for copper. Aluminium has naturally a passive oxide layer on the surface that hinders the formation of shear bands at the interface.

During impact, the copper particle's oxide shell is removed but some traces are found in the coating. Barradas et al [24] have identified the presence of oxide traces at the interface between copper powder grains in the coating. A part of the oxide shell can be found in the coating while most of it has been removed by the violence of the impacts. For copper deposition, measured critical velocities range from 290 to 640 $m.s^{-1}$ when the oxide content increases from 0.02 to 0.336 (wt%) [27].

2.8.2 The Substrate's Surface State

Thermal spray (HVOF, plasma, …) processes require a clean surface. In order to increase the quality of the bonding, usually grit blasting is done on the surface. The higher roughness increases the surface exposed to interact with the particle. Simultaneously, the powder particle has also a mechanical gripping to the surface. The cold spray process is different. If the surface is contaminated, the first particles will not bond and they will clean the surface and remove the surface oxides. The process "activates" the surface and prepares the surface. This delay before the coating builds up due to surface preparation corresponds to an incubation time. It depends on the speed of the particles and the number of impacts on the surface.

It is not necessary to grit blast cold spray surfaces in order to get good bonding. Work by T. Marrocco et al [29] has showed that if Ti is sprayed on TA6V (Ti- Al 6% V 4% alloy), it is better to polish the surface. On a polished surface, the bond strength is around 25 MPa while on a grit blasted surface the bond strength is around 10 MPa.

2.9 Technological Characteristics of the CGDS Process: Existing and Related Results

The cold spray process can be characterised by the deposition efficiency, it gives an important indication on the development of the process performance. The bond strength and microhardness are common standard measurements of the industry.

2.9.1 Deposition Efficiency

The efficiency gives a measure of the performance of the process. Figure 2-23 shows the performance of copper sprayed on Al substrate and of Aluminium sprayed on a Cu substrate. The deposition efficiency is a complex function of several characteristics:

- The powder size distribution.
- Spraying condition.
- Impact angle.
- Substrate and powder surface state (influence of oxides).

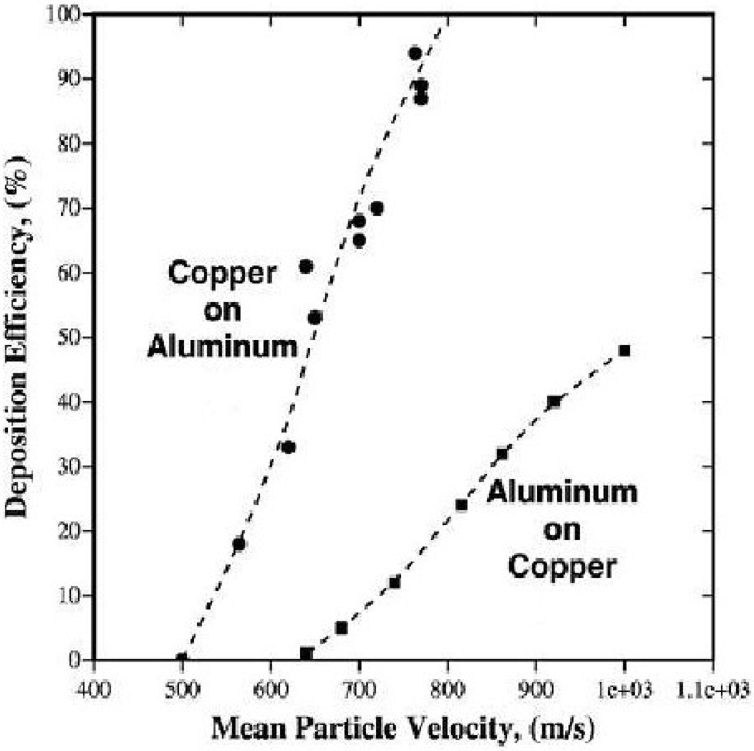

Figure 2-23 : Deposition efficiency of copper sprayed on Al and of Aluminium sprayed on copper. [16]

On Figure 2-23, the efficiency of copper sprayed on Al is high; it is easy to reach high deposition rates of 90%. The high ability of copper to form shear band allows it to bond easily on the aluminium surface. In contrast, the spraying of aluminium on a copper surface is more difficult. The aluminium powder has naturally an oxide shell. During impact, the shell has to burst and deform in order to get a good quality contact with the surface. As diffusion on a nano-scale could be a mechanism to explain bonding, the presence of an oxide shell will hinder the diffusion process.

2.9.2 Bond Strength

Bond strength can be tested with several techniques. The standard technique used in the industry is a pull-of test. A coating is sprayed on a substrate, and then covered with an epoxy resin. A counter surface in aligned with the substrate on the epoxy resin.

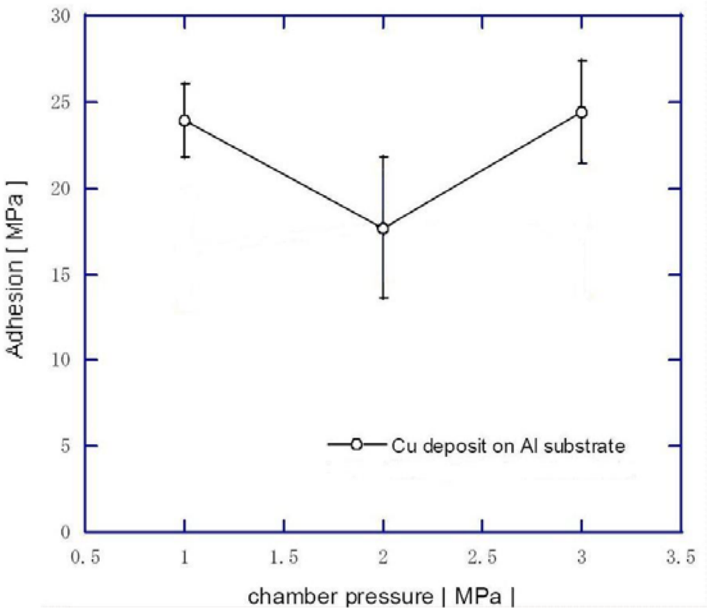

Figure 2-24 : Adhesion of copper deposits on aluminium substrates with N_2 as a process gas at 250°C. It is a tensile test on the coating.[30]

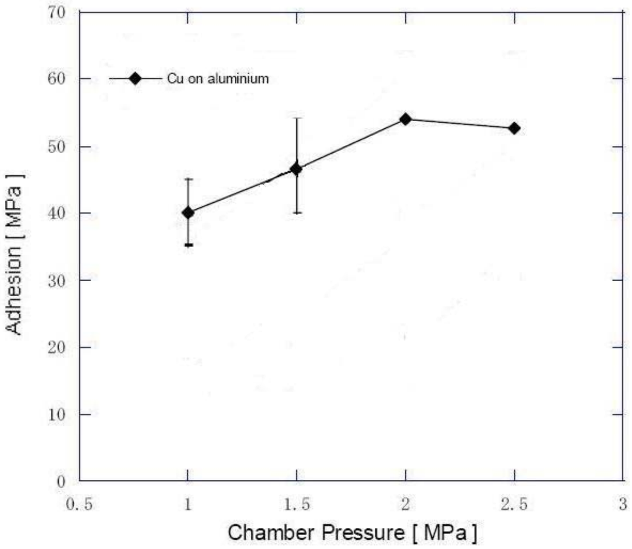

Figure 2-25 : Adhesion of copper deposits on aluminium substrates with He as a process gas at 200°C. [30]

Figure 2-24 shows that bond strength of copper on aluminium is in the range of 15 to 25 MPa and the Figure 2-25 shows that the bond strength of copper on aluminium ranges from 40 to 60 MPa when He is used as a spray gas. These results are from Fukanuma et al [30]. On the other hand, T. Stoltenhoff et al [31] have obtained bond strength of 40 MPa when the powder was sprayed with N_2 at 30 bars and 300°C.

2.9.3 Microhardness

With thermal spray coatings, microhardness characterizes the influence of the spray conditions on the coating properties. For copper coatings, a value of 160 HV_{200g} has been observed by T. Xiong et al [32]. Usually, the value of microhardness is associated with the hardening of the coating.

2.10 Microstructural Characteristics of Copper at High Strain Rates

As seen previously, copper coatings made by cold spray develop a nanostructure in the shear bands under the high strain rate and high pressure. Several other processes give rise to a nanostructure with high strain rate conditions.
During the cold spray process, material undergoes extreme conditions:

Table 2-5 : Typical orders of magnitude of flow parameters in the cold spray process.

Pressure (GPa)	1- 20
Strain rate $\dot{\varepsilon}$ (s^{-1})	$0.1\text{-}1.10^9$
Heating rate $\dot{T}$ ($K.s^{-1}$)	10^9

The extreme values in Table 2-5 can be also obtained by other processes. In order to recreate such high strain rate processes, two techniques are used:

- The flyers impact plate: a plate made with a hard material (WC) is accelerated towards a substrate material by explosive or a two stage light gas gun. When the plate hits the surface, a shock wave is generated in the substrate material.
- Shock laser: a high power laser sends a pulse on a surface that generates a pressure wave in the material. The high heat generation produces a shock deformation in the surface.

The field of a high strain rate and dynamical deformation has been studied by M.A. Meyers [21] extensively. Here are few considerations on the dynamical response of copper at high strain rate based of observations using shock laser and flyers plate impact technique.
In order to induce high strain rates in material, the approach used is to generate a shock pressure in the material. In other words, during a very short lap of time, the pressure on the material reaches several GPa's.

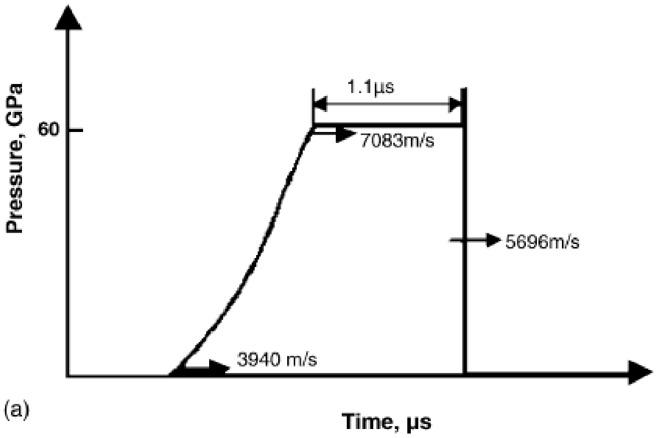

Figure 2-26 : Example of a shock loading during a plate impact.[33]

The high strain is generated during the pressure rise. In the case of a plate impact (Figure 2-26) , a constant step in pressure is maintained for few µs before the shock is released whereas in the case of laser shock (Figure 2-27) , the peak pressure and release waves are passed in a few ns.

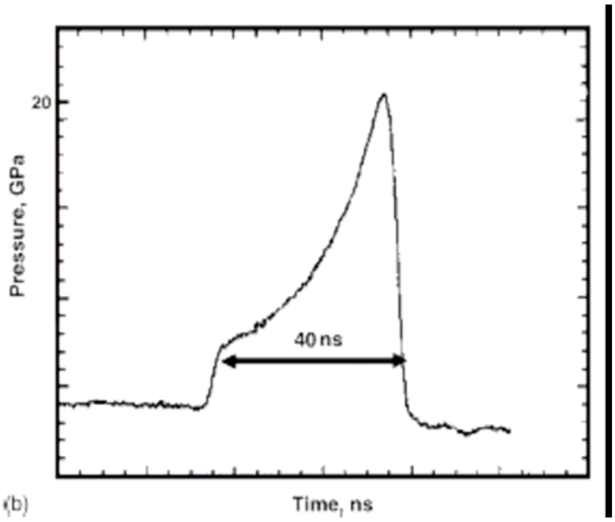

Figure 2-27 : Example of a shock wave generated by a laser pulsed shock. [33]

Both processes generate similar conditions than an impact of powder grain in the cold spray process. They differ in the duration and the shape of the pulse. The dynamic behaviour of copper under these conditions will induce shear bands as cold sprayed copper. Shocked laser seems to have a similar duration as a cold spray impact.

It is necessary to understand the mechanism of dislocation multiplication induced by a shock loading. Work by M. A. Shelhadeh[34] used multiscale dislocation dynamics to study the mechanisms induced by a laser shock in a single copper crystal.
The microstructure, at strain rates higher than 10^6 s^{-1}, is made of dislocation deformation bands where the dislocation density is very high. Figure 2-28 (a)-(c) shows the band like

dislocation cell walls that coincides with slip planes. These bands have a thickness and a dislocation density from one orientation to another.

A double cross-slip mechanism influences the thickness of these bands. A screw dislocation segment can cross slip to a secondary plane and glide on that plane for a short distance and return to its primary plane. The cross slip mechanism illustrated by Figure 2-28 (d) results into the generation of frank-read sources on adjacent and parallel slip planes. The dislocations on these parallel planes are of same type and they have a strong mutual attraction, hence they stabilize.

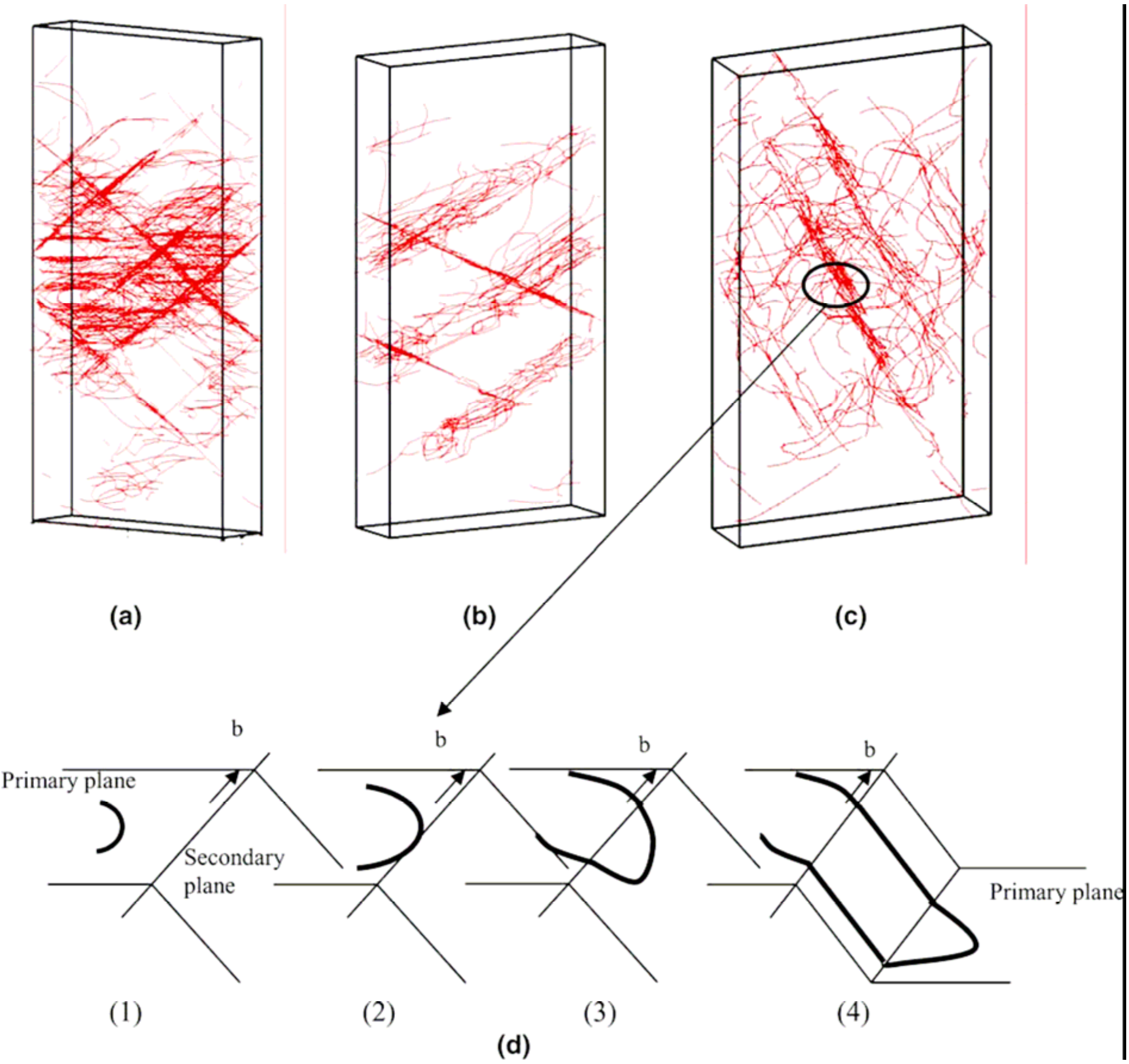

Figure 2-28 : The dislocation microstructure in copper crystal at 5.0 GPa peak pressure and 1.50 ns pulse duration for crystal oriented in: (a) (001); (b) (011); (c) (111) and (d) subsequent events that lead to the activation of the cross slip mechanism.[34]

2.11 Conclusion

Most of the work on cold spray has focused on three areas:

- Modelling of the aerodynamical process.
- Modelling of single impacts.
- Coating characterisation.

The process has been modelled by several authors [6],[7],[8],[9],[10],[11] in order to optimise the particle impact conditions. The geometry of the nozzle can be adapted to the type and size of the powders. Different computer fluid models are also compared. These works also model the behaviour of the gas outside the nozzle. Hence, it is possible with 2D and 3D models to optimize with more precision the effect of the bow shock on the particle impact conditions.
An impact of a powder particle with a speed between 300 and 1200 $m.s^{-1}$ takes about 40 ns. It is not possible to observe directly an impact and the deformation process. FEM is used to understand how the strain, stress and temperature evolve during the impact. The work done by the University of the Federal Armed Forces Hamburg has proved that the value of the critical speed is associated with the onset of adiabatic shear bands at the interface between the powder and the substrate [15]. Additional investigation by Grujicic et al [4],[16] has confirmed this with other materials. These models are based on a constitutive equation that describes the specific characteristics of the materials. These constitutive equations are based on existing experimental data and they have a limited range of validity. The scale of the flow parameters in cold spray is very high (Table 2-5) and no constitutive equation has a proven validity for so high values. Most of the high strain rate models are established for a strain rate $\dot{\varepsilon} \sim 10^4$ to 10^6 s^{-1} while the strain rate in the cold spray process reaches $\dot{\varepsilon} \sim 10^9$ s^{-1}.
The limitations of the models and unexplored issues are the following:

- The models do not take into account the presence of the oxide layer present on the surface of the powder and the substrate.
- Good constitutive equations do not exist for most materials. The high strain rate behaviour of many materials is not known.
- Different powders may have different hardnesses. No model has studied the effect of the powder materials elastic limit on the critical speed. The consequences on the onset of shear bands at the interface do not take into account this effect.
- The models are sensitive to the mesh size used when the interfacial temperature is estimated.
- The effect of the substrate temperature and powder temperature on the deposition process remains poorly investigated experimentally. The effect of the powder temperature has been investigated by FEM by Schmidt et al [14].

Many materials have been tested with cold spray: Cu ([31],[19]), Al [22], $Ti0_2$ [35], Ni [36], Ti [29], Zn[37], Fe-Si [38], MCrAlY ([39],[40]), Fe-Al intermetallic [41], Ti-Al6-V4 [42], Al-Al_20_3 composites [43]; complex alloys like : Al-Cu-Mg-Fe-Ni [44], rare earth iron alloys [45], CuZrTiNi bulk metallic glass [46], Fe-based Amorphous Alloy [47]. Copper has been the centre of a lot of publication since the deposition efficiency of this material is high. The high strain rate behaviour of copper has been studied by several other techniques ([20],[34], [33]) and literature on constitutive equations for copper is large ([21],[48]). Coatings are often characterized by several mechanical properties. The standard properties used to do a comparison are the bond strength and the microhardness. SEM images of microstructures are regularly used to characterize the microstructure of the coating. In the case of composites coatings, SEM images shows how elements are dispersed in the matrix.

From a scientific point of view, the interface between the substrate and the powder particle is the origin of the quality of the bonding. The work by Barradas et al [24] has analyzed the interface of copper coating sprayed on aluminium by several thermal spray techniques (plasma, HVOF, cold spray). More recently, work by Y. Ichikawa et al [40] has investigated the interface of cold sprayed MCrAlY coatings. In each of these studies, a large TEM work has been done to analyze the interface. A satisfying explanation on the nature of the bond and the process characteristics is still missing.

This thesis will investigate in detail how the copper coating build up is influenced:

- By the powder's size distribution
- By the powder's mechanical properties

This will be done by comparing how two different powders yield coatings with different deposition efficiencies and mechanical properties. The role of the oxide content will also be discussed. No published work gives a detailed analysis of the copper coatings properties and deposition properties.
The interface will be analyzed by using Auger spectroscopy which has not been attempted yet on cold spray coatings. The results will be correlated by TEM investigation.

Chapter 3 Modelling and Experimental Measurements of the Copper Particle's Speed with the CGDS Process

3.1 Introduction

The cold gas dynamic process accelerates powder using a supersonic gas flow. It is necessary to understand how the main spraying parameters (stagnation pressure P_0 and stagnation temperature T_0) affect the velocity and the temperature of each individual powder grains. The copper particle impact conditions (particles velocity and temperature) have to be linked to the main spray parameters and the nozzle geometry by using a gas model. The one dimensional isentropic gas model of a Laval type nozzle has been developed in section 2.3 .

This chapter will apply this model to get the particle impact conditions of the two nozzles used in this work:

- The nozzle of the University of Nottingham
- The CGT standard Nozzle used in the Kinetic 3000 installation

Several influences will be discussed:

- The choice of the carrier gas (He was used with the Nottingham nozzle)
- The influence of the gas pressure
- The influence of the gas temperature
- The influence of the geometry

These results will be compared to laser velocimetry experiments using the CPS2000 and DPV2000 measuring system applied to two copper powders. This system is standard in the thermal spray industry. The experimental results will be compared to the model results and the limitation of the model will be shown.

3.2 Particles Thermal and Velocity Model

The equation of movement of the powder particle in the gas flow is shown in section 2.3.3. The model needs to precise the expression of the drag coefficient.

$$\frac{1}{2} C_D \rho_{gas} \frac{\pi d_P^2}{4} \left(\vec{v}_{gas} - \vec{v}_P\right) \left|\vec{v}_{gas} - \vec{v}_P\right| = \rho_P \frac{\pi}{6} d_P^3 \frac{d\vec{v}_P}{dt}$$

ρ_P : density of the powder particle
d_P : diameter of the powder particle
$\vec{v}_P$: speed of the particle
C_D : drag coefficient of the powder particle
ρ_{gas} : gas density
$\vec{v}_{gas}$: gas speed

This study will analyse the velocity and temperature of copper particles sprayed with helium and nitrogen. Table 3-1 contains the gas properties and Table 3-2 holds the properties of copper used to solve the model.

The value of the powder temperature depends on the heat exchange with the gas by convexion.

$$\frac{dT_P}{dt} = \frac{hA_P}{m_P C_P}\left(T_g - T_P\right)$$

A_P : area of the particle's cross section
m_P : mass of the powder particle
T_g : temperature of the gas
T_P : temperature of the powder particle
h : thermal convectivity coefficient

Table 3-1 : Gas characteristics.

	Nitrogen N_2	Helium He
Thermal conductivity k ($W.mK^{-1}$)	0.24	0.1468
Molecular mass $g.mole^{-1}$	28	4
Specific heat C_p ($J.kg^{-1}.K^{-1}$)	1043	5193
Viscosity μ ($kg.m^{-1}.s^{-1}$)	0.000018	0.0000186

Table 3-2 : Copper material properties.

	copper
Copper density ($kg.m^{-3}$)	8920
Specific heat ($J.kg^{-1}.K^{-1}$)	379

3.2.1 Expression of the Drag Coefficient

The drag coefficient is expressed as a function of the Reynolds number [49].

$$C_D = \frac{24}{\mathrm{Re}}\left[1 + 0.15 \cdot (\mathrm{Re})^{0,687}\right] + \frac{0.42}{\left[1 + 4.25 \cdot 10^4 (\mathrm{Re})^{-1,16}\right]}$$

The drag coefficient expression is valid for spheres and for Re number < 10^5.

$$\text{The Reynolds number is: } \mathrm{Re} = \frac{\rho_{gas} \cdot \bar{v}_{gas} \cdot Diam_{\sec tion}}{\mu_{gas}}$$

The drag coefficient will allow us to solve the equation of movement by using the gas characteristics along the nozzle.

3.2.2 Expression of the Thermal Convectivity Coefficient

There are 3 ways of transferring heat from the gas stream to the particle: by convection, radiation and conduction. However it is assumed that the mechanisms here are mostly convection and conduction. It is assumed that the particles have no thermal gradient and are good heat conductors. This assumption is reasonable for copper powders.
The expression of the thermal convectivity coefficient:

$$h = \frac{k_g}{d_P}\left(2.0 + 0.6 \cdot \mathrm{Re}^{\frac{1}{2}}\,\mathrm{Pr}^{\frac{1}{3}}\right)$$

$$\mathrm{Pr} = \frac{\eta_g (c_P)_g}{k_g}$$

k_g : gas thermal conductivity

η_g : dynamical viscosity of the gas

c_P : gas specific heat

With this expression, it is possible to compute the value of the heat convectivity coefficient at each cross section of the nozzle.

3.2.3 Numerical Resolution

For numerical resolution, the problem has been divided in 4 parts:

- The mesh size of the convergent part of the nozzle is 1000.
- The mesh size of the divergent part of the nozzle is 1000.
- The mesh size of the standoff distance is 1000.
- The mesh size of the bow shock thickness is 1000.

The initial powder temperature is supposed to be 293 K and its initial velocity is 10 m.s^{-1}.

The time step used for solving the equation describing the powder particle velocity and temperature is 10^{-7} s

When powder particles are very fine (< 10 µm), their behaviour in the bow shock is very sensitive to numerical boundaries conditions. This leads to slight oscillations visible on Figure 3-6 and Figure 3-7. The effect of the bow shock of particles with a diameter between 1 and 2 µm is strong. The computation of drop of velocity for these particles requires sampling the size with more points. This leads to a sharp drop for copper powder particles as shown on Figure 3-7.

3.3 Nozzle Designs

In this study, two nozzles have been used. The geometry of the nozzle will determine the gas speed and density; hence it will determine the particle's impact conditions. Nozzle designs are subjected to patents. So, some information will not be included on the design.

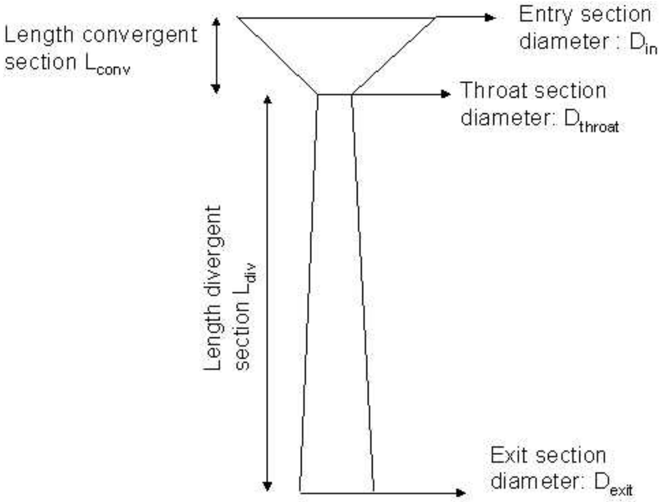

Figure 3-1 : Schematic of a nozzle.

Figure 3-1 shows a schematic of a nozzle. Extensive work is done to study the optimal profile between the different sections (inlet, throat and exit section) to get the optimum powder impact conditions.

The profiles between D_{in}, D_{throat} and D_{exit} are supposed linear. This simplifies the resolution of the one dimensional isentropic gas model in the nozzle.

Nottingham nozzle

$$L_{div} \ : 100\,\mathrm{mm}$$

$$\frac{D_{exit}}{\mathrm{D}_{\mathrm{throat}}} : 2.76$$

CGT nozzle

$$L_{div} \ : 68\,\mathrm{mm}$$

$$\frac{D_{ext}}{\mathrm{D}_{\mathrm{throat}}} : 2.9$$

3.4 *Gas Characteristics in the Nozzle*

In the equation of movement, the copper particle speed will be influenced by the gas speed and density. Therefore, it is a necessary to understand how these variables evolve in the nozzle to understand how the powder particle impact conditions are influenced. First, we will illustrate the evolution of the gas speed and gas density inside the nozzle in order to show the influence of the gas stagnation pressure and temperature. For this purpose, we will use the CGT nozzle. Secondly, we will discuss how the particle impact conditions are influenced by the initial stagnation temperature and pressure of the gas.

3.4.1 Influence of the Gas Temperature on the Gas Density and Speed in the Nozzle

At a fixed N_2 pressure of 30 bars, two values of stagnation have been compared. The evolution of the gas density and speed in the nozzle has been plotted.

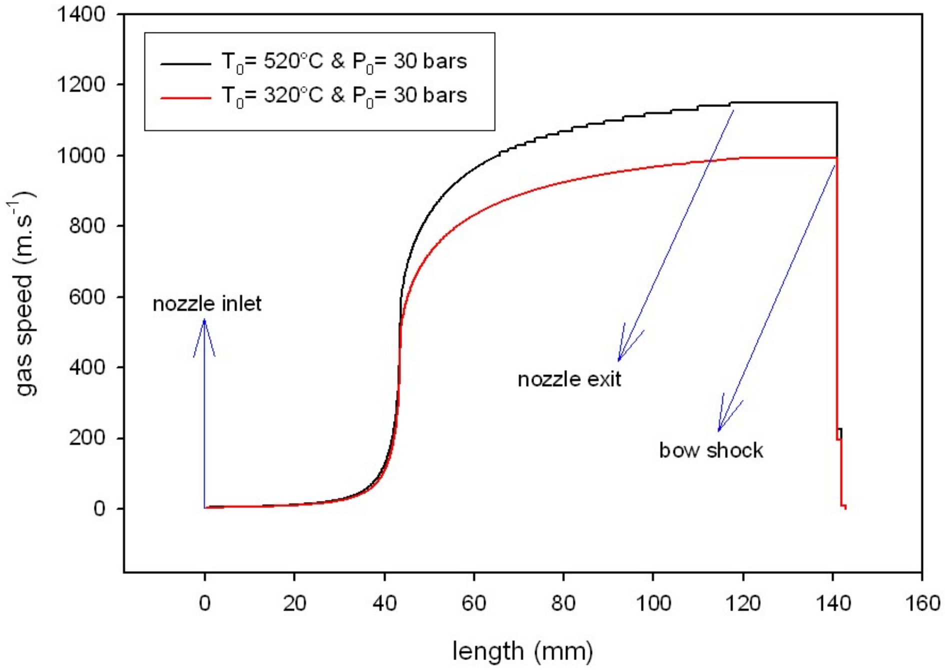

Figure 3-2 : Evolution of the N_2 gas speed inside de CGT Nozzle computed with the one-dimensional isentropic gas model for two values of stagnation gas temperature T_0 and a fixed pressure P_0.

Figure 3-2 shows the evolution of the N_2 gas speed inside the nozzle. At the inlet, the gas enters the convergent part of the nozzle. Its speed does not change significantly at first. When the throat is reached, the gas speed has increased to its sound velocity. After, in the divergent part, the expansion of the gas increases its velocity above the sound velocity.

Figure 3-3 shows the evolution of the gas density in the nozzle. In the convergent part, the gas density is dependent of the initial temperature. At 320°C the N_2 gas is less expanded than at 520°C hence, its density is higher. Once the throat is reached, the gas density drops fast. At 320°C, the gas density stays higher than at 520°C. The difference in gas density drops as the expansion in divergent part continues.

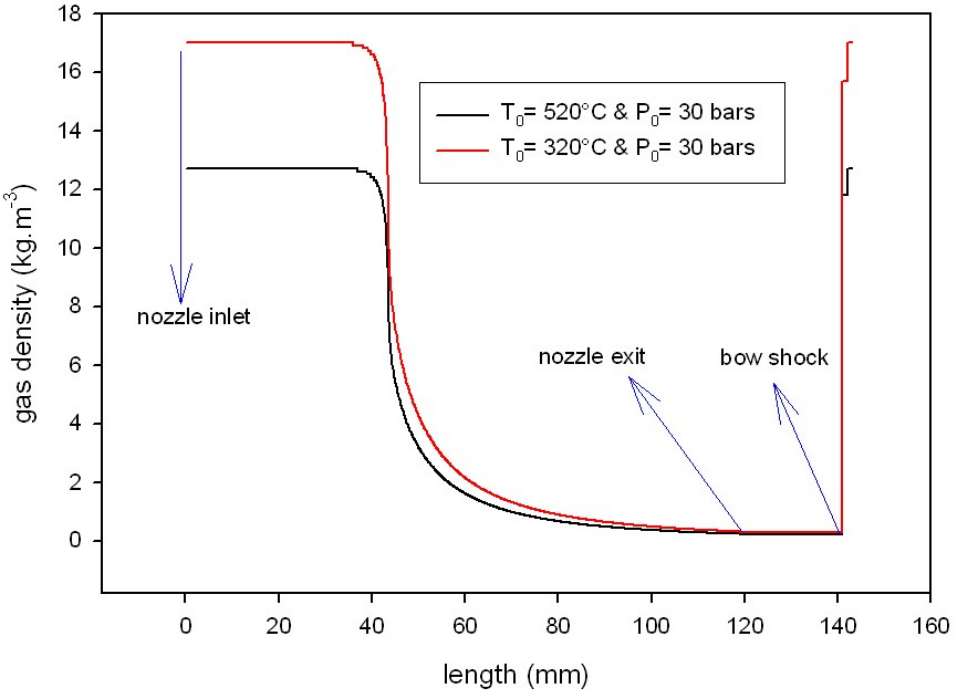

Figure 3-3 : Evolution of the N_2 gas density inside de the nozzle computed with the one-dimensional isentropic gas model for two values of stagnation gas temperature T_0 and a fixed pressure P_0.

A copper particle's speed in a gas flow on previous Figure 3-2 and Figure 3-3 will benefit from the increase in gas speed at 520°C. Hence an increase in stagnation gas temperature will increase the copper particle's speed by increasing the gas speed in the divergent part of the nozzle.

3.4.2 Influence of the Gas Pressure on the Gas Density and Speed in the Nozzle

At a fixed temperature of 520°C for the N2 gas, the evolution of the gas density and speed in the nozzle has been computed for a pressure of 22 bars and 30 bars.

Figure 3-4 shows the evolution of the gas speed when gas stagnation pressure P_0 is increased from 22 bars to 30 bars and the stagnation temperature T_0 remains fixed at 520°C. The two curves are totally superposed on the figure. The change in gas pressure did not modify the speed of the gas in the nozzle. In the Laval nozzle, the mass flow is determined by the nozzle geometry and design and the sound velocity. The gas sound velocity is determined by the temperature and the gas type. Hence, with a fixed throat and stagnation temperature T_0, the mass flow in the nozzle can not be changed.

Figure 3-5 shows that an increase in gas pressure will change the gas density evolution in the nozzle. The initial high stagnation pressure P_0 also implies a slow drop in density in the nozzle.

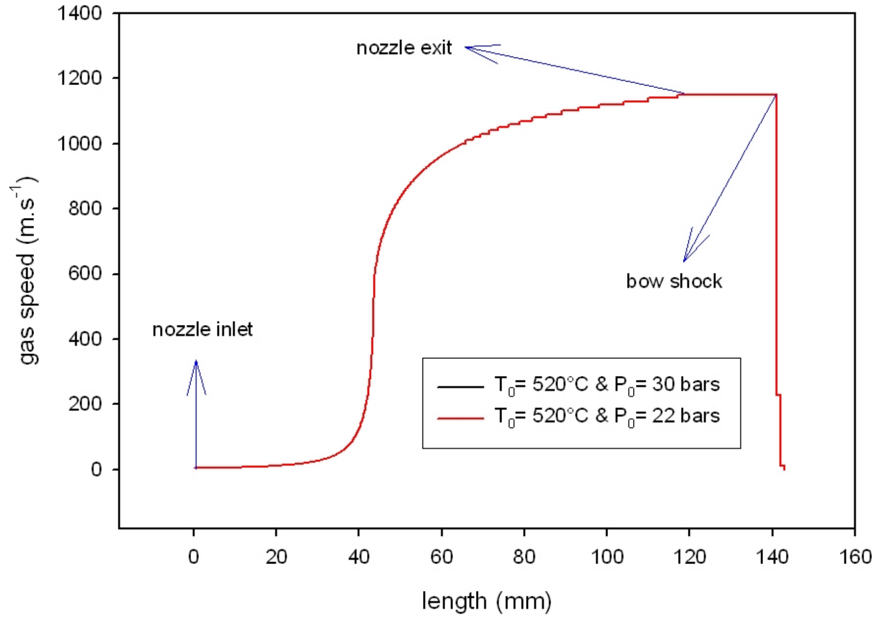

Figure 3-4 : Evolution of the N_2 gas speed inside de CGT Nozzle computed with the one-dimensional isentropic gas model for two values of stagnation pressure P_0 and a fixed stagnation temperature T_0.

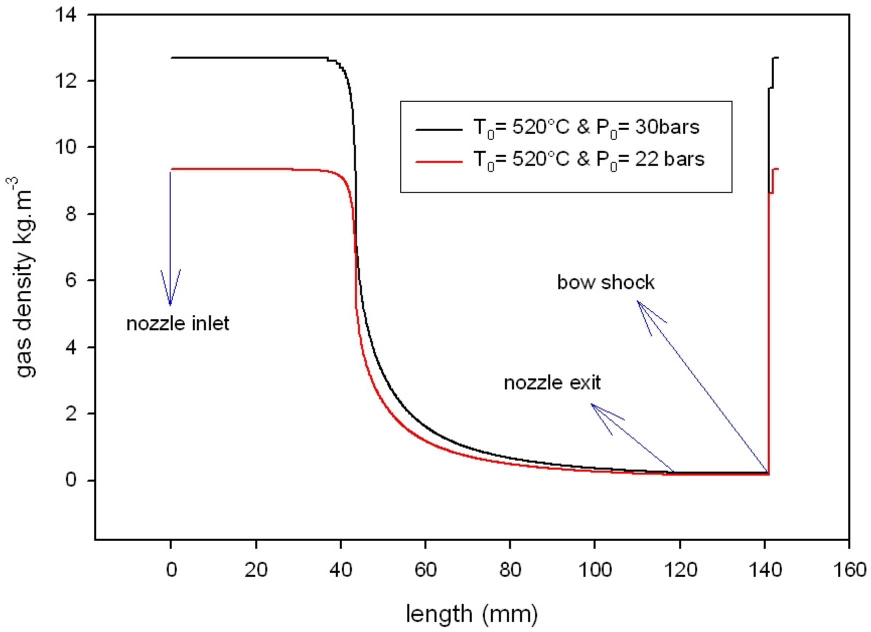

Figure 3-5 : Evolution of the N_2 gas density inside de CGT Nozzle computed with the one-dimensional isentropic gas model for two values of stagnation pressure P_0 and a fixed stagnation temperature T_0.

The movement equation of powder particles shows that a high gas density is favourable to the acceleration of powder particles. Hence copper powder will be better accelerated when the stagnation pressure is increased.

3.5 Influence of the Initial Stagnation Temperature and Pressure on the Particle Impact Conditions

The particle impact conditions (PIC) are the particle's speed and temperature. Once the gas conditions in the nozzle are known, the PIC has been computed using the models in section 3.2. The presentation of the data will be graphs of particle temperature and speed as a function of the copper particles diameters. The CGT nozzle with N_2 gas has been used to compute the PIC and illustrate how the stagnation pressure and temperature influences them. This model takes into account the presence of the bow shock by using the billing's approximation. The PIC is determined when the particle is in contact with the surface before starting to deform.

3.5.1 Influence of the Gas Stagnation Pressure and Temperature on the Particle's Speed

The Figure 3-6 shows the evolution of the copper particle's speed when the stagnation temperature increases from 320°C to 520°C.

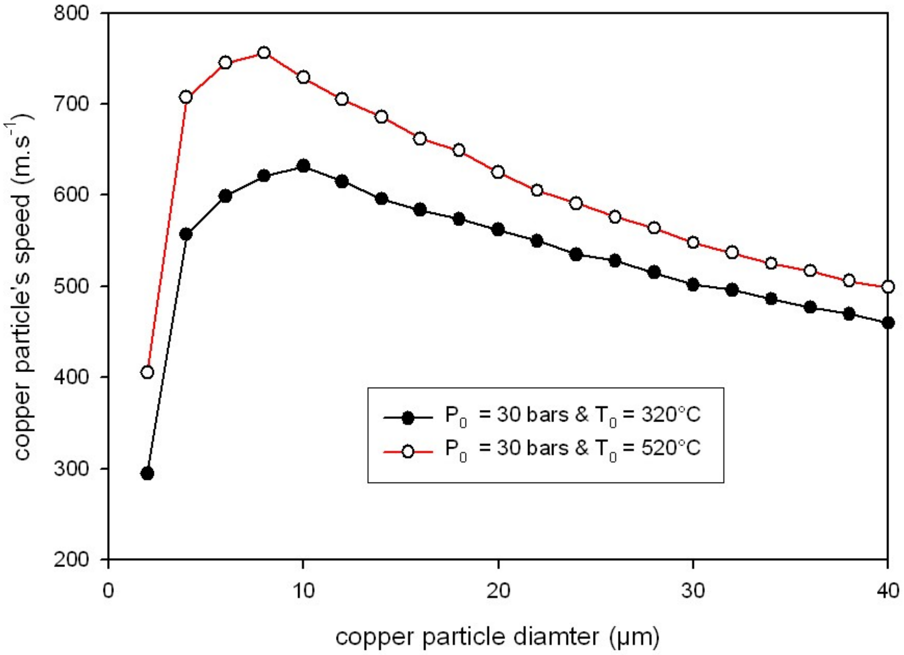

Figure 3-6 : Copper particle speed upon impact with two different initial stagnation gas temperatures.

The difference between the red and black curves on Figure 3-6 is larger when the particle's diameter decreases. The two curves tend to be parallel when the particle's diameter increases. Figure 3-7 shows the evolution of the copper particle's speed when the stagnation temperature is fixed and the stagnation pressure increases from 22 bars to 30 bars.

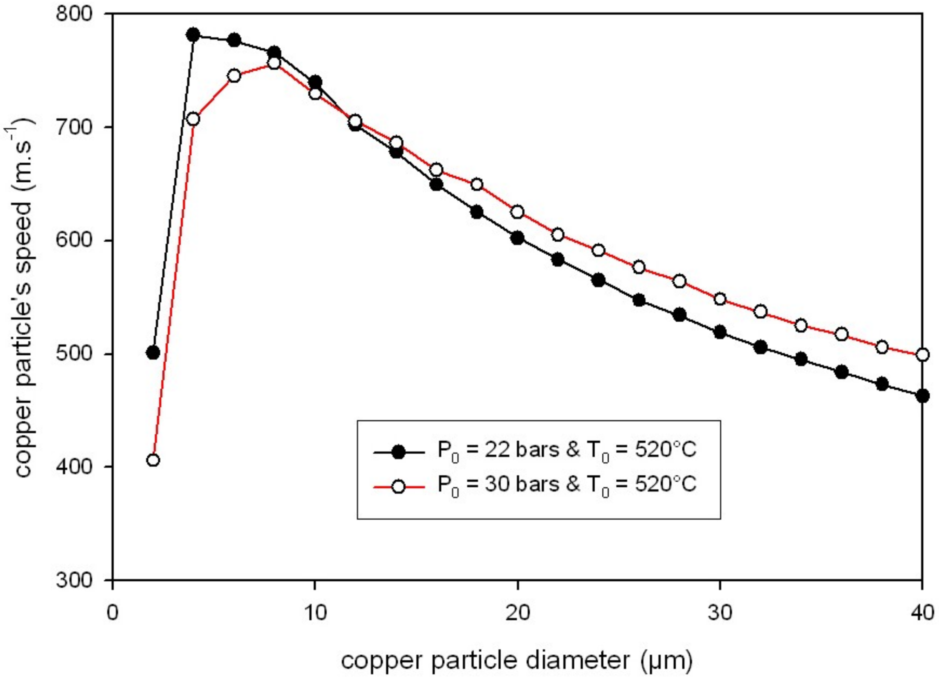

Figure 3-7 : Copper particle speed upon impact with two different initial stagnation gas pressures.

Changing the stagnation pressure P_0 or the stagnation temperature T_0 will not change the particle speed in the same way. By increasing the gas stagnation temperature (and keeping the pressure constant), the gas velocity inside the nozzle will increase steadily while the gas density drops (Figure 3-2 & Figure 3-3). Fine particles with their low inertia will be more sensitive to changes in the gas velocity. Hence, they will be more accelerated by an increase in gas stagnation temperature. Larger particle also benefit from the increase in the gas velocity but not as largely as small particles.

By increasing the gas pressure (at fixed temperature T_0), the velocity profile was not modified in the nozzle but the density of the gas in the nozzle was increased (Figure 3-4 & Figure 3-5). This improves the momentum transfer between the gas and the particle in the gas stream. Larger particle will benefit a lot from the increase in gas density. They expose a large surface to the gas stream that allows drag to be more efficient. The behaviour of fine particles (< 10 µm) is dominated by the bow shock effect. At 30 bars, the gas density in the bow shock is higher than at 22 bars and this will slow particles with a small inertia.

The gas bow shock at the surface of the substrate slows down copper particles with a diameter below 5 µm well under the critical speed. This has been confirmed by more sophisticated models [6].

3.5.2 Influence of the Gas Stagnation Pressure and Temperature on the Particle's Temperature

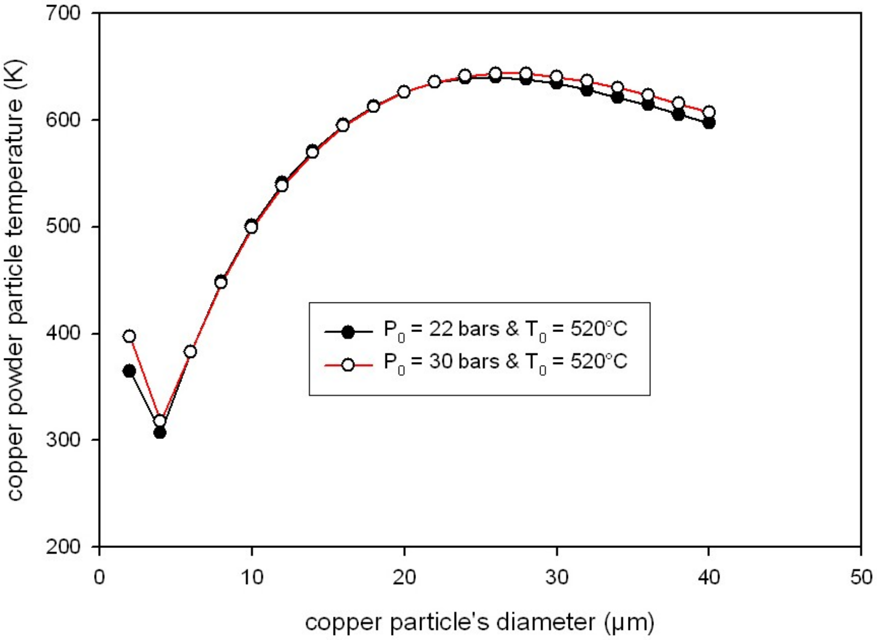

Figure 3-8 : Copper particle temperature evolution as a function of diameter's for two values of stagnation pressures P_0.

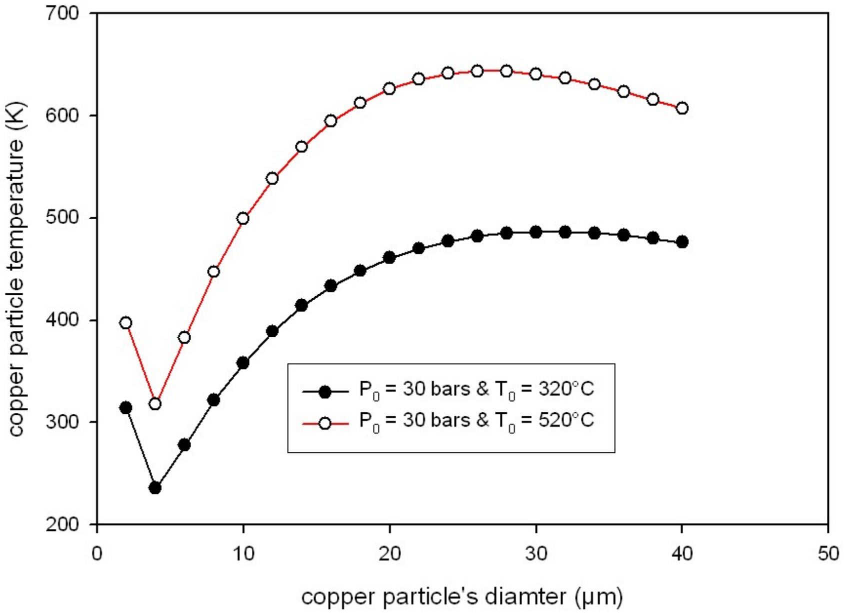

Figure 3-9 : Copper particle temperature evolution as a function of diameter's for two values of stagnation temperatures T_0.

Figure 3-8 shows that a change in gas pressure does not affect significantly the particle's temperature. On the contrary, Figure 3-9 shows that a change in the gas stagnation temperature changes significantly the copper particle's temperature.

The copper absorbs the heat from the gas during its passage in convergent part of the nozzle. In the divergent part of the nozzle, the gas expands and its temperature drops. During the passage of the copper particle in the divergent part, the heat is restored to the gas. Small particle have a small heat capacity, they absorb easily the heat in the convergent part and restore very quickly the heat to the gas in the divergent part. On Figure 3-9, copper particles with a diameter below 15 µm have a temperature that is determined by the stagnation gas temperature. The temperature variation for these copper particles is low (smaller than 100°C).

The bow shock influences the final temperature of very fine copper particles. The heat capacity of copper particles with a diameter below 5 µm is so small that they heat up again in the bow shock. These particles also have a very sharp drop in velocity in the bow shock. It is likely that they never bond on the surface.

3.6 Influence of the Spray Gas Choice

The model describes the behaviour of a single copper particle inside the Nottingham nozzle. The gas used with this nozzle is helium. Figure 3-10 shows the influence of the increase in He pressure form 11 bars to 29 bars on the copper particle speed as a function of the powder particle's diameter. All four values have been used in the next chapter to analyze single splats.

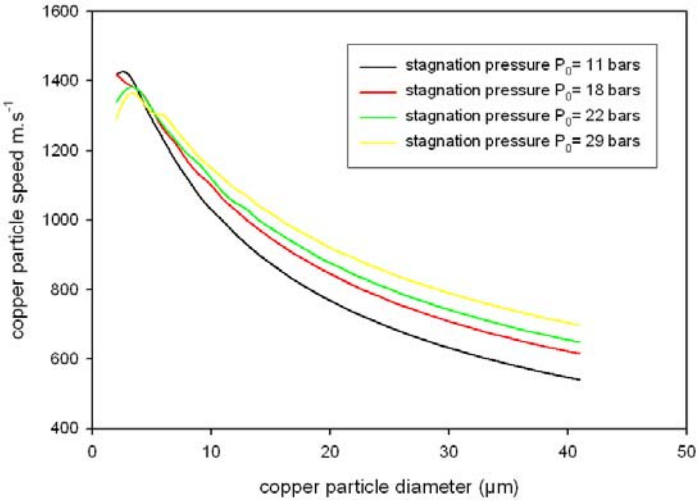

Figure 3-10 : Simulation of the copper particle speed with the Nottingham nozzle and He as spray gas.

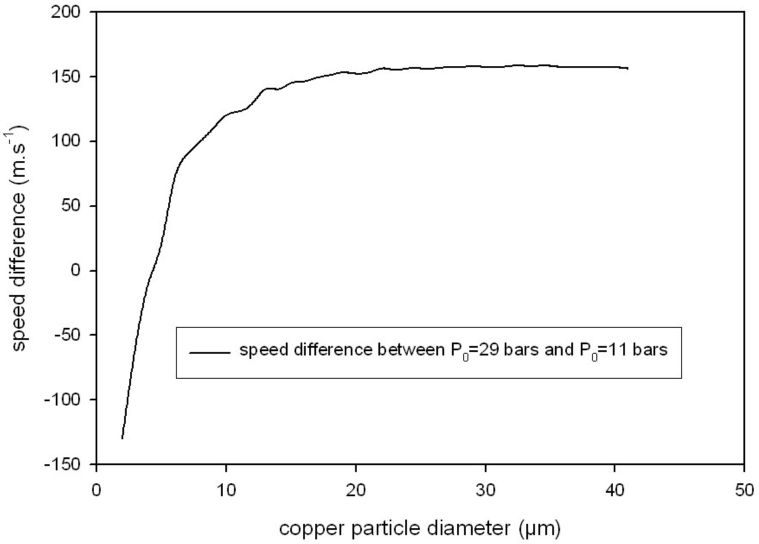

Figure 3-11 : Speed differences between the copper particles sprayed at P_0=29 bars and P_0=11 bars.

Figure 3-10 shows that that copper particles with a diameter below 10 µm have a final velocity that saturates around 1400 $m.s^{-1}$. This is the effect of the gas bow shock at the substrate's surface.

Figure 3-11 shows the speed difference between copper particles when a stagnation pressure of 29 bars and 11 bars are applied. This graph shows that copper particles with a diameter above 15 µm are on average 150m.s^{-1} faster when they are sprayed at a stagnation pressure of 29 bars. Copper particles with a diameter below 15 µm do not benefit as much from an increase in the gas stagnation pressure. This difference is explained by the evolution of the gas density in the nozzle. (Section 3.5.1)

The use of helium as a spray gas leads to much higher copper particle speed (Compare Figure 3-7 and Figure 3-10). The low molecular mass of the gas allows it to accelerate very easily but this is unfavourable to momentum transfer between the gas and the powder particle. In the CGDS process, helium yields the highest values of powder speed even if momentum transfer is less favourable than in the use of other gases. The high gas velocities compensate the less efficient momentum transfer.

3.7 Design of Experiment: Range of each Parameter

This study will investigate the effect of the stagnation pressure P_0 and temperature T_0 on the copper coating properties. It is needed to establish a design of experiment with a range for each of these variables. The range of each parameter has to allow a coating to form in each case. The Nottingham nozzle was used to study single splats with helium as a spray gas, these results will be presented in the next chapter. In this design of experiment using the CGT nozzle, nitrogen was used as spray gas.

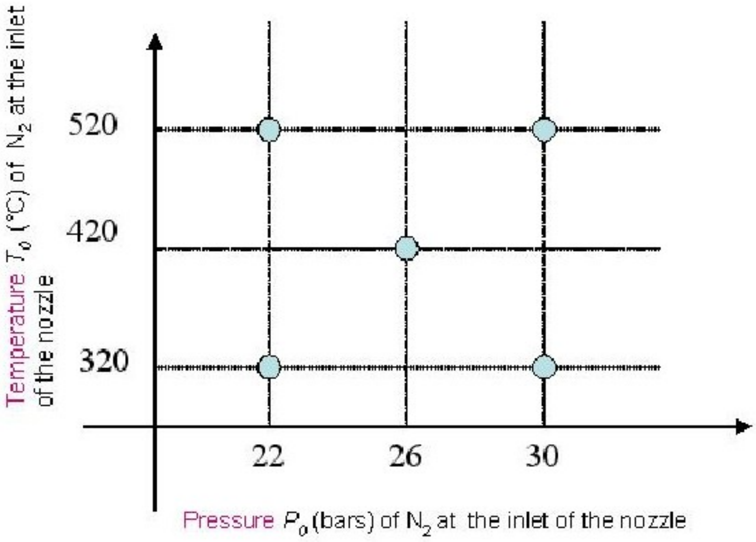

Figure 3-12 : Presentation of the design of experiment used in this study.

Figure 3-12 and Table 3-3 shows the set of parameters chosen for this study. Based on a literature review, it was established that these condition would have yielded coatings with sufficient thickness to be studied.

Table 3-3 : Set of spray parameters used in this study.

Stagnation pressure P_0 (bars)	Stagnation temperature T_0 (°C)
22	320
22	520
26	420
30	320
30	520

Each of these spray conditions have been modelled to analyse the evolution of the copper particle's speed as a function of its diameter. The results have been compared to laser velocimetry applied to the copper powders used in this study.

3.7.1 One Dimensional Model of the CGDS Process Applied to the Design of Experiment

The spray conditions described earlier have been modelled on Figure 3-13. The copper particle's speed increases until it is influenced by the presence of the bow shock. The powder's speed is significantly influenced by the size of the particle. It ranges from ~800 $m.s^{-1}$ to ~450 $m.s^{-1}$.

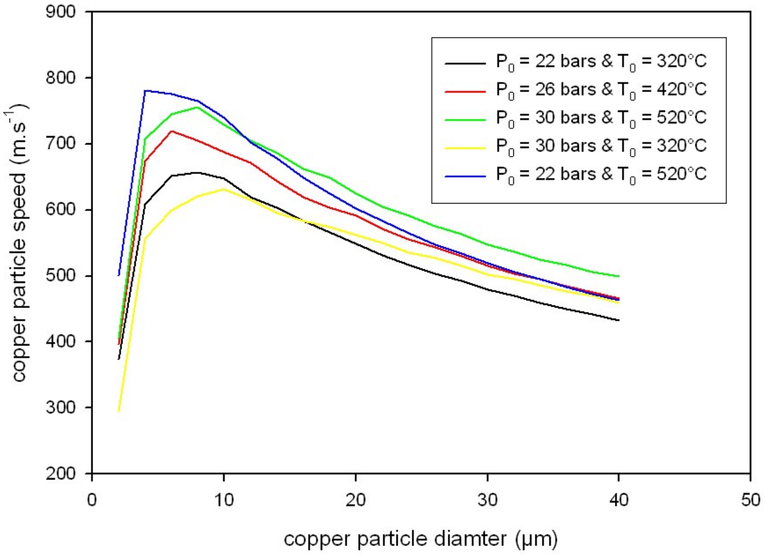

Figure 3-13 : Model of the copper particle speed with the spray conditions in the design of experiment.

As shown previously, the change in working pressure and temperature will not affect the copper particle's speed. Among these 5 spray conditions; it is interesting to isolate the ones that accelerate the powder uniformly on the diameter size range.

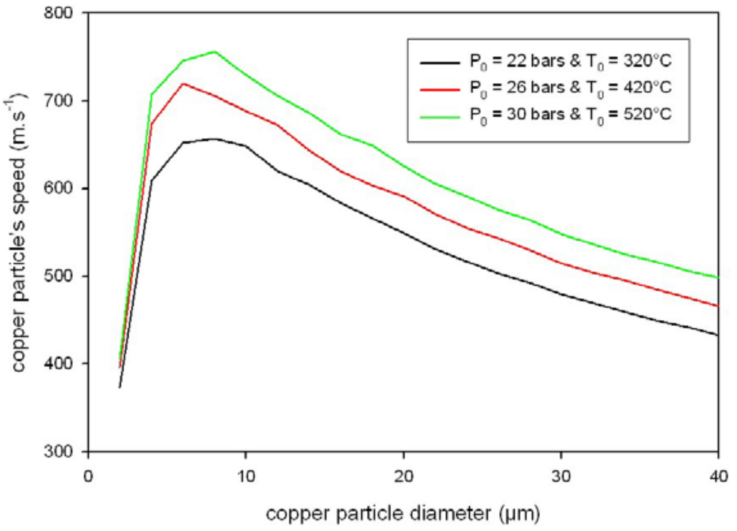

Figure 3-14 : These 3 selected spray conditions will accelerate uniformly the copper powder on its size range.

Figure 3-14 shows that these 3 selected spray conditions will increase the powder's speed uniformly on the size range. These three conditions correspond to a simultaneous increase in stagnation pressure and temperature. An increase in gas stagnation temperature will favour the speed of fine copper particles (below 10µm) while an increase in the gas stagnation pressure will increase the speed of larger copper particles. It is interesting to compare the speed between the back and green curve on Figure 3-14. The Figure 3-15 shows the difference in speed. It shows that by changing simultaneously the gas stagnation pressure and temperature from P_0=22 bars & T_0=320°C to P_0=30 bars & T_0=520°C, the copper particle's speed increases around 80 m.s^{-1}.

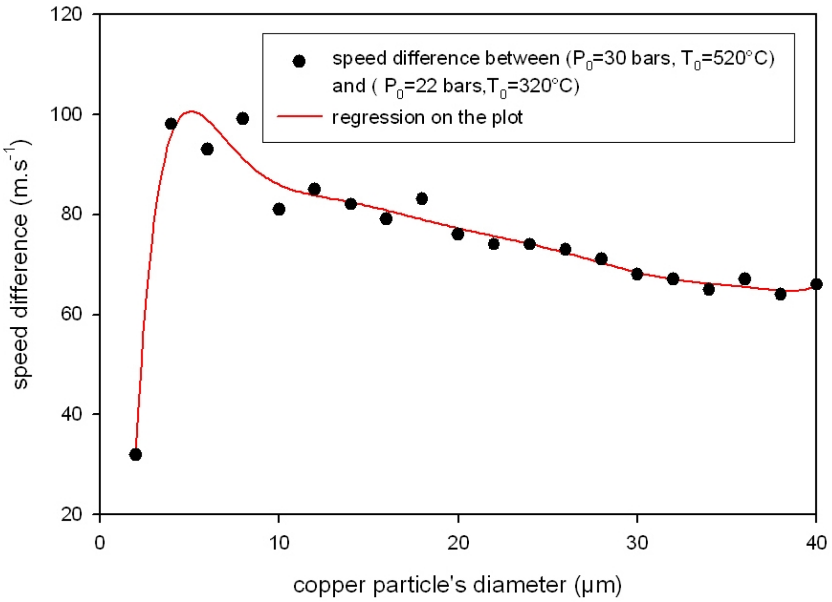

Figure 3-15 : Difference in copper particle speed between spray conditions (P_0=30 bars, T_0=520°C) and (P_0=22 bars,T_0=320°C).

The copper particle's final temperature is illustrated in Figure 3-16.

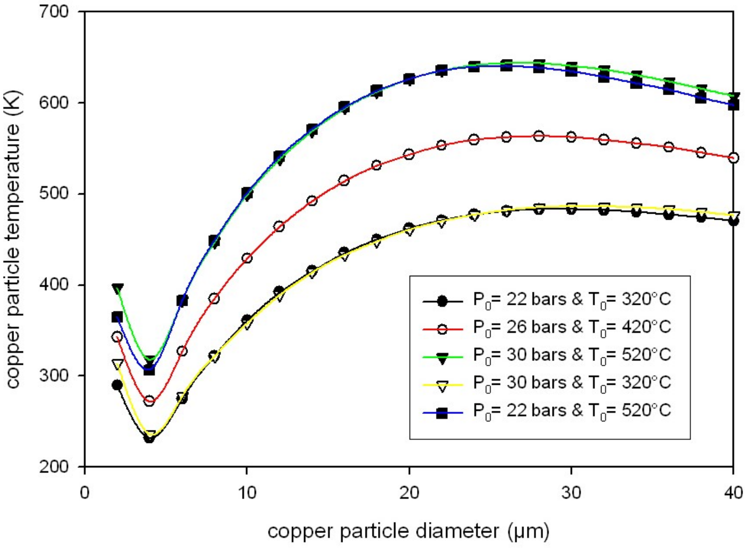

Figure 3-16 : Copper particle temperature evolution as a function the spray conditions in the DoE.

The final temperature of the copper particle is mainly determined by the initial stagnation temperature of the gas. The copper particle's final temperature will influence its ability to deform on impact. Fine particles loose their heat in the divergent part of the nozzle. Once they hit the gas shock wave, they heat up again.

Table 3-4 : Difference in speed between a copper particle with a diameter of 40 µm and 10 µm.

	P_0=22 bars & T_0=320°C	P_0=30 bars & T_0=520°C
Diameter: 10 µm	648 $m.s^{-1}$	729 $m.s^{-1}$
Diameter: 40 µm	433 $m.s^{-1}$	499 $m.s^{-1}$
Speed difference	215 $m.s^{-1}$	230 $m.s^{-1}$

Table 3-4 shows the difference in speed between copper particles with a diameter of 10 µm and 40 µm at 2 different spray conditions. Any commercial powder has copper particles with a size of 5 µm to 50 µm. The difference in speed between fine particles and larger particles is very important ~200 $m.s^{-1}$.

3.8 The Laser Velocimetry System: CPS2000 and DPV2000

The laser velocimetry system used for this work is the DPV2000 system from TECNAR (Canada). It allows measuring the speed, the size and the temperature of particles during spraying. The DPV2000 analyzes the light emitted by the hot particles during their flight.
The system has three components (Figure 3-17):

- the sensor head
- detection module
- the control module

The CPS2000 system is complement of the DPV2000 developed to measure the speed of cold powder particles. It is a laser that injects an infrared light in the powder flow. The detected signal depends on the way the powder particle scatter the light toward the detector. The CPS2000 component of the DPV2000 system is a solid state high power laser diode that produces a monochromatic infrared light. This light is brought to the powder flow by an optical fibre. The wave length is 780 nm.
Typically, the CPS2000 system allows to characterize powder particles as small as 10 µm for ceramics materials and 6 µm for metallic materials.

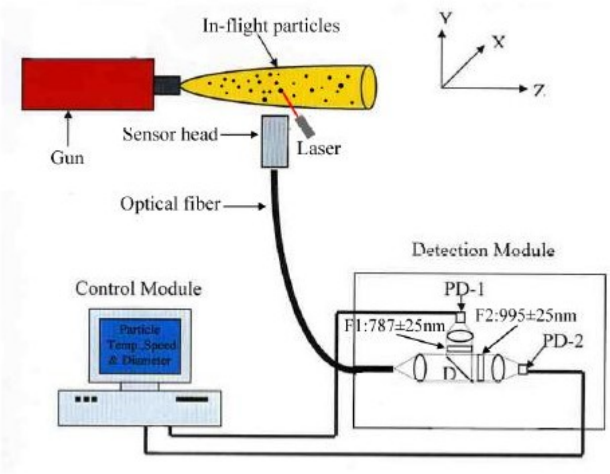

Figure 3-17 : The three components of the DPV2000 system.

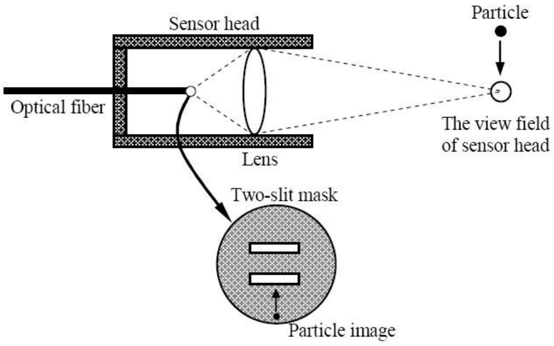

Figure 3-18 : Sensor head [50].

When a particle travels through the view field of the sensor head, an image will be formed by the scattering light at the plane where the two-slit mask is placed (Figure 3-18). The image formed in the mask moves and it is converted into a two-peak signal and transmitted to the detection module.

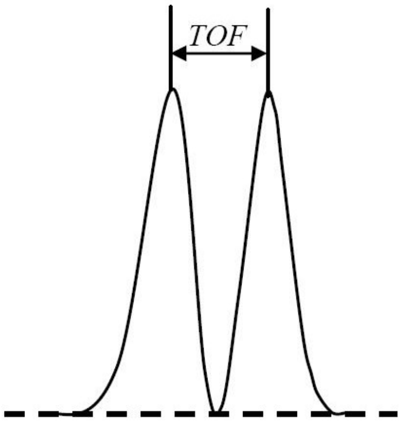

Figure 3-19 : Two peak signal detected.

The two peak signal on Figure 3-19 leads to the definition of the speed. The particle velocity "v" is defined as:

$$v = \frac{s}{TOF} \times \text{optical magnification of the lens}$$

Where s is the distance between the two slits and "TOF" is the time of flight when the particle image spot moves from the first slit to the second one.

3.8.1 Experimental Set Up

Laser velocimetry was applied to two copper powders. The system was set up in Advanced Coating S.A. on the industrial equipment.

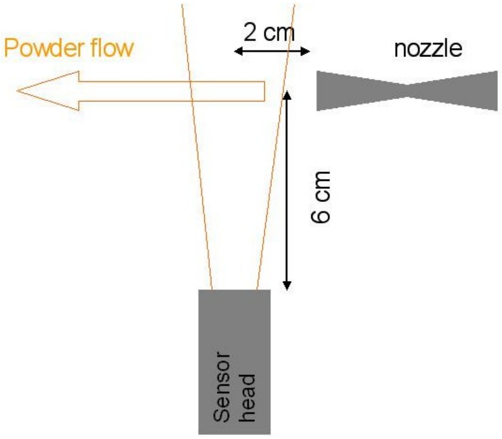

Figure 3-20 : Schematic of the set up.

Figure 3-20 shows a schematic of the set up. The laser and sensor head were placed at 2 cm from the exit of the nozzle. The distance between the sensor head and the measured volume is 6 cm. This distance is determined by:

- The necessity to protect the sensor head from the particle flow to avoid damage.
- The position of the laser. The laser crosses the powder flow and the sensors head detection plane at 6 cm from the sensor head.

In order to get a good statistical measurement of the speed, the speed was measured with 900 to 1000 particles detected.

3.8.2 The Sprayed Powder

In this study, two copper powders with a different size distribution were compared. Powders can be compared by several types of size distributions. Laser velocimetry will measure the speed of individual particles and, as shown by Table 3-4, the size of the particle has an important influence on the measured speed. The DPV system will give a speed distribution determined by the number of particles detected with a measured value speed. The powders can be compared by their size distribution weighted in number. It will give the percentage of particles with a given diameter among the total number of particle measured. More details on the size distribution types will be presented in Chapter 5.

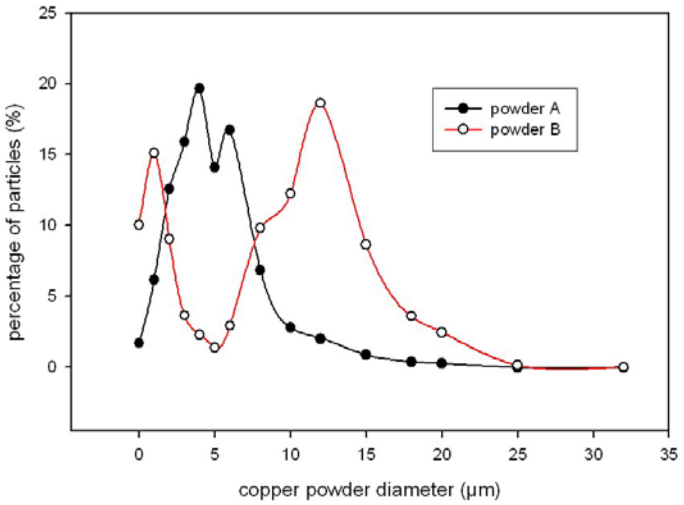

Figure 3-21 : Frequency size distribution (weighted by number) of both powders used in this study.

Powder A has an average size of 5.29 µm (±8.16 %) and powder B as an average size of 8.45 µm (±41 %). Powder B has two peaks in the size distribution (Figure 3-21); this yields a large standard deviation. The CPS2000 system is designed for metallic particles above 6 µm hence the small peak (<5 µm) in powder B's size distribution is not measured by this system.
Powder A has a peak distribution around 5 µm in diameter. The velocity measurement on this powder will be difficult to interpret and it will be the velocity's value of the powder with a diameter above 6µm.

3.8.3 Measured Results

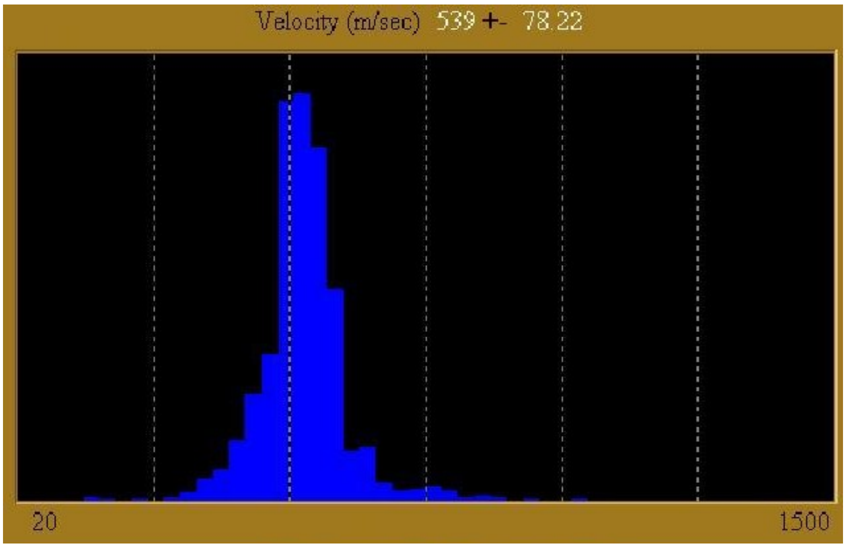

Figure 3-22 : Example of powder A measured velocity distribution with spray conditions P_0 = 30 bars & T_0 = 520°C.

Figure 3-22 shows an example of measured velocity distribution. Since a powder has a size distribution, copper particles with different sizes travel at a different speed and the system will measure a velocity distribution. Table 3-5 shows the results from the velocity measurements of both powders corresponding to the design of experiment (Figure 3-12).

Table 3-5 : Results from de DPV2000 and CPS2000 laser velocimetry measurement.

Spray conditions	Powder A : average speed	Std deviation on the speed of powder A	Powder B: average speed	Std deviation on the speed of powder B
22 bars & 320°C	512 $m.s^{-1}$	58.55 $m.s^{-1}$	439 $m.s^{-1}$	83.96 $m.s^{-1}$
22 bars & 520°C	518 $m.s^{-1}$	84 $m.s^{-1}$	464 $m.s^{-1}$	91 $m.s^{-1}$
26 bars & 420°C	507 $m.s^{-1}$	77.63 $m.s^{-1}$	495 $m.s^{-1}$	78.38 $m.s^{-1}$
30 bars & 320°C	513 $m.s^{-1}$	80.77 $m.s^{-1}$	486 $m.s^{-1}$	78 $m.s^{-1}$
30 bars & 520°C	539 $m.s^{-1}$	78.8 $m.s^{-1}$	516 $m.s^{-1}$	89.11 $m.s^{-1}$

Table 3-5 is presented in a 3D graph on Figure 3-23 and Figure 3-24. The increase in gas stagnation temperature T_0 and pressure P_0 leads ton an increase in the copper particle's speed.

- Powder A is finer than powder B, hence the measured velocity is higher than powder B.
- Powder A has a size distribution centred close to the limit of detection of the system. A large fraction of the powder's distribution is not measured.
- The simultaneous change in gas stagnation pressure and temperature yields the most significant increase in measured speed.

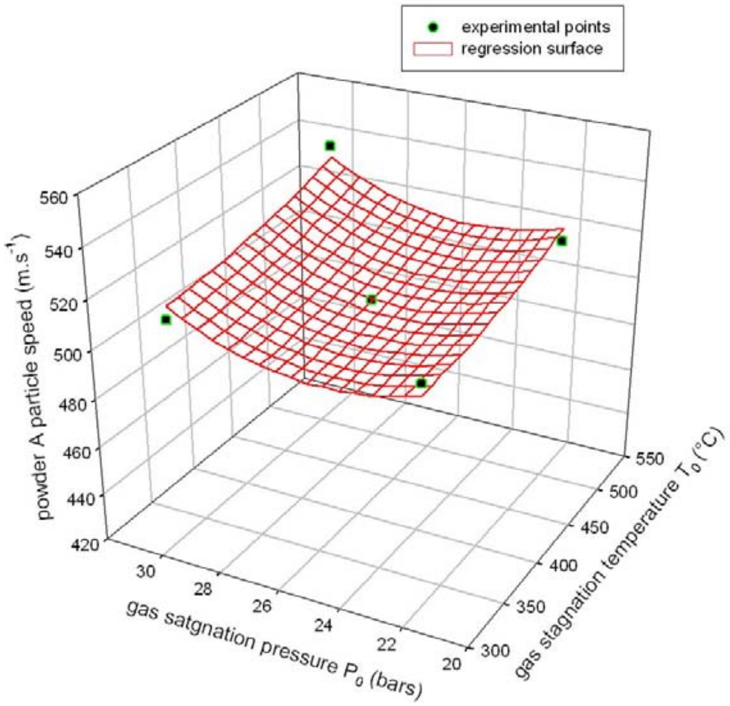

Figure 3-23 : 3D representation of the measured copper particle speed (powder A) on the design of experiment.

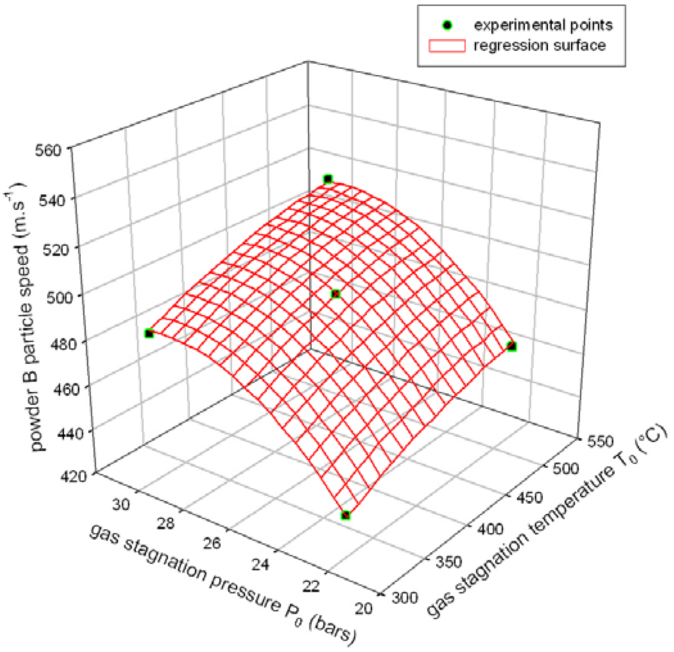

Figure 3-24 : 3D representation of the measured copper particle speed (powder B) on the design of experiment.

3.9 Conclusion

The use of one dimensional isentropic model to simulate the physics in the nozzle leads to computed velocities that do not take into account some effects. Even so, it gives a good understanding on the mechanism that lead to the particle acceleration. Dykhuizen et al [3] have used this model to treat the CGDS process with some success.

The two copper powders have a different size distribution; hence their speed will be different. These differences have been interpreted by using the one dimensional model of the process and compared to the experimental data. The model developed here does not take into account the effect of supersonic stream's expansion when it exits the nozzle. The behaviour of the gas was supposed to not change when it leaves the nozzle, before arriving to the gas bow shock. The laser velocimetry was done at 2 cm from the exit of the nozzle. It implies that the measured results are necessarily influenced by the gas behaviour outside the nozzle. While the copper particles travel the 2 cm distance from the nozzle's exit, they slow down due to friction, turbulences and mach disks at the exit. These features are not included in the one dimensional model. Therefore, the speeds of copper particles predicted are higher than the measured ones.

Powder A with a fine size distribution seems less sensitive to changes in the spray conditions. Its speed ranges from 507 to 539 m.s^{-1}. While powder B's speed range from 439 to 516 m.s^{-1}. As shown by the model on Table 3-4, the change in diameter of the powder particle can yield important changes in the final speed. Because of this, powder A has a faster velocity than powder B. Also, powder A has a size distribution centred around 5 µm hence it is sensitive to changes in the gas behaviour at the exit of the nozzle. Powder A has a lower inertia than powder B. Additionally, a large fraction of powder A is not measured by the laser velocimetry system. Therefore, powder A seems less sensitive to a change in spray conditions.

Some features of the model appeared in the results:

- A simultaneous increase in the gas temperature and pressure yields the most important increase in the measured speed. Figure 3-14 illustrates this with the model.
- Powder A is finer hence it is faster than powder B.

The powder's temperature can not be measured. Usually, the powder's temperature is measured by using the light emission from the powder in the flame or the plasma but, in the case of cold spray, no light is emitted from the powder particles. No equipment allows measuring the powder's temperature in the case of cold powder particles. With CGDS, the model shows that a change in gas stagnation temperature will determine the temperature of the copper powder on impact (Figure 3-16).

Chapter 4 The Cold Gas Dynamic Spray Process: Single Splat Analysis

4.1 Introduction

The deposition of the first layer on the substrate determines the quality of the coating's bonding. The role of the substrate's properties in the bonding process is not yet clearly understood. The computational analysis shows that the jetting occurs either on the substrate or on the particle. The presence of jetting is the visual manifestation of the shear bands and a change in material behaviour. The impact also modifies the roughness of the surface and produces mechanical gripping of the coating. Some authors ([16], [15],[24]) describe the bonding as "metallurgical" which suggests that the bonding has a chemical nature. It is difficult to isolate these two types of bonding mechanisms. One method is to compare the bonding between a very hard polished substrate and a soft polished substrate. The particles should not bond on a very hard substrate if the bonding is purely mechanical but should bond on the softer substrate.

In the cold spray process, internal compressive stresses accumulate and if the bonding on the substrate is not sufficient, the coating breaks of. In other thermal spray technologies, a grit blasting of the substrate is needed in order to improve the bond strength by mechanically gripping the coating or exposing a larger contact surface. The CGDS process is said to avoid the necessity of grit blasting, the first impacts grit blast the surface and the next layer bond mechanically to the substrate by shot peening of the layers.

The failure of a coating occurs at the interface between the substrate and the coating. Understanding how particles bond with the substrate is essential to improve the properties of each coating. Analyzing the first deposited layer and single splats would give us a significant insight in the effect of spray parameters on the deposition.

This chapter is the result of the collaboration with the University of Nottingham and the school of M3.

4.2 Experimental Method

4.2.1 Materials

Commercially available copper powders with particle size between 5 µm and 22 µm were sprayed. This is a gas atomised powder. Figure 4-1 shows the cumulative size distribution of the powder obtained by a laser diffraction method.

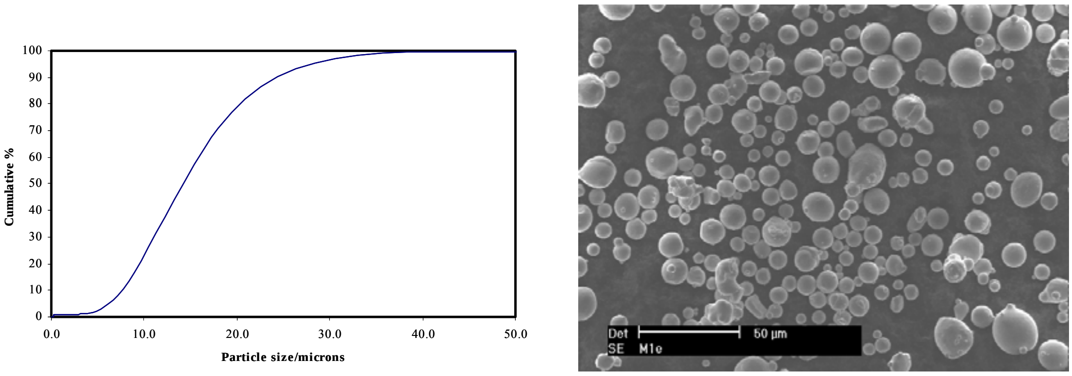

Figure 4-1 : Cumulative size of powder and morphology of the copper powder.

Two types of substrate have been chosen for their difference in Young Modulus and their difference in hardness. Each substrate has been heat treated in order to get different hardnesses. The first substrate is a rolled sheet of Aluminium-copper alloy AA2014 with the following chemical composition in Table 4-1.

Table 4-1 : Chemical composition the AA2014 alloy.

Al	Cu	Si	Mg	Mn	Fe	Cr	Sn
93.31%	4.4-4.8%	0.83-0.81%	0.61-0.68%	0.57-0.58%	0.24-0.22%	0.05-0.04%	0.03-0.04%

The second substrate is silver steel with the following chemical composition in Table 4-2.

Table 4-2 : Chemical composition of the steel

Fe	C	Mn	Cr	W	V
96.65	0.95%	1.20%	0.5%	0.5%	0.20%

Both of these substrates can be heat treated to a wide variety of hardnesses. This experimental work will be limited to the analysis of impacts on two values of hardness for each substrate.
The aluminium-copper alloy is the classical example precipitation hardening. Samples have a thickness of 0.505 mm. The copper has been solutionnized in the aluminium by a 30 min treatment at 500°C. Precipitation has been done at 160°C and 210°C for 48H.
The steel samples have a similar thickness and have been heat treated at 800C for 30 minutes in order to bring the steel to its martensitic form. The following heat treatments have been

done to get two very different hardnesses based on the supplier's recommendations. After the heat treatement, samples were quenched in oil. The temperatures of 150 °C and 600 °C for 30 minutes have been applied. The hardness measurements gave value of 100 HV_{10kg} and 147 HV_{10kg} with a Vickers indentation on AA2014. The hardness of the steel has been measured with a load of 20 kg and gave 394 HV_{20kg} and 866 HV_{20kg}.

4.2.2 Spray Deposition

Cold spraying was carried out at the University of Nottingham using an in house constructed cold gas dynamic spraying system. The carrier gas and the spray gas used is room temperature Helium. A De Laval nozzle was used to accelerate the gas to supersonic speeds. The maximum stagnation pressure available is 30 bars and a Praxair 1264HP powder feeder was employed. The nozzle was fixed vertically to a frame and the sample moved below the nozzle on a computer controlled X-Y table that allowed raster scans and different shapes to be deposited. In order to obtain single impacts of particles, the travel speed was set to 400 $mm.s^{-1}$ and the powder feed rate was set to 7.5 $g.min^{-1}$. This is the lowest possible setting for the powder feed rate. The stagnation pressure for the deposition was set successfully from 11 bars, 18 bars 22 bars, 26 bars to 29 bars. The constant spray parameters are summarized in Table 4-3.

Table 4-3 : Constant spray parameters used during deposition.

Stagnation temperature(°C)	22°C
Powder feed rate	7.5 $g.min^{-1}$
Stand off distance	20 mm
Gun travel speed	400$mm.s^{-1}$
Carrier gas	Helium

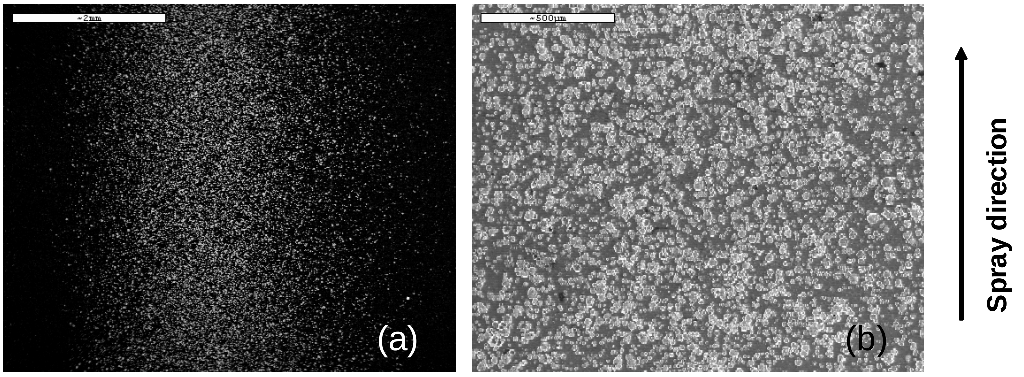

Figure 4-2 : (a) BSE (Back Scattered Electrons) image of a track deposited at 29 bars on aluminium alloy AA2014 with 147H_{10kg} hardness. The contrast shows the low density of impacts in the centre of the track (b) SE (Secondary Electrons) image, a zoom on the centre of the track, many single impacts are visible.

On each sample two tracks are sprayed for a given value of pressure. Each track corresponds to a single pass of the gun at 400 $mm.s^{-1}$. A track is a narrow band 40 millimetres wide (see Figure 4-2). The particle distribution in the gas stream gives a non uniform track. The centre of the track where the impacts are perpendicular to the surface has a higher density of particle than the edges of each track. Due to the very low powder feedrate and the high transverse gun velocity, single particle impacts were observed in the centre of the track. Even within those conditions, it was difficult to observe many isolated impacts. One other effect playing on the deposition is the powder pulsing. At such a low powder feed rate, the flow of particles was not regular along the track.

This means that some section of a track, even some entire tracks have been deposited with a very low powder feed rate. The value of 7.5 g.min^{-1} is most certainly not accurate on every section of the track. This value should be interpreted as an average rate for the whole track.
The Laval nozzle has an expansion ratio of 2.75 with 100 mm length for the divergent part and a linear profile between the throat and the exit. The particles enter the gas flow in the convergent part of the nozzle, and it is reasonable to assume that they follow the gas flow lines. This is valid if there are no interactions between the particles during the transport to the substrate and if the mass of the particle is sufficiently small to follow the flow lines. Based on this basic assumption it is possible to relate the position of the particle to the angle of impact between the perpendicular lines to the substrate surface at the throat. Figure 4-3 shows how the angle can be estimated.

The maximum possible angle of impact in these conditions is

$$\alpha = a\tan\left({}^{2}\!/_{120}\right) = 0.95° .$$

Most of the impact should occur in an almost perpendicular line to the substrate. In the following analysis we will concentrate on impacts between 0 ° and 0.47°.

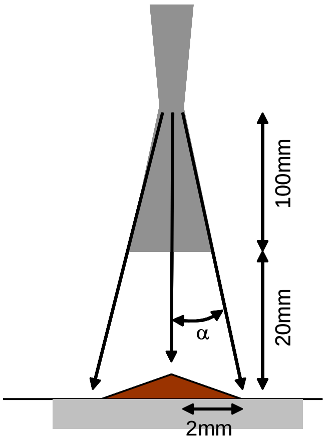

Figure 4-3 : Description of the angle of impact.

4.2.3 Particle Speed

The simple isentropic gas model with a simple model of the particle dynamic allows the discussion of the basic effects of pressure on the morphology of the splats. Only laser velocimetry could quantify the value of the speed. The bow shocks will reduce the speed upon impact; this effect can be neglected for particles with a diameter larger than 5µm. With a stand off distance of 2 cm, the bow shock effect is neglected and the exit velocity is assumed to be very close to the impact velocity.

4.2.4 Microstructural Characterization

The size distribution of the powder was determined using a laser diffraction method (Malvern Instruments Laser Mastersizer). A JEOL6400 Scanning Electron Microscope (SEM) was employed to investigate splats, powder morphology and microstructure utilizing back scattered electron (BSE) signals and secondary electrons (SE) signals to form images. Before deposition the samples were grinded to a 15.3 µm finish on silicon carbide paper and cleaned with acetone. Cross sections have been prepared in cold mount, they have been polished to a 0.6 µm level and the samples have been gold coated for SEM observations. Quantitative energy dispersive X-Ray analysis (EDX) of the metallic elements present was obtained by using an INCA X-sight from OXFORD instruments which is attached to the JEOL 6400 system.

4.3 Results

4.3.1 General Observations

Powder pulsing means that tracks deposited are not uniform. On all samples and at all pressure, the density of impacts is irregular. Therefore in some area of the track it is not possible to find single splats near the centre of the track. Due to the low deposit efficiency at low pressure, the number of particles bonding on all substrates is very low. At 11 bars on all substrates it is possible to find single splats near the centre of the track. At 29 bars, powder pulsing allowed a large portion of the track to be deposited with low particle density.
At 18 bars and 26 bars, it was possible to find near the centre of the track, but beyond a certain diameter, the particles closely packed. It is not possible to find isolated splats. On steel, splats flatten to such an extent that it is not possible to find isolated splats in the centre of the tracks. At 22 bars, the deposit efficiency is very large and it is impossible to find single splats around the centre of the track. The single splats in this case come from a region with α between 0.47 ° and 0.95 °. On the steel substrate with $866HV_{20kg}$ hardness, the thin copper layer debonded immediately. An analysis of this zone will follow in this chapter.

4.3.2 Influence of the Gas Pressure and Substrate Hardness on AA2014 Substrate.

Pressure will determine the speed of the particle. Using the isentropic perfect gas flow in a tube with a variable cross section developed by Dykhuizen [3], it is possible to get the evolution of the speed of the particle in the nozzle (Figure 4-15). Comparisons will be made with particles approximately the same size, around 10 microns, to ensure that they have the same exit velocity.

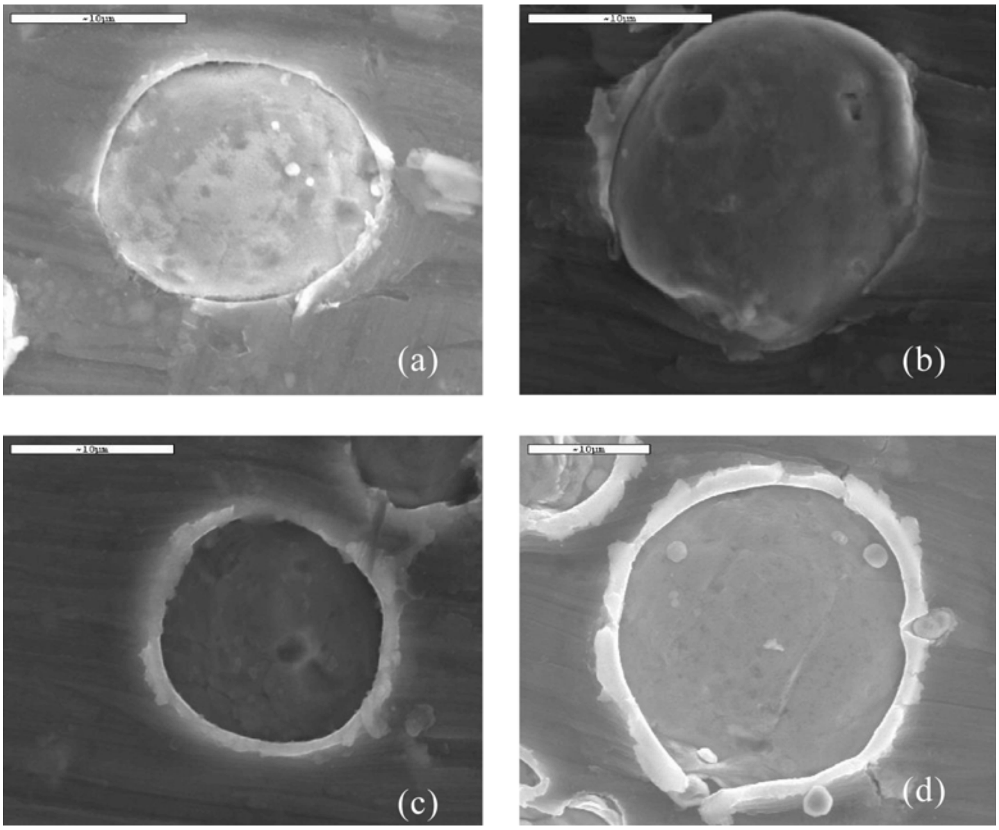

Figure 4-4 : SE images of copper impacts (a) P_0=11bar Al 100HV_{10kg} (b) P_0=11 bars Al 147HV_{10kg} (c) P_0=29 bars Al 100HV_{10kg} (d) P_0=29bars Al 147HV_{10kg}.

The Figure 4-4 shows singles splats (about 10 µm diameter) deposited on AA2014 at 11bars and 29 bars with hardnesses of 100 $HV_{10\ kg}$ and 147 $HV_{10\ kg}$. Comparing Figure 4-4 (a) and (b) with Figure 4-4 (c) and (d), we can see the effect of pressure on the depth of the impact. Mechanical gripping is much more significant if pressure goes up. Comparing Figure 4-4 (a) and (c) with Figure 4-4 (b) and (d); the hardness of the substrate modifies also the depth and the importance of the jetting. At 11 bars and on the 147$HV_{10\ kg}$ substrate, the particle does not penetrate. The jetting is not present on the entire rim; the substrate underwent an indentation.

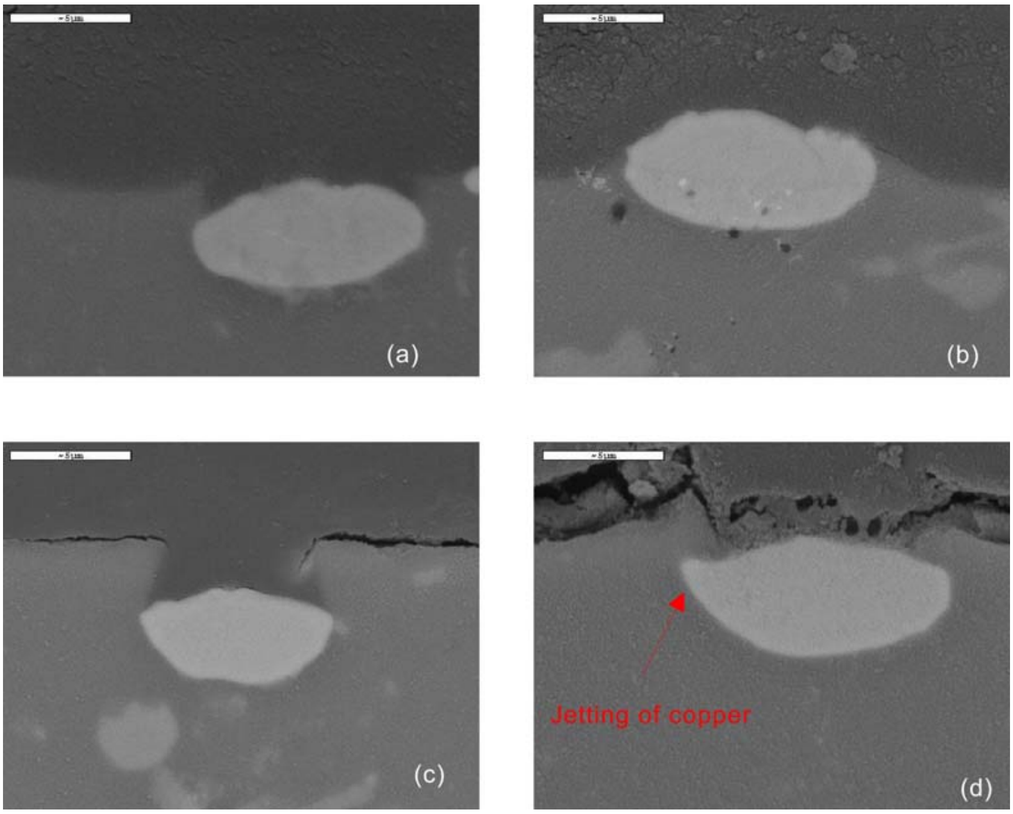

Figure 4-5 : BSE images of copper impacts cross sections (a) P_0=11bars Al 100 HV10kg (b) P_0=11 bars Al 147 HV_{10kg} (c) P_0=29 bars Al 100 HV_{10kg} (d) P_0=29 bars Al 147 HV_{10kg}.

The cross section work on Figure 4-5 shows the difference of depth due to pressure. Due to high pressure the particle penetrates deeper in the substrate and jetting is more significant. The shear bands have form to a great extent due to impact speed. The jetting on Figure 4-5 comes from the aluminium and not from the substrate. On high pressure impacts, copper shows the characteristics of jetting (Figure 4-5 (d)). The effects of hardness are visible in the depth of the impacts. On hard substrate; the particles have flattened more.

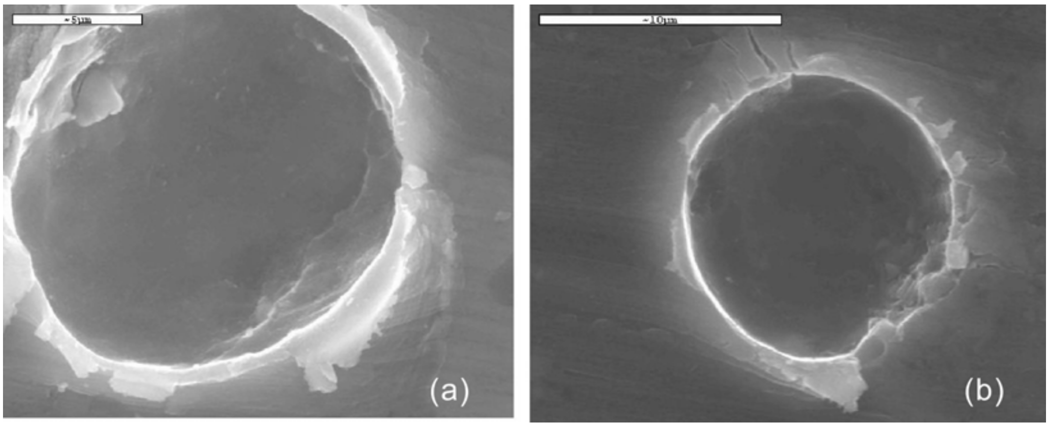

Figure 4-6 : (a) crater on AA2014 at P_0 =29 bars, jetting comes from the substrate (b) crater on AA2014 at P_0= 29 bars, the rim shows cracks. The presence of intermetallics in the substrates modifies the flow properties of the materials in some parts of the substrate.

The AA2014 is an alloy and the heat treatments involved in order to age hardened the substrate have precipitated the GP zone to modify the flow stress of the material. Large $CuAl_2$ zone show up on the backscattered images, and other intermetallics rich in iron and manganese modify the flow properties of the substrate, therefore the crater morphology appear different. On the 147 HV_{10kg} alloy, the impact strains the material around some precipitated intermetallics and cracks appear in the rim (Figure 4-6 (b)). EDX analysis shows that cracks on the rim are located on intermetallics precipitates rich in Fe and Mn. Most of the craters do not show cracking, the high impact velocity due to the 29 bars pressure allows jetting on the substrate to occur extensively. This lip formed on the rim comes from the substrate. Cross section work on Figure 4-5 does not show extensive jetting of the copper.

4.3.3 Influence of the Particle Size on the Bonding

For fixed stagnation pressure P_0 and temperature T_0, the particles size determines the impact speed. The kinetic energy of the particle will convert, on impact, at 80% in heat and the remaining 20% will be plastic deformation. Smaller particles should bond more easily since they reach the critical speed faster. The size distribution of the powder means that it is easier to find particles with a diameter of 10 µm but particles as small as 2 µm were observed on the aluminium AA2014 substrate.

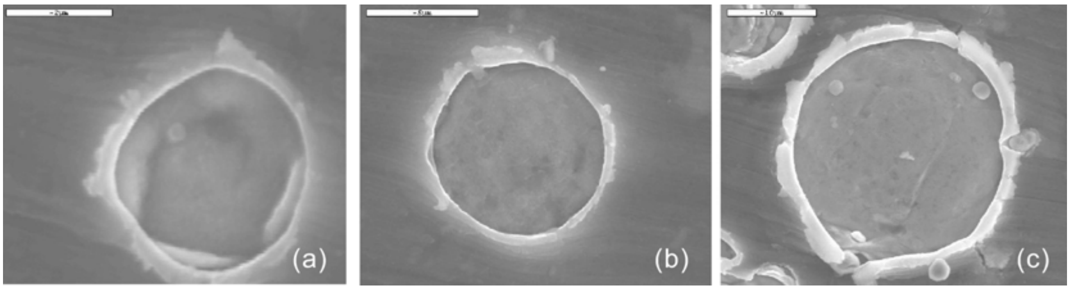

Figure 4-7 : All particles have been deposited on AA2014 at P_0=29 bars with 147 $HV_{10\ kg}$ hardness, they have the following diameters (a) D~2µm (b) D~5µm (c) D~12µm.

Figure 4-7 shows the single splats of copper particles on AA2014 with 147 HV_{10kg} deposited at 29 bars. The dimensions of the splats were estimated on the basis of the scale bar from SEM. The particles penetrate deep in the substrate; the jetting is extensive on all impacts. On the smallest particles, the copper exhibits jetting also. On Figure 4-7 (a), the small particle shows that heat generated by the impact diffused in a large fraction of the particle. The bottom part of the particle and the rim where heat generation is important became visquous. The fraction of the particle that did not soften pressed and penetrated in the visquous fraction of the particle. This led to the formation of copper lips in the rim on the impact on Figure 4-7 (a).

4.3.4 Effects of the Pressure on the Impacts on Steel

The splat shape on steel is a pancake that flattens completely. Figure 4-8 shows single splats at 11, 18 and 29 bars deposited on the 866 $HV_{20\ kg}$ substrate. The pressure will determine the amount of jetting observed on each particle. The kinetic energy available must be sufficient to get thermal softening. At 11 bars no large jetting is visible on the copper particle. At this pressure the deposition efficiency is so low that few particles bonded. The pressure will determine the impact speed; therefore the flattening ratio increases with the pressure. At 18 bars (Figure 4-8 (b)), the copper exhibits large jetting. The material has softened on the rim while the centre of the particle has remained solid. The substrate shows no signs of indentation.

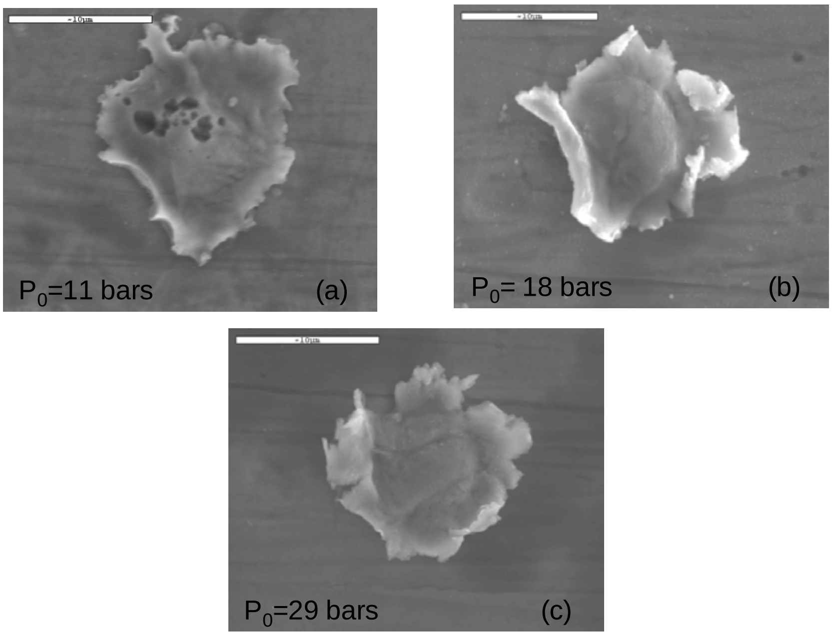

Figure 4-8 : Copper particle on steel with 866HV $_{20\ kg}$ hardness.

At 29 bars (Figure 4-8 (c)), the copper particle shows signs of fracture in the jetting. The very high speed impact has ruptured the copper. During impact the material strain hardened considerably due to the high strain rate, the heat generated allows the microstructure to recover. This recovery stage does not allow the flow stress to drop.

At 29 and 18 bars, the jetting seems to have rebounded on the surface of the substrate. The soft copper has not remained in contact with the substrate's surface. This is only visible on the steel with high hardness (866$HV_{20\ kg}$). The hardness of the steel will determine the amount of elastic energy available for a rebound. Even with this rebound, the particle still has enough adhesive force to maintain the contact with the surface.

4.3.5 Craters on Steel

Due to the steel high hardness compared with aluminium, the substrate undergoes almost no deformation on impact. In order to get significant deformation on the surface, high impacts velocities are needed. For a fixed pressure, the speed will be determined by the size of a particle. Smaller the crater, deeper the impact. Craters modify the surface roughness and will favour the deposition of the next layer of copper. The particles will have an improved grip on the surface.

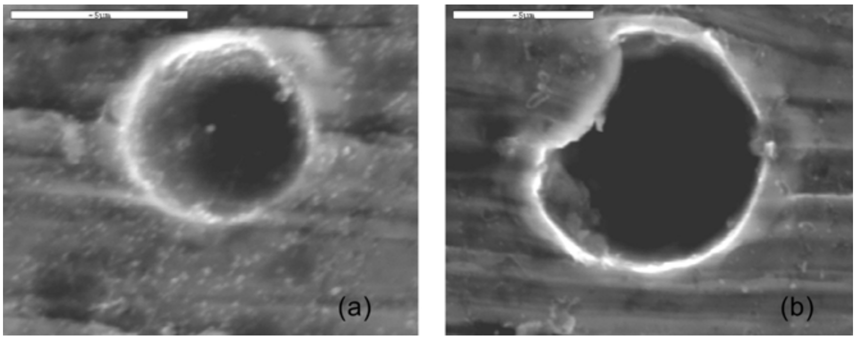

Figure 4-9 : Craters left by copper particles on steel 394 $HV_{20\ kg}$ at 18 bars.

Figure 4-9 shows two craters on steel 394 HV_{20kg} where jetting is visible. In a similar way than on aluminium, the substrate has reach in very local regions very high temperatures that has allowed the metal to soften. No such craters have been found on other steel substrates with higher values of hardness.

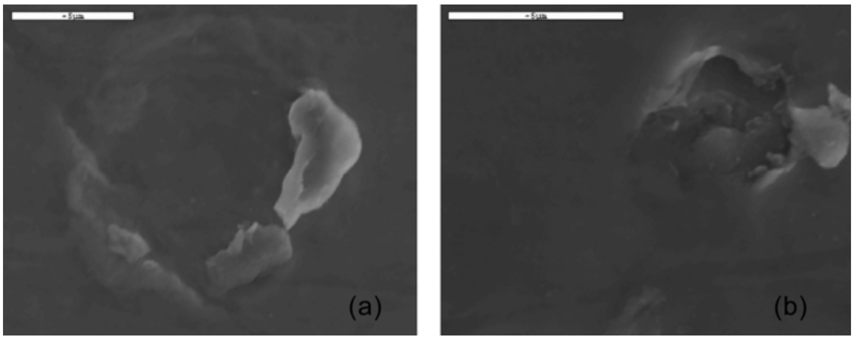

Figure 4-10 : Craters left by copper particles on steel 866HV_{20kg} at 22 bars.

Figure 4-10 shows damage on the surface left by copper particles. No jetting on the substrate is visible; two large lumps of copper particles have remained on the rim of the crater. The centre of the impact remains smooth; copper particles remain in contact on the rim.

4.3.6 Bond zone on a Crater of the AA2014 Substrate

On this substrate, the copper particles have penetrated deeper and bond very well usually. During impact, it is essentially the substrate that deforms and jetting is visible on the rim. Figure 4-11 represents a crater observed on AA2014 substrate. In the rim, cellular type of structures appears. The cells have about 1µm diameter and are spaced regularly. These structures are not common in craters. They are not visible at low pressure (11 bars) and at high pressure (29 bars). They can be found at 18, 22, and 26 bars on large craters, usually at least 8 µm in diameter. This shows that the bonding mechanism locates on the rim of the crater and the centre stays smooth.

These cells structures are linked to the bonding process, shear bands form on the rim of the crater and the materials (the particle and the substrate) become visquous. This change in behaviour of the material due to the high pressure, high strain rate, and the heat generated allows the surfaces to conform intimately. In the case of Figure 4-11 and Figure 4-12, the particle has rebounded and the honey comb structure shows ductile rupture on the rim.

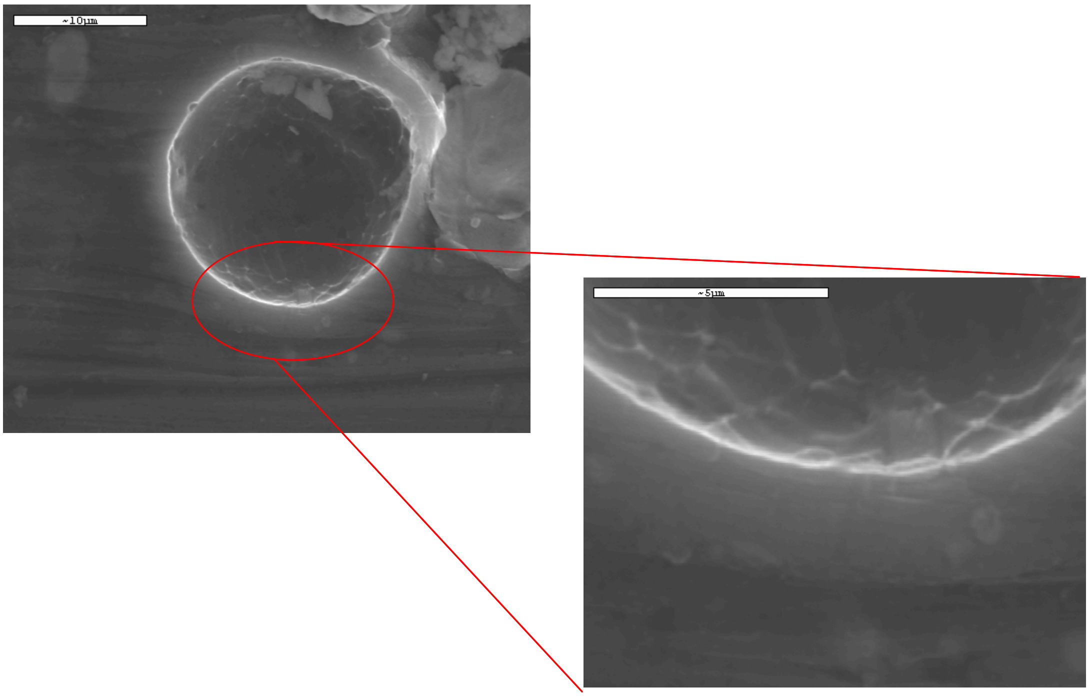

Figure 4-11 : Crater on aluminium 100HV$_{10kg}$ deposited at 22 bars. Honey comb structure due do the shear band on the Rim.

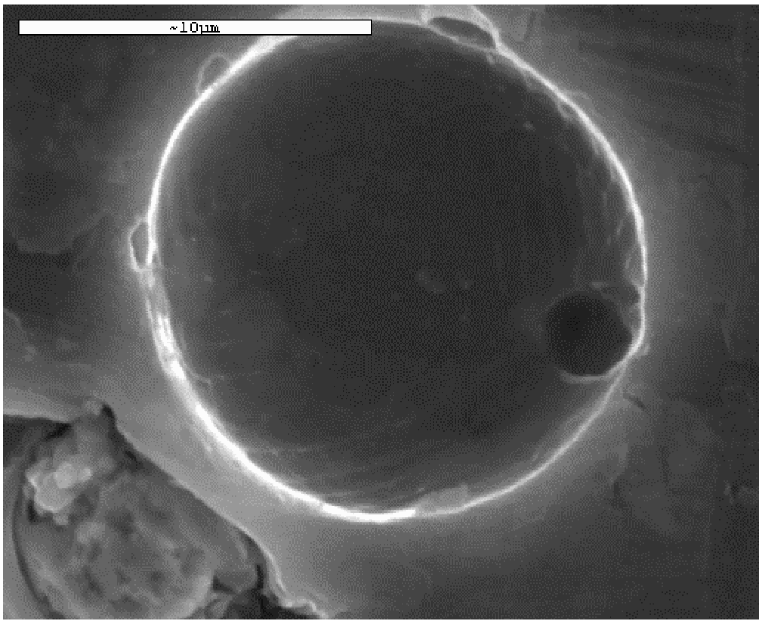

Figure 4-12 : Other crater on aluminium 100 HV$_{10kg}$ deposited at 22 bars. Honey comb structure due do the shear band on the Rim.

4.3.7 Analysis of the Debonded Zone on Steel with 866HV$_{20kg}$ Hardness at 22bars

During the deposition, the thin coating deposited with a high gun transverse speed (400 mm.s^{-1}) has debonded immediately on the hardest steel (866 HV$_{20\ kg}$). The debonding process comes from the accumulation of internal stresses in the coating that finally lead to the rupture with the substrate. In the cold spray process, the stresses are compressive. The successive impacts shot peen the previous deposited layer and introduces a compressive residual stress by strain hardening the existing coating. If the mechanical properties of the substrate differ significantly from the coating, the substrate can not adapt to stress field applied by the coating.

Figure 4-13 and Figure 4-14 show the steel substrate with copper debris located in the rim of the craters. They show that the bonding on the steel is very weak because it does not involve the jetting of the substrate. Only very few craters keep copper debris on the rim. Contrary to the steel with hardness 394 HV$_{20kg}$ where no debonding was observed, internal stresses have accumulated more significantly.

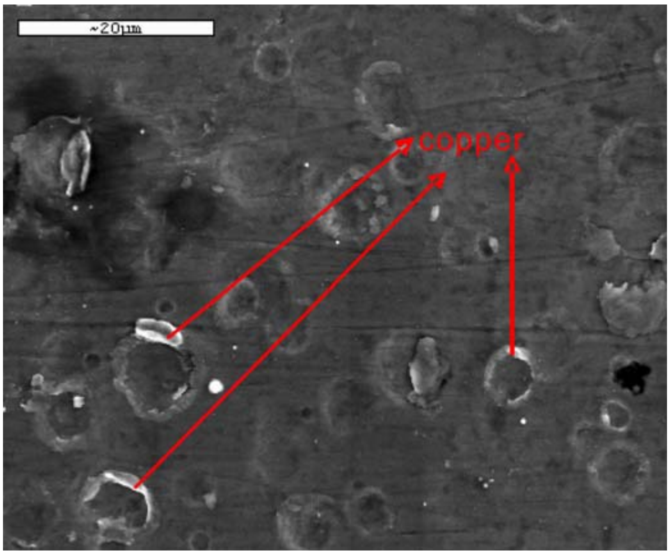

Figure 4-13 : SEM view of the debonded zone on steel 866HV$_{20kg}$ at 22 bars Lumps of copper particles have remained bonded to the surface. The rim of the craters keeps the copper. The bonding does occur in this zone.

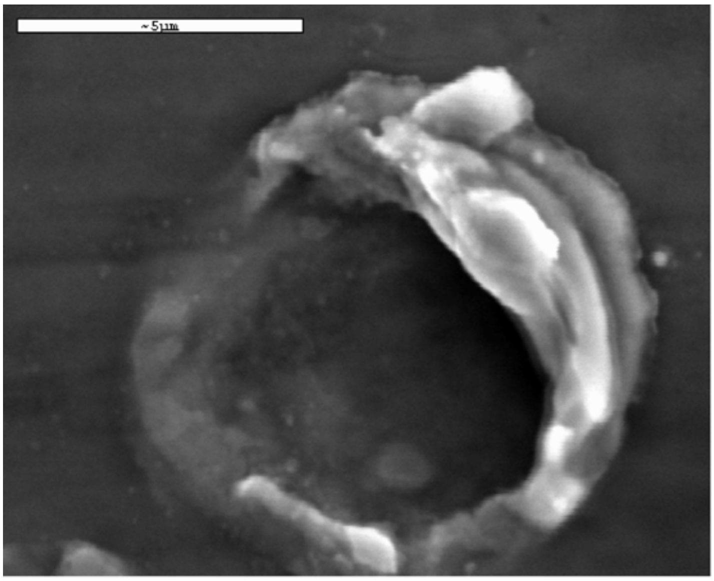

Figure 4-14 : View of a copper impact. Under internal stresses, the copper has been torn but not on the entire rim. Even on hard steel the small impacts remain tightly bonded.

4.4 Discussion

Assadi et al [15] have shown that the notion of critical speed for bonding of a particle can be related to shear band formation. At a high strain rate, competition between strain hardening and thermal softening determines the possibilities for shear band to appear. The same authors have shown that melting is not required to get good bonding; clear conformal and intimate contact between the surfaces and high pressure is sufficient. Fukanuma et al [30] have shown that bonding on aluminium reaches value of 40-60 MPa (see Figure 2-25) with increasing stagnation pressure whereas on steel the bonding ranges form 10 MPa to 40 MPa. In this study, the problem of substrate and particle interaction has been approached by comparing substrates with similar chemical composition but with various hardnesses. The possibility of melting in a thin layer could provide an explanation for the good metallic bonding observed. The impact speed of the particle would have to provide sufficient energy to melt the material.
Therefore, the speed of the particle determines the quality of bonding. Using the isentropic flow model developed by Dykhuyzen [3] and the Billing approximation [13] of the gas shock wave it is possible to get a realistic value of the particle's speed along the centre line of the nozzle. This will allow the discussion to centre around the effect of speed on splat formation.

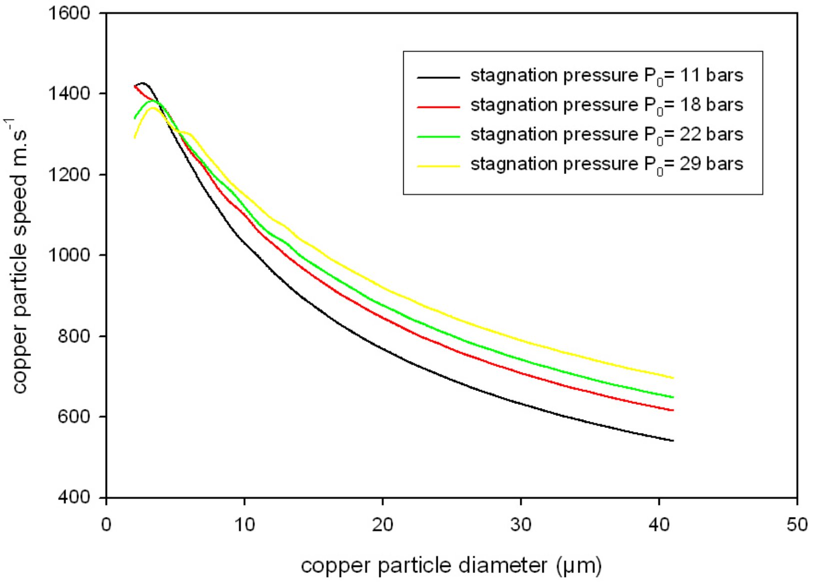

Figure 4-15 : Particle speed as a function of size for helium gas at various pressures.

4.4.1 Influence of the Gas Pressure

Splat formation on aluminium has shown that the copper particle does not deform considerably compared with splat formation on steel. The jetting comes from the substrates thermal softening under the high strain rate involved during impact (Figure 4-6 (a) and Figure 4-5). The aluminium has a melting temperature (940K) lower than copper (1360K), thermal softening will occur first on the substrate. Simulations of splats of copper on aluminium by Grujicic et al [4] at 600 $m.s^{-1}$ show jetting on the substrate and the cross section on Figure 4-5 (d) comes close to modelling results. At 29 bars, the particle does not have an elliptical form, the softening does occur. At 11 bars, the impact speed ranges from 600 $m.s^{-1}$ to 1000 $m.s^{-1}$ as shown on Figure 4-15 and the copper shows no signs of thermal softening. This suggests that softening of the copper would require higher impact velocities. The original hardness of the powder could explain the absence of jetting. The heat generated by the high strain rate ($\dot{\varepsilon}=10^9$ s^{-1}) competes with its evacuation by thermal conductivity. Harder particles would not reach sufficiently high strain rates and heat would be evacuated fast enough to prevent the temperature to approach softening.

On Figure 4-11, the crater shows a rich internal structure. The rim is formed with small grains that are elongated in the direction parallel to the rim and it is possible to see elongated grains pointing from the centre towards the rim. Grujicic et al [2] have shown that with an impact speed beyond 800 $m.s^{-1}$, the temperature peak reached is close to the melting temperature of aluminium. Melting can not be excluded. Simulations tend to overestimate the temperature reached during shear band formation; the evacuation heat by thermal conductivity is not taken into account. Due to the very short contact time, it is admitted that solid state diffusion does not take place. Barradas et al [24] has shown that diffusion zones are present by using TEM investigation. These zones are explained by the diffusion of copper in melted aluminium during impact.

4.4.2 Influence of the Particle Size

The effect of size on splat morphology is shown on Figure 4-7. For diameters of splats above 5 μm, the morphology is similar. Jetting occurs on the substrate and the copper penetrates in the AA2014. Particles with a diameter inferior to 5 μm have impact speeds above 1000 $m.s^{-1}$ but this estimation should be taken with care, the bow shock slows the particles. Even so, they exhibit intense softening during impact. The copper jetting is visible in the rim of each impact. The volume fraction of the particle heated up during impact is greater because of its size and its higher impact velocity (Figure 4-7 (a)). The work by Schmidt et al [29] confirms that shear localization in fine particles is more difficult. Heat diffuses through a larger fraction of the particle. This is well illustrated By Figure 4-7. Schmidt et al argue that this is unfavourable to get good bonding but on aluminium the finer particles penetrate deeper in the substrate.

4.4.3 Influence of the Hardness of the Substrate

The hardness and the Young Modulus of the substrate will determine the amount of elastic energy stored by the substrate. The hard substrate corresponds to a higher impact velocity for plastic straining and more energy for elastic rebound. Therefore adhesive energy has to overcome rebound energy in order to keep the particle on the substrate. In CGDS, this adhesive force is sufficient to avoid removing the deposited particle by the following impacts. On steel, the contact surface is considerably enhanced and the particle does not penetrate in the substrate. The absence of deformation of the substrate excludes the possibility of shear bond formation on the substrate. Some form of thermal softening is visible on soft steel 394 HV_{20kg} (Figure 4-9) for small craters. There rim is continuous and EDX analysis shows the presence of copper traces. These very small impacts have the highest values of speed. These craters are not visible on steel with high hardness (866 $HV_{20\,kg}$), instead, crater shows damage on the surface and lumps of the copper particle still remain in the rim. This suggests that some form of good bonding does exist. The adhesive energy was not sufficient to keep the whole particle on the substrate but a part of it remained. An analysis of the debonded zone shows that most of the impact did not create any form of bonding, copper lumps stay in some of the rims (Figure 4-10). Small particles, about 5 µm in diameter (Figure 4-14), even on high hardness steel can bond due do their high impact velocity. The copper bonds essentially on the rim and, in this case, most of the copper particle that has remained, has been torn off on half of the rim. This also suggests a very tight bonding between small copper particles and steel.

4.4.4 The Build Up of the Coating

The build up of the coating on an aluminium substrate is dominated by the deformation of the substrate, the particle does not show important thermal softening at spray pressure of 11 bars. At any pressure the substrate deforms sufficiently to ensure shear localization in it. The build up of the coating is easy.

The build up of a coating on steel can be associated with two processes. The first effect is a modification of surface roughness by the impacts of small particles. They provide activation and larger particle improves mechanical bond with the surface. The fact that some jetting occurs in the rim on soft steel indicates that the surface of the steel can be significantly modified and this will even further improve the mechanical grip of a larger particle. The second effect is the presence of copper particles fragments in the rim that provide some form of support for tight bonding. The internal stresses have removed the coating but these fragments have remained and some impacts zones provide anchorage for the built up of a coating. On the soft steel (394 HV_{20kg}), the copper particles have penetrated deeper in the substrate and have also formed tighter bonds with the substrate. On the hard steel (866 HV_{20kg}), the small depth of craters and few impacts, that have tightly bonded, do not provide enough anchorage for the coating.

4.5 Conclusions

Observations of single impacts have shown several important influences:

- The increase in gas pressure will increase the powder's speed in the nozzle. The gain in speed of each particle is determined by its diameter. The increase in impact speed leads to more softening in copper splats as shown on Figure 4-5 (d). The formation of softening on the particle means that the temperature reached at the interface increases with the impact velocity.
- On the aluminium substrate, the impact process is dominated by softening of the substrate. Changing the substrate's hardness will modify the depth of the impact and eventually some fracture will appear in the rim of the impact.

  On the steel substrates, the particles undergo all the deformation. Some very fine particles have managed to deform the soft steel's surface. On the hard steel surfaces, some copper lumps are found in the rim of some impacts. They provide anchorage points where some particles bond tightly with the surface. The rest of the coating builds up on top of these lumps and on the roughness created by the non bonding impacts.

Chapter 5 Optimisation of the Cold Spraying of Copper Powders

5.1 Introduction

The CGDS process needs to be optimized by placing a maximum number of powder particles inside the window of sprayability (section 2.4). The powder particles need to be above the critical speed for bonding and below the erosion velocity. Beyond the erosion velocity, the copper impacts are in the regime of hydrodynamic penetration and it produces debris. In the case of copper cold spraying, the erosion velocity can not be reached with nitrogen gas acceleration ($v_{erosion}$ ~800-1000 $m.s^{-1}$). It is needed to keep the powder particles above the critical speed of copper ~550 $m.s^{-1}$.
In this study, two copper powders with a slightly different size distribution will be compared. The criterion for optimisation is the Deposition Efficiency (DE). Once all the powder particles are above the critical speed, the DE is 100%. Both of these powders will be described in details and the DE will be compared. Two substrates have been used to do the comparison: Aluminium and TA6V (alloy Ti 6% Al 4% V). Both substrates have very different mechanical properties and they will give characteristic behaviour of the CGDS process.

This chapter will discuss:

- The influence of the spray conditions on the DE. By using the results in Chapter 4, it is possible to relate the impact speed with the evolution of the DE.
- The choice of the substrate. The properties of the substrate influence the formation of the first layer and can lead to coating with different values of DE.

5.2 Powder Characterization

A powder can be described by a series of characteristics:

- its size distribution
- its shape
- its mechanical properties

All these properties will influence the ability of single powder particle to bond with a given surface. The two first properties (size and shape) will influence the aerodynamical behaviour of the particle in the nozzle.

5.2.1 Powder Size Distribution

No industrial powder has a single powder size. The powder has particles with several different diameters and with different proportions. The description can be done by using 3 types of distributions:

- Size distribution weighted by number
- Size distribution weighted by surface
- Size distribution weighted by volume

All of these distributions give information on the powder's properties.
A size distribution weighted by number gives the proportion of particles with a given size. A size distribution weighted by surface gives the proportion of the surface (exposed by powder particles) with the corresponding diameter. A size distribution weighted by volume gives the proportions of the total volume occupied by powder particles with a given size.
All these type of distributions give a different aspect of the powder's properties.

5.2.2 Characterization Technique of the Size Distribution

The powder size distribution has been characterized by using a newly developed optical system suited for powder with a size range between 500nm and 500 microns called "alpaga 500 nano" ([52]). The optical system scans the powder spread on a glass plate. The optical image was obtained by using a UV diode and a cofocal lens. This allows having particles with different sizes in the same focal plane. The images of each individual particle are stored and specialized software allows analyzing details of the images. The size distributions can be obtained and also other shape factors.

5.2.3 Experimental Powder Size Distribution in this study

Two copper powders have been purchased at two different powder suppliers. They are respectively named "powder A" and "powder B". Both powders have been made by the gas atomised technique.

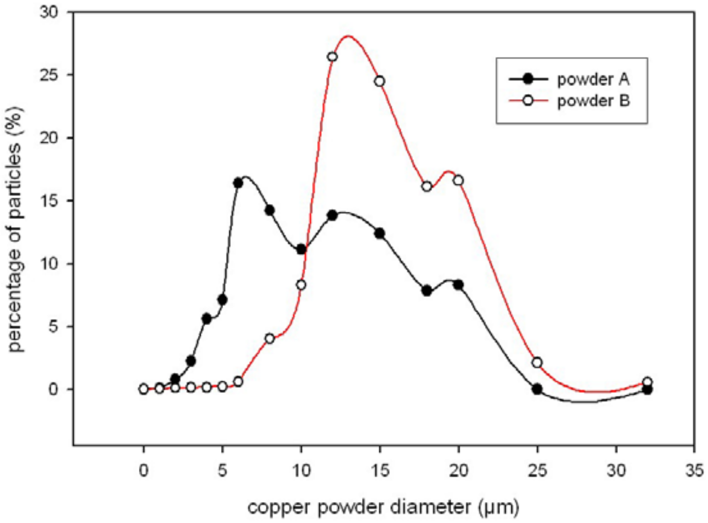

Figure 5-1: Size distribution weighted by volume.

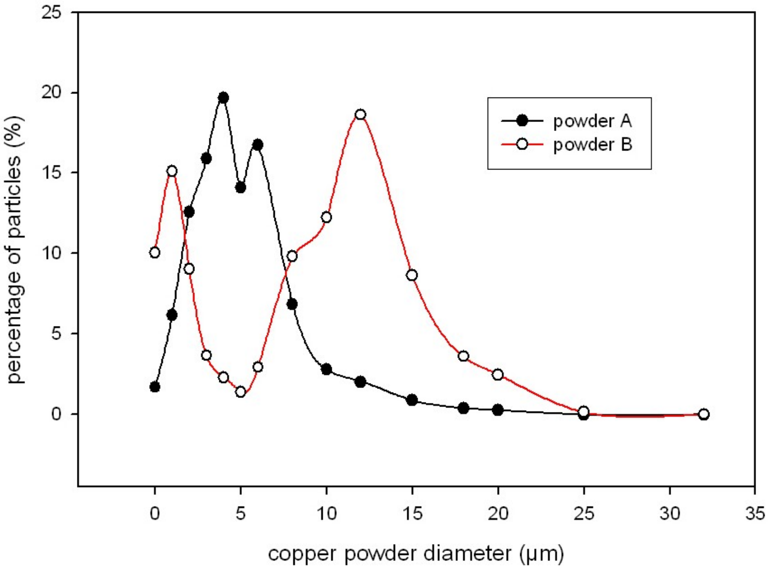

Figure 5-2: Size distribution weighted by number.

Figure 5-1 shows the size distribution weighted by volume and Figure 5-2 shows the size distribution weighted by number. The distribution weighted by volume increases the presence of large particle. The volume increases with ≈(diameter)^3 hence, the proportion of large particle appears more while the very fine ones with a negligible volume do not appear in the size distribution.
It appears from both of the previous figures that powder A has a smaller size than powder B.

5.2.4 Powder Production Technique

The gas atomised technique for powder production is used to produce powder for the thermal spray industry. Atomization is accomplished by forcing a molten metal stream through an orifice at moderate pressures. A gas is introduced into the metal stream just before it leaves the nozzle, serving to create turbulence as the gas expands (due to heating) and exits into a large collection volume exterior to the orifice. The collection volume is filled with gas to promote further turbulence of the molten metal jet. Air and powder streams are segregated using gravity.
The pumped energy is applied to droplet formation with very low efficiency (on the order of 1%) and control over the size distribution of the metal particles produced is rather poor. Other techniques such as nozzle asymmetry, nozzle vibration, multiple impinging streams, or molten-metal injection into ambient gas are all available to increase atomisation efficiency, produce finer grains, and to narrow the particle size distribution. Unfortunately, it is difficult to eject metals through orifices smaller than a few millimetres in diameter, which in practice limits the minimum size of powder grains to approximately 10 µm. Atomization also produces a wide spectrum of particle sizes, necessitating downstream classification by screening and remelting a significant fraction of the grain.

5.2.5 Shape Characteristics of the Powders

The powder's shape will influence its aerodynamical behaviour through the drag coefficient of the particle. The shape of the powder particles will also influence the flowability of the powder. This property is the ability of the powder to behave like a liquid. It is important to have a good flowability of the powder in order to master the injection of the powder in the nozzle and to get a good measure of the powder's feedrate. The shape can be measured with the 'alpaga 500 nano'. Since both powders have been made by the atomisation process, they have a very high roundness. The shape of the powder can be shown by using SEM microscopy (Figure 5-3 & Figure 5-4).

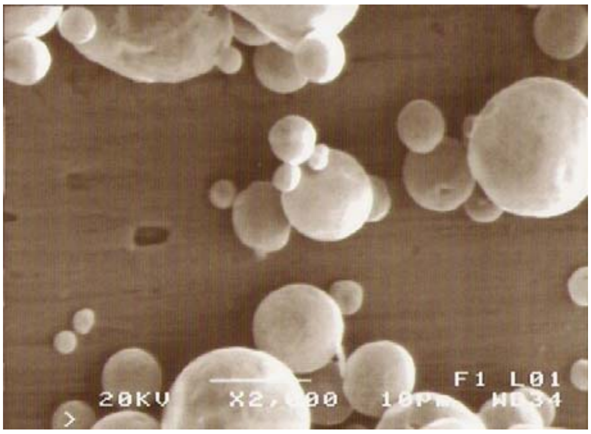

Figure 5-3: SEM picture of powder A.

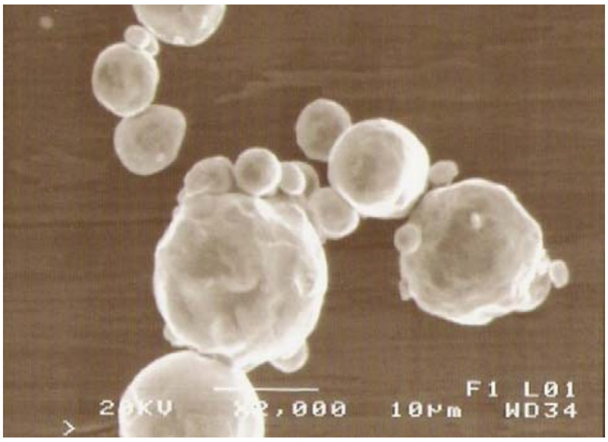

Figure 5-4: SEM picture of powder B.

5.2.6 The Oxide Content of the Powder

The oxide content in the powder plays a role in the bonding process as explained in section 2.8.1. The oxygen content is given by the powder suppliers. Powder A and powder B have respectively an oxygen content of 0.25 wt. % and 0.02 wt. %. The data comes from the powder supplier's specifications.

5.2.7 Etched Cross Section of the Powder

Both powders have been etched in order to observe their internal structure on Figure 5-5 and Figure 5-6. No obvious differences between powder's internal grain structures have been noted with optical micrographs. The powder has been etched with a solution composed of 50% of concentrated hydrogen peroxide and 50% of ammoniac.

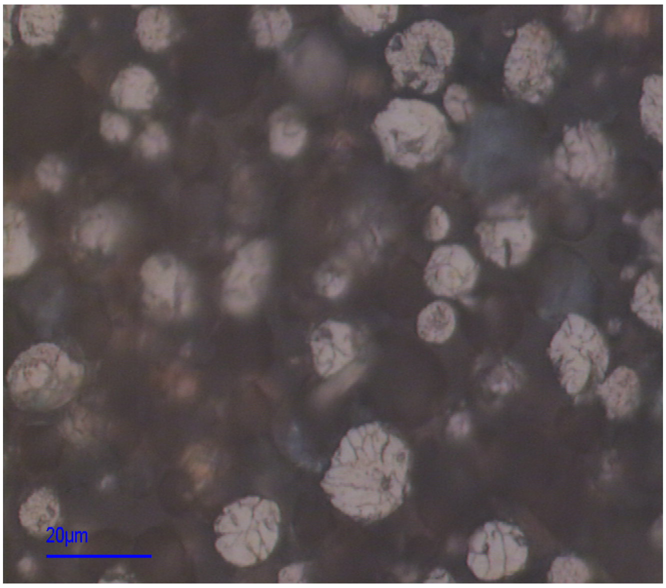

Figure 5-5: Optical image of the etched powder A.

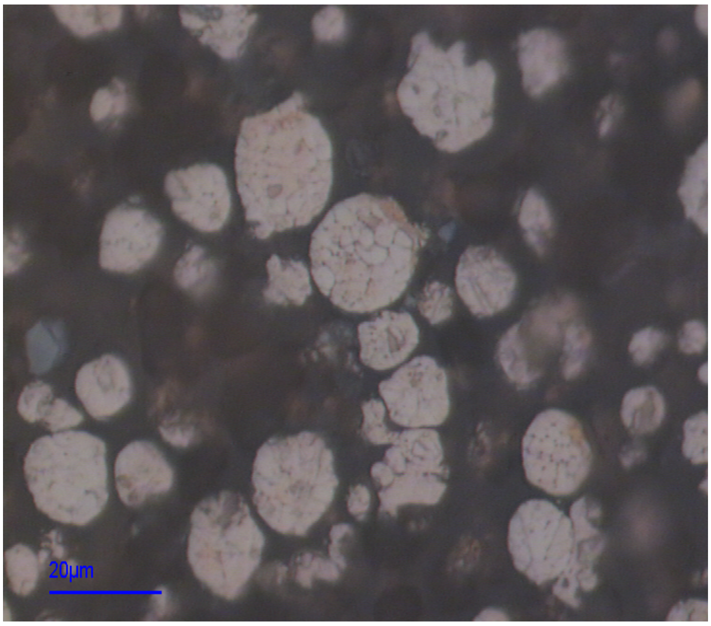

Figure 5-6: Optical image of the etched powder B.

5.3 Substrate Properties

Substrates are commercially available aluminium (1xxx series) and TA6V (Ti – 6 Al – 4 V or Ti 6-4) grade 5. The aluminium substrate has been polished and the TA6V has been sandblasted with F40 alumina at 3 bars. The hardness has been measured using a Vickers test. A load of 10 kg was applied on the aluminium substrate and a load of 20 kg was applied on the TA6V substrate.

Table 5-1: Substrate properties before spraying.

	Al substrate	TA6V substrate
Average roughness	0.2 µm Ra	3.8 µm Ra
Average Hardness	67.3 HV_{10kg}	257 HV_{20kg}

As shown in Chapter 4, the impact of copper particles on aluminium leads to the formation of adiabatic shear bands at the interface between substrate and particle. This favours good bonding. The formation of these shear bands is improved when the impact of the copper particle is perpendicular to the surface. Surface roughness will not allow the stress concentration and localization to be at optimum value in the rim of the impact. Hence, it is necessary to polish the surface and reduce the surface roughness. On hard surfaces, the copper will not create shear localization in the substrate. By creating roughness on the hard surface, copper particles will bond mechanically to the surface. The substrate's properties have been summarized in Table 5-1.

5.4 Cold Spray Installation

The cold gas dynamic spray installation was installed in the spraybooth of “Advanced Coating S.A.” in March 2003. The industrial installation is provided by “CGT Gmhb” in Germany. The configuration installed is the Kinetic 3000 composed of a control cabinet (Figure 5-7), a powder feeder (Figure 5-8), a gas heater (Figure 5-9) and the nozzle (Figure 5-10)

Figure 5-7: Control cabinet of the process.

Figure 5-8: Powder feeder.

Figure 5-9: Gas heater.

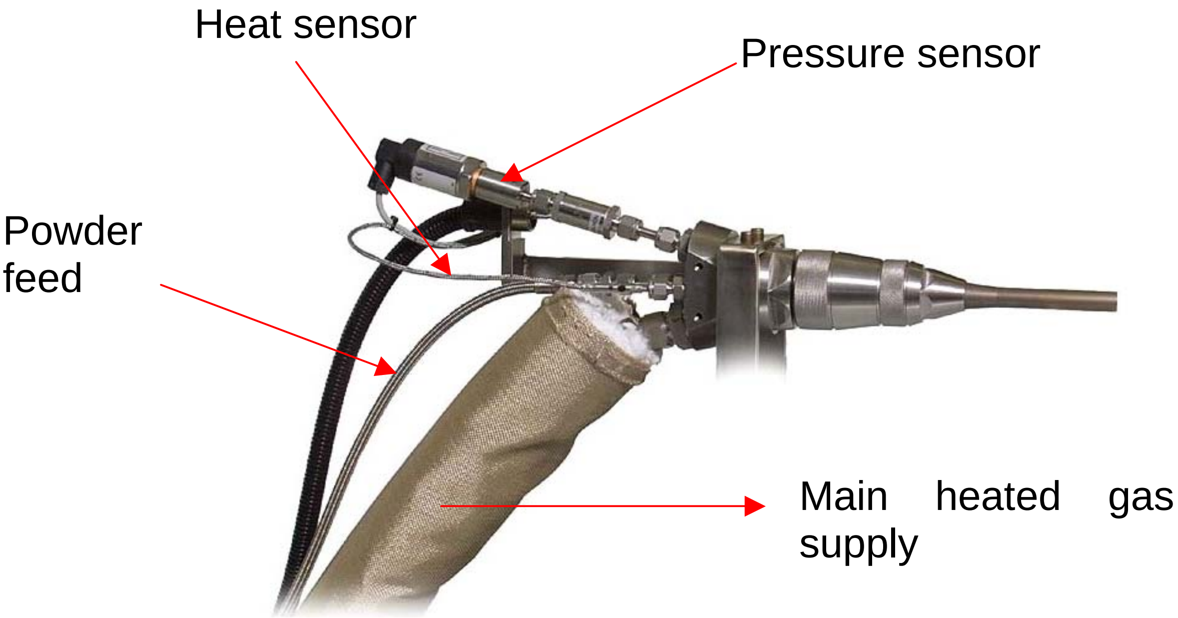

Figure 5-10: The cold spray gun composed with the nozzle and the different heat and pressure sensors.

The control cabinet regulates the pressure from the gas supply and divides the gas entry into two lines. One line is used as main gas supply and is sent to the gas heater. This line represents 90%-95% of the total gas flow in the system. The second line (5 to 10% of the total gas flow) is sent to the powder feeder and will be used to drive the powder to the injection point in the nozzle.

Figure 5-11: WC standard CGT nozzle.

The powder is injected in the convergent part of the nozzle close to the throat. The nozzle is shown on Figure 5-11. It is made of tungsten carbide which gives it a very high wear resistance. The two lines of gas reach the nozzle convergent part and the total mass flow exits the nozzle and accelerates the powder. Some characteristics of the nozzle design have been given in section 3.3.

The user of the system will fix the temperature and the pressure used for spraying as measured in the gun chamber before the powder enters the convergent part. The pressure sensor and the temperature sensor in the gun control the stability of the spray parameters used in real time.

5.5 Experimental Set Up in Advanced Coating

The experimental set up of installation is determined by the characteristics of the spraybooth used. The spraybooth is designed to spray on cylinders hence it is composed of a rotating plate and a robot that moves vertically with a given speed.

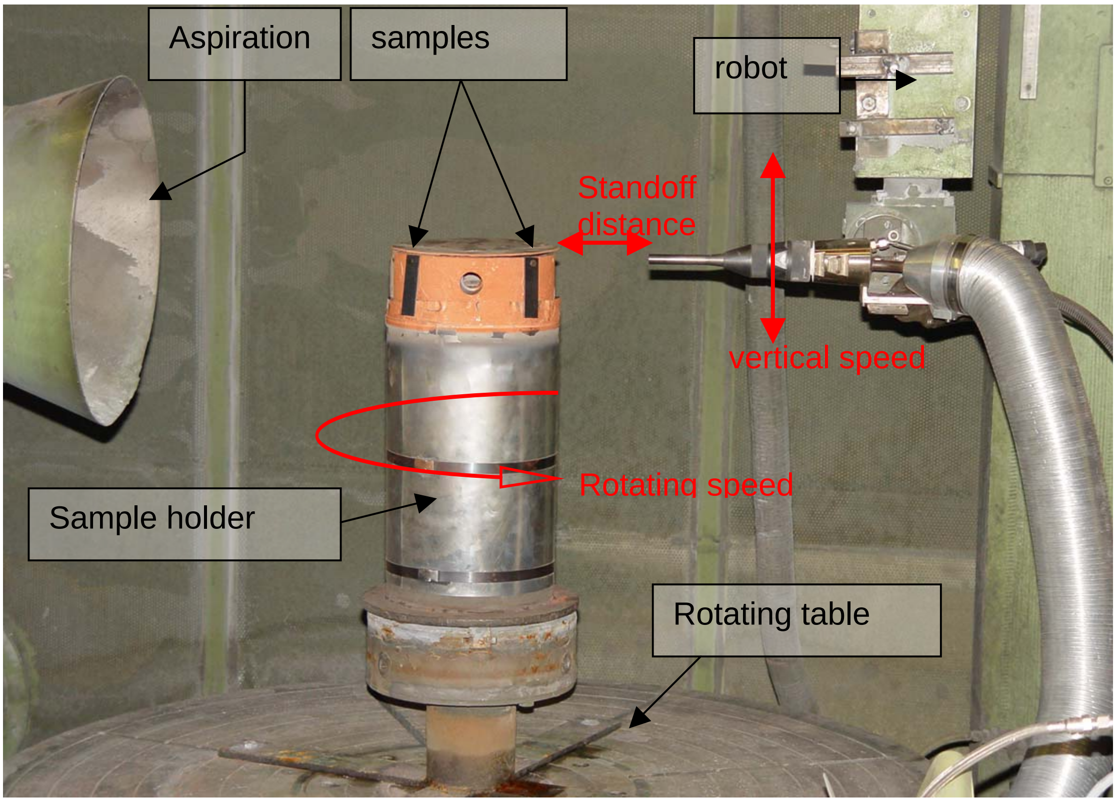

Figure 5-12: Experimental set up in Advanced Coating of the cold spray system in the spraybooth with the sample holder.

Samples used have a dimension of 2 cm by 6 cm and are fixed on the sample holder as shown on Figure 5-12. The sample holder can support 6 flat samples and 3 cylindrical samples for pull off tests.

During deposition, the samples rotate while the spray gun moves vertically at a constant speed. The rotating speed and the vertical speed have to be adapted so that, during deposition, the surface of the samples is uniformly covered by a copper coating. The width of a single track is 3 mm and the powder is not uniformly distributed on the tracks. There is more powder deposited at the centre of the track than at its edges. This gives a pyramid like shape to the track.

Hence, while the table does one rotation, the gun has to move for 1.5 mm. If the vertical movement is faster, then the surface will be wavy or with clear blanks between the tracks.

5.6 Design of Experiment:

Both copper powders have been sprayed to investigate the effect of the stagnation pressure P_0 and temperature T_0 on the copper coating properties. This design of experiment (DoE) has been established based on the knowledge of spray conditions used by other authors for copper. It was first necessary to ensure that a coating would be obtained.

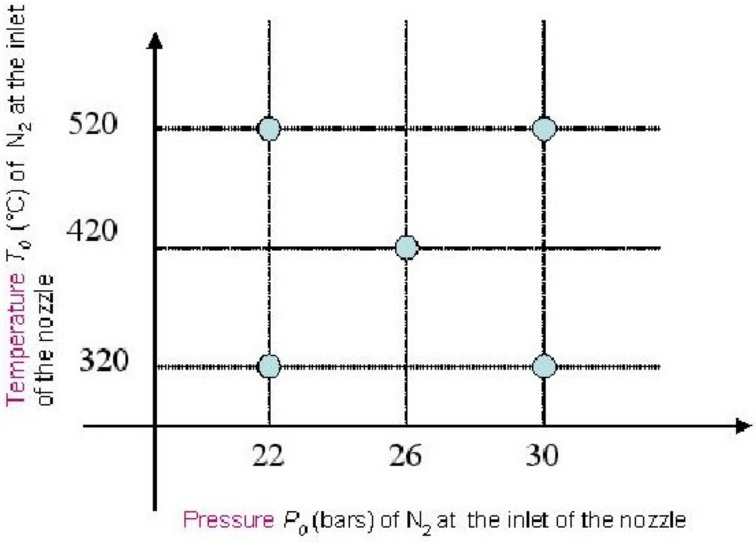

Figure 5-13: Presentation of the design of experiment used in this study.

Figure 5-13 and Table 5-2 show the set of parameters chosen for this study. 3 samples of aluminium, 3 samples of TA6V and 3 cylindrical Al samples for pull off tests were sprayed.

Table 5-2: Set of spray parameters used in this study.

Stagnation pressure P_0 (bars)	Stagnation temperature T_0 (°C)
22	320
22	520
26	420
30	320
30	520

Each powder was sprayed with the 5 conditions of the DoE on the same day. Two passes were done on the Al substrate. It appeared very quickly that spraying on the TA6V with 2 passes lead to the debonding of the coating. Therefore, deposition on this substrate was done with a single pass.

5.7 Measuring the Deposition Efficiency

The deposition efficiency (DE) is the ratio between the mass of copper in the coating and the mass that exited the nozzle towards the surface.

$$DE(\text{deposition efficiency}) = \frac{\text{mass of copper in the coating}}{\text{total of mass of copper that exited the nozzle}}$$

The mass of copper in the coating was obtained by subtracting the mass of the sample with the coating and the mass of the sample without the coating. The total mass that exited the nozzle is the product between the powder feed rate and the time of spray.

$$\text{total mass that exited the nozzle} = \dot{Q}_{powder} \times t_{spray}$$

The powder feed rate $\dot{Q}_{powder}$ can be obtained experimentally. The spray time t_{spray} is more complex to know. In the configuration on Figure 5-12, the spraying is not applied constantly on the samples. A large fraction of the powder is sprayed on the sample holder. The spray time t_{spray} corresponds to the time of passage of the spray gun in front of the sample's surface. The value of t_{spray} depends on the dimensions of the sample (L, l), the rotation speed of the sample holder (V_{rot}), the diameter of the sample holder(D), the number of passes (N_{passes}) and the increment of 1.5 mm to obtain a uniform coating.
A formula has been established to calculate the value of t_{spray}.

$$t_{spray} = \frac{N_{passes} \times L \times l}{1.5 \times V_{rot} \times \pi \times \left(\frac{D}{2}\right)}$$

5.8 Constant Spray Parameters

The constant spray parameters have been summarized on Table 5-3.

Table 5-3 : Constant spray parameters used with the DoE.

Powderfeed rate	40 g.min^{-1}
Gun speed	397 mm.s^{-1}
Standoff distance	40 mm
Used nozzle	CGT standard
Main gas	N_2

5.9 Results: the Deposition Efficiency

The measured results of copper sprayed on the Al substrate are shown on Figure 5-14. The 3D figure has the DoE variables in the horizontal plane and the DE is the vertical axis. Each point is the average between three measurements. The three samples attached to the sample holder (Figure 5-12).

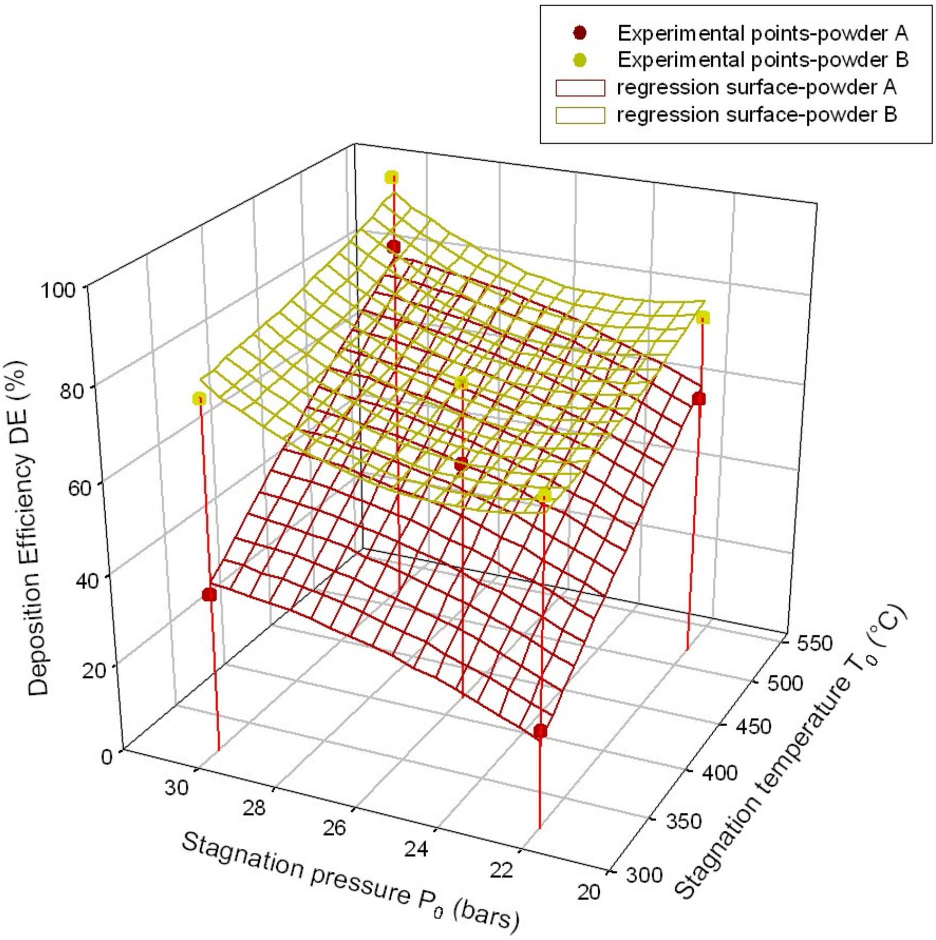

Figure 5-14: Results for the deposition efficiency of both copper powders on the Al substrate.

On Figure 5-14, a regression surface corresponding to each powder has been superimposed to show trends. It is a paraboloïde surface that best fits the experimental points. The thickness of the coatings on the Al substrate is summarized on Table 5-4.

It appears that powder B has a higher DE than powder A at every point in the DoE. It appears also that the highest increase in DE is obtained by changing simultaneously the stagnation pressure and temperature. This is explained by Figure 3-14 & Figure 3-16. The powder is accelerated on the whole range of its size distribution while the particle temperature increases steadily with the increase in stagnation temperature T_0.

Figure 5-15 shows the DE along the tree points that show the sharpest increase on the Al and TA6V substrate with the corresponding standard deviation. In some cases, the standard deviation is too small to appear on the figure.

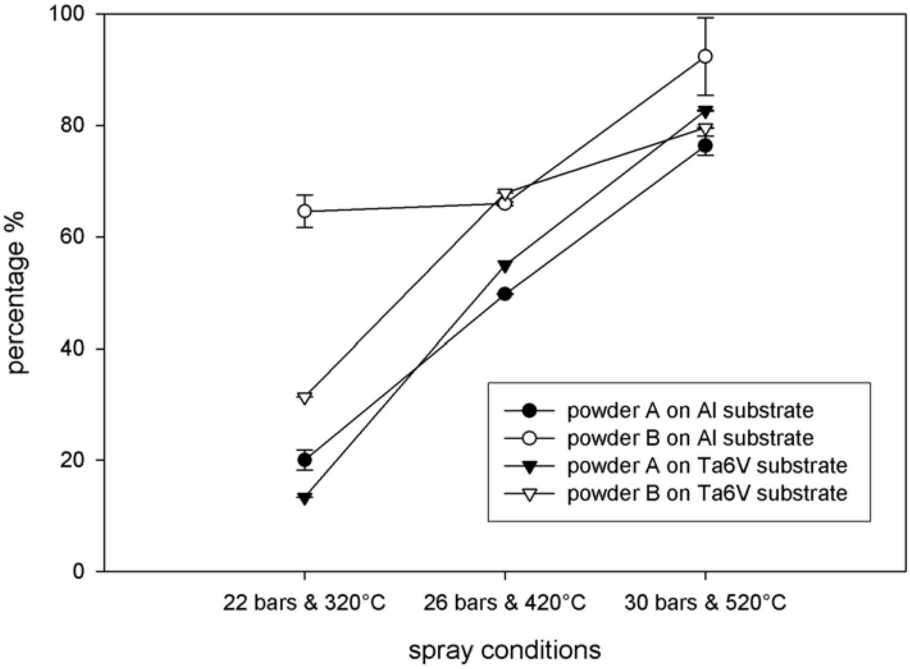

Figure 5-15 : Deposition Efficiency of both copper powders on Al and TA6V substrate along the most significant points of The DoE.

Table 5-4 : Copper coating thickness on the Al substrate.

Coating thickness (µm)			
Stagnation pressure P_0 (bars)	Stagnation temperature T_0 (°C)	Cu on Al	
		Powder A	Powder B
22	320	93	315
22	520	253	362
26	420	204	354
30	320	166	318
30	520	311	394

5.10 Etched Coating

The coatings have been etched with a solution composed of 50 % of concentrated hydrogen peroxide and 50 % of ammoniac. Etched coating can show differences in microstructure of the coating. Figure 5-16 and Figure 5-17 show respectively the etched coating made with powder A and with powder B. These coatings have been sprayed with a stagnation temperature T_0 = 520 °C and a stagnation pressure P_0 =30 bars. The coatings made with a stagnation temperature T_0 = 320 °C and a stagnation pressure P_0 = 22 bars have also been etched and the same differences appear. The etchant was also tested with lower concentration of hydrogen peroxide. It appeared that the hydrogen peroxide reveals the microstructure of the copper.

It is possible to distinguish the boundaries between the powder particles on both coatings. The coating made with powder A shows a more complex internal structure. In some copper particles, an internal cellular structure is present. The coating made with powder B shows the boundaries between the copper particles but no internal structure is present inside de copper particles.

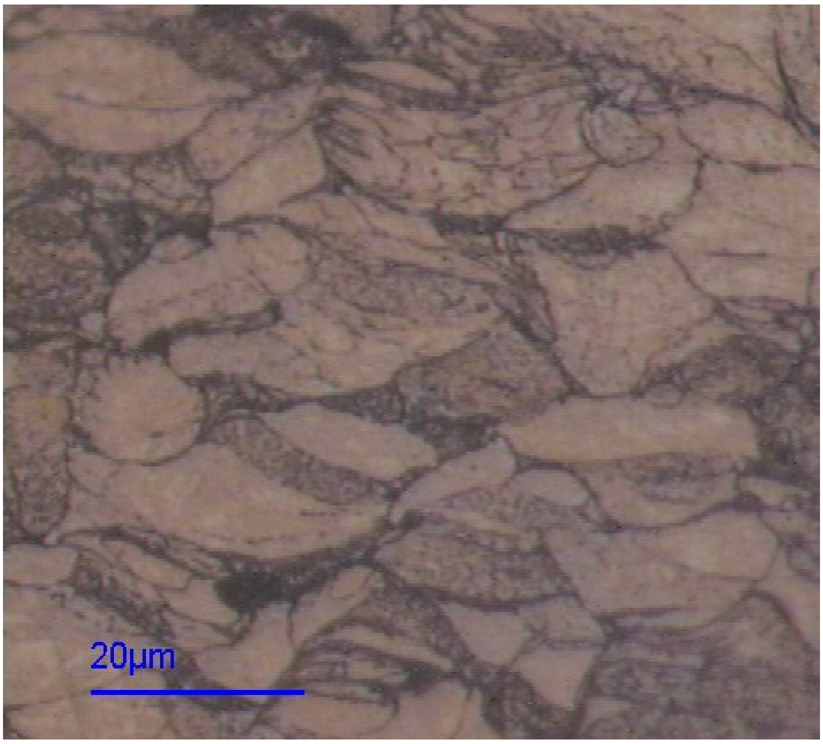

Figure 5-16 : Etched coating sprayed with powder A at 520 °C and 30 bars.

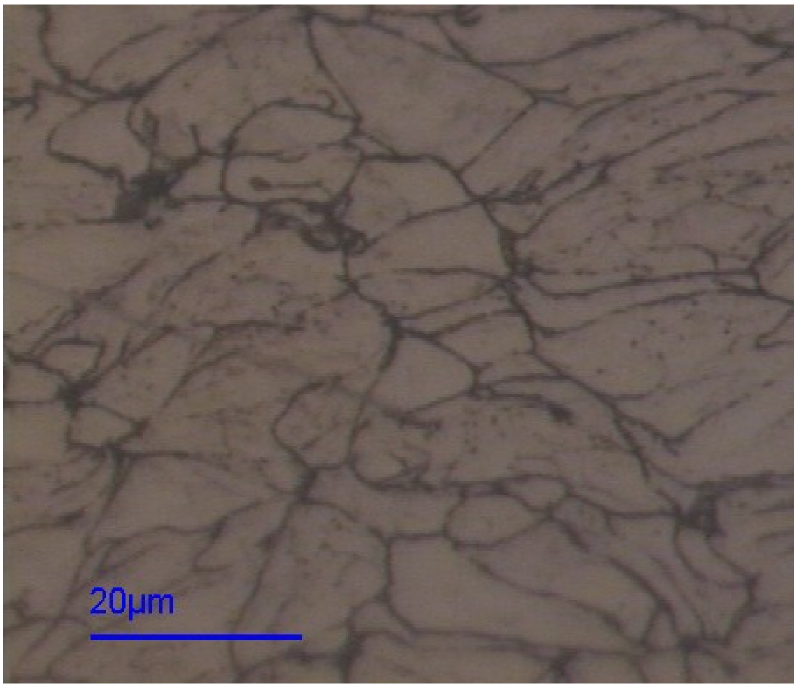

Figure 5-17 : Etched coating sprayed with powder B at 520 °C and 30 bars.

5.11 Discussion

The deposition efficiency value depends on:

- The fraction of the particle size distribution that is within the window of sprayability. This is determined by the spray conditions.
- The oxide content of the powder. C.-J. Li et al [27] (see also section 2.8.1) has shown that the critical velocity is sensitive to the level of oxide content in the powder. The oxide shell around the copper particles hinders the formation of the shear bands and the copper particles don't bond.

Observations on the used powders in this study are:

- Powder A has a higher oxide content than powder B. It would mean the powder A has a higher critical velocity than powder B.
- Powder A has a higher impact velocity than powder B. This has been observed on Table 3-5.

When the DE increases, it means that a larger fraction of the powder is within the window of sprayability. Therefore, more particles are above the critical velocity. Powder B has a higher DE than powder A on any substrate and what ever the spray conditions. As shown in section 3.8.3, powder B has a lower velocity than powder A since it has a higher particle size. The only explanation is that powder B has a critical velocity much lower than powder A. Because the oxygen content of powder B is lower than the one of powder A, its critical velocity will be below that of powder A.

Both coatings show also a different microstructure when etched (Figure 5-16 & Figure 5-17). The powders have deformed differently during the coating build up. This may be due to an initial difference between the mechanical properties of the powder (hardness, shear strength). This issue will be dealt with in Chapter 7. X-ray diffraction will quantify some aspects of the microstructure like the dislocation density, crystallite size and dislocation type.

In all cases Figure 5-15 shows that the increase in DE corresponds to an increase in the stagnation gas pressure and temperature. This allows placing more particles above the critical speed and the bonding occurs.

When both powders are sprayed on the Al substrate, it appears that powder B yields a larger DE than powder A when sprayed at 320°C and 22 bars. With these spray conditions, the copper particles do not bond immediately on the surface. They need to remove the oxide layer naturally present on the powder and the surface. Powder B with a low oxide content, has a thin oxide shell. Once the shell is broken, a clear contact and good bonding is obtained.
Powder A has a thicker oxide shell, hence, during impact, the velocity is not sufficient to break it. Therefore the DE of powder A is smaller.

The substrate properties will influence the bonding process. Chapter 4 shows that the first copper impacts are very different between the substrate made of steel and the one made of AA2014. On hard substrates like steel or TA6V, the first layer activates the surface but they do not bond. After these first impacts, the other particles start to bond. The consequence of this is a drop of the D.E. on the TA6V substrate compared to the Al substrate. Figure 5-15 shows that on the D.E. on TA6V is lower than the one on aluminium.

The fact that only one single pass could bond to the TA6V surface shows the importance of the first layer that bonds with the surface. Based on the results on steel in Chapter 4, it reasonable to assume that some impacts will provide anchors for the coating build up. When a second layer is sprayed on top of the first one, the violence of the impacts breaks the anchors and the coating debonds.

5.12 Conclusion

The D.E. is clearly influenced by two important factors:

- The spray conditions.
- The oxide content.

The effect of the spray conditions depends on the size distribution of the powder. Powder A, with a fine size distribution, has a higher velocity than powder B at every spray condition tested in the DoE (Table 3-5).
The presence of an oxide shell will hinder the metallurgical contact between the powders and the substrate. Hence, the value of the critical speed for copper with a low oxide content will drop.

Chapter 6 Mechanical properties of Cold Sprayed Copper Coatings

6.1 Introduction

The powder size distribution will have a crucial importance on the quality of the coating. The process is essentially influenced by the kinetic energy transferred to the particles. A different size distribution of the powder means that the kinetic energy is distributed differently. Mechanical properties such as bond strength and hardness will be affected by the size distribution. Chapter 5 shows that the DE is different when the size distribution changes. This chapter will show the sensitivity of coating properties on the size distribution of the powder.

The deposition on two substrates, aluminium and TA6V, has been compared. Nanoindentation has been used to get a local measurement of hardness. An attempt to show the effect of spray conditions on the strain hardening in the coating using this method is presented.

The microhardness and bond strength have been measured by using the equipment in Advanced Coating S.A. . Nanoindentation was performed in the Materials and Chemicals groups at the University of Brussels.

6.2 Coating Characterization

The coating properties have been characterized by several techniques: microhardness, bond strength and nanoindentation.

6.2.1 Microhardness

Microhardness measurements have been done using a Vickers indenter with an applied load of 300 g (2.94 N for 15 s). The load increase is 0.4 $N.s^{-1}$. The Vickers hardness value is obtained by using

$$\text{Vickers hardness} = \frac{0.189 \cdot F}{d^2} \ [\text{N/mm}^2]$$

Where F is the load applied and d the diagonal of the indentation. 10 measurements are done on a cross section of the coating.

6.2.2 Bond Strength

The bond strength was measured with a standard pull-off test on aluminium substrates using the standard NF L06 351. A coated plot is glued to a counter plot with a specific epoxy adhesive.

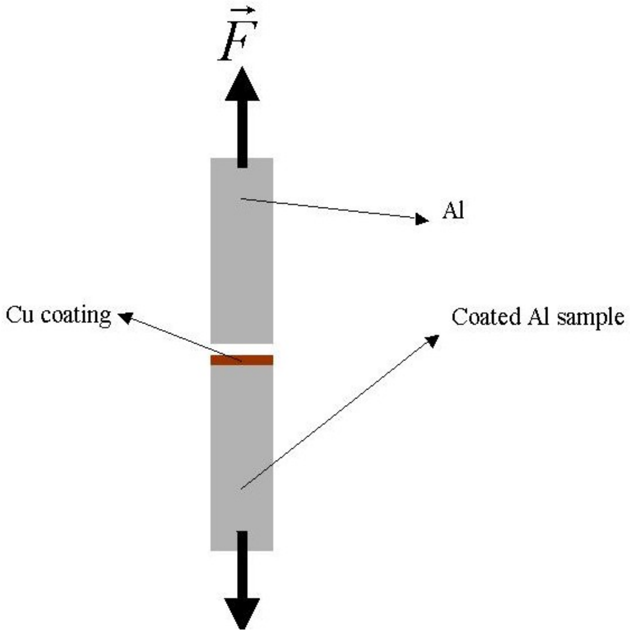

This type of measurement has limitations:

- Alignment between the plots must be perfect to avoid shear in the coating.
- The maximum bond strength measured is limited by the adhesive used.
- There is high dispersion in the results.

6.2.3 Nanoindentation

Nanoidentation tests were performed using a Hysitron TriboIndenter with a Berckovich tip on the cross section of the coating. The load function applied on the surface was a trapezoidal function with steady increase up to 6000 µN in 5 seconds followed by a constant load value for 2 seconds and a decrease from 6000 µN to 0 in 5 seconds. The mechanical response of the coating allowed measuring the hardness of the coating and its Young Modulus. Measurements were performed in which the tip of the indenter has been placed at the interface between the substrate and the copper coating and a series of 10 indentations spaced from each other by 10 micrometers have been done. On each coating, 3 profiles have been made and the data is presented as an average hardness with the corresponding standard deviation.

6.2.3.1 Theory

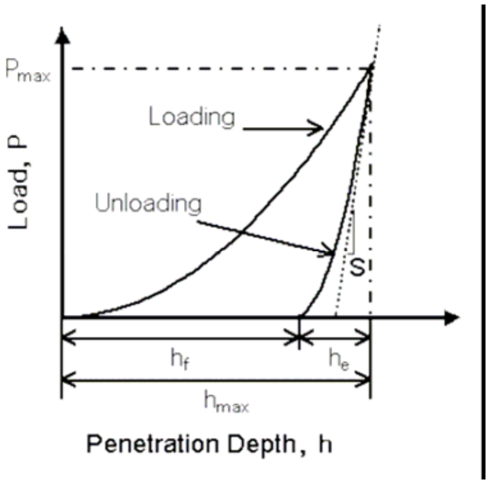

Figure 6-1 : Ideal loading-unloading curve measured during a nanoindentation test.

Figure 6-1 shows the ideal loading and unloading curve measured by the indentation test where P is the applied load, h the penetration depth, h_e is the elastic penetration depth and h_f is the final penetration depth. S is the contact stiffness measured on the unloading curve. It is the differential of the unloading curve at maximum load.

$$S = \left.\frac{dP}{dh}\right|_{P=P_{\max}}$$

The contact surface between the tip and the surface is determined by the Oliver & Pharr calibration method [54]. It gives a relation between the contact surface $A_c=f(h_f)$. The hardness is measured by:

$$H = \frac{P_{\max}}{A_c(h_f)}$$

The nanoindentation test gives a reduced value of the Young modulus that takes into account the Young modulus of the indenter and the coating.

$$\frac{1}{E_r} = \frac{1-\upsilon_i^2}{E_i} + \frac{1-\upsilon_s^2}{E_s}$$

E_r is the "reduced modulus", E_i and E_s are respectively the Young modulus of the indenter and the studied specimen, υ_i^2 and υ_s^2 are respectively the poisson ratio of the indenter and the specimen.

Sneddon developed a relation for the elastic deformation of an isotropic elastic material with a flat-ended cylindrical punch:

$$E_r = \frac{\sqrt{\pi}}{2} \frac{S}{\sqrt{A_c}}$$

This relation will give a value for the reduced modulus.

6.2.3.2 Surface Preparation

Cold mounting was used to prepare the samples. The copper coatings were polished 2 µm diameter MgO and after that they were polished with the OP-Solution and a solution with 0.3 µm alumina suspensions. Several polishing tests were attempted to evaluate surface preparation effects on the measurements.
The Hystron triboindenter allows measuring the surface roughness of the sample. The polishing kept the surface roughness Ra below 5 nm. Figure 6-2 shows the surface of the copper with an indentation on the surface.

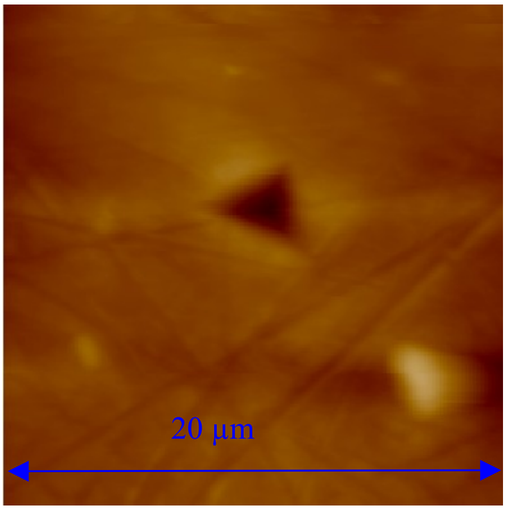

Figure 6-2: Copper surface observed with the tip of the indenter in AFM mode.

The influence of the surface preparation has been assessed by Liu et al [55] on a copper single crystal. The Figure 6-3 shows that mechanical polishing has a considerable influence on the hardness value when the indentation depth is low. This study has been done on a copper single crystal. The mechanical polishing of the single crystal will induce defect and surface rich in dislocations. It this study, the indentation depth is around 300 nm. The effect of the surface preparation will increase the measured hardness by 0.12 GPa.
The copper cold spray coatings are severely strain hardened. It has been observed that dislocations densities are very high $\rho \sim 10^{15}-10^{16}$ m^{-2}. The dislocations density of the copper coatings used in this study has been measured with X-ray diffraction in Chapter 7. Mechanical polishing on these coatings will induce an increase in dislocation density but it will not change dramatically the hardness of the surface.

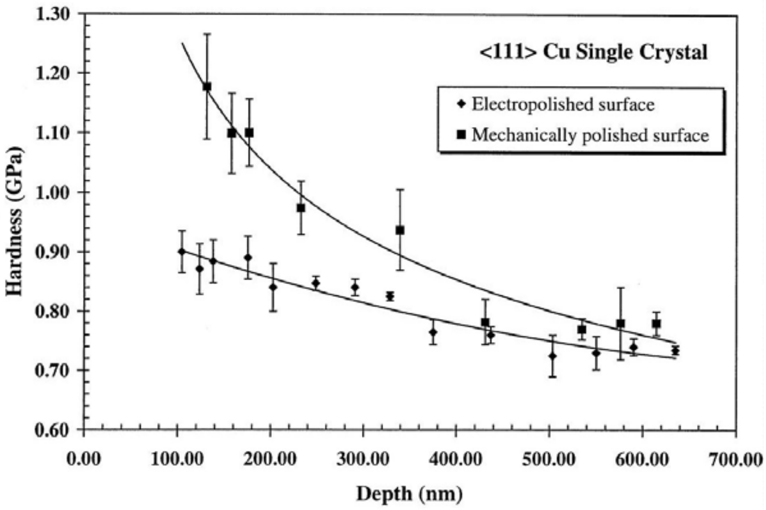

Figure 6-3 : Surface preparation influence on the hardness measurement [55].

6.3 Microhardness Results

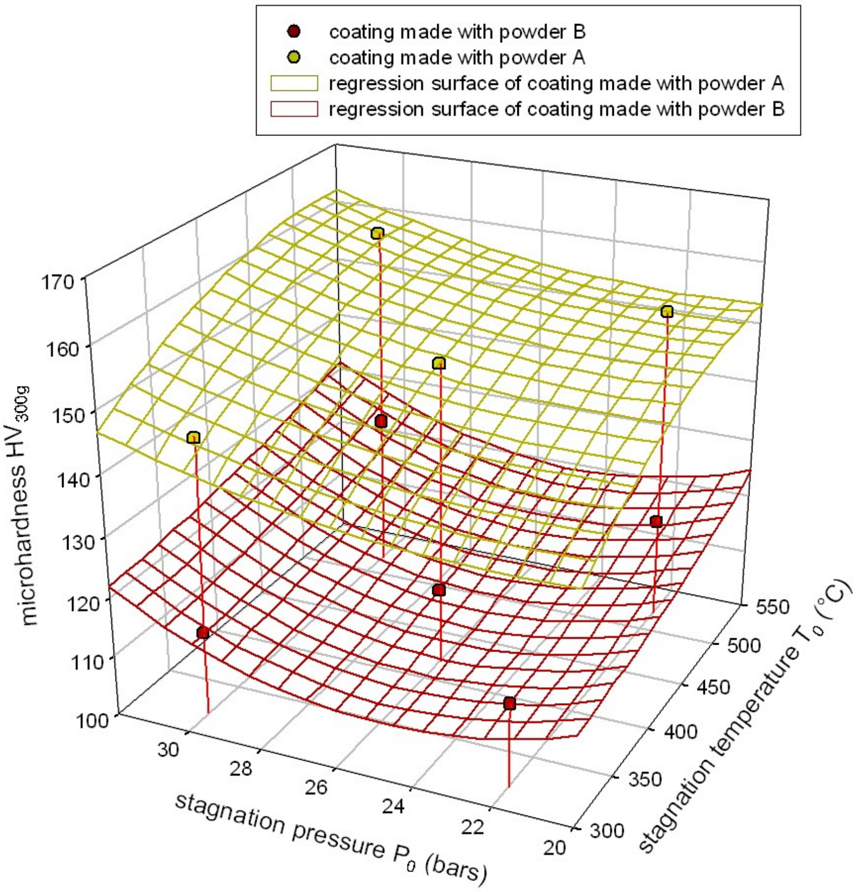

Figure 6-4: Microhardness on the DoE. Regression surfaces are added to experimental points to show trends.

Figure 6-4 shows the microhardness results of the design of experiment. The regression surface has been added to the experimental points to show the trends between the powders.

The measurements have been done on the Cu coating on the Al substrate. Figure 6-5 shows the microhardness values along the first diagonal of the DoE. Both figures show that the different powders have a very different microhardness. A change in spray conditions leads to a slight increase in the microhardness value.

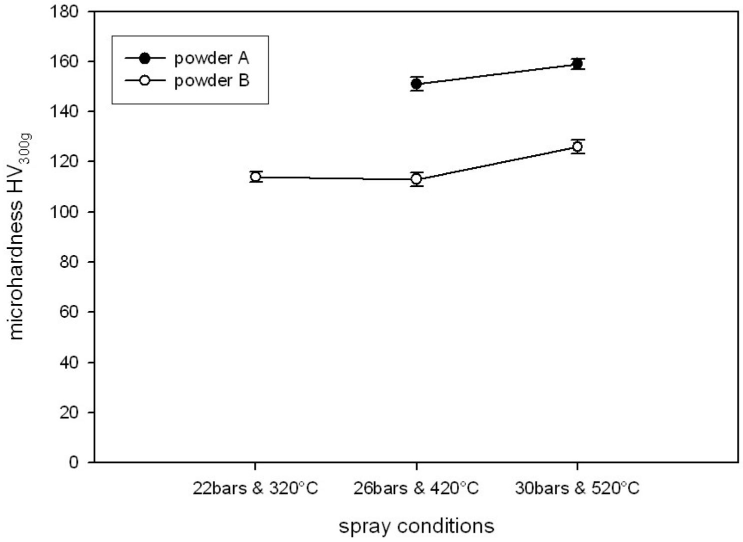

Figure 6-5: Values of the microhardness on the first diagonal of the DoE.

6.4 Bond Strength

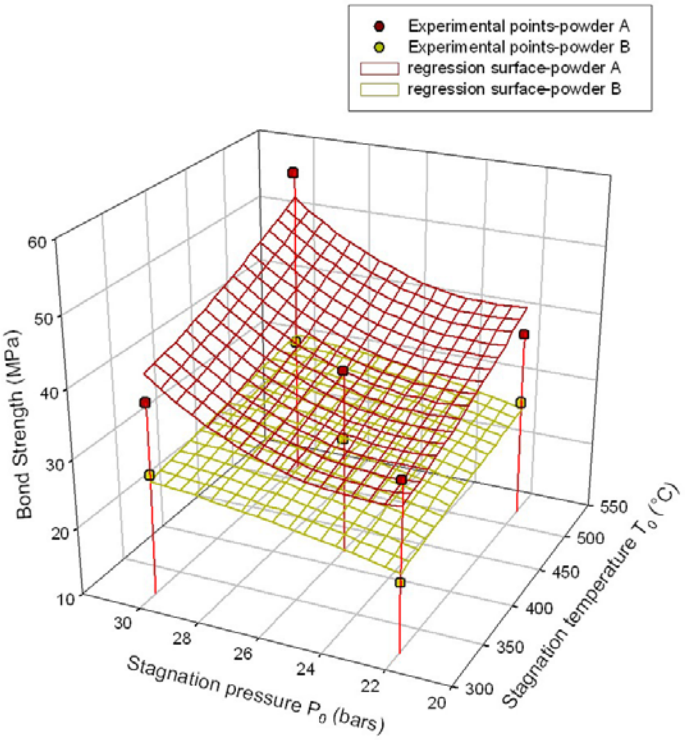

Figure 6-6: Bond strength on the DoE. Regression surfaces are added to experimental points to show trends.

Figure 6-6 shows the bond strength results of the design of experiment. The regression surface has been added to the experimental points to show the trends between the powders. The measurements have been done on the Cu coating on the Al substrate. Figure 6-7shows the bond strength values along the first diagonal of the DoE. Both figures show that the different powders have a very different bond strength value. A change in spray conditions leads to a slight increase in the bond strength value.

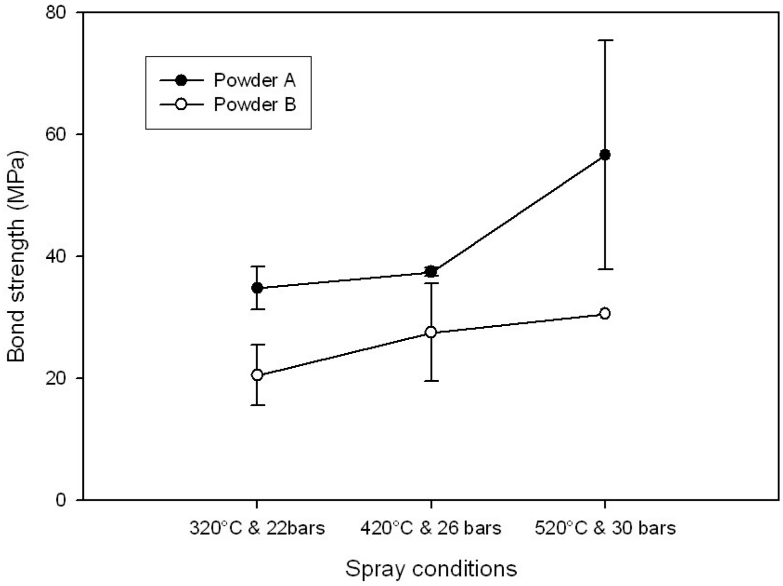

Figure 6-7: Values of the bond strength on the first diagonal of the DoE.

6.5 Nanoindentation Results

The profiles have been done perpendicular to the interface between the coating and the aluminium substrate. The techniques give a measurement of the Young modulus and the Hardness using the Oliver & Pharr technique. The coatings used for the comparison are the ones that have yielded the most significant difference in D.E., microhardness and bond strength. They correspond to the most extreme spray conditions used in the DoE

- Spray condition 1: A stagnation pressure of P_0 = 30 bars and a stagnation temperature of T_0 = 520°C.
- Spray condition 2: A stagnation pressure of P_0 = 22 bars and a stagnation temperature of T_0 = 320°C.

6.5.1 Comparison between powder A & B

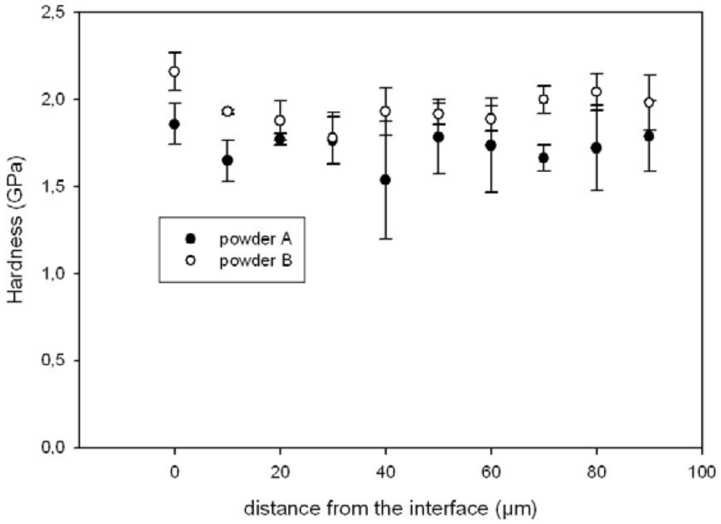

Figure 6-8 : Comparison between the hardness profiles of the coatings made with powder A & B sprayed at T_0=520°C and P_0=30 bars.

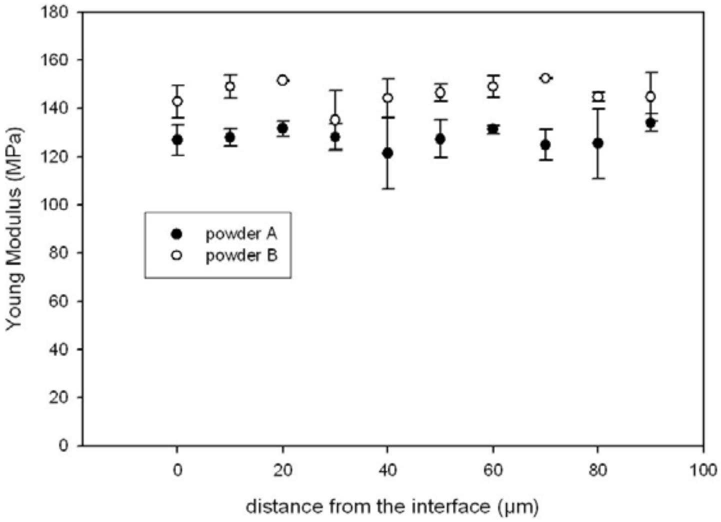

Figure 6-9 : Comparison between the "reduced modulus" profiles of the coatings made with powder A & B sprayed at T_0=520°C and P_0=30 bars.

6.5.2 Influence of the Spray Condition

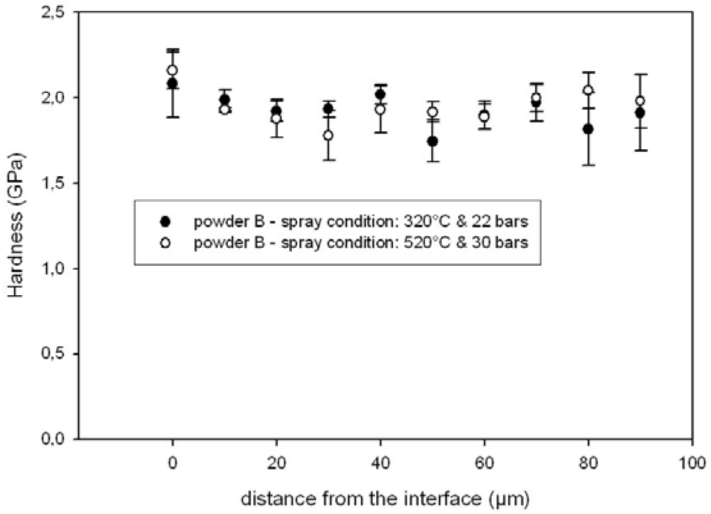

Figure 6-10 : Influence of the spray conditions on the coating made with powder B.

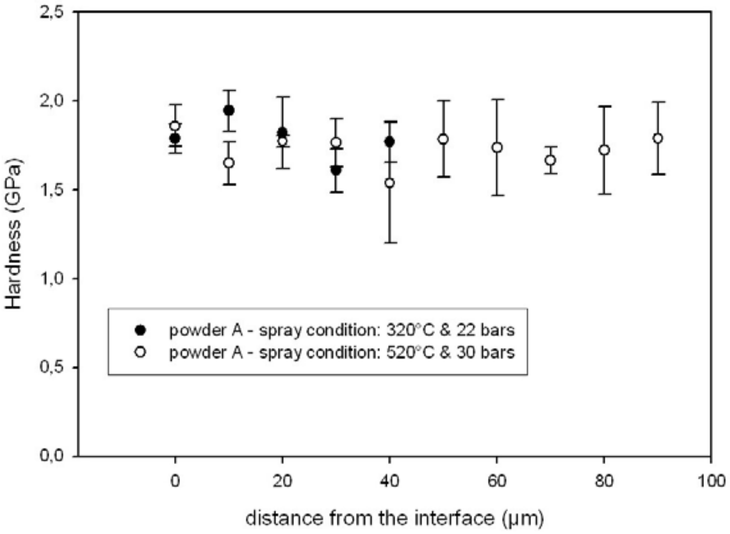

Figure 6-11 : Influence of the spray conditions on the coating made with powder A.

Table 6-1 : Average values of the hardness and "reduced modulus" of all the points measured on the coatings.

	Powder A	**Powder B**
Average Young Modulus E (GPa)	127.9	146
Standard deviation E (GPa)	3.7	4.9
Average hardness H (GPa)	1.73	1.95
Standard deviation H (GPa)	0.09	0.1

6.6 Discussion

Figure 6-4 & Figure 6-6 show that the differences in microhardness and bond strength come from the powder characteristics. Whatever the spray conditions, powder A has a higher microhardness and bond strength than powder B. Figure 6-5 & Figure 6-7 show that an increase stagnation gas pressure P_0 and temperature T_0 will lead to a slight increase in the microhardness and bond strength. As shown on Figure 3-13, the increase in gas stagnation pressure leads to an increase in impact speed. It has been confirmed by using laser velocimetry (Table 3-5), that the copper hits the surface with a higher speed when P_0 and T_0 increase. Figure 3-16 shows the evolution of the copper particle's temperature upon impact. High copper particle temperature combined with a high impact velocity favours the formation of shear bands. The consequence of this is an increase in bond strength with the aluminium substrate. It is also visible on the measure of the DE (Figure 5-15).

The main interest for using nanoindentation, compared to microhardness, is to measure the mechanical properties of the coating on a scale smaller than the powder grains size that constitutes the coating.

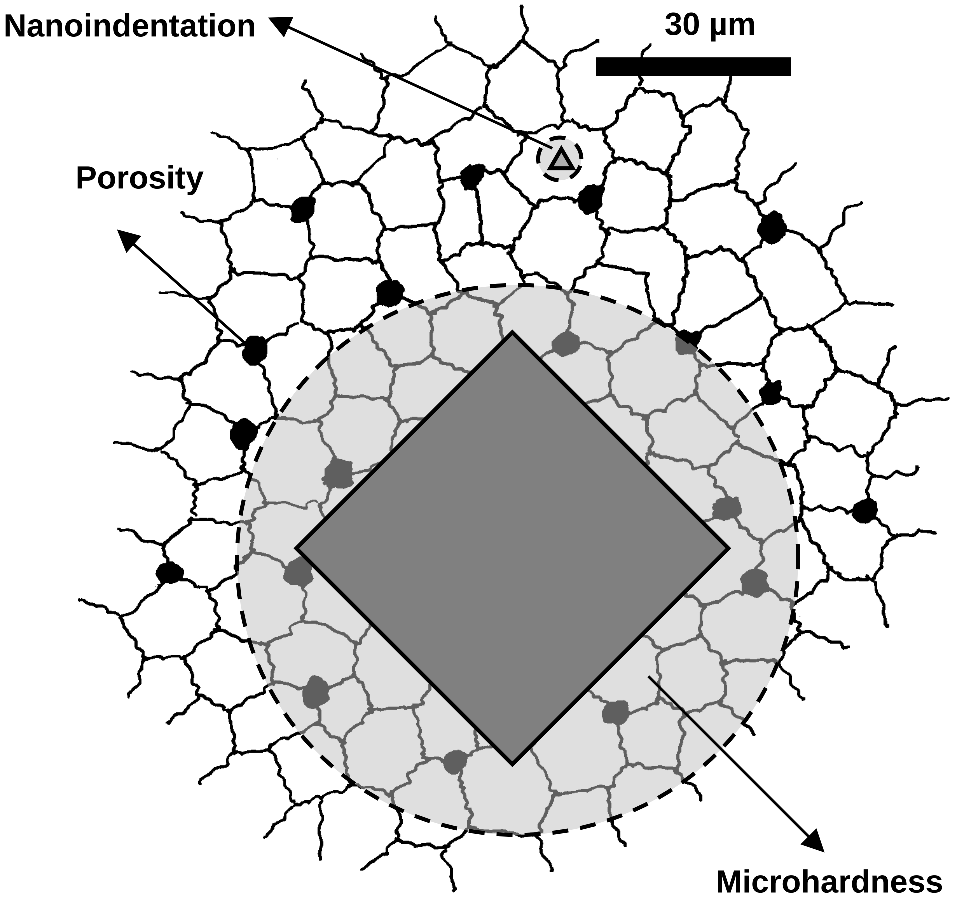

Figure 6-12 : Comparison between the scale of nanoindentation and microhardness.

Figure 6-12 shows the difference in scale between microhardness and nanoindentation. Microhardness results will be influenced by powder structure of the coating whereas nanohardness will be influenced by the mechanical properties of single impacted powder particles. The plastic deformation microhardness is clearly influenced by the obstacle of powder particle boundaries. Plastic deformation in the nanoindentation technique is limited to a scale within a powder particle. The plastic zone induced by nanoindentation has been evaluated by J. Chen et al [56]. The empirical relation obtained is:

$$\frac{R_p}{\delta_m} = -12.907 \cdot \frac{H}{E_r} + 4.5451$$

Where:

R_p : radius of the plastic zone

δ_{m} : indentation depth

When the indentation depth ranges from 250 nm to 350 nm, the radius of the plastic zone R_p has a variation between 1.1 µm and 1.5 µm. These values for copper are computed for a hardness value $H = 1.9$ GPa and a reduced Young modulus $E_r = 140$ GPa. This proves that the plastic zone is below the size of individual particles of powder A and B.

The copper's reduced Young modulus measured by Rabkin et al [53] has a value of ~140 GPa and a hardness with a strong depth dependence (1.5 to 2.2 GPa for as pressed ECAP copper). L. Lu et al [57] have analyzed the rate dependence of the hardness value on copper. These values of hardness range from 1.5 to 2.5 GPa. The values obtained in this study summarized in Table 6-1 are compatibles with existing results.

Cold spray copper coatings have a heterogeneous microstructure. It has been described in 2.6.1. During impact, a nanocristalline zone forms in the shear bands while other areas show large recrystallized grains. The successive impacts build up the dislocation density in the coating by deforming the impacted particles and inducing shear bands. This heterogeneity of the copper microstructure will influence the values by nanoindentation.

6.6.1 Influence of the Powder on the Nanohardness

Figure 6-8 shows that the coating made with powder A has a lower hardness than the coating made with powder B when sprayed at $P_0 = 520°C$ and $T_0 = 30$ bars. To understand this difference, some results from Chapter 7 are needed. X-ray diffraction of the powders has showed that powder A has a larger crystallite size than powder B and a lower dislocation density than powder B (Table 7-2). The coating is composed of very heterogeneous features. Inside a copper particle in the coating, shear bands have a nanostructure but they are highly localized. The flattening of the copper particle has lead to an increase in dislocation density on average but most of it is localized in the shear bands. The copper particles have kept a part of the powder's undeformed original microstructure. Therefore, the coating made with powder A has a lower value of hardness than powder B.

The coating made with powder A has pockets of the undeformed original microstructure but the impact has yielded important dislocations multiplication in the shear bands. The average dislocations density in the coating made with powder A is higher than the one of powder B (compare Table 7-3 and Table 7-4). Like as pressed ECAP annealed copper in reference [53], the cold sprayed coating is composed with pockets of ultrafine grains and pockets of larger grains. The nanoindentation process in this study did not distinguish these zones. No clear interpretation of the effect of the indentation process can be easily correlated between the microstructure and the differences in Young modulus in Figure 6-9. The Young modulus E_r is influenced by an additional plastic relaxation during unloading and creep phenomenons.

6.6.2 The Absence of Strain Hardening Profiles

Barradas et al [24] have shown the presence of a microhardness profile in the cold spray copper coatings. The presence of a nanohardness profile has not been detected on Figure 6-8, Figure 6-10 and Figure 6-11. The presence of a hardness profile should be the consequence of strain hardening due to the successive impacts. The absence of such a profile in this study comes from the differences in spray conditions:

- Barradas et al sprays with a stagnation temperature of 270°C.
- Barradas et al sprays with a nozzle speed of 25 mm.s^{-1}.

The formation of a hardness profile will be depending on the intensity of the peening and the time exposed to peening. In the cold spray process, it means that a hardness profile will form if the nozzle travel speed is low and the number of passes is high because this will allow a lot of peening to build up. The deposition efficiency is also important. If the DE is high, most of the particles will bond to the surface and will protect the first layers against the peening effect of non bonding impacts. If the DE is low, than many particles will not bond and a large fraction of the impacts will induce peening. In this study, the DE is high and the gun travel speed is 10 times higher than the one used in reference [24] and the process stagnation temperature ranges from 320°C to 520°C. It has for consequence a high DE and a low time exposed to peening.

6.6.3 Influence of the Spray Conditions on the Nanohardness Profile

The spray conditions will influence the speed and the temperature of the copper particles upon impact. Copper particles that bond have reached the critical velocity and they flatten the same way. The high nozzle travel speed and high DE prevents peening and strain hardening from accumulating in the nozzle. The strain hardening is essentially determined by the flattening of the powder particles above the critical speed.

6.7 Conclusion

The mechanical properties of the coatings are determined essentially by the characteristics of the original powder. Two powders with a different size distribution yield different microhardness values and bond strengths as showed by Figure 6-5 & Figure 6-7.

- The difference in microhardness is determined by the powder particle's size in the coating. Powder B is coarser than powder A. The indentation in powder B will be less influenced by the obstacle of particle boundaries. Hence, powder B has a lower microhardness than powder A.
- The bond strength is very different from one powder to the other. Powder A with a fine size distribution will be accelerated faster in the nozzle. Hence, its impact speed will be higher than the one of powder B. It will favour the quality of the contact between the copper and the substrate.

Results from Chapter 7 shows that the two powders have a very different initial microstructure. This influence will be discussed later.

Nanohardness results show also that the mechanical properties of the original powder are important. The absence of hardness profile in the coating is associated with the high nozzle speed, the high DE and the low number of passes needed to build up the coating. Some reservation can be made on the influence of the surface preparation on the measured results.

Chapter 7 X-ray Diffraction of CGDS Copper Powders and Coatings

7.1 Introduction

X-ray diffraction has been used for several years to characterize microstructures in metals and materials. This method identifies different phases of materials present if the volume of each phase is sufficient to be detected. The shape, the asymmetry and the position of the diffraction peaks are influenced by several factors:

- Dislocations
- Twins and staking faults
- Grain boundaries
- Sub grain boundaries
- Vacancies
- Inclusions
- Misfits between different phases

Developments of this method allow to identify how diffraction patterns are affected by these defects. Ungár et al [59],[60] have developed the classical Hall-Williamson method and Warren-Averbach method to take into account the strain anisotropy of the X-ray peaks diffraction and the influence of dislocations and planar faults on peak broadening. A number of publications analyse the microstructure of copper with these diffraction methods [61],[62],[63].

This chapter aims at describing how two different copper powders with a different grain size distribution and a different microstructure build up into the coating. Two spraying conditions have been compared. An attempt to link the microstructural characteristics with the formation of adiabatic shear bands is discussed.

7.2 Coating Characterization

Coatings have been mounted (Figure 7-2) and mechanically polished to remove surface roughness. The effect of mechanical polishing compared to chemical etching has been done by Ungár [59] and is illustrated in Figure 7-1. The polishing does not change largely the plots used to characterize the microstructure.

Samples have been analyzed in a Siemens D5000 with a Cu anode operating at 40 kV and 40 mA. The Kα2 component of the Cu radiation was eliminated by software substraction. The X-ray patterns have been done between 40 and 140 °C. The angular step is 0.02° and each step was measured during 40 s. The LaB_6 sample (for instrumental broadening characterization) has been analysed with the same angular step but with a 10 second measuring time. The X-ray peaks of the five first peaks have been used for the Hall-Williamson analysis with the following miller index: 111, 200, 220, 311, and 222. For the W-A procedure, the 5th peak was not used. Its shape was insufficiently resolved for the W-A method. Figure 7-17 shows peaks measured on powder B and on the coating sprayed with powder B superposed for 2 orders hkl of diffraction.

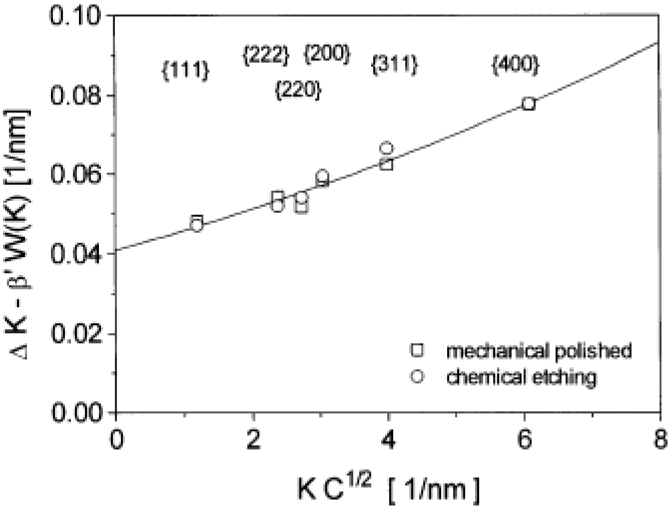

Figure 7-1 : Effect of mechanical polishing compared with chemical etching analyzed by Ungár [59] on the modified Hall-Williamson plot.

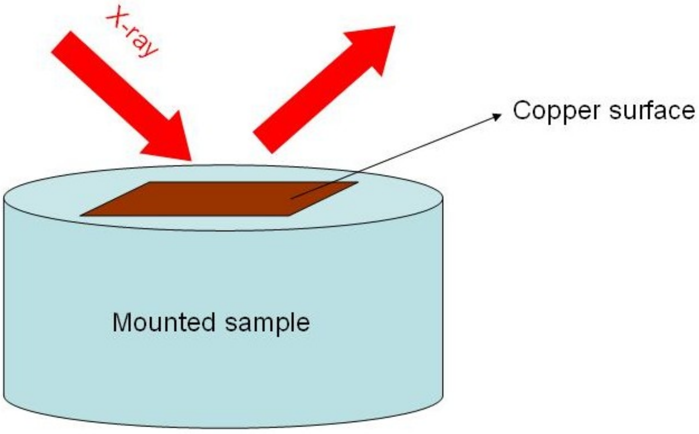

Figure 7-2: Coating samples were mounted and the diffraction was done on the top surface.

Figure 7-2 shows the mounted copper sample. X-ray diffraction was done on the top surface of the sample. The data comes from the last copper particles that have been deposited during spraying.

The coatings chosen for X-ray analysis have been done with the two spray conditions that yield the maximum difference in the particle impact conditions:

- Spray condition 1: A stagnation pressure of P_0 = 30 bars and a stagnation temperature of T_0 = 520°C.
- Spray condition 2: A stagnation pressure of P_0 = 22 bars and a stagnation temperature of T_0 = 320°C.

With these spray condition the DE difference is maximum and the bond strength difference is maximum.

7.3 Methods

7.3.1 Instrumental Broadening Substraction

The X-ray diffraction pattern is the convolution between the “pure” material broadening effect and the instrumental broadening. It is necessary to substract the instrumental broadening to the measured profile [64]. The measured Full Width at Half Maximum (FWHM) is the sum between the “pure” FWHM and the instrumental FWHM.

$$I(2\theta)^{measured} = I(2\theta)^{pure} \times I(2\theta)^{instrumental}$$
$$FWHM^{measured} = FWHM^{pure} + FWHM^{instrumental}$$

The procedure uses a LaB_6 references samples to model the effect of instrumental broadening. The instrumental Full Width at Half Maximum and the shape factor (m) are fitted with a second order polynomial function. This allows the synthesis of instrumental FWHM at any desired angle and the asymmetrical instrumental line profile at any desired angle with a split Pearson VII function.

$$FWHM^2_{instrumental} = a \cdot \tan^2(\theta) + b \cdot \tan(\theta) + c$$
$$m_{instrumental} = d \cdot (2\theta)^2 + e \cdot (2\theta) + f$$

The use of this approach requires only one standard regardless of peak positions and the analyzed specimen. It minimizes the error of standard parameters by averaging over a large number of reflections.

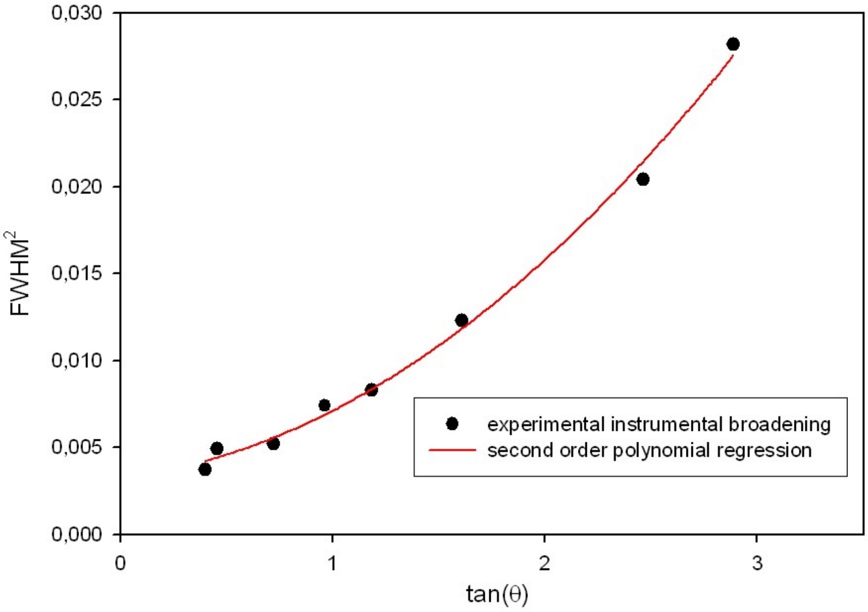

Figure 7-3: Expression of the instrumental FWHM measured on LaB_6.

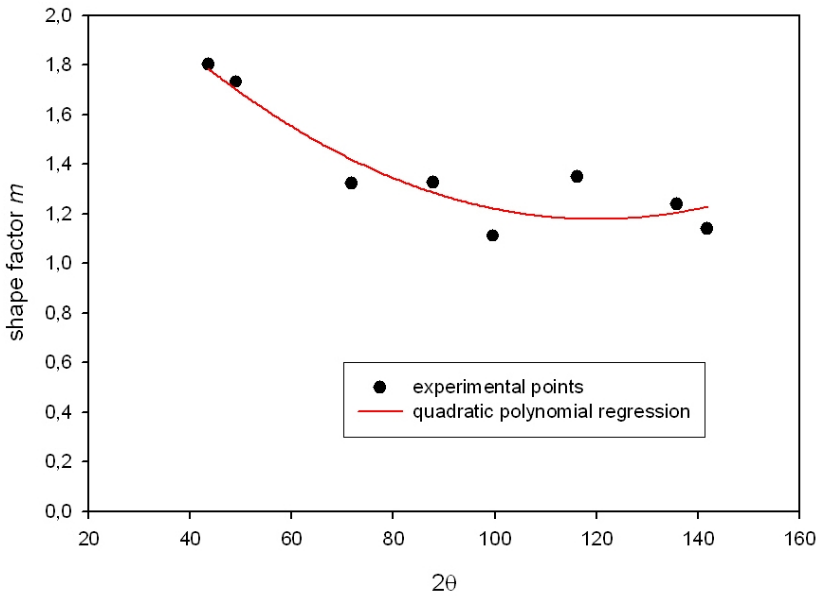

Figure 7-4: Instrumental shape factor measured on LaB_6.

7.3.2 Classical Hall-Williamson

The classical Hall Williamson method (H-W) is described by Calla et al [65]. It gives the value of the crystallite size D and the microstrain.

This model associates the peak broadening in direct space to the contribution of the two terms. The first term is the peak broadening associated with the crystallite size ($\propto 1/\cos\theta$) and the second term is associated with microstrain ($\propto 1/\tan\theta$). To determine the value of microstrain and crystallite size, the value of $FWHM \cdot \cos(\theta)$ has to be plotted as a function of $\sin(\theta)$. The least square linear relation between the experimental points will give the values of $\frac{\Delta d}{d}$ and D.

$$FWHM \cdot \cos(\theta) = -2\frac{\Delta d}{d}\sin(\theta) + \frac{0{,}9 \cdot \lambda}{D}$$

où

d : distance between the diffracting planes

Δd : changes in the distance between the diffracting planes

$\frac{\Delta d}{d}$: microstain in the sense of Hall - Williamson

The results of the fitting procedure are shown on the following figures:

- Figure 7-5 shows the classical Hall-Williamson plot for both powders.
- Figure 7-6 shows the classical Hall-Williamson plot for the coatings sprayed at T_0 = 520°C and P_0 = 30 bars made with both powders.
- Figure 7-7 shows the classical Hall-Williamson plot for the coatings sprayed at T_0 = 320°C and P_0 = 22 bars made with both powders.

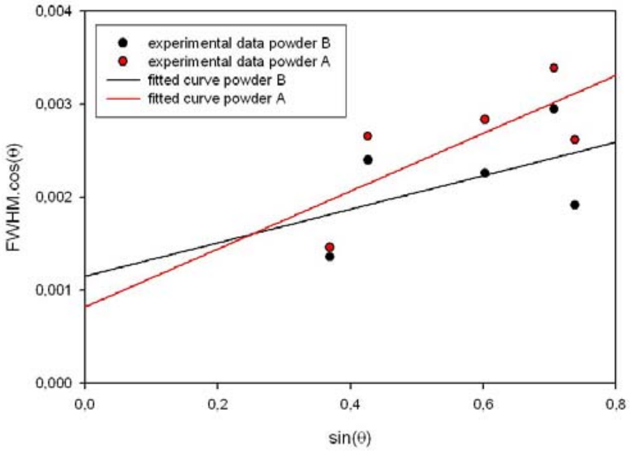

Figure 7-5: Classical Hall-Williamson plot for powder A & B.

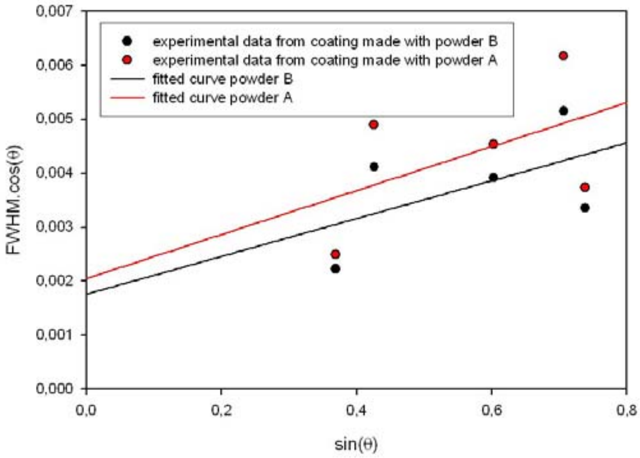

Figure 7-6: Classical Hall-Williamson plot for the coatings made with powder A & B sprayed at 520 °C and 30 bars.

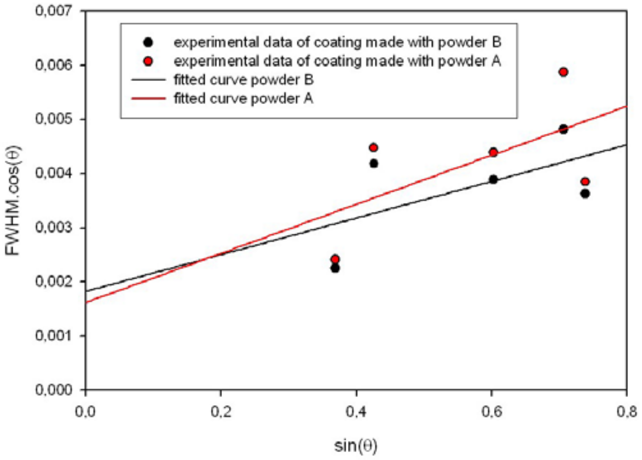

Figure 7-7: Classical Hall-Williamson plot for the coatings made with powder A & B sprayed at 320 °C and 22 bars.

7.3.3 Modified Hall-Williamson

7.3.3.1 Theory

By assuming that the main source of strain in the crystal is associated with dislocations and planar faults, the classical H-W can be improved. The modified Hall-Williamson plot takes into account the effect of strain anisotropy by the introduction of the dislocation contrast factor, C. The contrast factor depends on the relative orientation between Burger vector, line vector, the diffraction vector and the crystal's elastic tensor. If the material shows no texture, the average dislocation contrast factor for FCC metals can be written

$$\overline{C}=\overline{C}_{h00}\cdot\left(1-q\cdot H^{2}\right)$$

where:

$$H^{2}=\frac{h^{2}k^{2}+h^{2}l^{2}+k^{2}l^{2}}{\left(h^{2}+k^{2}+l^{2}\right)^{2}}$$

In the case of copper [60], $\overline{C}_{200}=0.304$ is a calculated value based on an average of edge and screw dislocations with the burger vector $\vec{b}=\frac{a}{2}\langle 110\rangle$ (*a* is the cell length of the FCC copper) on the slip plane $\{111\}$. q depends on the edge or screw character of the dislocations. By comparing the experimental value of q with calculated value, it is possible to establish the dislocation character in the coating. For copper, theory gives a value of q = 1.68 for pure edge dislocations and a value of q = 2.37 for pure screw dislocations. The modified Hall-Williamson (H-W) equation that includes planar faults is:

$$\Delta K-\beta'\cdot W(\vec{g})=\frac{0.9}{D_{H-W}}+A_{1}\cdot\left[\left(K\overline{C}^{1/2}\right)\right]+A_{2}\cdot\left[\left(K\overline{C}^{1/2}\right)\right]^{2}$$

where,

$$\Delta K=\frac{2\cos(\theta)\cdot FWHM}{\lambda},\ K=\frac{2\sin(\theta)}{\lambda}$$

The planar fault density β' includes the effect of twinning and faulting and the $W(\vec{g})$ coefficient are given by Warren in Table 7-1 [66].

Table 7-1: Warren coefficient for the determination of the planar fault density [66].

$\vec{g}\{hkl\}$	$\{111\}\{222\}$	$\{200\}\{400\}$	$\{220\}$	$\{311\}$	$\{313\}$
$W(\vec{g})$	0.43	1	0.71	0.45	0.8

D_{H-W} is the crystallite size in the sense of the H-W method and *A1*, *A2* are fitted constants. The modified Hall-Williamson plot corresponds to the plot of ΔK as a function of $K\overline{C}^{1/2}$

7.3.3.2 Fitting procedure

The fitting procedure is divided in two steps:

- Firstly, the value of q has to be determined. It will give the type of dislocation
- Secondly, the value β' has to be done.

A second order least square fit will allow determining the value of each parameter.

The first equation to solve is the following. This equation has to be fitted to the experimental data for every value of q ranging between 1.68 to 2.37. For each fit, a value of the residue will be obtained. When the residue is minimum, the corresponding real value of q will give the nature of the dislocation type.

$$\Delta K = \frac{0.9}{D_{H-W}} + A_1 \cdot \left[\left(K\overline{C}^{1/2}\right)\right] + A_2 \cdot \left[\left(K\overline{C}^{1/2}\right)\right]^2$$

where

$$\overline{C} = \overline{C}_{hoo}\left(1 - qH^2\right)$$

The second step corresponds to the determination of the planar fault density.

$$\Delta K - \beta' \cdot W(g) = \frac{0.9}{D_{H-W}} + A_1 \cdot \left[\left(K\overline{C}^{1/2}\right)\right] + A_2 \cdot \left[\left(K\overline{C}^{1/2}\right)\right]^2$$

This equation has to be refitted on the experimental data (using the final value of q) for several value of β'. For each fit a corresponding residue will be determined. When the residue is minimum, the final value of β' is reached.

The results of the fitting procedure are show on the following figures:

- Figure 7-8 shows the modified Hall-Williamson plot for both powders.
- Figure 7-9 shows the modified Hall-Williamson plot for the coatings sprayed at T_0 = 520°C and P_0 = 30 bars made with both powders.
- Figure 7-10 shows the modified Hall-Williamson plot for the coatings sprayed at T_0 = 320°C and P_0 = 22 bars made with both powders.

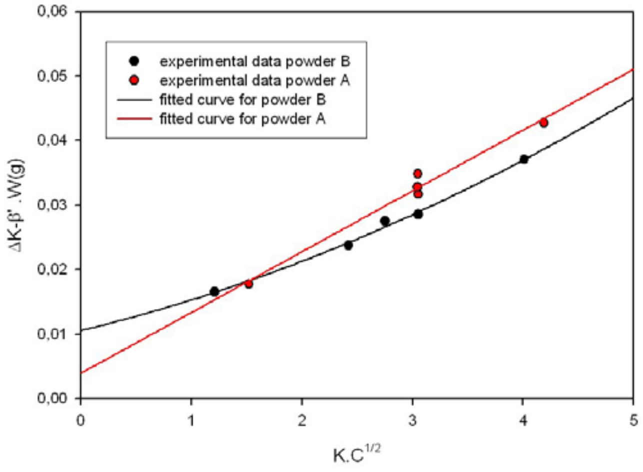

Figure 7-8: Modified Hall-Williamson plot for powder A & B.

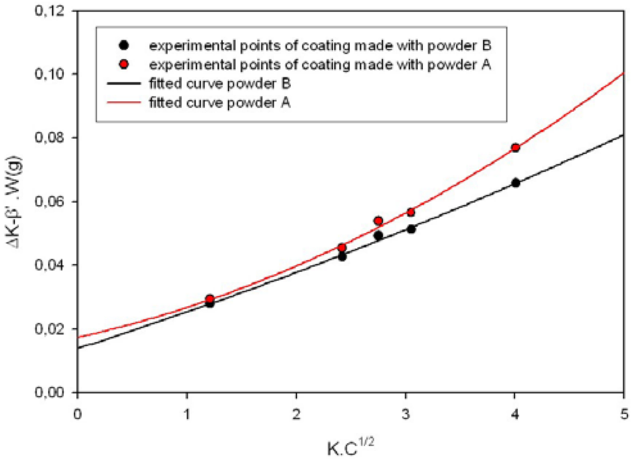

Figure 7-9: Modified Hall-Williamson plot for the coatings made with powder A & B sprayed at 520 °C and 30 bars.

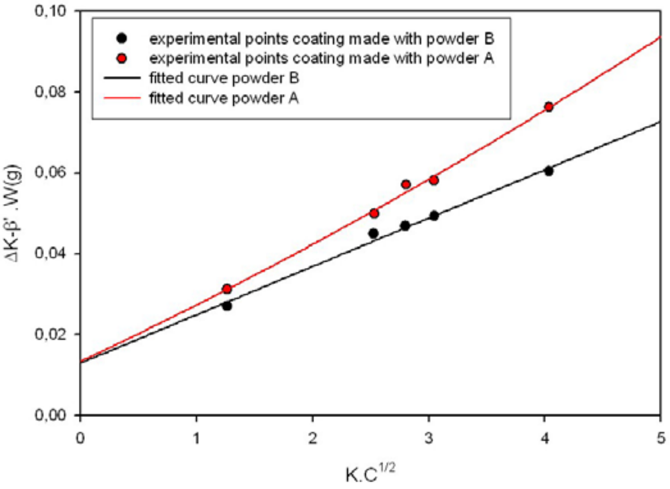

Figure 7-10: Modified Hall-Williamson plot for the coatings made with powder A & B sprayed at 320 °C and 22 bars.

7.3.4 The Modified Warren-Averbach Method

7.3.4.1 Theory

The Warren-Averbach (W-A) method allows a peak analysis without any hypothesis on the shape of the peak. This method is based on the analysis of the real part of the Fourier coefficient analysis $A(n)$. The basic approach is to dissociate the contribution of size and distortion on the Fourier coefficient,

$$\ln(A(n)) = \ln\left(A^S(n)\right) + \ln\left(A^D(n)\right)$$

where $A^S(n)$ and $A^D(n)$ are respectively the size and distortion contribution to the real part of the Fourier coefficient.

The modified W-A equation that takes into account planar fault is:

$$\ln(A(L)) + L\beta' W(g) \cong -\frac{L}{D_{W-A}} - \rho^* B L^2 \ln\left(\frac{R_e}{L}\right)\left(K^2\overline{C}\right) + Q^* B^2 L^4 \ln\left(\frac{R_1}{L}\right)\ln\left(\frac{R_2}{L}\right)\left(K^2\overline{C}\right)^2$$

where D_{W-A} is the crystallite size in the sense of the W-A method, $\rho*$ is the “formal” dislocation density, *Re* is the outer cut off radius, $L = n \cdot a_3$ is the Fourier variable and B is linked to the burger vector of the slip system [66]. $a_3 = \lambda / [2(\sin(\theta_2) - \sin(\theta_1))]$ where λ is the wavelength of the diffraction and θ_1 - θ_2 is the angular range of the measured diffraction profile. Second order terms in the W-A equation are Q^* , R_1 and R_2 . The constants R_1 and R_2 have no physical meaning. The modified W-A plot corresponds to the plot of ln(A(L)) as a function of $K^2\overline{C}$.

7.3.4.2 Interpretation of the outer cut-off radius *Re*

Wilkens introduced the restricted random distribution characterized by the dislocation density and the cut-off radius *Re*. The cut-off radius gives the radius of the region within which the distribution is random. It is a measure of the correlation in the dislocation distribution [67]. When the dislocations are organized as cell structures, the correlation of the dislocation organisation is low. This corresponds to a low value of *Re*.

7.3.4.3 Interpretation of the Factor Q^*

$Q^* = \left\langle \rho^{*2} \right\rangle - \left\langle \rho^* \right\rangle^2$ is the fluctuation square of dislocation density where the brackets denote average values. When the microstructure is made of cells rich in dislocations and interiors with a lower dislocation density, the value of Q^* gives a measure of the variation of dislocations density between the cell wall and the cell interior [68].

7.3.4.4 Fitting Procedure

The substraction of the instrumental broadening effect is done by a procedure called the "Stokes method". This method allows building the Fourier coefficient of a "pure" signal based on the knowledge of the Fourier coefficient from the experimental peak $I_{Fourier}^{\text{experimental}}$ and the Fourier coefficient of the instrumental broadening effect $I_{Fourier}^{\text{instrumental}}$. The instrumental broadening peak has to be built based on the knowledge of the instrumental broadening FWHM and shape factor obtained in section 7.3.1. The first hypothesis is that the instrumental broadening peak has the shape of a split Pearson VII function:

$$f^{PearsonVII}(x) = I_0 \cdot \left(1 + \frac{x^2}{m \cdot \left(\beta \cdot \frac{\Gamma(m)}{\left[(m \cdot \pi)^{1/2} \cdot \Gamma\left(m - 1/2\right) \right]} \right)^2} \right)^{-m}$$

$$\begin{aligned} &où \\ &1 \le m \le \infty \\ &\Gamma : \text{gamma function} \\ &\beta : \text{integral breath of the peak} \end{aligned}$$

Once the instrumental peak is obtained, the values of the corresponding Fourier coefficient is computed, $I_{Fourier}^{\text{instrumental}}$. The real part of the pure signal *A(n)* and the imaginary part *B(n)* of the pure signal are obtained by the stokes method:

$$A(n) = \frac{\mathrm{Re}\,al\left(I_{Fourier}^{experimental}\right) \cdot \mathrm{Re}\,al\left(I_{Fourier}^{instrumental}\right) + \mathrm{Im}\left(I_{Fourier}^{experimental}\right) \cdot \mathrm{Im}\left(I_{Fourier}^{instrumental}\right)}{\left(\mathrm{Re}\,al\left(I_{Fourier}^{instrumental}\right)\right)^2 + \left(\mathrm{Im}\left(I_{Fourier}^{instrumental}\right)\right)^2}$$

$$B(n) = \frac{\mathrm{Im}\left(I_{Fourier}^{experimental}\right) \cdot \mathrm{Re}\,al\left(I_{Fourier}^{instrumental}\right) - \mathrm{Re}\,al\left(I_{Fourier}^{experimental}\right) \cdot \mathrm{Im}\left(I_{Fourier}^{instrumental}\right)}{\left(\mathrm{Re}\,al\left(I_{Fourier}^{instrumental}\right)\right)^2 + \left(\mathrm{Im}\left(I_{Fourier}^{instrumental}\right)\right)^2}$$

7.3.4.4.1 Computation of the Dislocation Density ρ and Re*

The computation of the dislocation density and Re is done with the coefficient of the first term in $K\overline{C}^2$ of the Warren-Averbach equation. Lets note $X(L) = -\rho^* \cdot B \cdot L^2 \cdot \ln\left(\frac{\mathrm{Re}}{L}\right)$ as the coefficient of this first term and we can use the experimental data to plot the graph of $X(L) / L^2$ as a function of $\ln(L)$.

With a linear least square regression, the following equation can be fitted:

$$\frac{X(L)}{L^2} = -\rho^* \cdot B \cdot \ln(\mathrm{Re}) + \rho^* \cdot B \cdot \ln(L)$$

The slope of the linear relation is the formal dislocation density ρ^* whereas the independent term is related to the cut-off radius *Re*.

7.3.4.4.2 Computation of Q*

The computation of the fluctuation of the dislocation density is done from the second order term in $K\overline{C}^2$ of the Warren-Averbach modified equation. Lets write $Y(L) = Q^* \cdot B^2 \cdot L^4 \cdot \ln\left(\frac{R_1}{L}\right) \cdot \ln\left(\frac{R_2}{L}\right)$ and use the experimental data to plot the function $Y(L)/L^4$ as a function of $\ln(L)$.

With a least square fit, the experimental data is fitted to the second order equation:

$$\frac{Y(L)}{L^4} = Q^* \cdot B^2 \cdot L^4 \cdot \left(\ln(R_1) \cdot \ln(R_2) - \ln(R_1 + R_2) \cdot \ln(L) + \ln^2(L)\right).$$

The coefficient in front of $\ln^2(L)$ gives the value of Q^*.

The final results after all the fitting procedures are shown on the following figures called the modified Warren-Averbach plot:

- Figure 7-11 & Figure 7-12 show the modified Warren-Averbach plot for both powders.
- Figure 7-13 & Figure 7-14 shows the modified Warren-Averbach plot for the coatings sprayed at T_0 = 520°C and P_0 = 30 bars made with both powders.
- Figure 7-15 & Figure 7-16 shows the modified Warren-Averbach plot for the coatings sprayed at T_0 = 320°C and P_0 = 22 bars made with both powders.

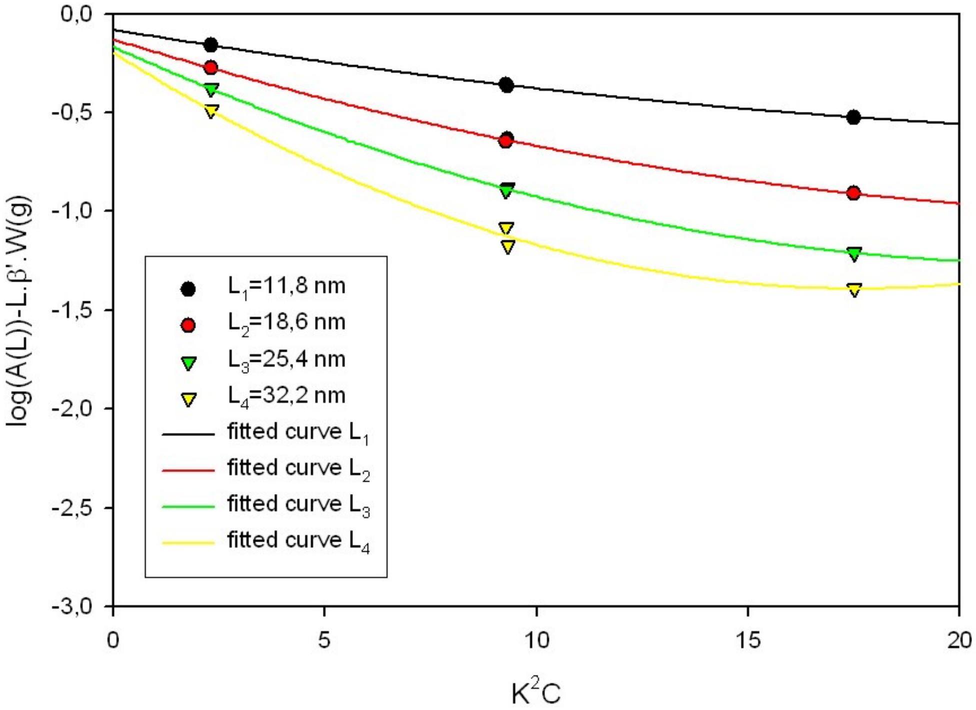

Figure 7-11: Modified Warren-Averbach plot for powder A.

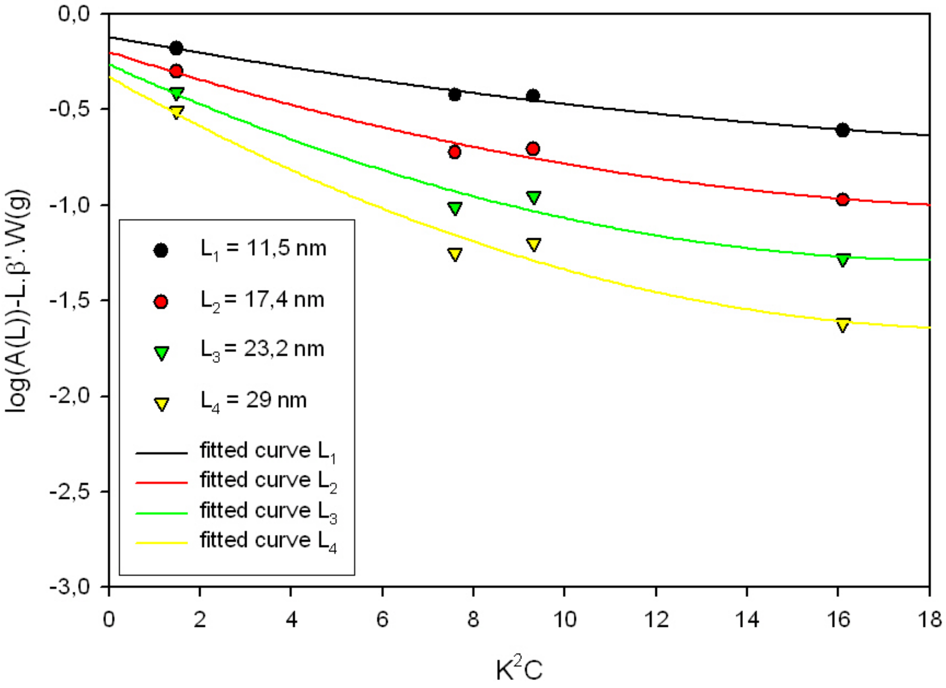

Figure 7-12: Modified Warren-Averbach plot for powder B.

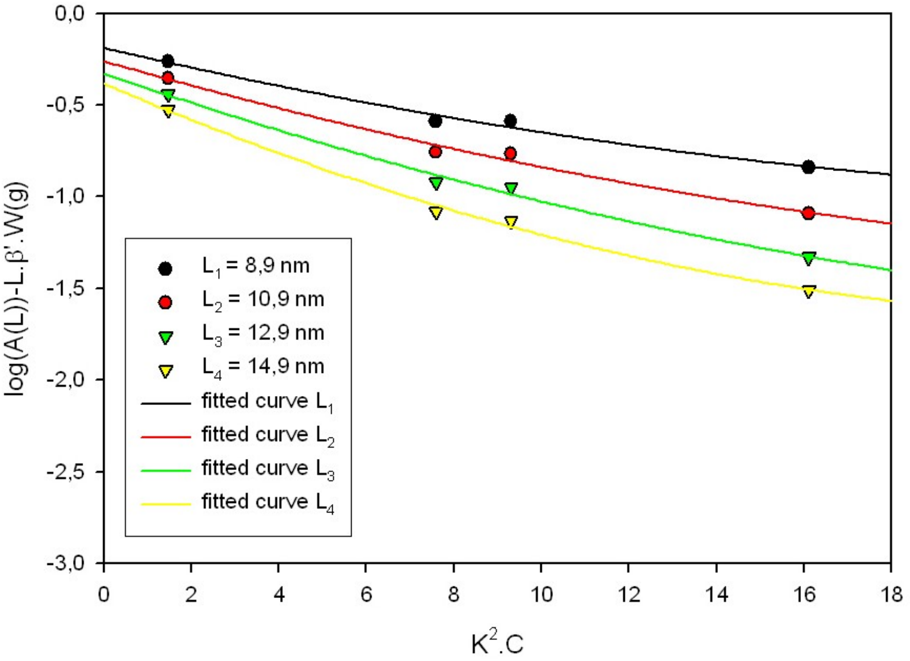

Figure 7-13: Modified Warren-Averbach plot for the coating made with powder A sprayed at 520°C and 30 bars.

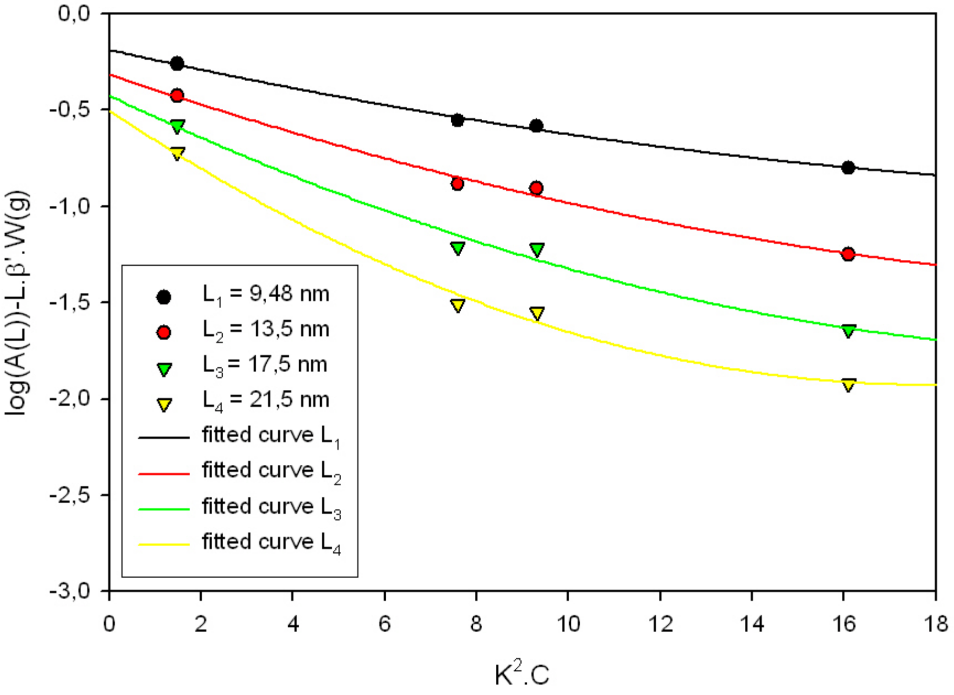

Figure 7-14: Modified Warren-Averbach plot for the coating made with powder B sprayed at 520°C and 30 bars.

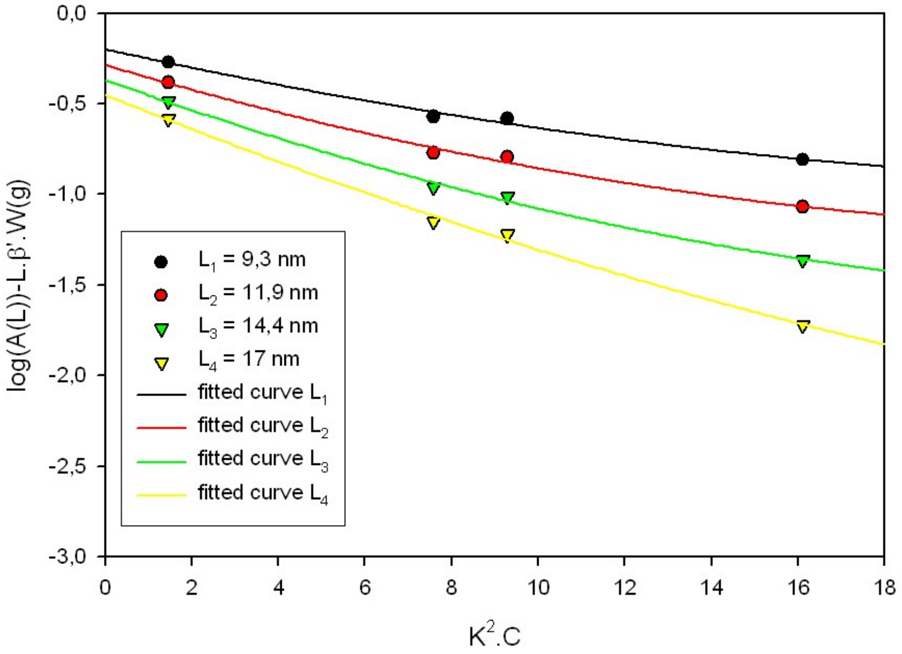

Figure 7-15: Modified Warren-Averbach plot for the coating made with powder A sprayed at 320°C and 22 bars.

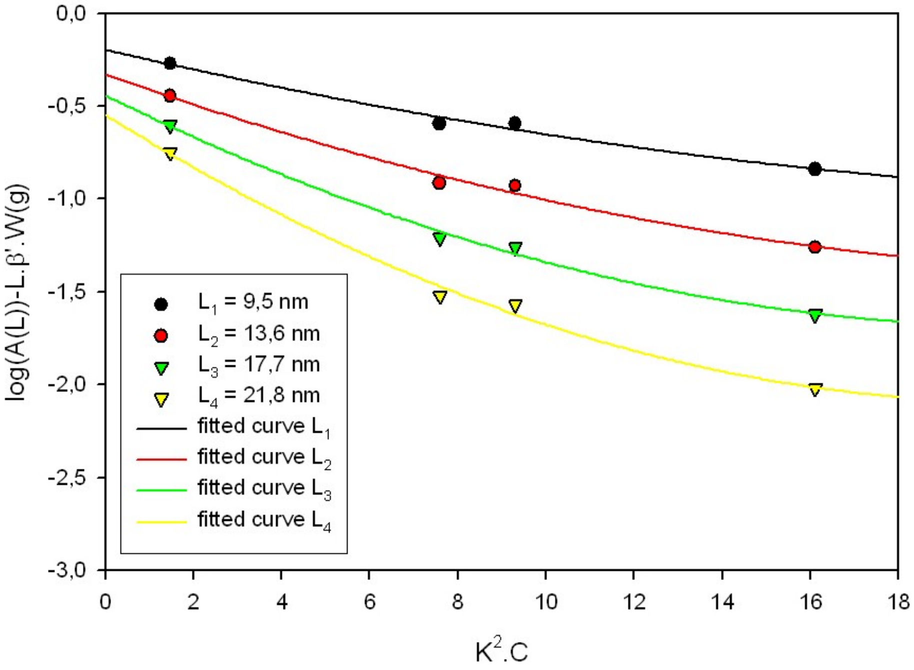

Figure 7-16: Modified Warren-Averbach plot for the coating made with powder B sprayed at 320°C and 22 bars.

7.3.5 Limitations of the Methods

The classical Hall-Williamson Method does not take into account the effect of strain anisotropy. Points in the Hall-Williamson plot are scattered around the fitted line. It makes it difficult to interpret physically the data (Figure 7-5, Figure 7-6, Figure 7-7).

The introduction of the contrast factor allowed modifying the Hall-Williamson plot to improve the fitting procedure (Figure 7-8, Figure 7-9, Figure 7-10).

The W-A method is more precise than the H-W method, it used the whole peak to get information. The peak broadening analysis of the real part of the Fourier coefficient gives information on the crystallite size, the dislocation density ρ^*, the outer cut off radius and the higher order terms give information on dislocations organisation. The imaginary part of the Fourier coefficient is associated with the polarisation of the dislocation structure. The accuracy of the peak measurement limited the use of more than 4 peaks for the W-A analysis and prevented the interpretation of high order terms in the analysis. Second order terms were included in the calculation as support terms but not interpreted. This approach has also been taken by Chen et al [69] for the analysis of laser shocked copper single crystals.

7.4 Results

7.4.1 Powder Analysis

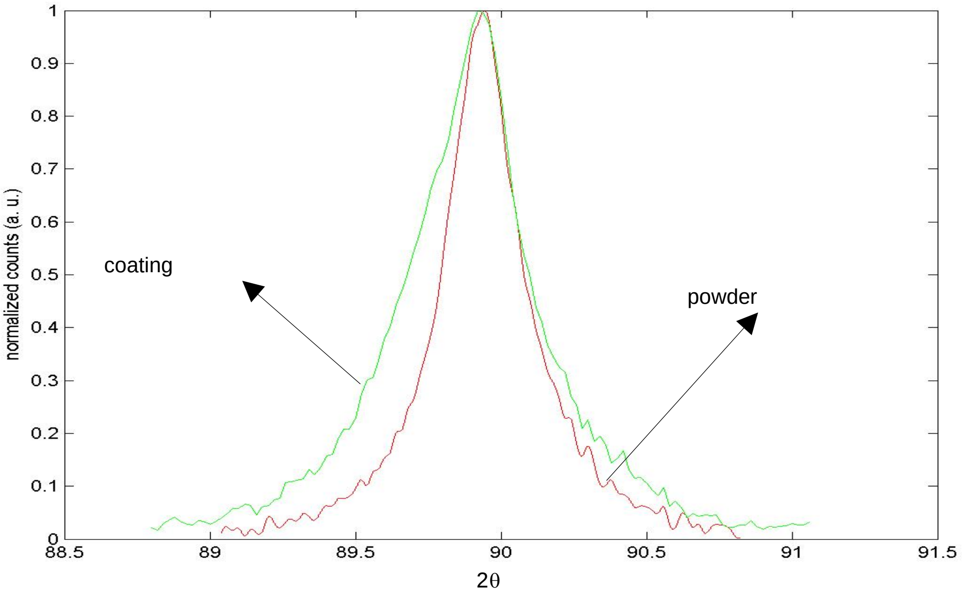

Figure 7-17 : Superposed peaks of the powder B and coating sprayed with spray condition 2—peak order 311.

The data in Table 7-2 compiles the results from the classical and modified H-W and the W-A method. Both powders have a similar dislocation density but the crystallite size is on the whole bigger in powder A than in powder B.

Table 7-2: X-ray diffraction results on the copper powders A and B.

	powder A	**powder B**
H-W classical		
Diameter (nm) D	168	120
Microstrain (%)	0.1	0.15
H-W modified		
Diameter (nm) $D_{H\text{-}W}$	223	85
Density SFE & twin: β'(%)	0.269	0.25
q	2.01	2.37
W-A modified		
Diameter (nm) $D_{W\text{-}A}$	105	97.11
Formal dislocation density (m^{-2}) ρ*	1.37*10^{15}	1.71*10^{15}
Radius Re (nm)	67.6	73
Density SFE & twin: β'(%)	0.5	0

7.4.2 Coating Analysis

Both coatings have also been analysed with x-ray diffraction. Results listed in Table 7-3 correspond to a stagnation gas pressure of 30 bars and a stagnation temperature of 520°C. In Table 7-4 are listed the properties of copper coatings sprayed with a stagnation gas pressure of 22 bars and a stagnation temperature of 320°C.

Table 7-3: X-ray diffraction results on the copper coating made with both powders sprayed at 520 °C and 30 bars.

	Coating with powder A	**Coating with powder B**
H-W classical		
Diameter (nm) D	67	78
Microstrain (%)	0.2	0.17
H-W modified		
Diameter (nm) $D_{H\text{-}W}$	51.7	64.3
Density SFE & twin:β' (%)	0.7	0.21
q	2.37	2.37
W-A modified		
Diameter (nm) $D_{W\text{-}A}$	57.3	53
Formal Dislocation density (m^{-2}) ρ^*	$4.43*10^{15}$	$3*10^{15}$
Radius Re (nm)	40	61.6
Density SFE & twin: β' (%)	0	0

Table 7-4: X-ray diffraction results on the copper coating made with both powders sprayed at 320 °C and 22 bars.

	Coating with powder A	**Coating with powder B**
H-W classical		
Diameter (nm) D	85.4	75.8
Microstrain (%)	0.22	0.17
H-W modified		
Diameter (nm) $D_{H\text{-}W}$	66	68
Density SFE & twin:β' (%)	0	0.49
q	2.37	2.37
W-A modified		
Diameter (nm) $D_{W\text{-}A}$	56.56	52.31
Formal Dislocation density (m^{-2}) ρ^*	$4.4*10^{15}$	$3.47*10^{15}$
Radius Re (nm)	36	51
Density SFE & twin:β' (%)	0	0

7.5 Discussion

X-ray diffraction will give an average view on the microstructural changes in a large volume of materials. The highly localized deformation contribution to the peak broadening at the interface between powder particles cannot be clearly distinguished from the global deformation of the powder grain. A large part of the contribution to peak broadening will come from the nanostructure present in shear bands formed during dynamic recovery. A description of the microstructure in shear bands is done in section 2.6.1. The dislocations and microstructure in the particle but not only in the shear bands will also contribute to peak broadening. This means that the data, given in previous tables, shows an average change in the microstructure during the coating formation.

The dislocations densities measured by the Warren-Averbach method in this study range from 1.3 to 4.7 10^{15} m^{-2}. Borcher et al has reported a dislocation density of $10^{16}m^{-2}$ inside the shear bands by TEM investigations. X-ray gives a broader picture of the microstructure hence the dislocation density value is lower than the value obtained by TEM. Chen et al [69] have used the Warren-Averbach to characterize the dislocation density of a laser shocked copper single crystals. In this case, the dislocation density measured ranges from 0.5 to 1.5 10^{15} m^{-2}. M. A. Shehadeh et al [34] have modelled the effect of a laser shock on the microstructure of a copper single crystal and dislocation densities are in the range 10^{15} to 10^{16} m^{-2}.

7.5.1 Powder Comparison

Each method used to characterize the copper powders has shown that powder A has a larger crystallite size than powder B (Table 7-2). The formal value of the dislocation densities is lower for powder A than powder B. The value of the crystallite size is important to determine the mechanical properties of coatings. A material with a large crystallite size will have a higher elastic limit than a powder with a fine nanostructure. Both powders are gas atomized (section 5.2.4). The raw material is melted and than atomized in a controlled atmosphere. This process involves very high quench rates. Small differences in the quench rate at the producer’s site may explain the results. Planar faults seem to be present in more important quantities in powder A. The difference in quench rate between both powders is the most significant factor that leads to these differences even if it was not visible on the optical micrographs. The size distribution of powder A being finer than powder B, it has a high sensitivity to spray conditions. It is likely that powder A will deform more than powder B on impact.

The value of q for powder A is 2.01. Therefore, powder A has about 50% of edge and screw dislocations where powder B has essentially screw dislocations.

7.5.2 Influence of the Powder on the Dislocation Arrangement

Copper coatings show a decrease in the crystallite size compared with the powder. As it was expected, dislocations have multiplied during deformation and a small scale cell structure has formed. The CGDS have strain hardened the coating compared with the initial powder.

Copper is a material with a relatively low staking fault energy compared to other FCC material like Ni and Al. Therefore, the coating microstructure is non uniform. Powder A with the smallest initial powder size distribution underwent the most significant grain refinement. The initial low dislocation of powder A density has allowed extensive dislocation multiplication in the coating. Powder B is initially rich in dislocation jogs and boundaries that are obstacles to dislocation movements compared with powder A. All coatings contain essentially screw dislocations since the value of $q=2.37$.

The exclusive presence of screw type dislocations is explained by the multiplication mechanism of dislocation during coating build up. First, work by M. A. Shehadeh et al [34] has used dislocation dynamics to simulate shock loading in copper. They have shown that the use of Frank-Read dislocations loops as a generation source of dislocations leads to the formation of band like dislocation cell walls that coincide with the slip plane. This mechanism is associated with the double cross slip of screw dislocations in the material. This explains the presence of essentially a majority of screw dislocations in the coating. They have the ability to cross slip (see section 2.10).

Secondly, the presence of dislocations loops has been detected by Borcher et al [70] and they could explain the source for screw dislocations. These loops have formed during the bonding of a particle and after another particle hit this particle and generate new screw dislocations in the coating.

On the other hand, the contribution of the defect type to broadening is based on the decay of strain field around the defect. This allows a classification of the defect contribution. It is not possible to distinguish the contribution of these loops to the broadening. As explained by Kuzel et al [67], the high screening by the dislocations in the coating modifies the displacement fields of some defects. Dislocation loops have not been clearly identified by this method. They still play a crucial role in dislocation organisation during deformation.

7.5.3 Influence of the Powder on the Coating Dislocation Density

The main differences between the coatings are the dislocations density and the value of *Re*. The spray conditions do not seem to have any influence on the crystallite size. Powder with an initially low dislocation density gives a coating with a very high dislocation density and a small radius *Re*. The physical meaning of *Re* is more complex. Its meaning is related to the restricted random distribution of dislocation introduced by Wilkens and is linked to the length scale within which the distribution is random [67]. This parameter can be taken as a measure of correlation in dislocation distribution. This small value of *Re* implies a high correlation between dislocations in the cell walls in the shear bands. As shown in section 2.6.1, the deformation mechanism of the shear bands in dynamic recovery is described by the formation of cell structures by rearrangements of dislocations. When the cell structure is strong, correlation in the dislocation organisation will be high and the value of *Re* will be low.

For powder A, the length to which dislocations are distributed randomly is small. The initial low elastic limit of powder A allowed the dislocations to reorganize on a larger scale. With powder A, it is likely that more dislocations are organised in the cell walls than in the case of powder B which is rich in obstacles to dislocation motion.The change in the dipole character of dislocations in the coating made with powder A that become more significative [68].

Since powder B is also coarser than powder A, it will have a smaller impact velocity (powder velocities measured in section 3.8.3). This powder will not deform as largely as powder A and dislocations will not have sufficient energy to integrate the cell walls in the shear bands and they will be distributed more uniformly in the coating. The difference in dislocation density ρ^* is also a consequence of the powders initial microstructure. Powder B with more obstacles to dislocation motion and multiplication will keep a lower dislocation density in the coating.

This explains the higher values observed for *Re* and lower dislocation density ρ^* in the case of powder B.

7.5.4 Influence on the Mechanical Properties

The crystallite size of powder A is smaller than powder B, adiabatic shear bands have formed more extensively and grain refinement was more important. Due to the non-uniform microstructure, grain refinement has occurred in the shear bands while the centre of the particle has deformed less. When the nanoindetation tip penetrates the copper close to the centre of a powder particle, it will indent a softer material. This explains the difference in nanohardness observed in the coating (Figure 6-8). The coating sprayed with powder A has a lower nanohardness than the one sprayed with powder B.

The X-ray data shows also that the crystallite size between spray conditions 1 and 2 (see section 7.2) is not very different. This implies that spray conditions have not influenced significantly the formation of the shear bands, in both cases. This can be explained by two effects:

- In both case, the powder particles in the coating have bonded with a minimum impact velocity. They will deform with a high impact velocity.
- The dislocation multiplication mechanism in the coating.

This last point is related to the FCC structure of copper and its value of stalking fault. The FCC structure has a large number of sliding planes that allow a good deformability because of the large number of slip systems. Copper has good deformability and a relatively low melting temperature. The critical resolved shear stress is the minimum value of stress needed to make a dislocation move. Its value is determined by athermal obstacles (elastic interactions, strong pinning sites). In order to liberate themselves from these obstacles, they do need to cross slip. The activation of cross slip is also an athermal process. Because the decomposition into partial dislocations, the cross slip cannot be activated by the thermal vibration of the lattice. When the stacking fault energy decreases, the decomposition into partial dislocations is easy. During impact, the partial dislocations in copper have to recompose a dislocation to be able to cross slip. This could explain why the final dislocation density in the coating is so sensitive to the initial powder microtsructure. Powder B with a higher dislocation density than powder A will exhibit a lot more obstacles to deformation and its behaviour will be different. This also explains the relative insensitivity of the dislocation density with the spray conditions shown in Table 7-3 and Table 7-4.

This fact is coherent with the nanohardness profiles (Figure 6-8) that do not show influence from the spray conditions.

7.6 Conclusion

- The microstructural features of the copper coatings are mainly determined by the powder original microstructure. The powder grains that have reached the critical velocity undergo the formation of adiabatic shear bands and bond on the surface. The grain refinement in the coating is mainly determined by material state of the initial powder.
- Spray conditions do not seem to influence the crystallite size in the coating. The grain size distribution will influence the impact speed of the powder. This may explain to some extent the difference in dislocation density between powders. Higher deformation upon impact has induced more dislocation multiplication.

Chapter 8 Auger Electron Spectroscopy Interface Analysis of cold sprayed coating on Al and TA6V substrates

8.1 Introduction

The bonding between a copper particle and a surface has been associated with the onset of adiabatic shear bands at the interface between the particle and the substrate. The nature of bonding can be of several kinds:

- Chemical
- Vanderwaals type
- Diffusion type
- Mechanical

As described in section 2.7, it is likely that several mechanisms are involved but, to this day, it is difficult to identify a general rule that correlates the type of bonding in the cold spray process with the material properties. Barradas et al [24] have observed the presence of intermetallics at the interface on a distance of 200-400nm.

This section will attempt to detect such a zone by using auger spectroscopy. It will also be attempted to show the influence of the spray conditions and the powder choice on this diffusion zone. These results will be correlated to TEM observations. One TEM thin lamella has been analyzed for copper on Al but it was not possible to obtain a lamella for copper on TA6V. The Auger results will be described by a plausible mechanism involving diffusion under shock loading conditions.

8.2 Auger Spectroscopy

8.2.1 Theory

Auger spectroscopy is based on the analysis of electrons emitted by complex rearrangements in atoms. Auger electron emission is stimulated by bombarding the sample, with an electron beam. The incident particle removes the first electron from a core level of an atom to produce a vacancy. A second electron falls from a higher level into the vacancy with release of energy. The resulting energy is carried out with the Auger electron which is ejected from a higher energy level. Auger electron emission is one of the two relaxation mechanisms possible in an excited ion.

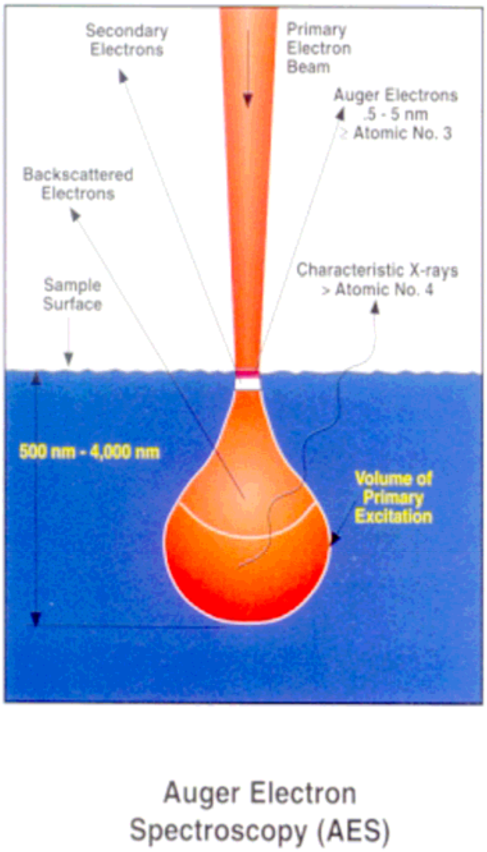

Figure 8-1: when an electron beam hits a surface, it has several types of electron emitted from the surface.

Auger electrons are emitted from a depth ranging from 0.5 to 5 nm. When combined with an ion gun, it is possible to sputter layers and get an in depth composition analysis.

8.2.2 Equipment - Experimental set up

The equipment comes from the PHI Company (Physical Electronics) and is of type SAM (Scanning Auger Microscope) 650. Therefore a PHI SAM 650 has a LaB_6 source and a CMA analyser (Cylindrical Mirror Analyser). An Ar ion gun was used to sputter the surface (2x2mm area).

The cold spray coatings have an irregular interface with high roughness and are very thick. It is not suitable to sputter the coating using the ion gun because of this. Samples were mounted, and a cross section of the sample was polished. Auger profiles analyses were done perpendicularly to the interface between the substrate and the coating. By doing so, the lateral resolution of the electron beam was used to get a composition analysis.

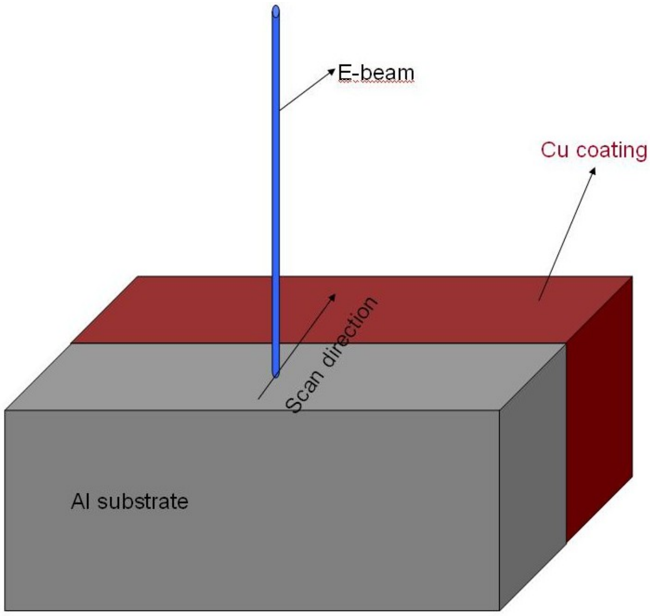

Figure 8-2: Schematic of the scan direction done with the electron beam.

The low depth resolution of this techniques means that the surface needs to be cleaned from the oxidation on contact with oxygen and air contaminants. The analysis is done under high vacuum. Sputtering Ar ions are used to clean and remove the oxide layer on the surface.

Before analysis:

- The surface of the samples was sputtered for 15 min with ion guns at 15 keV
- During analysis, a light sputtering was maintained to avoid the oxygen deposition on the surface.
- The bias voltage for the electron beam was 30 keV and the spot size was 300-400nm wide. This allowed good signal intensity for detection.

Samples analysed were sprayed with the two spray conditions that yield the highest difference in impact conditions:

- Spray condition 1: Stagnation temperature T_0 = 520°C and stagnation pressure P_0 =30 bars.
- Spray condition 2: Stagnation temperature T_0 = 320°C and stagnation pressure P_0 =22 bars.

Profiles were done on Al substrate and TA6V substrates. On the TA6V substrate, only de Ti element was detected.

Profiles will present the atomic concentration of the element analysed along a scan line perpendicular to the interface. The method gives semi quantitative results. Concentration values should be interpreted with caution. It is possible to calibrate the signal with a reference sample and to get good quantification of the elements present but this was not done in this study.

8.3 Example of a Diffusion Zone on Al Substrate

Figure 8-3 shows a selected zone at the interface between the Cu coating made with powder B and the Al substrate sprayed at T_0=520°C and P_0=30 bars. The red line is the scan line where the Cu and Al elements are monitored. Figure 8-4 shows the evolution of the atomic concentration of Al and Cu along the scan line.

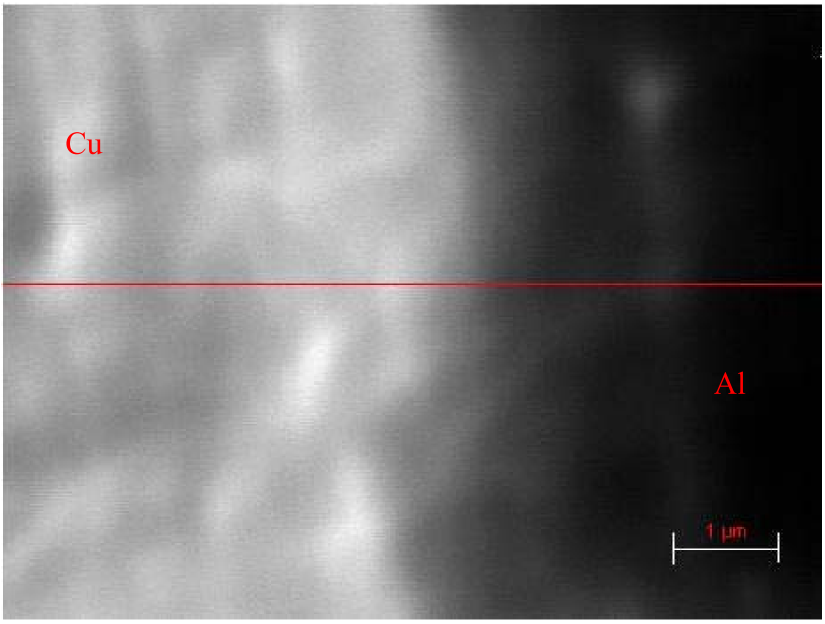

Figure 8-3: SEM of the interface between Cu and the Al substrate where the scan line is in red.

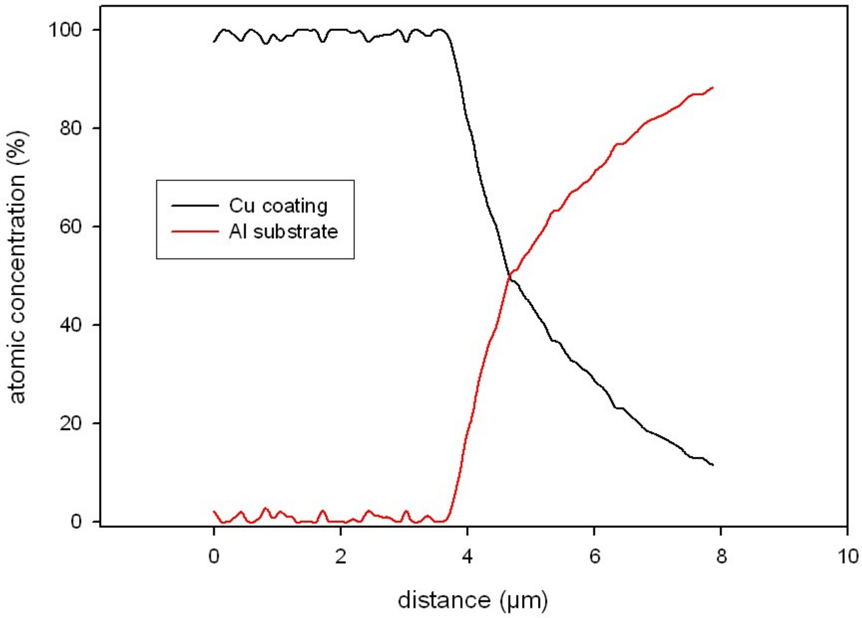

Figure 8-4: Scan along the red line on Figure 8-3.

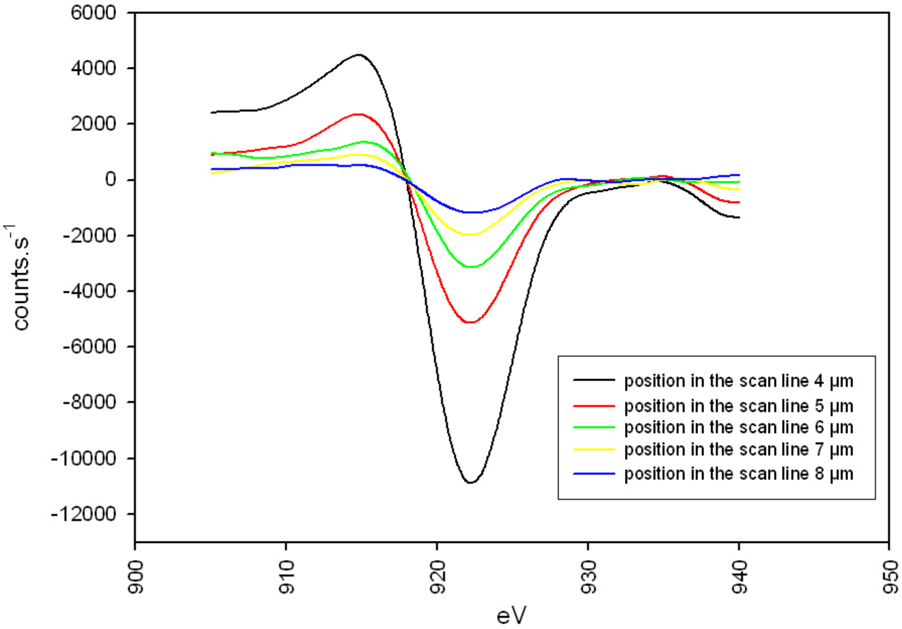

Figure 8-5: Cu spectrum along the scan line at position 4µm-5µm-6µm-7µm-8µm on Figure 8-4.

The SEM picture of the analysed zone shows that the interface has a low roughness and an electron beam will scan perpendicularly the interface. Figure 8-5 shows 5 Cu spectrums along the line scan of Figure 8-4. It shows the presence of a Cu signal 3µm from the interface.

8.4 Results on Al Substrate

8.4.1 Influence of the Spray Condition on the Interface of the Coating Made with Powder A

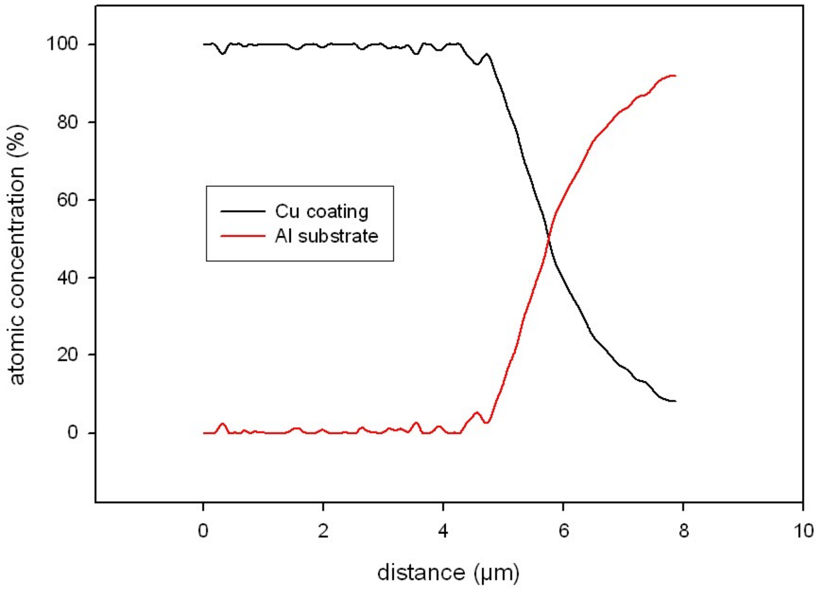

Figure 8-6: Coating made with powder A sprayed at 520°C and 30 bars.

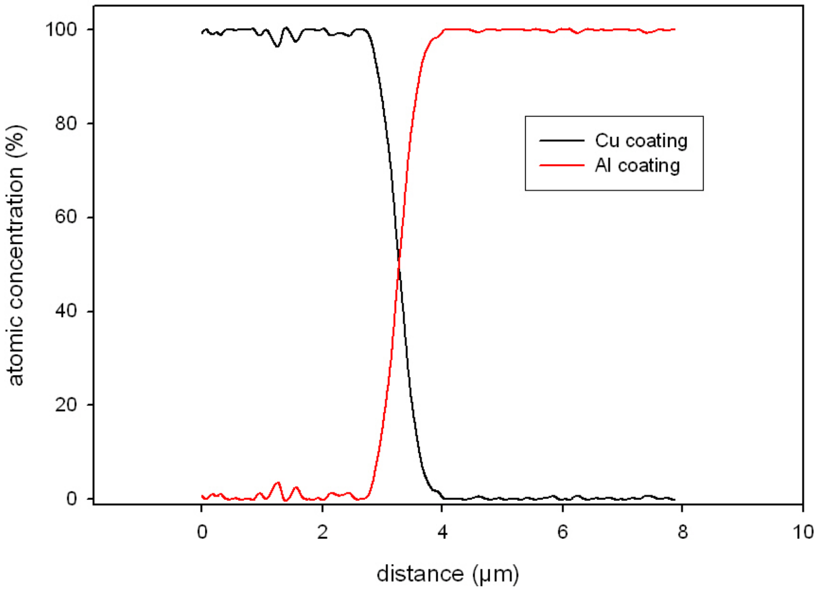

Figure 8-7: Coating made with powder A sprayed at 320°C and 22 bars.

Figure 8-6 and Figure 8-7 show an Auger analysis of the interface of the coating made with powder A sprayed respectively with the spray condition 1 and spray condition 2. The spray conditions have an influence on the formation of diffusion zone at the interface.

8.4.2 Influence of the Spray Condition on the Interface of the Coating Made with Powder B

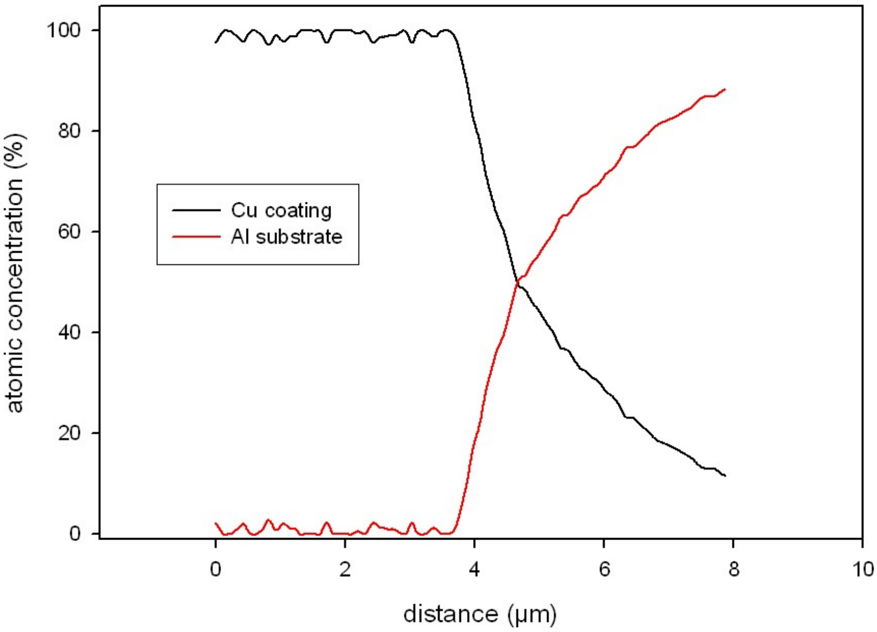

Figure 8-8: Coating made with powder B sprayed at 520°C and 30 bars.

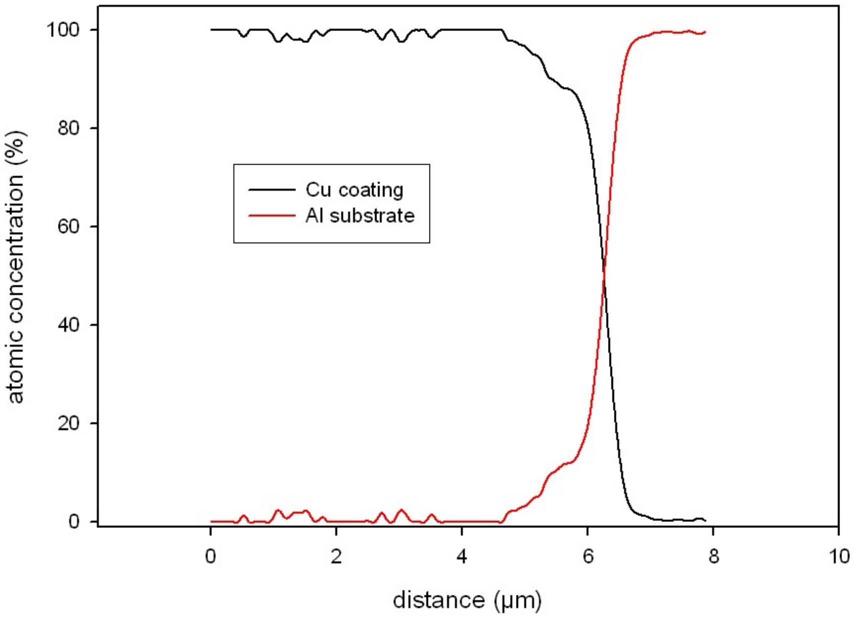

Figure 8-9: Coating made with powder B sprayed at 320°C and 22 bars.

Figure 8-8 and Figure 8-9 show an Auger analysis of the interface of the coating made with powder B sprayed respectively with the spray condition 1 and spray condition 2. The spray conditions have an influence on the formation of diffusion zone at the interface.

8.5 Example of a Diffusion Zone on the TA6V Substrate

Figure 8-10 shows a selected zone at the interface between the Cu coating made with powder B and the TA6V substrate sprayed at T_0=520°C and P_0=30 bars. The red line is the scan line where the Cu and Ti elements are monitored. Figure 8-11 shows the evolution of the atomic concentration of Ti and Cu along the scan line.

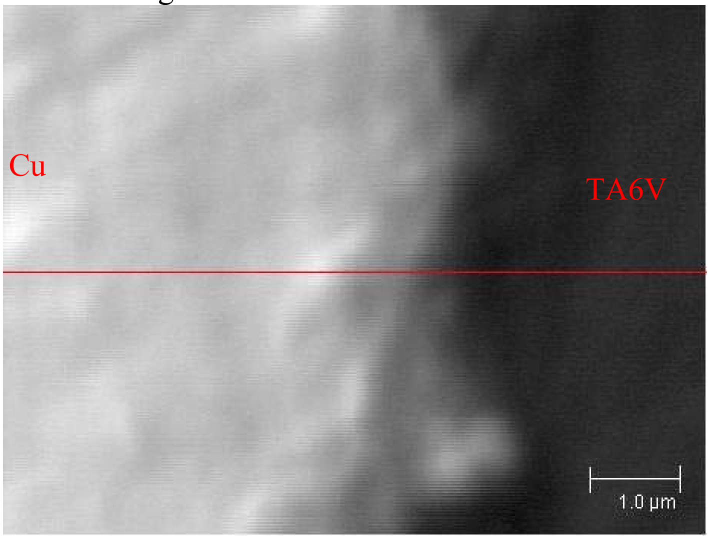

Figure 8-10: SEM image of the Cu/TA6V interface. The red line is the scan line that is showed on Figure 8-11.

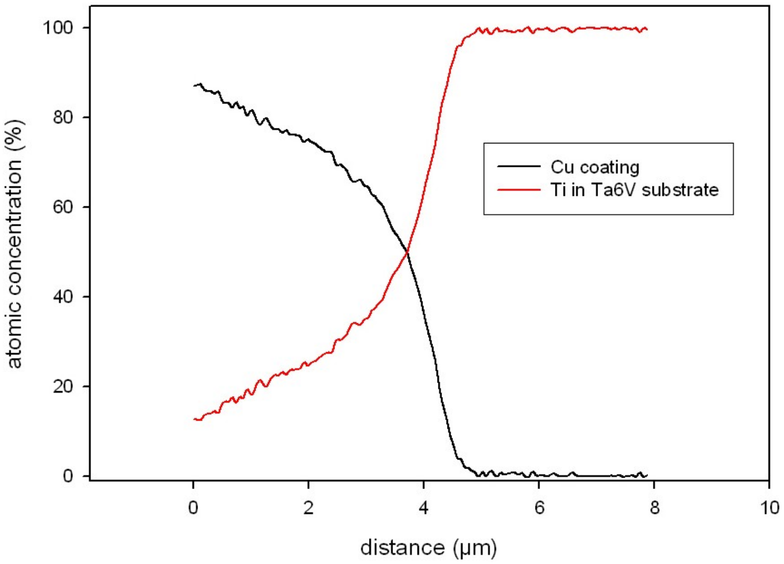

Figure 8-11: Scan along the red line on Figure 8-10.

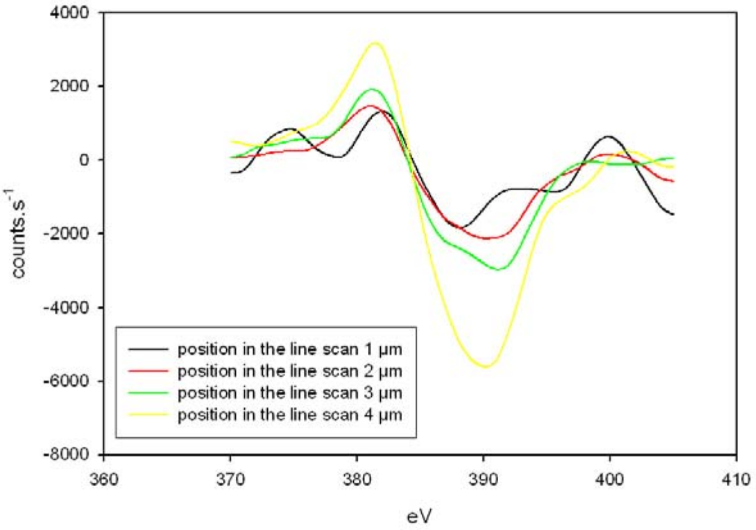

Figure 8-12: Ti spectrum along the scan line at position 1 µm-2 µm-3 µm-4 µm-5 µm on Figure 8-10.

Figure 8-12shows 5 Ti spectrums along the line scan of Figure 8-11. It shows that the presence of a Ti signal at a position 2 µm on that figure while the interface is positioned at 5 µm.

The presence of a diffusion zone has also been detected on the coating made with powder A. Figure 8-13 shows a SEM picture of the coating on TA6V made with powder A sprayed at 520°C and 30 bars.

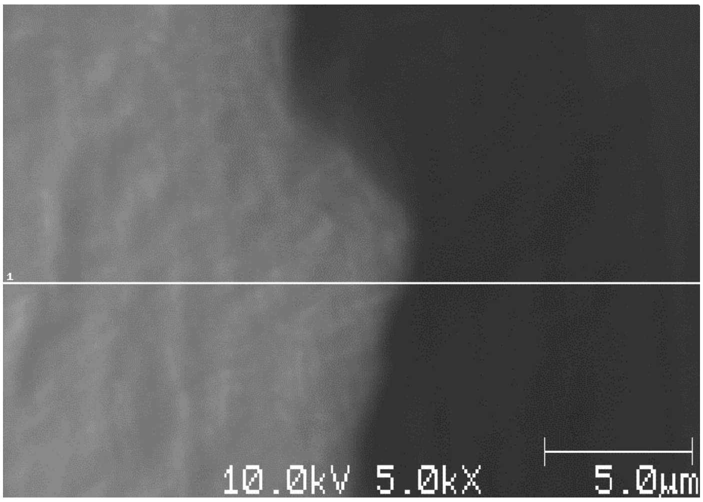

Figure 8-13: SEM image of the Cu/TA6V interface. The white line is the scan line that is showed on Figure 8-14.

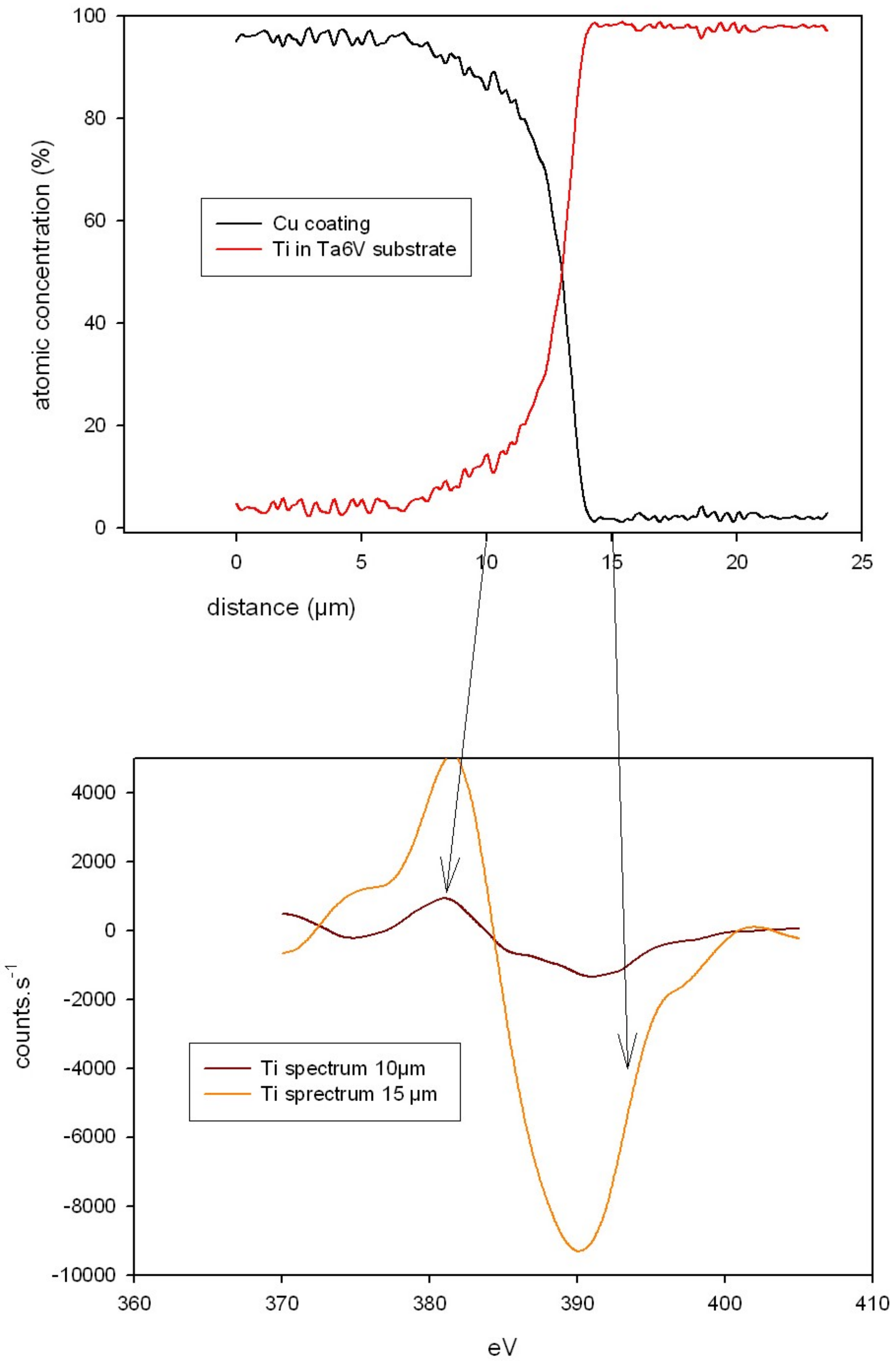

Figure 8-14: Evolution of the atomic concentration of Cu and Ti along the white line on Figure 8-13. Two Ti spectrums at 10µm and 15 µm on the interface are presented.

8.6 Results on TA6V Substrate

8.6.1 Influence of the Spray Condition on the Interface of the Coating Made with Powder A

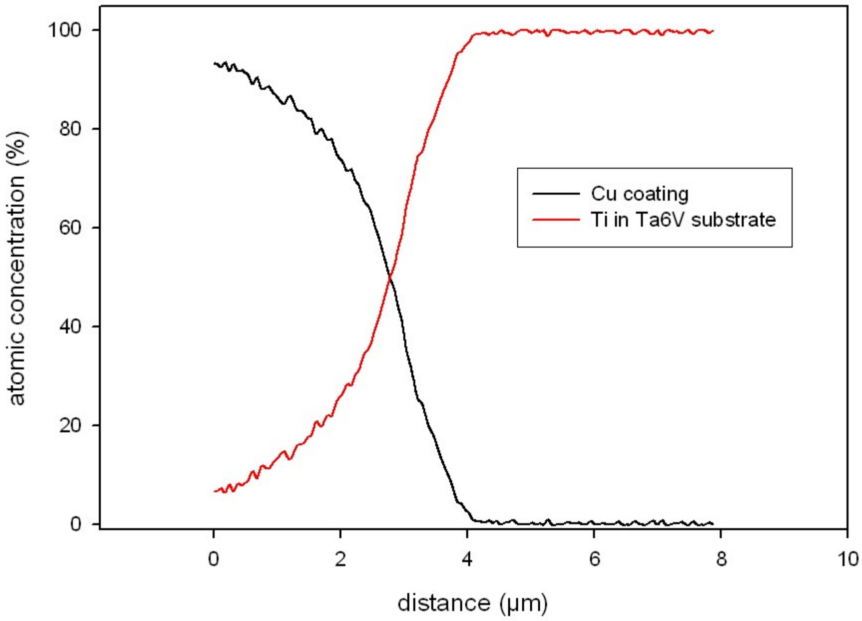

Figure 8-15: Coating made with powder A sprayed at 520°C and 30 bars.

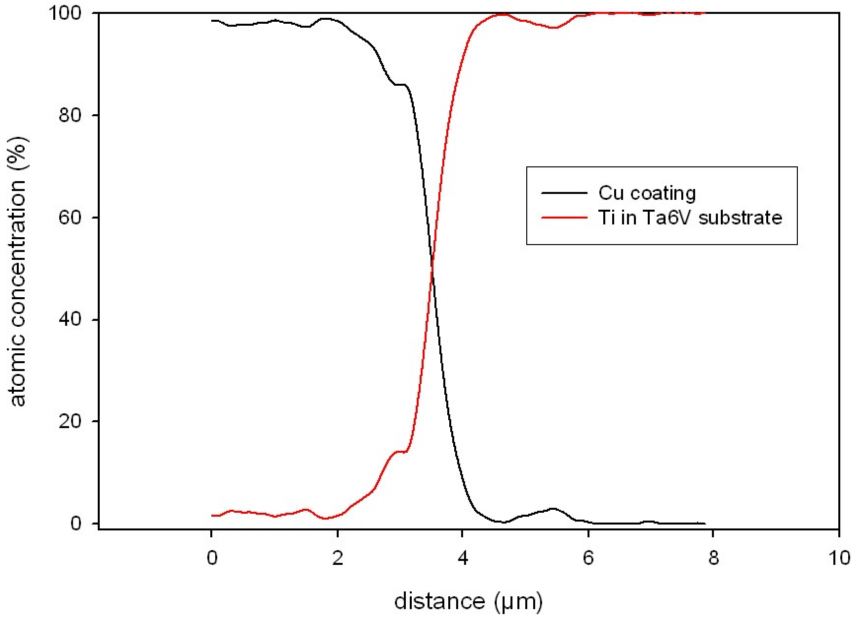

Figure 8-16: Coating made with powder A sprayed at 320°C and 22 bars.

Figure 8-15 and Figure 8-16 show an Auger analysis of the interface of the coating made with powder A sprayed respectively with the spray condition 1 and spray condition 2. The spray conditions have an influence on the formation of diffusion zone at the interface. Ti atoms have penetrated in the Cu coating on Figure 8-15.

8.6.2 Influence of the Spray Condition on the Interface of the Coating Made with Powder B

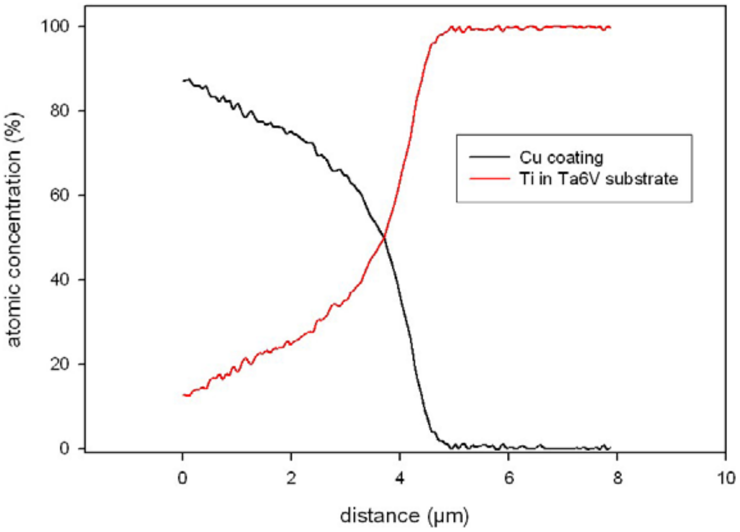

Figure 8-17: Coating made with powder B sprayed at 520°C and 30 bars.

Figure 8-17 shows an Auger analysis of the interface of the coating made with powder B sprayed with the spray condition 1. The spray conditions have an influence on the formation of diffusion zone at the interface. Ti atoms have penetrated in the Cu coating Figure 8-17.
With spray condition 2 (320°C and 22 bars), the coating did not bond on to the surface. No analysis could be performed.

8.7 TEM Observations

TEM analysis requires a fine lamella of the material to study. This is done by using an FIB (Focused Ion Beam) with ion milling.

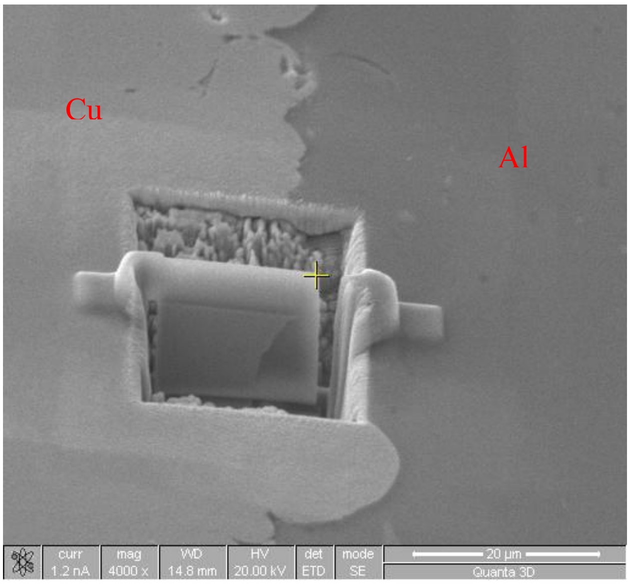

Figure 8-18: thin lamella obtained with the FIB on the cold sprayed Cu on Al coating sprayed at 520°C and 30 bars.

Figure 8-18 shows the milling of a lamella at the interface between the copper coating and aluminium substrate sprayed at T_0 = 520°C and P_0 = 30 bars. The lamella is ions milled until it reaches a thickness of 100nm by using the Quanta3D FIB in the department.

8.7.1 Interface Analysis on TA6V

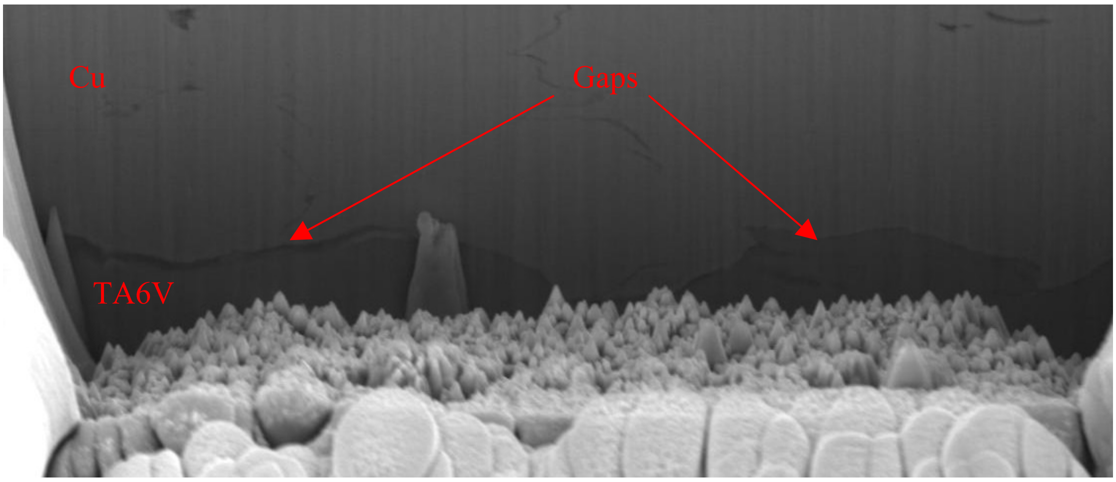

Figure 8-19:FIB milled copper coating sprayed with powder A on TA6V at 520°V and 30 bars. The interface has gaps and the quality of bonding is poor.

Figure 8-19 shows that the bonding between the TA6V substrate and the Cu coating is of poor quality. Many gaps are present. For this reason it was not possible to get a thin lamella for TEM observations. The milling was done by FEI on a Quanta 3D FEG with 75 nA of Ga ions intensity.

8.7.2 Cu-Al Cold Spray Interface Analysis

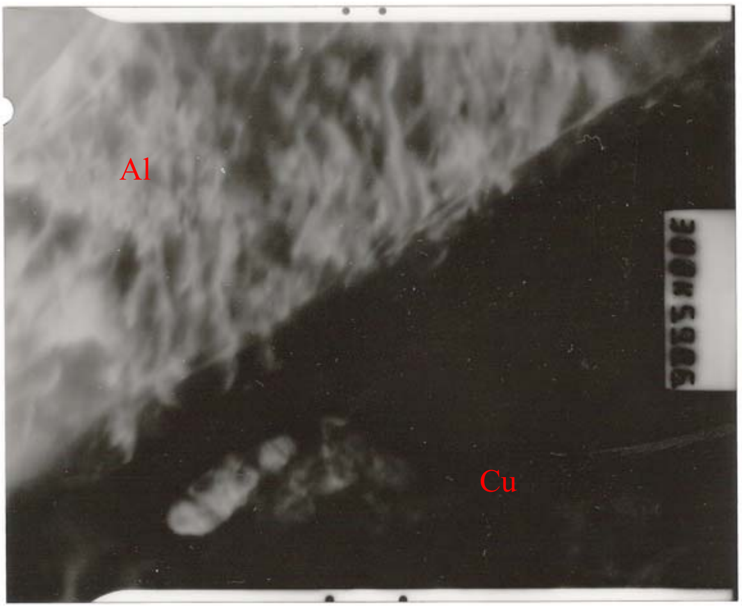

Figure 8-20: TEM observation of the interface of copper Al sprayed at 520°C and 30 bars with powder A. The magnification is 300000 times.

Figure 8-20 shows the interface of the Cu on Al substrate. No intermetallics were observed. By using STEM, a small diffusion zone of 20 nm could be observed.

8.8 Discussion

The Auger results show that when coatings are sprayed on the Al substrate at 520°C and 30 bars a diffusion zone of Cu in Al is visible (compare Figure 8-6 and Figure 8-7 and compare Figure 8-8 and Figure 8-9). Figure 8-5 shows the spectrum obtained for Cu at different distances from the interface along the scan line. The signal is detected 3 µm from the interface.

This shows that a diffusion zone is present but several measurement artefacts can induce false presences:

- This could be copper redeposited after the sputtering.
- This could be electron reflection on the copper.

Several analysis were done along the same line at different magnifications with a 15 min sputtering between them. During analysis a light sputtering was maintained to avoid oxygen redeposition on the surface. If copper had been redeposited on the surface, its presence would have been affected during that light sputtering and removed. It seems unlikely that electrons would come from the reflection at the interface. A diffusion zone would have been detected on both Figure 8-6 and Figure 8-7. Measurements far from the interface were done to ensure that no copper was detected from the sample holder.

Work by Price et al [71] has showed that the contact between copper and Al is of metallurgical nature on the whole of the interface. Price et al sprayed blended copper-aluminium powders at 29 bars with He and heat treated the coating (Figure 8-21). The growth of the diffusion zone along the interface depends of the spray pressure. The oxide layer at the interface would be a barrier of diffusion but the localized adiabatic shear bands have removed the oxides.

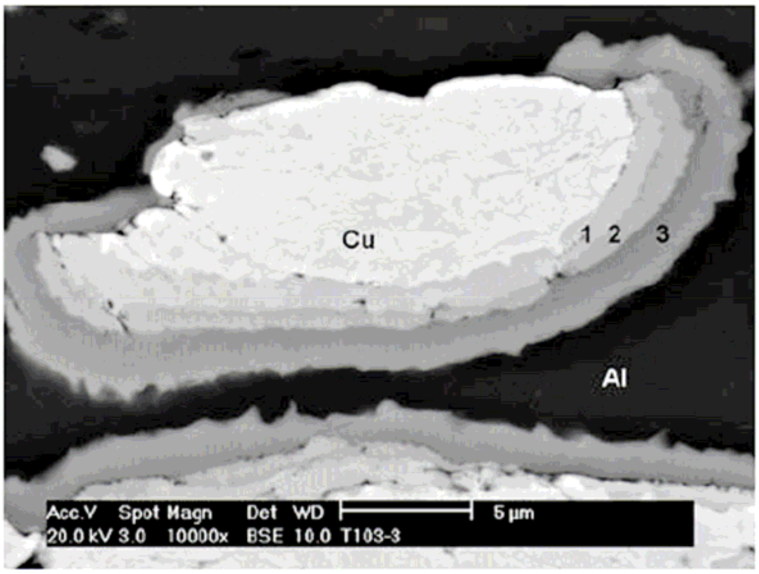

Figure 8-21 : BSE image of the heat treated Al-Cu deposit sprayed at 29 bar at high magnification showing Cu, bright, Al, dark, and three distinct intermetallic layers at the interface. Spray direction top to bottom [71]. This proves that the metallurgical contact is obtained on the whole of the interface when the impact speed is sufficiently high.

The Auger measurements on the TA6V substrate have also yielded a diffusion zone of Ti in the Cu coating (compare Figure 8-15 and Figure 8-16). The coating sprayed with powder B at 22 bars and 320°C did not bond on the surface. No measurements were possible. The spectrums on Figure 8-12 show that a signal is detected 3 µm from the interface in the copper coating. Even so, this result was not expected. An attempt to obtain a thin lamella for TEM observation was done by using the FIB. The coating was milled from the top surface without needing any surface preparation. The coating was milled on more than 200 µm with Ga ions. Figure 8-19 shows that gaps are present at the interface on large areas where SEM pictures of the interfaces analyzed by Auger do not show these gaps (Figure 8-10 and Figure 8-13). The samples used for AES were polished before analysis. It had for consequence that the gap between the substrate and the coating was closed. No thin lamella could be obtained for TEM analysis. TEM analysis was performed on one lamella of the Cu-Al interface but only a small diffusion zone of 20 nm could be observed.

So the issue is: what has been observed by the AES technique? The data presented in the previous graphs is atomic concentrations. The method does not give a quantitative measurement; the values are obtained with an internal software standard. In order to get a quantitative value, the signal should be calibrated against a sample with a known concentration of Cu or Ti. The values can overestimate the real atomic concentration value by 100%. The analysis of the spectra along the line scan shows that there is interpenetration of atoms of Cu in Al on 1 to 2 µm and of Ti in Cu on 1-2 µm. The comparison between samples made with the two extreme spray conditions confirm that a diffusion zone is observed. The scale of these zones is over estimated because of the size of the electron beam spot (300-400 nm). They are most likely smaller than 1 µm. No measurement artefact seemed to create this diffusion zone.

The issue of diffusion taking place at the interface during cold spraying is still an open question. In order to get diffusion and formation of intermetallic compounds, it is needed to have:

- Time
- Heat

During cold spraying, the heat is generated into the shear bands during a time laps of 40-50 ns. Sources of heat during impact are not sufficient to generate diffusion in a solid state process.

The other heat source in the process is the gas stagnation temperature. When the supersonic gas hits the surface, the gas becomes subsonic and its heat increases. A heat transfer between the substrate and the powder in this area can occur. The temperature of the substrate will depend on:

- The standoff distance
- The nozzle travel speed
- The initial gas stagnation temperature
- The substrate heat conductivity

The influence of the gas temperature on the substrate temperature has been analyzed in the book by Papyrin [72]. The final substrate temperature is determined by the heat transfer coefficient that is a complex function of the impinging gas dynamics on the substrate.

The first assumption is that this high travel speed could not allow the gas temperature to heat up the substrate significantly. In this study, the nozzle travel speed is 397 mm.s^{-1}. The heat from the gas could not be the source of diffusion.

The diffusion process is described by a gradient in concentration between the two elements that are transported through random jumps of the atoms in the lattice vacancies. The process is well described by the Fick’s law. But does the Fick law apply in every case?

When a powder particle hits the surface, a shock wave is generated in the coating. The high pressure wave generated and high temperature will have a specific relaxation time. It will have an influence on the relaxation time of the system.

The effect of a shock wave on the diffusion mechanisms have been analyzed by A.N. Bekrenev et al ([73],[74]). The contribution of interstitials atoms to mass transport is advanced as a possible explanation of diffusion under impulse loading. The interstitials atoms are captured by moving dislocations will increase the mass transport. If one observes the results on Figure 8-6 and Figure 8-15, the copper has penetrated in the Al substrate in one case while the Ti has penetrated the copper coating. When the copper particles hits the Al substrate, the Al coating will deform more than the particle (see Figure 4-6 in Chapter 4) and dislocations will multiply largely in the substrate. In that case, the copper atoms would have been captured by the Al substrate. When the copper is sprayed on the TA6V substrate, the high hardness of the substrate induces a large deformation of the particle. The dislocations are mainly generated in the copper and the dislocation in the impinging particle captures Ti atoms on the surface.

The density of the atoms transported is very low <10% in atomic concentration. The Auger concentration values in this study largely overestimate the real value. The atoms are in a solid solution and they did not form an intermetallic. None has been observed on the TEM lamella on Figure 8-20. The effect of this mass transport of atoms has not leaded to the bonding in the case of Cu on TA6V (see gaps on Figure 8-19).

Levitas et al ([75],[76]) have studied the occurrence of chemical reaction in shear bands in mixtures of materials under shock loading. The initiation of chemical reaction is possible by explosive welding. This has been studied in the case of Ti – Si mixtures. It appears that it is possible to initiate a chemical reaction under extreme conditions associated with high strain rate and high pressure.

8.9 Conclusion

The Auger measurements have shown a slight diffusion of copper in the Al substrate and a diffusion of Ti on the Cu coating. These results have never been reported by another author but no other author has tested the Auger spectroscopy on CGDS coatings and reported the data. After analysis, the data seems to be relevant but no confirmation has been possible by TEM. Only one TEM lamella was analysed and the TEM analysis is a very local analysis. More lamellas should be analysed.

The diffusion mechanism can be argued by taking into account the effect of shock loading on the surface. In this case, the diffusion mechanism involves interstitial diffusion but these mechanisms are still poorly understood. It seems clear that new Auger measurements on another apparatus with a smaller spot size would be needed to confirm these observations.

The use of the fick law to describe the diffusion process in the case of cold sprayed materials seems tedious. The processes described during shock loading ([74],[75]) involve the use of irreversible thermodynamics to add the contribution of pressure and strain rate to the diffusion process.

Chapter 9 Discussion, Conclusion and Perspectives

The Cold Gas Dynamic Spray process (CGDS) is based on the acceleration of powders to very high velocities and the coating builds up due to the formation of adiabatic shear bands at the interface between the surface and the powder particle. What are the optimal powder characteristics? This study has focused on the study of copper powders. Copper is a material that has a high ductility (depending on its microstructure) and it forms easily shears bands when sprayed at high velocity.

9.1 Influence of the Powder Size Distribution on the particle impact conditions

The powder size distribution will have a direct consequence on the particle impact condition: speed and temperature.

- As shown by Figure 3-13, the size of the particle will have a dramatic influence on the final impact speed. The inertia of the powder particle is determined by its density and volume. Table 3-4 shows that the variation of speed due to size differences is important.
- Both the initial stagnation pressure P_0 and temperature T_0 play an important role on the acceleration of the powder. But the influence of the spray conditions does not change largely the measured copper powder velocities (Table 3-5) when compared to the influence of the size effect.
- As shown by Figure 3-16, the initial gas stagnation temperature T_0 and particle size will determine the final impact temperature value. The stagnation pressure P_0 does not change the powder temperature.

Any commercial powder will have a size distribution centred on an average value. In this study, powder A has a smaller average size distribution than powder B (Figure 5-1 & Figure 5-2). The consequences on the particle impact conditions will be the following:

- Powder A is likely to have a higher impact speed than powder B. This has been confirmed by laser velocimetry measurements (Figure 3-23 and Figure 3-24).
- The copper particle impact temperature for both powders is likely to be very close. Only the change in stagnation temperature seems to yield an important effect on its final value. Unfortunately it is difficult to measure the actual temperature of the powder upon impact.

Any optimisation of the process involves insuring that the impinging powder has the minimal critical velocity for bonding. The optimisation is done by plotting the deposition efficiency as a function of the impact speed. The difference between the powders comes also from the influence of other factors on the critical velocity (oxide contact, substrate properties) but they were not investigated further.

9.2 Influence of the Powder Choice on the Deposition Efficiency

The deposition efficiency is an important measure of the performance of the system. It is a complex function of:

- the impact conditions
- the impact angle
- the powder oxide content
- the surface properties

The critical velocity for bonding depends on the ability of the materials for shear localization during impact loading. This ability is dependent on the impact speed and the materials' mechanical properties. The quality of the metallurgical contact between the particle and substrate in the shear bands is also influenced by the oxide shell around the particle and the oxide layer on the surface.

- Powder A has a fine grain size distribution but a higher oxide content than powder B. As observed by other authors [27], high oxide content is associated with higher critical velocity. The DE of powder A is lower than the one of powder B on both substrates on Figure 5-15.
- The spray conditions have an important effect on DE. They affect the powder by changing the particle speed and temperature on impact. By changing simultaneously the stagnation pressure and temperature of the gas, the DE increased significantly (Figure 5-15).

One other aspect that can influence the DE is the mechanical properties of the powder. X-ray diffraction allows the measurement of the crystallite size in the powder before spraying. The crystallite size can be linked to the elastic limit of the material with the Hall-Petch law. Powder A has a higher crystallite size and a lower dislocation density than powder B (Table 7-2). Hence it would appear that powder A is more ductile than powder B. It would be reasonable to assume that a powder with a lower elastic limit would deform more easily and the DE should increase. Powder A has also a higher oxide content than powder B. It appears that the oxide shell hinders the metallurgical contact between the impinging particle and the substrate. The role of the oxide shell seems dominating the DE when the spray conditions change.

9.3 Influence of the Powder Choice on the Mechanical Properties of the Coating

The mechanical properties measured in this study are:

- The bond strength
- The microhardness
- The nanohardness

The value of the microhardness is essentially determined by the original powder size distribution. When the indenter deforms the coating, the plastic deformation is hindered by the presence of particle boundaries in the coating. These boundaries contain oxide remains that have been trapped during the impacts and that will also hinder the deformation. Powder B

with a large particle size distribution compared with powder A, will naturally have a lower microhardness. X-ray diffraction shows also that the coatings made with powder B have a lower dislocation density than the coating made with powder A (Table 7-3 and Table 7-4). This difference in strain hardening contributes to the low microhardness of powder B compared with the one of powder A.
The influence of the spray conditions on the microhardness is described on Figure 6-4. There is a slight increase in microhardness when the coating is sprayed at 520°C and 30 bars compared with other spray conditions. This slight increase does not seem related to a strain hardening accumulation. The dislocation density has not changed a lot when the spray conditions are different (compare Table 7-3 and Table 7-4). This increase could be related to a different grain size population that has bonded to the surface. When one looks at the DE on Figure 5-15, one sees that, at 520°C and 30 bars, there is a significant increase in its value. The fraction of the powder that has reached the bonding conditions is much higher than in other cases. The fraction of the particles size distribution that has entered the coating is different than at other spray conditions. The assumption made here is that more fine particles have entered the coating in both cases. Fine particle hit other larger particle copper particles in the nozzle and form larger particles that bond to the surface. Their presence will increase the microhardness values.

The bond strength measured with a pull off test gives a macroscopic view of the bonding phenomenon. From a microscopic point of view, the bonding process has a mechanical origin and a metallurgical one. The mechanical bonding is associated with the interlocking of powder particles on the surface roughness, while the metallurgical origin is associated with the formation of shear bands on the surface.
In this study, powder A has significantly higher bond strength on Al than the values obtained when powder B is sprayed on Al. The interpretation of these values is based on the differences between the powders. The quality of the metallurgical contact between the powders and the substrate is associated with two variables:

- The impact speed has to be sufficiently high to ensure a close and conformal contact.
- The oxide content has to be low so that upon impact, the oxide shell is removed.

Powder A has the highest impact velocity, the highest oxide content and the lowest initial dislocation density. Upon impact, powder A deforms more than powder B and dynamic recovery reorganizes the microstructure on a larger scale. This is visible on the X-ray diffraction data (Table 7-3 and Table 7-4). The final dislocation density in the coating made with powder A is higher than the one made with powder B. It is likely that shear bands formed more extensively on powder A upon impact. This favours the quality of the bonding. But powder A has also higher oxide content. It is likely that the oxide shell around powder A is thicker than the one around powder B. This will hinder the metallurgical contact between the surface and the particle. It hinders it so significantly that it reduces the DE of powder A well below the one of powder B. But once the oxide shell is removed by the impact, the particles have a stronger metallurgical link with the surface since they deform more easily.

The nanohardness profiles show that powder A remains softer than powder B even after the cold spraying stage. A part of powder A in the coating has kept the powder initial microstructure after the spraying. Since the nanohardness measurements are more influenced by the microstructure of individual particles than by the boundaries between particles in the coating (Figure 6-12), it's likely that the coating made with powder A has a slightly lower nanohardness than the one made with powder B (Figure 6-8).

9.4 The Bonding Mechanism during Copper Cold Spraying

The source of bonding is highly localized at the interface between the impinging particle and the substrate surface. The value of the critical speed is associated with the formation of shear bands at the interface. During impact (about ~40 ns), these shear bands are heated up to temperatures close to the materials melting points and pressure values in these bands are in the range of 0.1 GPa to several GPa. These extreme conditions are the source of the high quality bonding in the materials. Work by Barradas et al [24] have showed that Cu intermetallics were present. This is explained by the diffusion of copper in liquid aluminium.

In this study, the Auger measurements of Chapter 8 suggest that the copper has diffused in the Al substrate and that Ti has diffused in Cu coating. The diffusion process cannot be confirmed by TEM observations. It appears that there are many gaps between the Cu coatings on the TA6V substrate and that no intermetallic is present between the Cu and the Al coating. The Auger concentration values are overestimated but they are below 10 % in atomic concentration.

The use of the Fick law to describe the diffusion process is difficult. During impact, high strain rates and high pressures will affect the value of the diffusion coefficient ([73], [74]). This could explain the Auger results presented in this study. Also, work by Levitas et al analyses the role of strain on induced chemical reactions ([75], [76]). The strain rate and pressure conditions could initiate chemical reactions at the interface without requiring melting.

The issue of melting during impact is complicated to treat and further work is needed to prove its occurrence at the particle/ substrate interface.

9.5 The Cold Spraying Copper and other Materials: the Influence of the Crystal Structure.

The materials with an FCC structure are ideal for cold spraying. They have a large number of sliding planes that allow a good deformability because of the large number of slip systems. Copper and aluminium have good deformability and a relatively low melting temperature. This good deformability is characterized by the dislocation mobility in the material. The critical resolved shear stress is the minimum value of stress needed to make a dislocation move. Its value is determined by athermal obstacles (elastic interactions, strong pinning sites). In order to liberate themselves from these obstacles, they do need to cross slip. The activation of cross slip is also an athermal process because the decomposition into partial dislocations cannot be activated by the thermal vibration of the lattice. When the stacking fault energy decreases, the decomposition into partial dislocations is easy. This could explain why the results in this study are so sensitive to the initial powder microtsructure. Powder B with a higher dislocation density than powder A will exhibit a lot more obstacles to deformation and its behaviour will be different. This also explains the relative insensitivity of the dislocation density with the spray conditions shown in Table 7-3 and Table 7-4.

Two observations have to be kept in mind:

- The heat of the spray gas does not affect the dislocation density because of the high gun travel speed (~397 mm.s^{-1}) hence, the microstructure has been restored.
- The powder particles that bond to the surface all have a minimum speed what ever the spray condition in the design of experiment (Figure 5-13).

The diffraction data in Table 7-3 and Table 7-4 comes from the top surface where the particles have hit the surface with the minimum critical velocity.

BCC metals have a lower packing density and the energy to activate the mobility of screw dislocation at high strain rates is higher than for FCC metals. This is due to higher lattice friction forces. The activation of dislocation mobility is dependent on the temperature for BCC metals.
HCP metals with a low melting temperature show a good ability to form a coating when cold sprayed [78]. Any metal that needs to be processed by this technology has to show a good deformability. (like Zn, Co, Mg)
A new cold spray system heats up the powder up to ~800°C before spraying. It facilitates the spraying of BCC materials such as Mo or W.

9.6 Final Conclusion

This study has shown that two copper powders with a different size distribution yield very different performances measured by:

- The deposition efficiency.
- The mechanical properties of the coating.

The sources of these differences are to be found in:

- The powder size distribution.
- The oxide content of the powder.
- The microstructure of the powder.

An optimal copper powder should have:

- A size distribution optimized to get the impact velocity that allows shear localization and high pressure.
- A low oxide content to facilitate the metallurgical contact with the substrate and get a good bonding.
- A microstructure with a very low dislocation density in order to decrease its elastic limit. Copper with a low dislocation density has very low number of obstacles to dislocation motion and reorganisation.

These characteristics will allow an extensive thermal softening in the shear bands and, in combination with the impact pressure, will allow the metallurgical bond to be established.
For any industrial application, the aim will be to find the right powder that yield the coating with the right properties. Other practical recommendations would be:

- Clean the surface to be sprayed on.
- Avoid cold spraying on hard surfaces or use a system to soften the surface.
- Conserve the powder in a protected environment to avoid its oxidation.

9.7 Future Developments

The cold gas dynamic spray process allows the build up of a coating based on powder material without oxiding the initial material. The ability to get a bonding with a surface is based on the ability of materials to deform which is significantly influenced by the material properties and temperature. From and industrial point of view, the integration of heating systems for the powder will allow the process to diversify by spraying new materials like (W, Mo, Cr) with good performances.

The bonding results depend also of the substrate composition and its mechanical properties. It is likely that systems that heat up the substrate will improve the quality of the bonding with hard surfaces.

When compared to other spray processes, the cold spray process prevents extensive oxidation of the materials, but the effect of temperature is very important. It determines the deformability of the material by activating dislocation mobility. This effect is strongly dependent on the crystal structure and the physical properties of the materials.

From a scientific point of view, many challenges still remain. During the bonding process, the materials reach extreme conditions for which the behaviour of some materials is not well understood. The high strain rate behaviour ($\dot{\varepsilon} > 10^6 s^{-1}$) involves complex dislocations behaviour (drag effects of dislocations
[79], [80]).

The role of the gas stagnation temperature T_0 is important in the process:

- It accelerates the powder particle by increasing the expansion of the gas in the nozzle.
- It transfers heat to powder. The amount of heat stored by the powder depends on the powder thermal properties and its size. This heat transfer happens in the convergent part of the nozzle when the gas speed is slow and its temperature is high.
- The heated gas impinges the surface and heats it up. Depending on the standoff distance and the nozzle travel speed, the temperature of the surface will be modified.

No study quantifies the influence of the substrate temperature (induced by the impinging gas jet) on the bonding process involved in cold spray.

The nature of the bond between the surfaces is most certainly of metallurgical nature in some cases. A satisfying global explanation on how and why these bonds are generated still lacks. In some cases, the formation of intermetallics at the interface has been proved present but these cases are rare.

An experimental investigation on the effect of the oxide shell around the powder and its influence on the bonding process still deserves more attention. No authors have published measured results of the shell thickness and its influence on the coating properties.

Chapter 10 References

[1] www.gordonengland.co.uk/homepage.htm

[2] PhD F. Raletz "Contribution au développement d'un procédé de projection dynamique à froid (P.D.F.) pour la réalisation de dépôts de nickel",7 octobre 2005, L'Université de Limoges

[3] *"Gas Dynamic Principles of Cold Spray",* R.C. Dykhuizen, M.F. Smith, Journal of Thermal Spray Technology , Vol 7, 1998, p205-212

[4] "*Adiabatic shear instability based mechanism for particles/substrate bonding in the cold-gas dynamic-spray process*", M. Grujicic, C.L. Zhao, W.S. DeRosset, D. Helfritch, Materials & Design, (2004)

[5] cours "*Mécanique des fluides* ", S. Candel, DUNOD édition

[6] "*Cold Spray Nozzle Mach Number Limitation*", B. Jodoin, Journal of Thermal Spray Technology (2002) 11(4), 496-507

[7] "*Cold spray flow modeling and validation*", B. Jodoin, F. Raletz, M. Vardelle, *Thermal Spray 2005: Explore its surface potential*, ASM International, May 2-4, 2005 (Basel, Switzerland)

[8] "*A fundamental study of the kinetic spray process*", Taeyoung Han, Zhibo Zhao, Bryan A. Gillispie, John R. Smith, Proceedings of the International Thermal Spray Conference, Thermal Spray Solutions, Advances in Technology and Application, May 10 - 12, 2004, Osaka, Japan

[9] "*Computational Modelling of Cold Spray Process: Effect of Substrate and Particle Size on Gas –particle Flow*", Q. Zhu, A. Dolatabadi, Proceedings of the 2006 International Thermal Spray Conference, May 15-18, 2006, Seattle, Washington, (USA)

[10] "*Optimizing the Cold Spray Process*", R.C. Dykhuizen, R.A. Neiser, Thermal Spray 2003: Advancing the Science & Applying the Technology, (Ed) C. Moreau and B. Marple, published by ASM International, Materials Park, Ohio, USA, 2003

[11] "*Optimization of The Cold Spray Process*", T.Stoltenhoff, H. Kreye, H.J. Richter, H. Assadi, Thermal Spray 2001: New Surfaces for a New Millenium (Ed) C.C. Berndt, K.A. Khor, and E.F. Lugscheider, published by ASM international, Materials Park, Ohio, USA, 2001

[12] "*Analysis of the Impact Velocity of Powder Particles in the Cold Gas Dynamic Spray Process*", M. Grujicic, C.L. Zhaoa, C. Tonga, W.S. DeRosset b, D. Helfritch, Materials Science and Engineering, 368 (2004) 222-230.

[13] "*Optimal Particle Size for Cold Spray*", D. Helfritch, V. Champagne, Proceedings of the 2006 International Thermal Spray Conference, May 15-18, 2006, Seattle, Washington, (USA)

[14] *"High Velocity Impact Phenomena and Coating Quality in Cold Spray"*, T. Scmidt, F. Gartner, T. Stoltenhoff, H. Kreye; H. Assadi, International Thermal Spray Conference & Exposition, May 2-4, 2005, ASM International, p 232-238

[15] "*Bonding mechanism in cold gas spraying*", H.Assadi, F.Gärtner, T.Stoltenhoff, H.Kreye, Acta Materialia, 51 (2003) 4379-4394

[16] "*Computational Analysis of the Interfacial Bonding between Feed-powder Particles and the Substrate in the Cold Gas Gynamic Spray Process*", M. Grujicic, J.R. Saylor, D.E. Beasley, W.S. DeRosset, D.Helfritch ; (2003) Applied Surface Science, 219(1) , p 211-327

[17] *"Cold spray deposition:. Significance of particle impact phenomena."*, S. V. Klinkov, V. F. Kosarev, M. Rein, Aerosp Sci Technol,. 2005, (9) p 582-591

[18] "*Plasticity: Adiabatic Shear Localization*", M. A. Meyers, Encyclopedia of Materials: Science and Technology, p. 7093-7103

[19] "*Microstructural and Macroscopic Properties of Cold Sprayed Copper Coatings*", C. Borchers, F. Gärtner, and T. Stoltenhoff, H.Assadi, H. Kreye, Journal of Applied Physics Vol 93 (2003), n°12 10064-10070

[20] "*Microstructural Evolution in Copper Processed by severe plastic deformation*", A. Mishra, V.Richard, F. Grégori, R.J. Asaro, M.A. Meyers, Materials Science and Engineering A 410-411 (2005) p. 290-298

[21] "*Constitutive description of dynamic deformation: physically-based mechanisms*", M.A. Meyers , D.J. Benson, O. Vo¨hringer, B.K. Kad, Q. Xue, H.-H. Fu, Materials Science and Engineering A322 (2002) 194–216.

[22] "*Aluminium Coatings via Spray with Relatively Large Powder Particles*", T.H. Van Steenkiste, J.R. Smith, R.E. Teets, Surface and Coatings technology 154 (2002) 237-252

[23] "*Diffusion Processes in Advanced Technological Materials*", edited by Devendra Gupta, William Andrew publishing, Springer

[24] PhD Sophie Barradas, "Etude à l'aide du choc laser, des mécaniques d'adhérences aux interfaces cuivre aluminium et cuivre obtenues par projection thermique", 7 décembre 2004, Ecole des Mines de Paris.

[25] "*Investigation of Interface Boundary Occurring During Cold Gas Dynamic Spraying of Metallic Particles*", Nuclear Instruments and Methods in Physics Research A 470 (2001) 249-252

[26] "*High-Resolution Microstructural Investigation of Interfaces Between Light Metal Alloy Substrates and Cold Gas-Sprayed Coatings*", A. Wank, B. Wielage, H. Podlesak, T. Grund, J. of Thermal Spray Technology, Volume 15(2) June 2006, p 280-283

[27] "*Examination of the Estimating Approaches for the Critical Velocity in Cold Spraying*", C.-J. Li, G.-J. Yang, C.-X. Li, H.S. Bang, H.S. Bang, W.-Y. Li, Thermal Spray 2007: Global Coating Solutions (Ed.) B.R. Marple, M.M. Hyland, Y.-C. Lau, C.-J. Li, R.S. Lima, and G. Montavon Published by ASM International®, Materials Park, Ohio, USA

[28] "*Numerical simulation of deformation behaviour of Al particles impacting on Al substrate and effect of surface oxide films on interfacial bonding in cold spraying*", W.-Y. Li, H. Liao, C.-J. Li, H.-S. Bang, C. Coddet, Appl. Surf. Sc, 253 (2007) 5084-5091.

[29] "*Production of Titanium Deposits by Cold Gas Dynamic Spray*", T. Marrocco, D.G. McCartney, P.H. Shipway, A.J. Sturgeon, *Thermal Spray 2005: Explore its surface potential*, ASM International, May 2-4, 2005 (Basel, Switzerland)

[30] *"A study of Adhesive Strength of Cold Spray Coatings",* H. Fukanuma, N. Ohno, Thermal Spray 2004, Proceedings ITSC (2004)

[31] "*Microstructure and key properties of cold –sprayed and thermally sprayed copper coatings*", T. Stoltenhoff, C. Borchers, F. Gartner, H.Kreye, Surface and coating technology, 2005

[32] "*Study on cold-sprayed copper coating's properties and optimizing parameters for the spraying process*", T. Xiong, Z. Bao, T. Li, Z. Li, International Thermal Spray Conference & Exposition, May 2-4, 2005, ASM International, p. 178-183

[33] "*effect of shock compression method on the defect substructure in monocrystalline copper*", B.Y. Caoa, D. H. Lassila, M. S. Schneider , B. K. Kada, C. X. Huang, Y. B. Xuc, D. H. Kalantar, B. A. Remington, M.A. Meyers, Materials Science and Engineering A 409 (2005) 270–281

[34] "*Multiscale Dislocations Dynamics Simulations of Shock Compression in Copper Single Crystals*", M.A. Shehadeh, H. M. Zbid, T. Diaz de la Rubia, Int. J. Plasticity, 21, 2005, 2369-2390

[35] "*Formation of TiO2 photocatalyst through cold spraying*", Chang-Jiu Li, Guan-Jun Yang, Xin-Chun Huang, Wen-Ya Li, Akira Ohmori, Proceedings of the International Thermal Spray Conference, Thermal Spray Solutions, Advances in Technology and Application, May 10 - 12, 2004, Osaka, Japan

[36] "*Characterization of cold-sprayed nickel-base coatings*", F. Raletz, G.Ezo'o, M. Vardelle, M. Ducos, Proceedings of the International Thermal Spray Conference, Thermal Spray Solutions, Advances in Technology and Application, May 10 - 12, 2004, Osaka, Japan

[37] "*Impact fusion phenomenon during cold spraying of zinc*", Chang-Jiu Li, Wen-Ya Li, H. Fukanuma, Proceedings of the International Thermal Spray Conference, Thermal Spray Solutions, Advances in Technology and Application, May 10 - 12, 2004, Osaka, Japan

[38] "*Characterization of Microstructure of Nanostructured Fe-Si Coating Deposited by Cold*

Spraying", Chang-Jiu Li, Wen-Ya Li, Wen-Hua Ma, H. Fukanuma, Proceedings of the International Thermal Spray Conference, Thermal Spray Solutions, Advances in Technology and Application, May 10 - 12, 2004, Osaka, Japan

[39] "*Properties of Cold Spray Nickel Based Coating*", P. Richter, B. Jodoin, E. Sansoucy, L. Ajdelsztajn, G.E. Kim, *Building on 100 Years of Success: Proceedings of the 2006 International Thermal Spray Conference*, B.R. Marple, M.M. Hyland, Y.C. Lau, R.S Lima, and J. Voyer, Eds., May 15-18, 2006 (Seattle,WA,USA), ASM International.

[40] "*Deposition Mechanisms of Cold Gas Dynamic Sprayed MCrAlY Coatings*", Y. Ichikawa, K. Sakaguchi, K. Ogawa, T. Shoji, S. Barradas, M. Jeandin, M. Boustie, *Thermal Spray 2007: Global Coating Solutions* (Ed.) B.R. Marple, M.M. Hyland, Y.-C. Lau, C.-J. Li, R.S. Lima, and G. Montavon Published by ASM International, Materials Park, Ohio, USA

[41] "*Formation of Fe-Al Intermetallic Compounds Coating Through Cold Spraying*", H.T. Wang, C.-J. Li, G.-J. Yang, C.-X. Li, *Building on 100 Years of Success: Proceedings of the 2006 International Thermal Spray Conference*, B.R. Marple, M.M. Hyland, Y.C. Lau, R.S Lima, and J. Voyer, Eds., May 15-18, 2006 (Seattle,WA,USA), ASM International.

[42] "*Spray forming titanium alloys using the cold spray process*", R.E. Blose, *Thermal Spray 2005: Explore its surface potential*, ASM International, May 2-4, 2005 (Basel, Switzerland)

[43] "*Investigation of Al-Al_2O_3 Cold Spray Coating Formation and Properties*", E. Irissou, J.-G. Legoux, B. Arsenault C. Moreau, *Thermal Spray 2007: Global Coating Solutions* (Ed.) B.R. Marple, M.M. Hyland, Y.-C. Lau, C.-J. Li, R.S. Lima, and G. Montavon Published by ASM International, Materials Park, Ohio, USA

[44] "*Cold spray of Al-Cu-Mg-Fe-Ni alloy with Sc addition*", L. Ajdelsztaj, A. Zúñiga, B. Jodoin, E.J. Lavernia, *Thermal Spray 2005: Explore its surface potential*, ASM International, May 2-4, 2005 (Basel, Switzerland)

[45] "*Kinetic Sprayed Rare Earth Iron Alloy composite coatings*", T. Van Steenkiste, *Building on 100 Years of Success: Proceedings of the 2006 International Thermal Spray Conference*, B.R. Marple, M.M. Hyland, Y.C. Lau, R.S Lima, and J. Voyer, Eds., May 15-18, 2006 (Seattle,WA,USA), ASM International.

[46] "*Deformation Behavior and Properties of a CuZrTiNi BMG Kinetic Spray Coating*", J. S. Kim, Y. M. Xiong, C. Lee, H. S. Choi, H. J. Kim, *Thermal Spray 2007: Global Coating Solutions* (Ed.) B.R. Marple, M.M. Hyland, Y.-C. Lau, C.-J. Li, R.S. Lima, and G. Montavon Published by ASM International, Materials Park, Ohio, USA

[47] "*Cold Gas Dynamic Spraying of Fe-based Amorphous Alloy*", L. Ajdelsztajn, E.E. Lavernia, B. Jodoin, P. Richer, E. Sancoucy, *Building on 100 Years of Success: Proceedings of the 2006 International Thermal Spray Conference*, B.R. Marple, M.M. Hyland, Y.C. Lau, R.S Lima, and J. Voyer, Eds., May 15-18, 2006 (Seattle,WA,USA), ASM International.

[48] "*A critical review of experimental results and constitutive models for BCC and FCC metals over a wide range of strain rates and temperatures*", R. Liang, A. S. Khan, International Journal of Plasticity 15 (1999) 963-980

[49] “*Drag coefficients of irregularly shaped particles*”, S. Tran-Cong, M. Gay, E. E. Michaelides, Powder Technology 139 (2004) 21– 32.

[50] “*Study on the influences of DPV2000 software parameters on the measured results in cold spray*”, *Building on 100 Years of Success: Proceedings of the 2006 International Thermal Spray Conference*, B.R. Marple, M.M. Hyland, Y.C. Lau, R.S Lima, and J. Voyer, Eds., May 15-18, 2006 (Seattle,WA,USA), ASM International.

[51] “*The cold spray process and its potential for industrial applications*”; F. Gärtner, T. Stoltenhoff, T. Schmidt and H. Kreye, *Thermal Spray 2005: Explore its surface potential*, ASM International, May 2-4, 2005 (Basel, Switzerland)

[52] “*Advanced Particle Characterization for Improved Understanding of Spray Coating Quality*”, E. Pirard, F. Campana, J.-P. Janssen, *Building on 100 Years of Success: Proceedings of the 2006 International Thermal Spray Conference*, B.R. Marple, M.M. Hyland, Y.C. Lau, R.S Lima, and J. Voyer, Eds., May 15-18, 2006 (Seattle,WA,USA), ASM International.
Website: www.occhio.be

[53] “*Correlation between the nanomechanical properties and microstructure of ultrafine-grained copper produced by equal channel angular pressing*”, E. Rabkin, I. Gutman, M. Kazakevich, D. Gorni, Mater. Sci. Eng. A, Vol 396, 2005, p 11-21

[54] “*An improved technique for determining hardness and elastic modulus using load and displacement sensing indentation experiments*” W.C.Oliver and G.M.Pharr, J.Mater. Res., 7(6):1564-1583, 1992.

[55] “*Depth Dependence of Hardness in Copper Single Crystals Measured by Nanoindentation*”, Y. Liu, A.H.W. Ngan, Scripta mater. 44 (2001) 237–241

[56] “*On the relationship between plastic zone radius and maximum depth during nanoindentation*”, J.Chen, S.J. Bull, Surf. & Coat. Technology, 201(7), (2006), p. 4289-4293

[57] “*No-sized twins induce high rate sensitivity of flow stress in pure copper*”, L. Lu, R. Schwaiger, Z.W. Sha, M. Dao, K. Lu, S. Suresh, Acta Mater. 53 (2005) 2169-2179

[58] “*Microstructural and Macroscopic Properties of Cold Spayed Copper Coatings*”, C. Borchers, F. Gärtner, T. Stoltenhoff, H. Assadi, H. Kreye, J. Appl. Phys., Vol 93 (12), 2003, p 10064-10070

[59] “*Dislocation, Grain Size and Planar Faults in Nanostructured Copper Determined by High Resolution X-ray Diffraction and a New Procedure of Peak Profile Analysis*”, T. Ungár, S. Ott, P.G. Sanders, A. Borbely, J.R. Weertman, Acta Mater., Vol 46, 1998, p 3693-3699

[60] “*Dislocation densities, arrangements and character from X-ray diffraction experiments*”, T. Ungár, Mater. Sc. & Eng. A, 309–310 (2001) 14–22

[61] "*Measurement of screw and edge dislocation density by means of X-ray Bragg profile analysis*", E. Schafler, M. Zehetbauer , T. Ungár, Materials Science and Engineering A319–321 (2001) 220–223

[62] "*Microstructural parameters from X-ray diffraction peak broadening*", T. Ungár, Scripta Materialia 51 (2004) 777–781

[63] "*Asymmetric X-ray Line Broadening of Plastically Deformed Crystals. II. Evaluation Procedure and Application to [001]-Cu Crystals*", T.Ungár, I. Groma, M. Wilkens, J.Appl. Cryst. (1989), 22, p 26-34

[64] "*Profile fitting of X-ray diffraction lines and Fourier analysis of broadening*", D. Balzar, J. Appl. Cryst, 25, 1992, p 559-570

[65] "*Effect of heat treatment on the structure and properties of cold sprayed copper*", E. Calla, D.G. McCartney, P.H. Williams, Thermal Spray 2005: Explore its surface potential, ASM International, May 2-4, 2005 (Basel, Switzerland), p. 170

[66] "X-*ray studies of Deformed Metals*", B.E. Warren, Prog. Metal Phys., 8, 1959, p 147-201

[67] "*Dislocation Line Broadening, Z. Kristallogr.Suppl*", R. Kuzel, 23, (2006), p 75-80

[68] "*Second Order phase transformation of the dislocation structure during plastic deformation determined by in situ synchrotron X-ray diffraction*", E. Schafler, K. Simon, S. Bernstorff,P. Hanak, G. Tichy, T. Ungár, M.J. Zehetbauer; Acta Mater., 53, 2005, p 315-322

[69] "*Fourier analysis of X-ray micro-diffraction profiles to characterize laser shock peened metals*", H. Chen, Y. L. Yao, J. W. Kysar, I. C. Noyan, Y. Wang, International Journal of Solids and Structures, 42 (2005) 3471–3485

[70] "*Formation of Persistent Dislocation loops by ultra-high strain-rate Deformation during Cold Spraying*", C. Borchers, F. Gärtner, T. Stoltenhoff, H. Kreye, Acta Mater., 53, 2005, p 2991-3000

[71] "*A Method for Characterizing the Degree of Inter-particle Bond Formation in Cold Sprayed Coatings*", T.S. Price, P.H. Shipway, D.G. McCartney, E. Calla, D. Zhang, Journal of Thermal Spray Technology

[72] "*Cold Spray Technology*", edited by Anatolii Papyrin, Elsevier, First edition, 2007

[73] "*Mass transport in Metals under Intensive Impulse reaction*", A.N. Bekrenev, Journal of Physics and Chemistry of Solids 63 (2002) 1627-1631

[74] "*Mass Tranfer in field of fast-moving deformation disturbance*", A.N. Bekrenev, International Journal of Heat and Mass Transfer 46 (2003) 1665-1673

[75] "*Strain-Induced Structural Changes and Chemical Reactions -I. Thermomechanical and Kinetic Models*", V. I. Levitas, V. F. Nesterenko and M. A. Meyers, Acta Mater. Vol. 46, No. 16, pp. 5929-5945, 1998

[76] "*Strain-Induced Structural Changes and Chemical Reactions II. Modelling of Reactions in Shear Band*", V. I. Levitas, V. F. Nesterenko and M. A. Meyers, Acta Mater. Vol. 46, No. 16, pp. 5947-5963, 1998

[78] "*A systematic approach to material Eligibility for the Cold Spray process*", J. Vleck, L. Gimeno, H. Huber, E. Lugscheider.*Thermal spray 2003: Advancing the Science & Applying the Technology*, C. Moreau, B.R. Marple, Eds., May 5-8, 2003 (Osaka), ASM International.

[79] "*Dynamics of fast dislocations*", C.-H. Woo , Mater. Sc. and Eng. A350 (2003) 223-232

[80] "*High-speed dislocations in high strain-rate deformations*", A. Roos, J.Th.M. De Hosson, E. Van der Giessen, Computational Materials Science 20 (2001) 19-27.